Nanoconfinement for production of platform molecules from carbon oxides

Ana Katiuce Fellenberg

To cite this version:

Ana Katiuce Fellenberg. Nanoconfinement for production of platform molecules from carbon oxides. Catalysis. Université de Lille, 2023. English. NNT : 2023ULILR069 . tel-04552301

HAL Id: tel-04552301
https://theses.hal.science/tel-04552301
Submitted on 19 Apr 2024

THESE DE DOCTORAT

PRESENTEE PAR

Ana Katiuce FELLENBERG

POUR L'OBTENTION DU TITRE DE

DOCTEUR DE L'UNIVERSITE DE LILLE

Ecole Doctorale: Sciences de la Matiére, du Rayonnement et de l'Environnement

Spécialité: Chimie Theorique Physique Analytique

Unité de Chimie et Catalyse du Solide – UCCS (CNRS UMR 8181)

Unité Matériaux et Transformations – UMET (CNRS UMR 8207)

Titre de la these:

Nanoconfinement pour la Synthèse de Molécules Plateforme à Partir des Oxydes de Carbone

Nanoconfinement for Production of Platform Molecules from Carbon Oxides

Soutenu le 13 décembre 2023 devant la Commission d'Examen composée de:

Président du jury et rapporteur: Prof. Pascal FONGARLAND, Université Claude Bernard Lyon 1, France
Rapporteure : Dr Sylvette BRUNET, Directrice de recherche HDR au CNRS, Université de Poitiers, France
Examinateur : Prof. Mark SAEYS, Université de Gand, Belgique
Directeur de thèse : Dr. Andrei KHODAKOV, Directeur de recherche HDR au CNRS, Université de Lille, France
Co-directeur de thèse : Dr Gang JI, Chargé de recherche HDR au CNRS, Université de Lille, France

Nunca desista daquilo que você não passa um dia sem pensar.

Contents

Abstract

Energy and environmental impacts are driving the industrial processes. A sustainable route to produce fuels starts using biomass as raw material. Fischer-Tropsch (FT) synthesis is a promising alternative way for conversion of renewable feedstocks to chemicals and fuels. Even FT synthesis is considered a well-established technology, there are chemistry fundamentals to be better and deeply understood. Besides, the FT process depends strongly on the catalyst performance. The utilization and transformation of CO_2 into value-added chemicals have been of global interest, from both theoretical and practical viewpoints. One example of CO_2 conversion to a useful liquid hydrocarbon is hydrogenation of CO_2 to formic acid (HCOOH). The state-of-the-art hydrogenation of CO_2 to formic acid is produced over homogeneous catalysts. However, there are a few works showing that highly dispersed supported metal catalysts are able to carry out this reaction. The high activity of these catalysts could be assigned to their ability to stabilize the active metal in a state of single-metal atoms or heterogenized metal complexes, which may demonstrate a higher activity than metal atoms on the surface of metal nanoparticles.

In this work we have considered two different confined spaces of carbon-based materials, CNTs and COFs, and evaluated the nanoconfinement of iron, copper and ruthenium active species for CO and CO_2 hydrogenation reactions to produce value-added chemicals and platform molecules.

In the iron catalysts for FT synthesis supported by carbon nanotubes, the active phase was nanoconfined inside the channels or localized on the outer surface. In most of previous works, the distribution of metal nanoparticles inside or outside carbon nanotubes is considered to be immobile during the catalyst activation or catalytic reaction. In this work, we uncovered remarkable mobility of both iron and copper species in the bimetallic catalysts between inner carbon nanotube channels and outer surface, which occurred in carbon monoxide and syngas, while almost no migration of iron species proceeded in the monometallic catalysts. This mobility is enhanced by noticeable fragility and defects in carbon nanotubes, which appear on their impregnation with acid solutions of metal precursors and precursor decomposition. Remarkable mobility of iron and copper species in bimetallic catalysts affects the genesis of iron active sites, and enhances interaction of iron with the promoter. In the bimetallic iron-copper catalysts, the major increase in the activity was

attributed to higher reaction turnover frequency over iron surface sites located in a close proximity with copper.

For CO_2 hydrgenation to formic acid, we propose a strategy based on COF materials with different structures and chemical compositions for mediation of ruthenium dispersion and design of efficient catalysts. Operando characterization combined with catalytic tests revealed that the density of nitrogen functional groups in the COF matrix was the key factor affecting the dispersion and performance of COF-supported ruthenium catalysts. The catalyst performance primarily arises from ruthenium capability to persist as single atoms in specific sites and resist its reduction to the metallic state. The proposed strategy for mediating metal dispersion can be extended to develop a variety of COF-supported single-atom catalysts for different reactions.

Résumé

Les impacts énergétiques et environnementaux ont conduit les processus industriels. L'utilisation de la biomasse comme matière première constitue un moyen durable de produire des carburants. La synthèse Fischer-Tropsch (FT) est une alternative prometteuse pour la conversion des matières premières renouvelables en produits chimiques et en carburants. Même si la synthèse Fischer-Tropsch est considérée comme une technologie bien établie, certains principes chimiques fondamentaux doivent être mieux compris et approfondis. En outre, le procédé FT dépend fortement de la performance du catalyseur. L'utilisation et la transformation du CO_2 en produits chimiques à valeur ajoutée ont suscité un intérêt mondial, tant du point de vue théorique que pratique. L'hydrogénation du CO_2 en acide formique (HCOOH) est un exemple de conversion du CO_2 en un produit chimique utile. A l'état de l'art aujourdhui, l'hydrogénation du CO_2 en acide formique est réalisée à l'aide de catalyseurs homogènes. Cependant, quelques travaux montrent que des catalyseurs métalliques supportés hautement dispersés sont capables de réaliser cette réaction. L'activité élevée de ces catalyseurs pourrait être attribuée à leur capacité à stabiliser le métal actif dans un état d'atomes métalliques uniques ou de complexes métalliques hétérogénéisés, qui peuvent démontrer une activité plus élevée que les atomes métalliques à la surface des nanoparticules métalliques.

Dans ce travail, nous avons considéré deux espaces confinés dans de matériaux à base de carbone, les NTC et les COF, et évalué le nanoconfinement des espèces actives de fer, de cuivre et de ruthénium pour les réactions d'hydrogénation du CO et du CO_2 afin de produire de produits chimiques à valeur ajoutée et de molécules plates-forme.

Dans les catalyseurs à base de fer pour la synthèse FT supportés par des nanotubes de carbone, la phase active était nanoconfinée à l'intérieur des canaux ou localisée à la surface extérieure. Dans la plupart des travaux antérieurs, la distribution de nanoparticules métalliques à l'intérieur ou à l'extérieur des nanotubes de carbone est considérée comme immobile pendant l'activation du catalyseur ou la réaction catalytique. Dans ce travail, nous avons découvert une mobilité remarquable des espèces de fer et de cuivre dans les catalyseurs bimétalliques entre les canaux intérieurs des nanotubes de carbone et la surface extérieure, qui se produit dans le monoxyde de carbone et le gaz de synthèse, alors qu'il n'y a pratiquement pas de migration des espèces de fer dans les catalyseurs monométalliques. Cette mobilité est renforcée par une fragilité

et des défauts notables dans les nanotubes de carbone, qui apparaissent lors de leur imprégnation par les solutions acides de précurseurs métalliques et de la décomposition des précurseurs. La mobilité remarquable des espèces de fer et de cuivre dans les catalyseurs bimétalliques influe la genèse des sites actifs du fer et renforce l'interaction du fer avec le promoteur. Dans les catalyseurs bimétalliques fer-cuivre, l’augmentation de l'activité a été attribuée à une *turnover frequency* (TOF) plus élevée sur les sites de surface du fer situés à proximité du cuivre.

Pour l'hydrogénation du CO_2 en acide formique, nous proposons une stratégie basée sur des matériaux COF avec différentes structures et compositions chimiques pour la médiation de la dispersion du ruthénium et la conception de catalyseurs efficaces. La caractérisation *in-situ* couplée à des tests catalytiques a révélé que la densité des groupes fonctionnels d'azote dans la matrice COF était le facteur clef affectant la dispersion et la performance des catalyseurs de ruthénium supportés par COF. Les performances du catalyseur découlent principalement de la capacité du ruthénium à persister sous forme d'atomes isolés dans des sites spécifiques et à résister à sa réduction à l'état métallique. La stratégie proposée pour la médiation de la dispersion des métaux peut être étendue au développement d'une variété de catalyseurs à atome unique supportés par COF pour différentes réactions.

Literature review

General Introduction

Energy is of utmost importance for the development of modern society and is derived from two main sources: renewable and non-renewable (**Figure 1**). Currently, the energy demand is still almost completely met by fossil fuels, however, there is a drastic depletion of petroleum resources and an immense need to find an alternative to oil-based fuels (Cai, 2015).

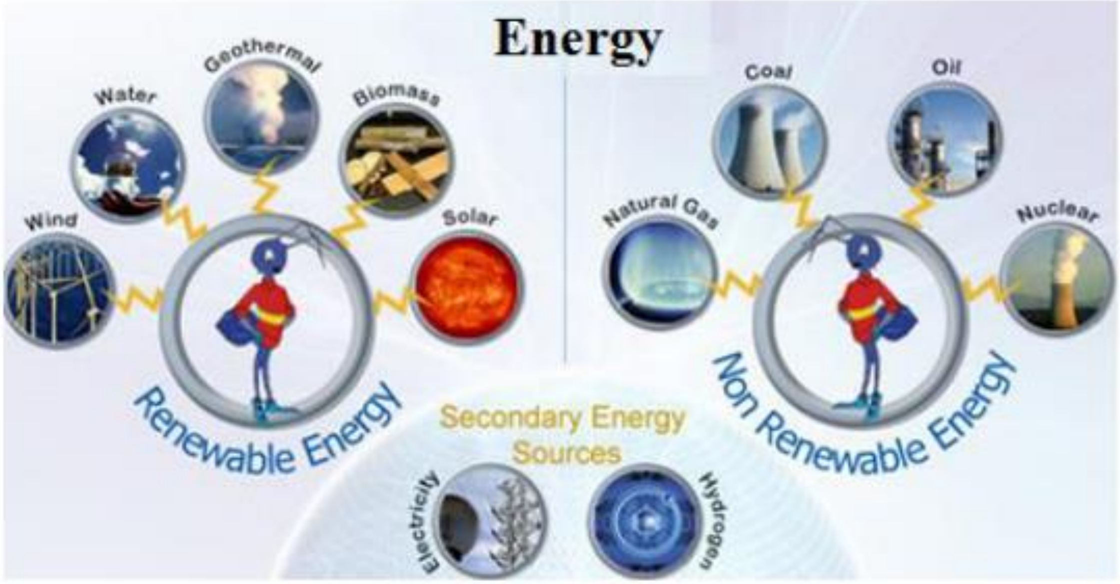

Figure 1. Types of energy(Cai, 2015).

Developing new catalytic processes with low energy consumption also is of utmost importance. The global annual energy demand is over of 12 billion tons of oil equivalent and could double until 2050, which will almost double the annual CO_2 emission if only fossil energy is used (Védrine, 2019).

Fossil fuels are still the main energy source (**Figure 2**) (IEA, 2023), the emitted CO_2 is recognized as very polluting and harmful for the environment and climate (**Figure 3**) (IEA, 2023). In this sense, there are many efforts have been done to identify possible alternatives that are cleaner and more sustainable (Santos & Alencar, 2019).

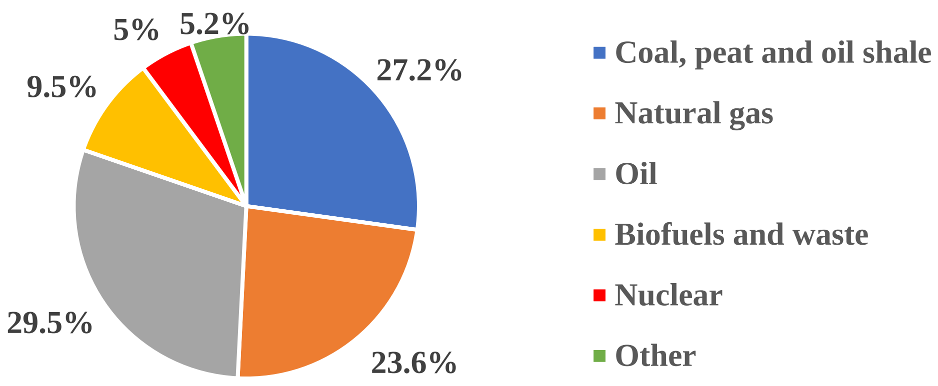

Figure 2. Distribution of total energy supply by product of 2021(IEA, 2023).

The biomass valorization is an important option for energy and chemical production. Nowadays, the outlook of renewable energy appears to be positive. More and more the costs of it is declining, mainly due to the increase in the productivity and efficiency of manufacturing, and large investments in the renewable energy sectors. On the other hand, the costs of energy produced by fossil fuel-based power plants is increasing because of new regulations for carbon, nitrogen oxides and sulfur oxides emissions (Basu, 2018b).

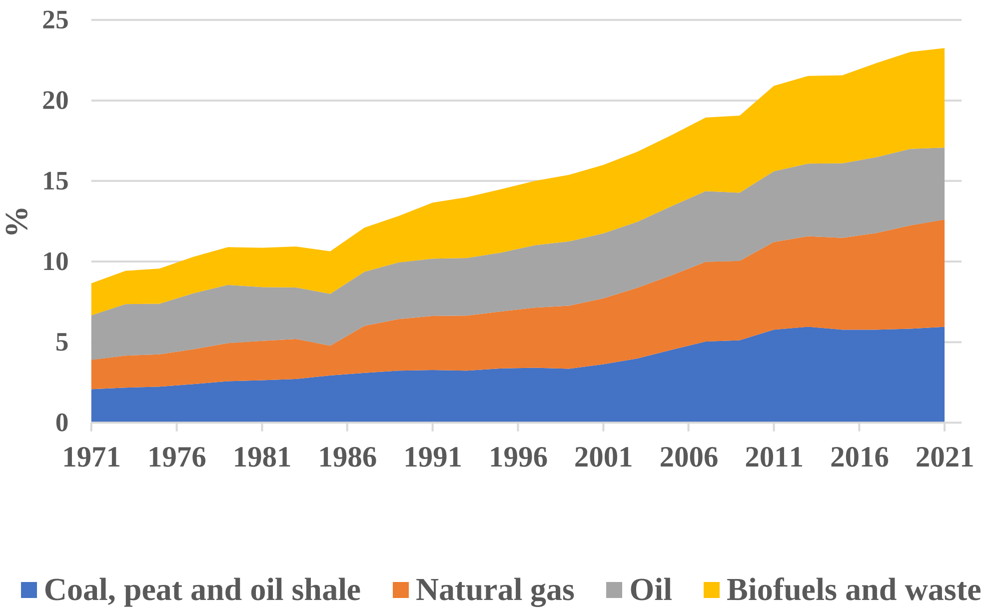

Figure 3. Distribution of total greenhouse gases emissions from fuel combustion by product from the last few decades (IEA, 2023).

Biomass refers to any organic material derived from living or recently living organisms that can be used as a source of renewable energy, as well as for various other applications. It is available not only as solid materials such as fats and grease oils, but also as liquid and gaseous products recovered from the decomposition of non-fossilized and biodegradable organic materials (Basu, 2018a). To be used as feedstock, biomass should be properly characterized with regard to its physical (density, thermal conductivity) and chemical properties (polymeric composition), which are essential for efficient biomass conversion.

Biomass forms through photosynthesis using carbon dioxide and water. As the carbon dioxide released from biomass combustion or degradation is absorbed again by the biomass itself, the biomass is considered neutral to the emission of greenhouse gases (Basu, 2018a).The sources of biomass are plants, agricultural residues, forestry residues, animal manure, algae, organic waste, wood waste, energy crops. These feedstock materials can be used as feedstock or fuel (Basu, 2018a). The most common sources of biomass come from the agriculture, forests, cities, household or municipal waste and energy crops. Based on their origin, biomass can be classified and specified under four broad categories: woody, herbaceous, fruit, blend and mixtures (Alakangas, 2011). Biomass may also be divided into two broad groups: virgin and waste biomass. The first one could be still subclassified as terrestrial (forest, grasses, energy and cultivated crops) and aquatic (algae and water plant); the second one is subclassified as municipal (municipal solid waste, biosolids, sewage, landfill gas), agricultural solid waste (agricultural crop residue, livestock and manures), forestry residues (bark, leaves and floor residues) and industrial wastes (demolition wood, sawdust, waste oil and fat) (Basu, 2018a).

CO hydrogenation : FT synthesis

Fischer-Tropsch (FT) synthesis, developed in the 1920s by Frans Fischer and Hans Tropsch (B. H. Davis, 2009; Khodakov et al., 2007), is an alternative for synthesizing clean liquid fuels, hydrocarbons and oxygenates via non-trivial catalytic polymerization of adsorbed CHx intermediates produced from syngas (i.e. CO and H_2), (Q. Cheng et al., 2018). The syngas is one of the most important platforms for using non-oil carbon resources to supply energy and chemicals (K. Cheng et al., 2017; W. Zhou et al., 2019) (**Figure 4**).

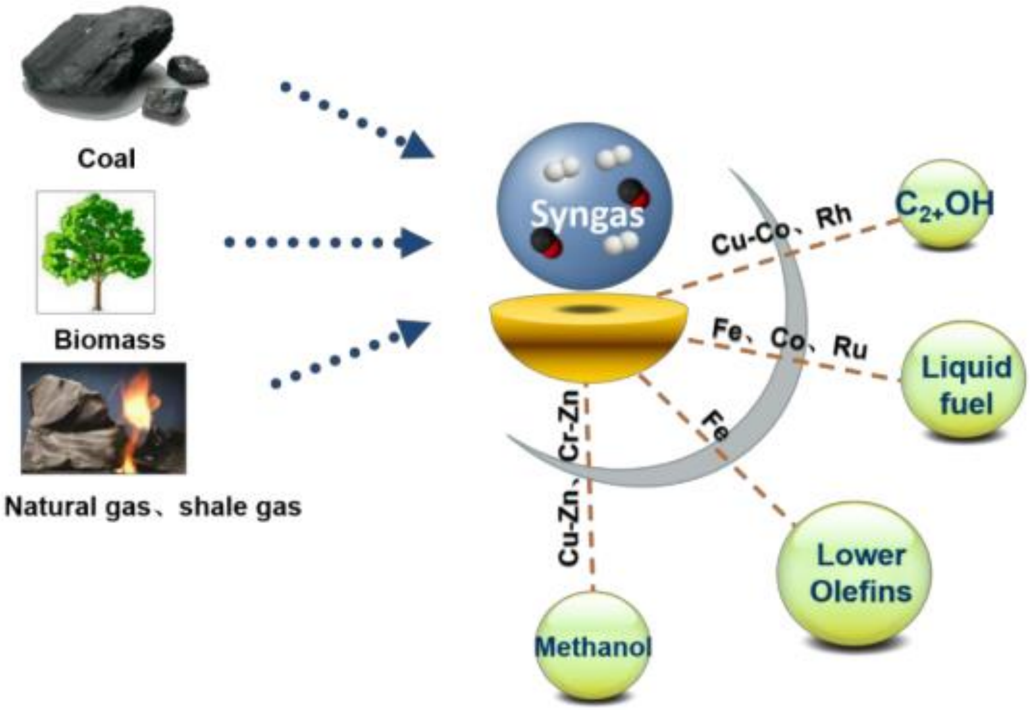

Figure 4. Utilization of non-oil-based carbon resources via syngas conversion to liquid fuels and chemicals (Gu, 2019).

Syngas can be defined as a gaseous mixture composed of hydrogen (H_2) and carbon monoxide (CO) at different ratios and can be used as starting material for fuels and petrochemicals (Lee, 1996). Traditionally, the synthesis gas is obtained from coal, natural gas, residual oils, and petroleum, however, the syngas obtained through biomass (termed biosyngas) is a more sustainable substitute to the fossil-derived syngas (Santos & Alencar, 2019).

In addition to being considered an important route to clean fuels, FT synthesis is also receiving attention due to greater concerns about supply of conventional energy feedstocks (oil, gas) and the implementation of more stringent environmental legislation (Q. X. Luo et al., 2019).

Besides the synthesis of high quality paraffins, gasoline, diesel and wax, the FT synthesis can be adjusted to synthesize platform molecules such as olefins, higher alcohols and aldehydes. Even the direct synthesis of higher alcohols and olefins from syngas via FT is a promising route and despite the efforts already made, an industrial process has not yet been developed (Z. Zhao et al., 2018). The industry is considering using the FT synthesis process as an alternative way to compensate for the depletion of crude oil resources (C. H. Zhang et al., 2006). FT synthesis can produce a wide range of fuels and chemicals (**Figure 5**).

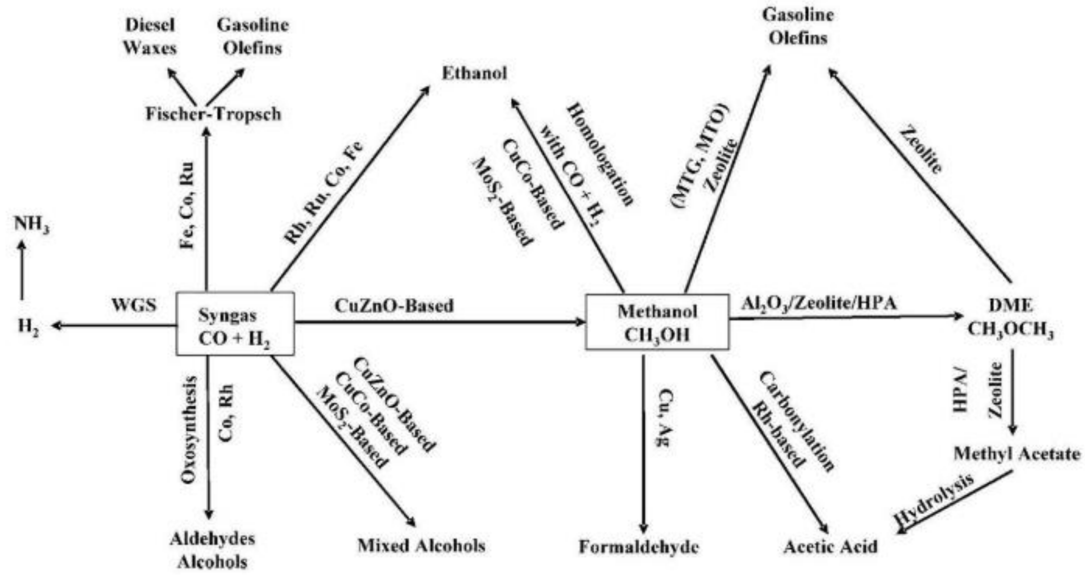

Figure 5. Opportunities for catalytic conversion of syngas to fuels and chemicals: WGS = water–gas shift; MTG = methanol-to-gasoline; MTO = methanol-to-olefin; DME = dimethyl ether; HPA = heteropoly acid(J. Wang, 2012).

FT synthesis produces predominantly linear hydrocarbons suitable for high-quality diesel, sulfur-free and aromatic-free liquid fuels and valuable by-products. The yield of products in the gasoline range can be increased with optimization of process conditions and catalyst properties. Several metals exhibit remarkable activity in the synthesis of hydrocarbons from syngas, however, even after so long time, only iron and cobalt catalysts have found industrial application (Eriksson, 2008).The most suitable catalysts from an economic point of view and generally the most used in FT processes, are the catalysts based on iron and cobalt. The supported cobalt-based catalysts represent the ideal choice for the synthesis of long-chain hydrocarbons, and the most studied supports are silica, alumina, zirconia, carbon, mesoporous or zeolite supports. However, Fe-based catalysts have an interesting feature, they are able to correct the H_2/CO ratio in syngas through the water-gas-shift (WGS) reaction (Abelló & Montané, 2011).

One of the important platform molecules for the chemical industry are light olefins. Also important as feedstocks, light olefins can be synthetized by different ways and the research and development of light olefin synthesis has been prioritized not only by the academia, but also by the industry. Between different methods of synthesis of light olefins, we can mention the cracking of oil fractions, FT synthesis, dehydrogenation, oxidative dehydrogenation, Methanol to Olefins process, methanol-mediated CO and CO_2 hydrogenation, electrocatalytic reduction of CO_2. These approaches vary as functions of raw materials, which cover a diversity of renewable and fossil raw materials, catalysts and reaction conditions. The main groups of light olefins synthesis using carbon oxides as feedstock include the FT synthesis with CO (See **1.2.2**) and CO_2, the electrocatalytic CO and CO_2 reduction and the methanol-mediated CO and CO_2 hydrogenation (Chernyak et al., 2022).

Considering the raw materials, CO and CO_2 becoming more and more important feedstocks for the synthesis of fuels and chemicals. Syngas, in particular, is being extensively explored due to environmental concerns and sustainability, driving the development of new technologies for synthesizing light olefins (Chernyak et al., 2022).

Mechanisms for CO hydrogenation

The CO hydrogenation reaction could take different pathways, because of its complex mechanism, and the large number of species that are produced. During the FT reaction, the reactants CO and H_2 will adsorb in the active sites of the catalyst. The adsorption of H_2, in the majority of metal transition active sites, occurs in the dissociative way and, at the reaction conditions, it can take place in one or two sites. The adsorption of H_2 is specially affected by the temperature. Also, CO and H_2 can compete for the same active sites (Beiramar, 2013).

Generally, the first step in the FT reaction mechanism, is CO adsorption. Some theoretical studies showed that CO activation mainly proceeds by the H-assisted CO dissociation via HCO intermediate on the different superficies (Pham et al., 2014). Once the CO molecule is adsorbed on the metal, an associative or dissociative mechanism can occur, depending on the nature of the metal present on the surface and the reaction temperature(Beiramar, 2013).

At room temperature, only a small part of the transition metals to the left of the periodic table produces a dissociation of the CO molecule. On the other hand, under the conditions of the Fischer-Tropsch reaction, more transition metals in the right side of the Table cause dissociation of CO (Beiramar, 2013). After CO dissociation, CH_x species can polymerize and yield hydrocarbons. Some metals such as copper or palladium are unable to dissociate carbon monoxide and have a high selectivity of methanol, instead of hydrocarbons, in FT reaction. The metal-carbon bond is a key parameter in the selectivity of CO hydrogenation. If the bond is too strong or too weak, methane will form, and if the bond is intermediate it will form longer hydrocarbons. The stability of transition metal carbides changes over the periodic table, increasing to the left. In the case of metals like Ni and Fe, the stability of Fe carbides will be higher than the stability of Ni carbides. Likewise, Fe catalysts have higher selectivity for hydrocarbons, while Ni catalysts have higher selectivity for methane (Gracia et al., 2009).

Historically, two mechanisms have been proposed for the FT process (Muetterties & Stein, 1979). The carbide theory was first proposed by Fischer and Tropsch in 1926 (Fischer & Tropsch, 1926). According to this theory, adsorbed carbon monoxide is reduced to surface carbide which can then be hydropolymerized to hydrocarbons. A second mechanism involves the formation of unstable intermediates containing C, H, and O atoms such as HCOH surface complex (Henrici-Olivé & Olivé, 1976). The carbide theory has been revised to include initiation, propagation, and termination steps, and the modified theory is consistent with the Flory-Schultz distribution of produced hydrocarbons (Biloen et al., 1979; Elvins & Nash, 1926; Muetterties & Stein, 1979; Helmut Pichler, 1952).

Nowadays, the three main mechanisms that have been proposed for iron catalysts. They involve surface carbide, surface enol and CO insertion mechanisms(E. De Smit & Weckhuysen, 2008). The surface carbide mechanism is the first and mostly accepted mechanism for FT synthesis on iron proposing the chain growth by CH_2 insertion (**Figure 6**).

Initially proposed by Fischer and Tropsch (Fischer & Tropsch, 1926) for bulk carbide and surface carbide species, the "carbide" mechanism proceeds via complete dissociation of CO in C and O with subsequent hydrogenation of atoms, hydrogen-assisted dissociation of CO and H interaction with non-CO decoupled.

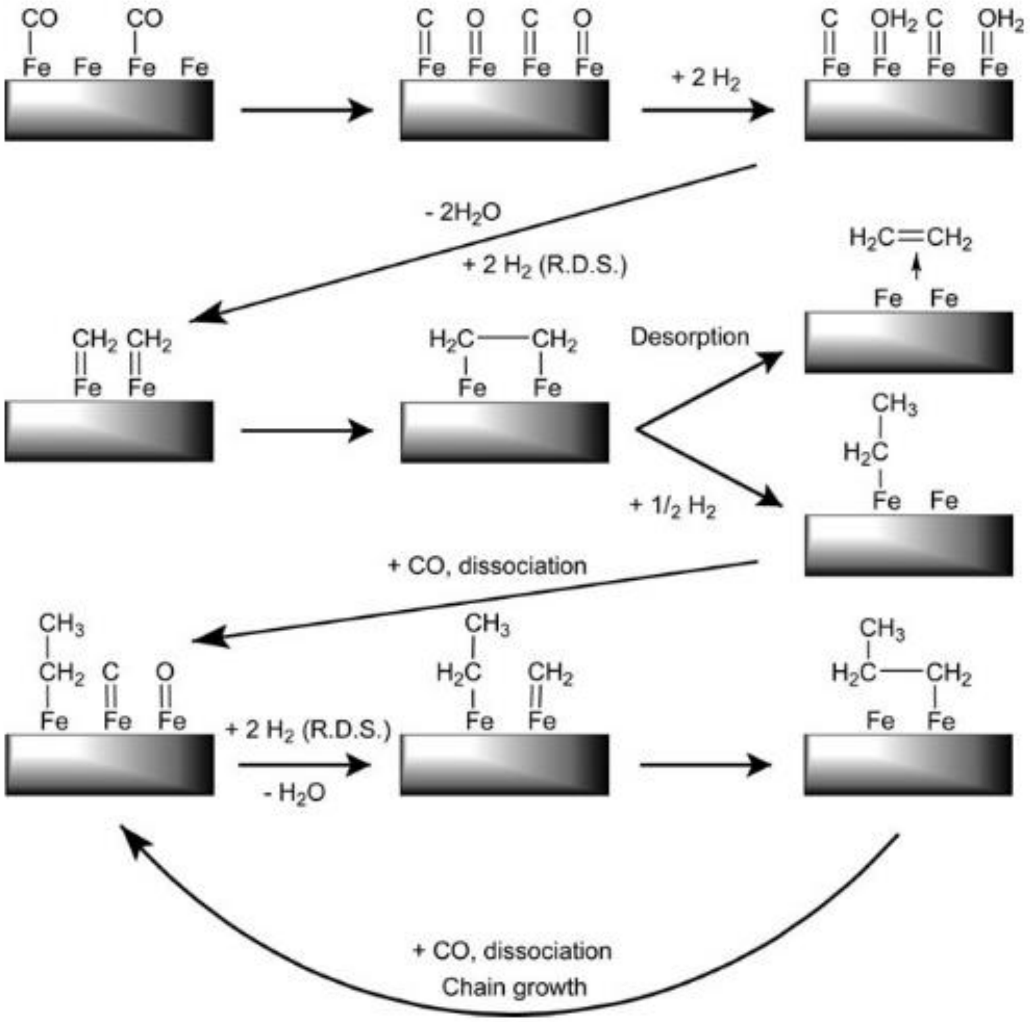

Figure 6. Representation of the surface carbide mechanism (RDS: rate determining steps) (E. De Smit & Weckhuysen, 2008).

As showed in the scheme above, this mechanism presumes the dissociative adsorption of CO and H_2, followed by the formation of CH_2 entities which can combine and insert in the growing chains. The chain termination could be either by abstraction or addition of a hydrogen atom from or to the growing chain. In this mechanism, the CH_2 species should be either fixed to the catalyst surface, which implies the need for them to adsorb; alternatively, it can be assumed that the CH_2 (and CH and CH_3) species are more mobile and are able move over the catalyst surface (E. De Smit & Weckhuysen, 2008; Muetterties & Stein, 1979).

The second mechanism proposes chain growth through non-dissociative adsorption of CO (**Figure 7**) (Biloen et al., 1979; E. De Smit & Weckhuysen, 2008; Kummer & Emmett, 1953; Vannice, 1976).

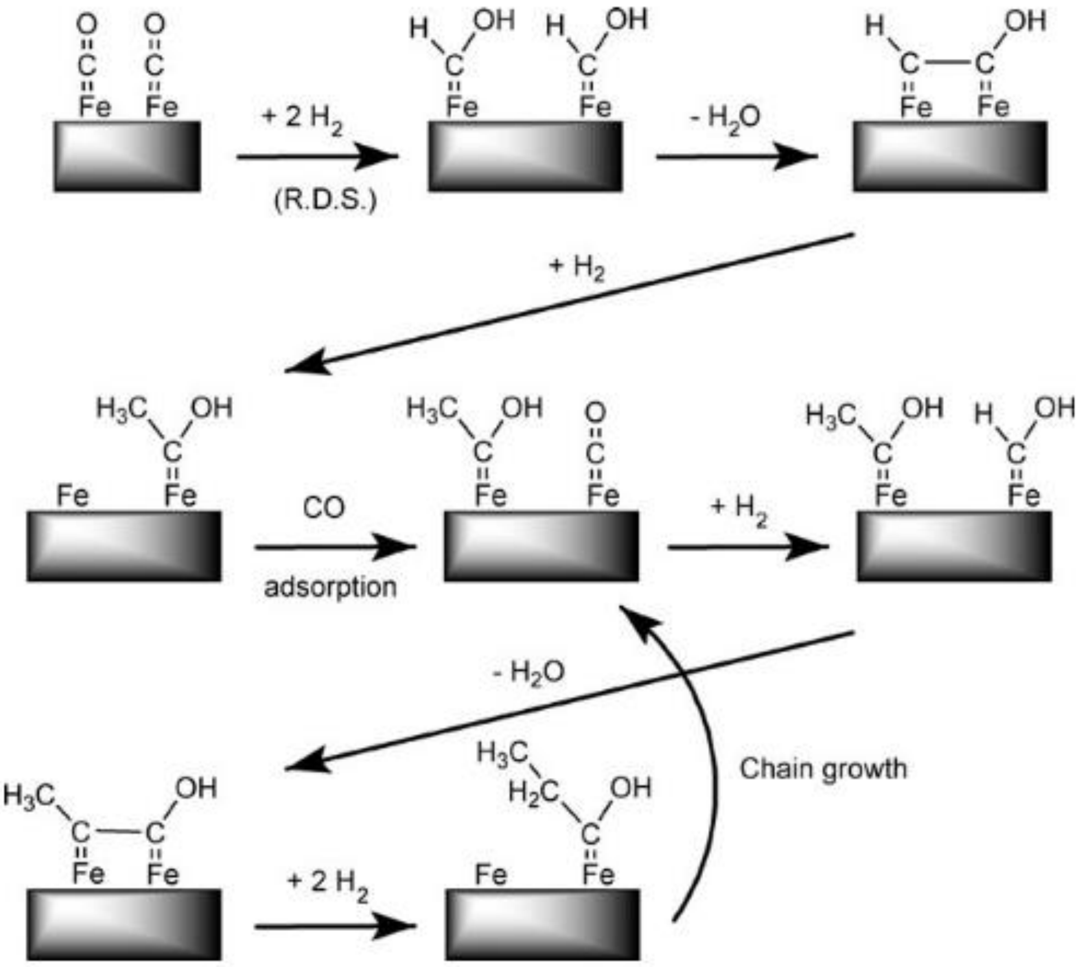

Figure 7. Representation of the surface enol mechanism (RDS: rate determining steps)(E. De Smit & Weckhuysen, 2008).

In the oxygenation mechanism, first reported by Emmett (Podgurski et al., 1950) and then by Davis (Davis, 2009), the chain growth involves the insertion of CO, which leads to hydrocarbons and oxygenates (V. V. Ordomsky et al., 2015).

The surface enol mechanism says that the surface hydrogen atoms react with the chemisorbed CO groups to form enolic (HCOH) entities, which can either combine through a surface polymerization condensation reaction with a loss of water (Kummer & Emmett, 1953). Many studies performed by Emmett and co-workers (Blyholder & Emmett, 1959; Hall et al., 1960; Hall et al., 1957; Kummer et al., 1951; Kummer & Emmett, 1953) using ^{14}C-tracer corroborated this mechanism. Other alternative option for this mechanism is the individual hydrogenation of the enolic entities, forming water and CH_2 groups (Biloen et al., 1979; Huff & Satterfield, 1984; Vannice, 1976).

The third reaction mechanism involves chain growth through insertion of CO molecules in the metal–carbon bonds (**Figure 8**).

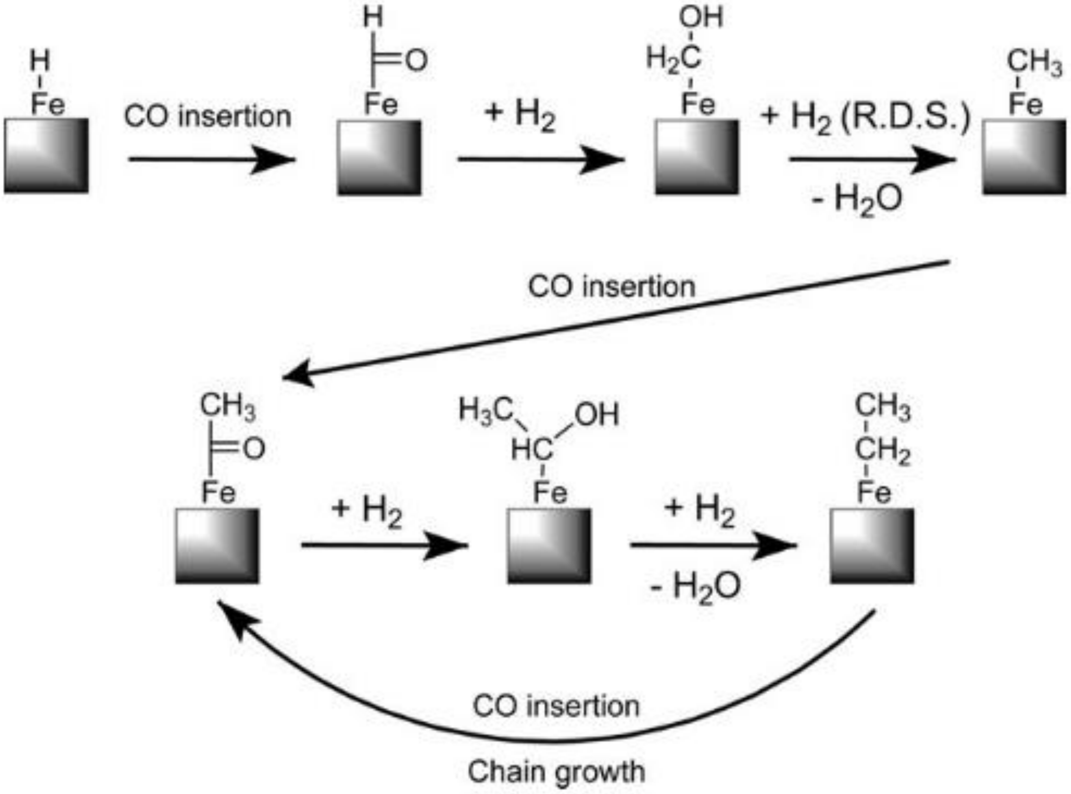

Figure 8. Representation of the CO insertion mechanism (RDS: rate determining steps)(E. De Smit & Weckhuysen, 2008).

The CO insertion mechanism was proposed for the first time by Pichler and Schulz (H. Pichler & Schulz, 1970) and further modified by Henrici-Olivé and Olivé (Henrici-Olivé & Olivé, 1976) and Masters (Masters, 1979). According to this mechanism, a CO molecule is inserted into the metal–H bond in the first (initiation) step. Then, the formed surface aldehyde species are hydrogenated to CH_3 by nearby chemisorbed hydrogen atoms (rate limiting step). Next, CO can be inserted into the metal–carbon bond and the resulting enol species can be hydrogenated again. The chain growth occurs by the repetition of this last step. The termination happens by hydrogenation of the growing chain, which results in a free olefin molecule and an adsorbed hydrogen atom (E. De Smit & Weckhuysen, 2008).

These mechanisms presume, in general, six elementary reaction steps as followed: (1) Reactant adsorption; (2) Chain initiation; (3) Chain growth; (4) Chain termination; (5) Product desorption; and (6) Olefin readsorption and other side reactions (Adesina, 1996).

In most cases, the steps 2 through 4 can be accurately described by Anderson–Schulz–Flory (ASF) kinetics model. This model, which is the most widely accepted to describe the distribution of products, assumes that the FT reaction is an ideal linear polymerization reaction in which there is one single growth probability, α, which determines the hydrocarbon chain length distribution (E. De Smit & Weckhuysen, 2008). In this model, the probability of chain growth is defined between 0 and 1 (Gu, 2019). The molar fraction M_n can be calculated from the chain growth probability (E. De Smit & Weckhuysen, 2008):

$$M_n = (1 - \alpha)\alpha^{n-1} \qquad \textbf{(Eq. 1)}$$

where M_n is the Cn hydrocarbon weight fraction with n carbon atoms in the product mixture, α is the probability of chain growth and (1 – α) is the probability of chain termination. The α is independent on the mole fraction of hydrocarbon (M_n) and chain length (n), being defined as a ratio between the rates of propagation (R_p) and termination (R_t) (E. De Smit & Weckhuysen, 2008):

$$\alpha = \frac{R_p}{R_p + R_t} \qquad \textbf{(Eq. 2)}$$

This equation is represented graphically (**Figure 9**), where the variation of the percentage by weight of the different hydrocarbon fractions is plotted against the chain growth probability.

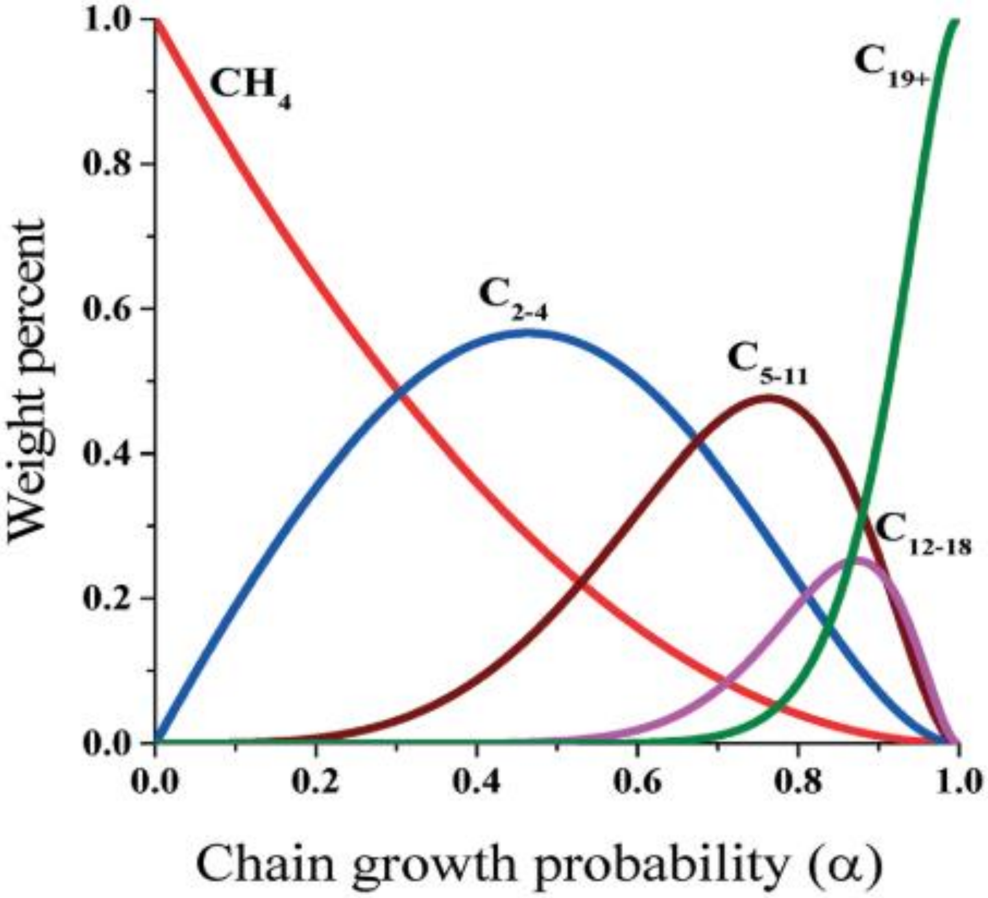

Figure 9. Hydrocarbon weight fraction as function of the chain growth probability factor (α) (Qiang Wang et al., 2019; H. Yang et al., 2017).

Typical FT products follow ASF (Anderson–Schulz–Flory) distribution, which includes large amounts of saturated alkanes and long chain hydrocarbons (Zhiqiang Yang et al., 2012). The selectivity of C_2-C_4 hydrocarbon products does not exceed 58%, limited by the ASF distribution. For hydrocarbons in the gasoline range (C_5-C_{11}) and for hydrocarbons in the diesel range (C_{10}-C_{20}), the maximum selectivity according to the ASF law is around 45% and 39%, respectively. The optimal a value for the FT process depends on the target hydrocarbon fraction (E. De Smit & Weckhuysen, 2008; Qiang Wang et al., 2019; H. Yang et al., 2017).

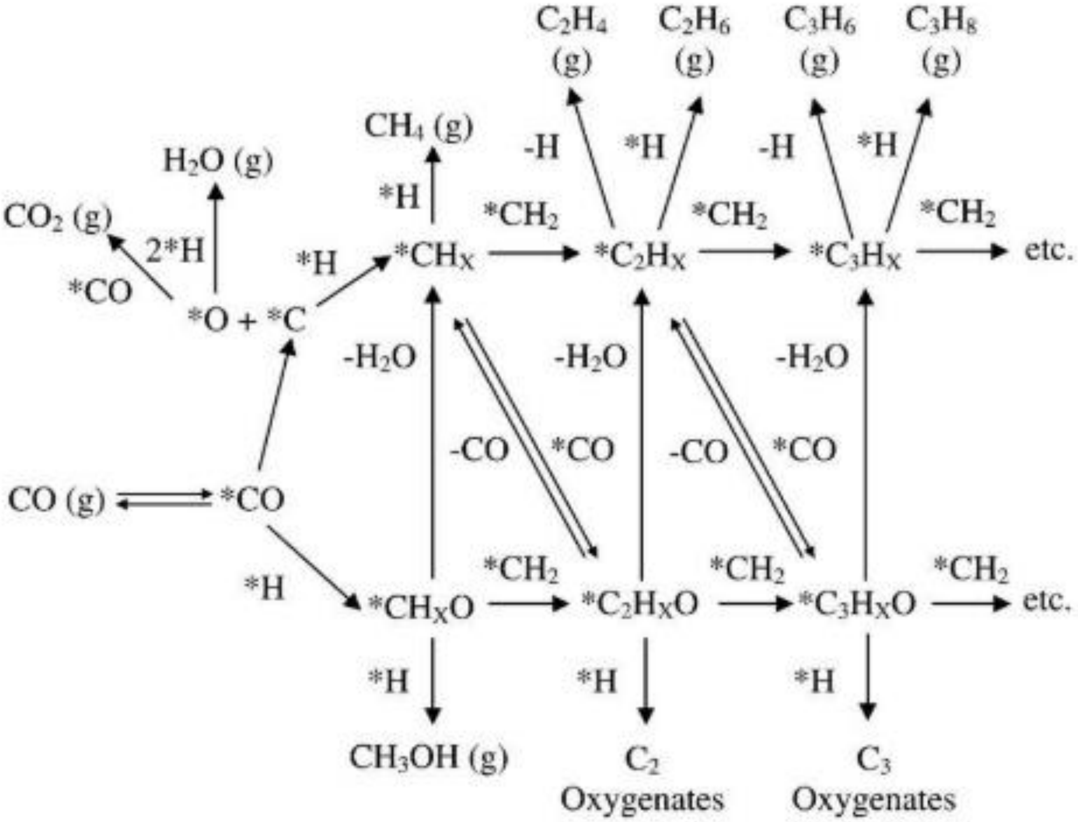

Figure 10. CO hydrogenation network(J. Wang, 2012).

Typically, FT synthesis produces a mixture of multiple products, including alcohols, paraffins, olefins, and other chemicals (See **Figure 10** above). Some important reactions are listed as follows: (An et al., 2017; K. Cheng et al., 2017; Q. Zhang et al., 2014)

Paraffins: $$nCO + (2n+1)H_2 \rightarrow C_nH_{2n+2} + nH_2O \quad \textbf{(Eq. 3)}$$

Olefins: $$nCO + 2nH_2 \rightarrow C_nH_{2n} + nH_2O \quad \textbf{(Eq. 4)}$$

Alcohols: $$nCO + (2n-1)H_2 \rightarrow C_nH_{2n-2}OH + (n-1)H_2O \quad \textbf{(Eq. 5)}$$

CO in the syngas stream can be also converted to CO_2 and H_2 through the water–gas shift (WGS) reaction(F. Li & Fan, 2008):

Water-gas shift reaction: $$CO + H_2O \rightarrow CO_2 + H_2 \quad \textbf{(Eq. 6)}$$

During the production of syngas, the water–gas shift (WGS) reaction is usually employed for the adjustment of the H_2/CO ratio. The FT synthesis typically requires a suitable H_2/CO ratio (~2). Hence, for the syngas (lower H_2/CO ratio) arising from biomass gasification, the WGS reaction should be applied. However, the WGS process consumes large quantity of H_2O and produces CO_2 (K. Cheng et al., 2017; F. Li & Fan, 2008). WGS reaction can increase or decrease the FT rate (Barrios Medina, 2023).WGS occurs on iron catalysts, while on cobalt counterparts, WGS is not significant.

WGS reaction represents one of the possible reaction pathways for the CO_2 production in FT synthesis. Usually, the WGS reaction is expected to be more significant at higher CO conversion when water production is getting more important (Gu, 2019). Higher CO_2 selectivity at higher CO conversion is usually observed over iron FT catalysts and can be relevant to the higher rate of water gas shift reaction due to intensive water production at high CO conversion (Gu, 2019). The CO conversion to hydrocarbons can be described as the total conversion of CO minus the CO converted in the WGS reaction (Tavasoli et al., 2009).

Apart from alkali promoters, WGS reaction may also tune the methane selectivity at different CO conversions, especially at conversion levels higher than 80%. The methane selectivity increased significantly with H_2/CO ratio in that range. When CO conversion is higher than 70%, the WGS reaction becomes significant compared to FT synthesis and the CH_4 selectivity increases rapidly due to higher H_2/CO ratios caused by the WGS reaction(J. Yang et al., 2014).

Selectivity of Fischer-Tropsch Synthesis

One of the most difficult challenges in FT synthesis is the control of selectivity. Following the Anderson-Schultz-Flory (ASF) statistics, the hydrocarbon chain length distribution is generally quite broad and non-selective. The application of the FT process for specific hydrocarbon fractions ends up being significantly limited by the low selectivity. An example of this is diesel, a fuel consisting mainly of C_{10}-C_{20} hydrocarbons; however, the FT reaction does not selectively produce gaseous methane to solid C_{60}-C_{80} waxes from hydrocarbons. Some strategies can be used to restrict the wide distribution of FT hydrocarbons to a specific range of hydrocarbons. Such as, the addition of a catalytic cracking stage to the FT technology, to update the reaction products to a specific fuel, with a narrow hydrocarbon distribution. However, catalytic cracking has several stages and this ends up significantly reducing the efficiency of synthetic fuel production(Subramanian et al., 2016).

Several strategies can be applied to break the broad ASF hydrocarbon distribution. The first strategy is bifunctional catalysts, which combine an active phase of FT, such as cobalt, and an acid catalyst, such as zeolites. However, bifunctional catalysts can suffer from deactivation and low selectivity and these problems may increase with time in operation, due to the different deactivation rates of the FT reaction and hydrocarbon cracking (Subramanian et al., 2016).

The molecular size of the reaction products can also be controlled by the shape selectivity, that is, the transformation of the reactants into products will depend on how the processed molecules adjust to the active site of the catalyst(B. Smit & Maesen, 2008). The effect of shape selectivity on FT synthesis was discovered in 1980 by Fraenkel (Fraenkel & Gates, 1980), who demonstrated that cobalt metal agglomerates embedded in very small cavities of zeolite A (1.1 nm) produced mainly propane and propylene. The selectivity phenomena in catalysts with different pore sizes can also be attributed to different dispersions of metal. Higher selectivity of long-chain hydrocarbons can be due to the larger size of the metal agglomerates (Subramanian et al., 2016).

Our group proposed (Subramanian et al., 2016) a new approach to control the selectivity of FT synthesis by using nanoreactors with incorporated metal nanoparticles. Encapsulation of Co nanoparticles in nanosized porous silica spheres results in higher activity per catalyst weight and stability with a shift of the chain length distribution of hydrocarbons to lower values in comparison with FT synthesis over impregnated catalysts. These effects are due to the presence of well dispersed isolated and stable Co nanoparticles inside of nanoreactors and shape selectivity effect which restricts the chain growth by the walls of nanoreactors. This approach resulted in one step selective production of diesel range hydrocarbons from syngas.

To improve the selectivity of liquid fuels, hydrocracking is usually performed. For the production of liquid fuels to be effective and efficient in terms of energy and economy, the process must be direct rather than multi-stage. That is why it is so important to design FT catalysts capable of segmenting products with high performance and selectivity (Q. Cheng et al., 2018).

Fischer-Tropsch Synthesis for Light Olefin Production

Light C_2−C_4 olefins are basic feedstocks and conventionally obtained in a massive scale in industry, mostly produced by thermal or catalytic cracking of shale gas or petroleum fractions. One sustainable alternative for direct light olefin synthesis from syngas, derived from fossil and renewable feedstocks, is the high-temperature Fischer−Tropsch synthesis (Vitaly V. Ordomsky, Luo, et al., 2017).

The high-temperature FT (HTFT) synthesis presents narrower C number distribution and higher light olefin selectivity in comparison with the low-temperature FT (LTFT) synthesis (**Figure 11**). For Fe-based catalysts, the operations in HTFT synthesis have some limitations such as low product selectivity, catalyst agglomeration and sintering. The particle size of Fe species, Fe precursors, promoters and supports are most important parameters that will have influence in HTFT reaction (Wu et al., 2019).

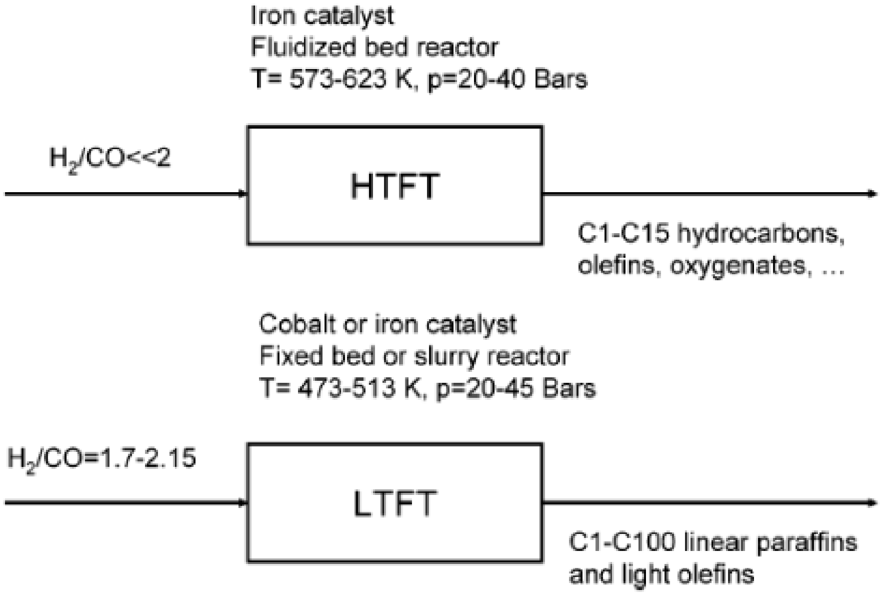

Figure 11. High- and low-temperature FT processes(Hong, 2009).

The direct conversion of syngas using the FT synthesis produces S- and aromatic-free hydrocarbons, which render the FT process more sustainable and still interesting owing to its industrial feasibility (Wu et al., 2019). Light olefins can be used to synthesize many products, such as polymers, solvents, drugs, cosmetics, and detergents. But, due to the shortage of crude oil reserves and environmental constraints, it is necessary to develop alternatives to making full use of resources and ensuring national energy security. Besides the main cracking and reforming, others processes such as catalytic dehydrogenation of light alkanes, oxidative coupling of methane and syngas to olefins including the FT synthesis and methanol-to-olefins process have become more important. But principally, developing a process for direct conversion of syngas to olefins is of vital significance, since it is possible to produce syngas by gasifying of coal, methane reforming, or even gasifying biomass (Wu et al., 2019).

The strategy based on the production of lower olefins from syngas can be categorized in direct and indirect processes (**Figure 12**). The most environmentally interesting and economically most profitable process is the direct process of converting syngas into Fisher-Tropsch to Olefins (FTO) (Y. Cheng et al., 2016).

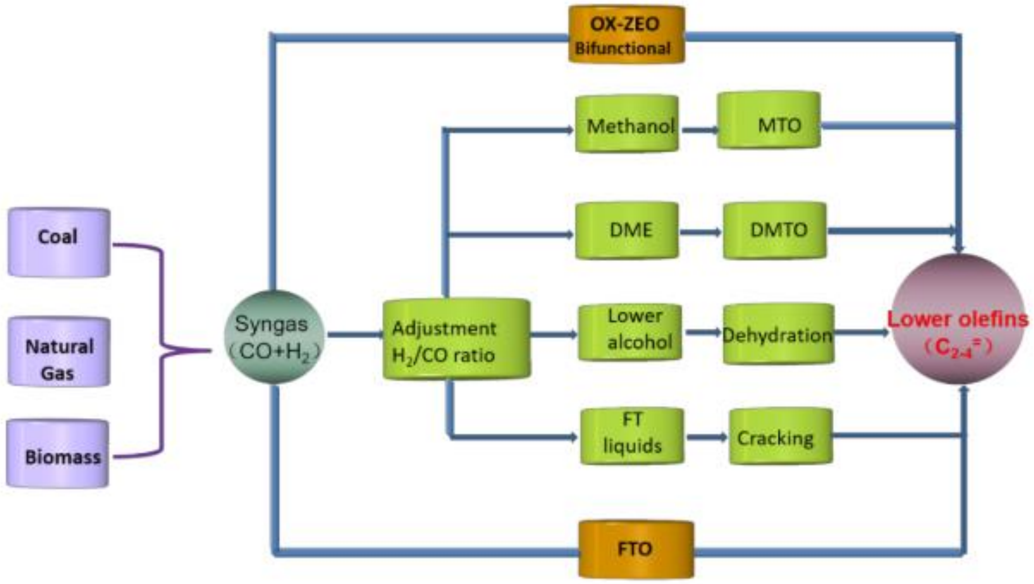

Figure 12. Process for the transformation of CO-rich synthesis gas into light olefins(Gu, 2019).

The iron-based FT catalysts appear to be more promising for direct synthesis of light olefins from syngas, due to relatively higher olefin selectivity and lower methane selectivity. Low stability of iron catalysts against oxidation under reaction conditions restrict their commercial application at an industrial scale (Zhiqiang Yang et al., 2012)

The olefin selectivity of iron-based catalysts depends on the relative number of phases present in the active catalyst. The phases present in the calcined catalyst are quite different from those present in the catalyst during the reduction and in the initial reaction period. Fe-based catalysts undergo rapid changes and convert mainly to metallic iron or iron carbides: $Fe_2O_3 \rightarrow Fe_3O_4 \rightarrow Fe_5C_2$ (D. Das et al., 1997).

Yang et al incorporated iron nitride (FeN) nanoparticles into the channels of carbon nanotubes (CNTs) and used them as a catalyst for light olefin synthesis from syngas. Theoretically predicted earlier, the cubic iron nitride phase was achieved and facilitated by the confinement inside CNTs. Because of its higher resistance to oxidation under reaction conditions, this CNT-confined iron nitride catalyst exhibited a much higher activity than the reduced iron catalyst. Probably due to a higher concentration of cubic phase iron nitride and restriction of the particle size inside CNTs, the CNT-confined iron nitride catalyst was also more active than iron nitride particles dispersed on the outer walls of CNTs (Zhiqiang Yang et al., 2012).

In FTO processes, Fe-based catalysts occupy an indispensable status, not only for their low cost and high water-gas exchange activity, but also for their high selectivity to olefins with low methane productivity at high reaction temperatures. With regard to the supports for the Fe catalysts, the carbon materials appear to be promising for use in FTO, due to the support-metal interaction (Y. Cheng et al., 2016). Even more than 90 years of study in FT synthesis field, the Fe-based catalyst systems have remained the first choice for commercial FT plants, due to their low cost and tendency to yield high amounts of olefins.

Catalysts for Fischer-Tropsch synthesis

Cobalt and iron are industrially important catalysts for FT processes (see **Table 1** for a comparison). Cobalt presents a reasonable balance between activity, selectivity for long-chain hydrocarbons, price and reservoir. Metallic cobalt (Co^0) is considered to be the active phase in FT synthesis, and to increase its exposure to syngas, cobalt is generally loaded on supports with a high surface area, as well as increasing the dispersion of Co^0 decreasing its size is a commonly used strategy practiced for the development of a more efficient catalyst (Q. X. Luo et al., 2019).

Table 1. Comparison of cobalt and iron FT catalysts (Hong, 2009; Khodakov et al., 2007).

Parameter	Cobalt catalyst	Iron catalyst
Cost	More expensive	Less expensive
Lifetime	Resistant to deactivation	Less resistant to deactivation
Activity at low conversion	Comparable	
Productivity at high conversion	Higher; Less significant effect of water on the rate of CO conversion	Lower; Strong negative effect of water on the rate of CO conversion
Maximal chain growth probability	0.94	0.95
Water gas shift reaction	Not very significant; more noticeable at high conversions	Significant
Maximal sulfur content	< 0.1 ppm	< 0.2 ppm
Flexibility (temperature and pressure)	Less flexible; significant influence of temperature and pressure on hydrocarbon selectivity	Flexible; methane selectivity is relatively low even at 613 K
H_2/CO ratio	~ 2	0.5 – 2.5
Attrition resistance	Good	Not very resistant

Catalysts based on cobalt, ruthenium and iron are conventional catalysts in FT synthesis. Co-based catalysts have the advantage of low activity in water gas shift reaction and high catalytic activity and stability in the FT processes. The catalytic activity and selectivity of FT synthesis can be drastically affected by the size of cobalt crystallites (Q. Cheng et al., 2018).

The size of cobalt crystallites can be controlled by different preparation routes, such as incipient moisture impregnation, electrostatic adsorption and homogeneous deposition precipitation. Generally, throughout the process of the FT reactions, cobalt gradually aggregates, which can bring conflicting results depending on the size of the cobalt crystallites in the selectivity of the products. A strategy to stabilize and immobilize metallic crystallites may lay through confinement. This can restrict the sintering of crystallites at high temperatures and also effectively inhibit the aggregation of metallic crystallites (Q. Cheng et al., 2018).

Cheng et al.(Q. Cheng et al., 2018) synthesized uniformly sized Co_3O_4 nanocrystals, which were incorporated into the mesoporous SiO_2 support to prevent aggregation in the FT synthesis. The actors were able to adjust the selectivity of the FT synthesis products from the diesel fraction (66.2%) to the gasoline fraction (62.4%) by controlling the crystallite sizes from 7.2 to 11.4 nm of the confined cobalt catalysts (Q. Cheng et al., 2018).

Known for their high selectivity and low costs, Fe-based catalysts can be the best candidates for converting syngas into liquid fuels and olefins. Iron-based catalysts are widely applied in FT synthesis because they are cheaper, flexible to changes in temperature, pressure and different H_2/CO ratios (Zhiqiang Yang et al., 2011). These catalysts in addition to having less methane selectivity and greater water gas shift (WGS) reaction activity, allowing the use of a CO-rich syngas feed (Y. Liu et al., 2015). There are several methods of synthesis of Fe-based nanocatalyst: precipitation, hydrothermal synthesis, solvent-thermal method and microemulsion method. Precipitation is the simplest method, it can lead to agglomeration of primary particles that have a wide size distribution (Wu et al., 2019). Iron oxide precursors are often synthesized by the addition of an iron nitrate solution and a sodium carbonate solution. However, the average crystallite size of the precipitated hematite phase is typically large while nanometer-sized iron particles are essential to obtain high selectivity and good stability in FT processes. Nanomaterials can offer a different morphology and improved surface area, which should theoretically produce higher reaction rates, due to the increase in available active sites (Y. Liu et al., 2015).

In the Fe-based catalysts supported on carbon nanotubes (CNTs), under conditions of FT reaction, the Fe_3O_4 change irreversibly and quickly to Fe carbides and vice versa, while the activity can be correlated with the Fe carbide surface area, active phase in the FT reaction. It is likely that, due to the rapid transformation of the catalytic phases, the C atoms on the surface are incorporated into the reaction products.

Pan et al. (Pan & Bao, 2011) studied the effect of confinement on the FT synthesis by comparing external iron (Fe-out) and internal iron (Fe-in). According to the authors, more than 70% of the Fe particles were distributed within the CNT channels for the confined Fe-in catalyst. For Fe-out, almost all the Fe particles were on the outside of CNTs. The confined catalyst Fe-in favoured the conversion of CO and also the formation of long-chain hydrocarbons. The conversion of CO to Fe-in was almost 1.5 times greater than to Fe-out, and the yield of C_{5+} hydrocarbons from Fe-in was 2 times greater compared to Fe-out. Pan et al.(Pan & Bao, 2011) also used carbon black XC-72, with a surface area similar to that of MWCNTs for comparison and the Fe-in yield was 6 times higher than this.

Pan et al. (Pan & Bao, 2011) also found that the confinement of a two-component RhMn catalyst in the CNT channels (RhMn-in) also increased its catalytic activity for the conversion of syngas into C_2 oxygenates in relation to the external catalyst (RhMn-out). The authors noted that particle size was not the only factor that affected activity, because the two fresh catalysts had similar size distributions, suggesting that spatial restriction may not have been the only effect. According to the authors, Raman's spectra indicated that the activation of CO may have been modified within the CNTs. The oxophilic Mn could remain in a more reduced state within the CNT channels compared to the external Mn species, which could facilitate the dissociation of CO within the channels and, on the other hand, the tendency of external Mn to attract O from CO could be weaker and the CO dissociation activity would be less on the outside of the channels (Pan & Bao, 2011).

Iron-based catalysts commonly used in FT reactions contain promoters, which improve their activity and selectivity. Promoters such as potassium, manganese, copper and magnesium for example, are used in small amounts. Promoters can facilitate WGS, in the case of potassium, or they can also facilitate the reduction of Fe, as is the case with copper, which can result in high activity of the catalysts. Magnesium, in turn, can increase the rate of hydrocarbon formation, change the selectivity of FT synthesis to smaller hydrocarbons, improve the conversion of CO and suppress the formation of methane, in addition to improving WGS (Y. Liu et al., 2015). Transition metals such as Cu and Mn and alkali metals such as potassium have been also proposed as promoters for light olefin selectivity (Vitaly V. Ordomsky, Luo, et al., 2017).

Copper is often used to improve the performance of the catalyst and to compensate for the disadvantages of the structure promoters of Fe-based catalysts. This because copper can facilitate the reduction at low temperature and improve the formation of the active phase of the FT synthesis (C. H. Zhang et al., 2006). The control of nanostructures in the active phase of the bimetallic catalyst could be a strategy useful for the development of efficient catalysts (S. He et al., 2019). Basically, copper can be characterized by its existing stable forms Cu, Cu_2O and CuO, with various oxidation states under environmental conditions. Among these popular Cu compounds, cuprous oxide (Cu_2O) has its applications in gas detection, CO oxidation, photocatalysis, photocurrent generation and organic synthesis, due to its non-stoichiometric semiconductor type p. The physical and chemical properties involved in the surface or interface structure of Cu_2O-based materials can directly govern its performance, that is why the crystalline surface of Cu_2O plays an important role in the oxidation of CO and the photocatalytic decomposition of dyes(D. Zhao et al., 2017).

Copper-based catalysts have active copper sites responsible for selective hydrogenation of C-O bonds. These same active copper sites are also relatively inactive for the hydrogenolysis of

C-C bonds, so copper-based catalysts have been explored for hydrogenation reactions. However, there is a certain impediment to the stable performance of this catalyst, the tendency of Cu nanoparticles to grow in larger crystallites through the migration and coalescence of particles, or through the transport of monoatomic or molecular species between individual particles. As well as one of the main causes of deactivation of many supported catalysts is the loss of active surface area due to the growth of metal particles. Some strategies to mitigate the growth of particles are not applicable, as they restrict the composition and chemical functionality of catalysts. In copper-based catalysts, there is still a debate about the nature of active sites. Metallic copper is considered an active phase, since the activity of the catalyst is generally proportional to the surface area of Cu. The balanced surface species Cu^0 and Cu^+ can significantly improve the catalytic performance of the catalysts, however, the strong reduction of oxidizing H_2 and C-O make the Cu^0 and Cu^+ species unstable in the reaction (Yue et al., 2013).

Generally, the CO hydrogenation reactions are carried out on metal catalysts (**Figure 13**) (Phaahlamohlaka et al., 2016).

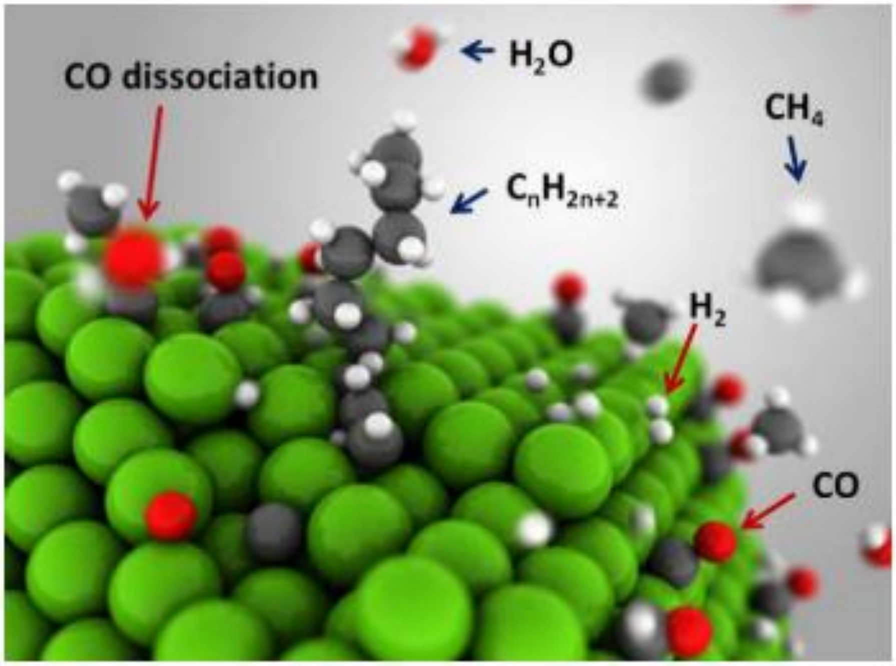

Figure 13. Scheme for hydrogenation of CO on transition metal catalyst (green: transition metal atoms, black: carbon atom, red: oxygen atom, white: hydrogen atom) (K. Cheng, 2015).

Deactivation of FT catalaysts

Describing the performance of a catalyst requires consideration not only of its activity and selectivity but also its stability.Under realistic conditions, the stability of a catalyst is extremely important, as it can be very expensive to replace it in a commercial process. In addition to representing a piece of productivity, in case the process needs to be closed temporarily. When studied and improved, the stability of a catalyst can results in environmental improvements as well as financial savings. The deactivation of catalyst is due to several phenomena, and although there are several chemical, mechanical and thermal causes, there is always a process of loss of active surface area involved. The deactivation processes have consequences for the activity as well as for the selectivity of the catalyst. The control of the chemical and structural properties of the catalyst represents a starting point for the possible identification of the changes that occur in the materials during and / or after the operation. There are some strategies that make it possible to reduce catalyst deactivation and also limit its main causes (Cargnello, 2019).

The deactivation of catalysts is still the main challenge in syngas conversion and in other catalytic process. The catalyst deactivation can involve several phenomena and also the interaction between these phenomena. The catalyst deactivation may result in lower efficiency of the process, periodic regenerations, high energy consumption and even the catalyst loss. It is a complex mechanism, which can involve from the sintering of metals to the deposition of carbon (Jacobs et al., 2002; Saib et al., 2010; Tsakoumis et al., 2010).

Several research groups have proposed various catalyst deactivation mechanisms, including: (1) poisoning of active sites (2) re-oxidation of cobalt metal, (3) cobalt-support mixed compound formation, (4) sintering (5) carbon formation (6) surface reconstruction and (7) catalyst attrition. The sintering of metals can occur mainly during the beginning of the reaction and the deposition of carbon mainly during the reaction, accumulating refractory carbon species on the catalyst surface (Gu, Bahri, et al., 2019). Sintering is one of the main deactivation phenomena responsible for the loss of performance of catalysts under reaction conditions at high temperatures. The sintering process leads to the agglomeration of active phase and the reduction of the area / volume ratio of the surface, and is related to the migration of atomic species or entire particles on the surface of a support or through the gas phase. The mechanisms of particle migration and coalescence and Ostwald ripening are responsible for sintering. The knowledge of which process is active under specific reaction conditions is crucial to develop a mitigation strategy for these sintering mechanisms(Cargnello, 2019).

Overcoming the high rates of deactivation in the FT processes remains the main challenge in the development of new iron-based catalysts. One of the most important factors, which leads to the deactivation of iron catalysts, is the tendency of oxidation under reaction conditions (Zhiqiang Yang et al., 2011).

CO_2 hydrogenation

Even though methane and CO_2 are both significant components of the main greenhouse gases contributing to global warming, CO_2 is particularly concerning due to its high potential for long-term atmospheric retention. The emitted CO_2 may last more than 100000 years, causing serious damage to our climate. Its pollution can be considered as the primary culprit of the increasing in the ocean water level. For all these reasons, it is crucial and necessary to mitigate CO_2 emissions from the atmosphere (Garba et al., 2021).

Carbon sequestration is involved in the long-term storage of carbon dioxide or other forms of carbon, to mitigate or delay global warming, and to solve problems related to climate change. This process, also called Carbon Capture and Storage (CCS), can control the accumulation of carbon in the atmosphere and the marine accumulation of greenhouse gases resulting from the burning of fossil fuels. In addition to storage, the carbon sequestered from the flue gases can later be used for the production of value-added chemicals (Behera & Prasad, 2020).

The lack of technology for the storage or use of CO_2 on a large scale also contributes for the increasing in the CO_2 emissions. The reduction in the cost of CO_2 handling is a crucial issue for many industries. Therefore, the abundant CO_2 could be used as a very low-cost raw material which will contribute to the overall reduction of CO_2 in the atmosphere.(Garba et al., 2021) Carbon capture and utilization (CCU) is a set of technologies and processes designed to capture carbon dioxide emissions from various sources and then convert or utilize that captured CO_2 for productive purposes.

While interest in converting non-conventional carbonaceous feedstocks (such as biomass, organic waste, non-conventional gas, and coal) into chemical products has been growing in recent decades, in the past few years, the primary focus has shifted towards the chemical conversion of CO_2. To ensure the sustainability of the CO_2 hydrogenation reactions, the CO_2 must be produced using renewable energy and without additional CO_2 emissions (Chernyak et al., 2022). This called green strategy refers to the conversion of CO_2 by various catalysts, via different catalytic processes using renewable sources under effective conditions (Mazari et al., 2021).

The catalytic chemical transformation of CO_2 is a good alternative for the production of fuels and platform chemicals, minimizing the huge dependence on carbon-rich fossil fuels (Mazari et al., 2021). However, its industrial conversion requires high energy consumption, elevated temperatures and pressures: around 300 °C and up to 100 bar, once CO_2 is a stable molecule and highly active catalysts (Betsy et al., 2020). In addition, heterogeneous catalysis also faces another major challenge, the use of renewable sources based mainly on biomass derivatives (Védrine, 2019).

Table 2. Important target products and typical reactions using CO_2 (Vitaly V. Ordomsky, Dros, et al., 2017).

Typical reactions	Target products
CO_2 hydrogenation	
	Methanol
	Dimethyl ether
	Formic acid
	Methane
FT synthesis	Paraffins
	Olefins
CO_2 for oxidation	
Oxidative dehydrogenation	Olefins
Benzene oxidation	Phenol
CO_2 reactions with hydrocarbons	
Methane dry reforming	Syngas
Paraffin carboxylation	Carboxylic acids
Olefin carboxylation	Acrylic acid
Alkyne carboxylation	Propiolic acid
Aromatic carboxylation	Benzoic acid

In addition to the synthesis of organic compounds and hydrocarbons by CO_2 hydrogenation (Védrine, 2019), there are several other ways to utilize CO_2 (**Table 2**) (Vitaly V. Ordomsky, Dros, et al., 2017). Between the several platform compounds that can be obtained from CO_2, the most targeted molecules are methanol, dimethyl ether, formate/formic acid, light olefins due to their valuable addition in the energy and chemical sectors (Betsy et al., 2020). The challenge for CO_2 hydrogenation reactions remains availability of cheap and green hydrogen, which is principally produced by water electrolysis.

CO_2 hydrogenation to formic acid

Among the many products that can be obtained by CO_2 hydrogenation, formic acid and formates have attracted much attention due to their direct employment as chemical feedstock and for hydrogen storage. Besides, the CO_2 conversion to formic acid may be the first indispensable step in the conversion of CO_2 into other chemicals of fuels, such as methanol (Bulushev & Ross, 2018; Qiyan Wang et al., 2021a). Formic acid is one of the most promising feedstocks for hydrogen storage, fuel cells, grass silage, leather tanning, textile dyeing, finishing, food additives, natural rubber, drilling fluids and various chemical processes. It can be used in the production of esters, which are used to produce a variety of organic derivatives such as aldehydes, ketones, carboxylic acids and amides. It may also be considered as a good candidate for methanol alternative fuels in fuel cells, as the direct fuel for electricity generation and as fuel for automobiles, due to its good electrochemical oxidation (Hao et al., 2011). Formic acid is regarded as promising liquid organic hydrogen carrier. Besides its theoretical hydrogen content and volumetric density, formic acid also presents the advantages of stability, less toxic, biodegradable, easier to transport and store (Betsy et al., 2020).

Currently, industrial production of formic acid proceeds via a multistep process such as the carbonylation of methanol with subsequent hydrolysis of methyl formate (Betsy et al., 2020; Hao et al., 2011). As these traditional methods consume a large amount of energy and produce hazardous waste, the development of a clean method of formic acid synthesis is of high priority. (Hao et al., 2011)

These two essential products of CO_2 conversion can be obtained through various catalytic reactions, such as hydrogenation, electrocatalytic, electrochemical and photocatalytic reduction (Mazari et al., 2021) and different pathways (see **Figure 14**) (Bulushev & Ross, 2018).

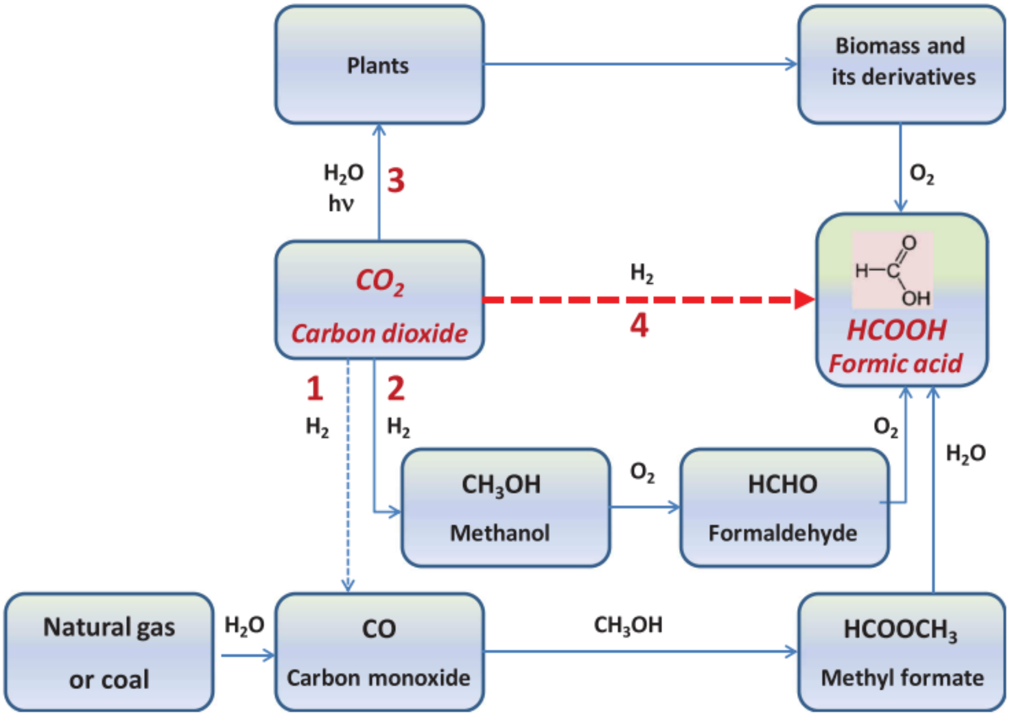

Figure 14. Pathways of CO_2 conversion to formic acid or formats (Bulushev & Ross, 2018).

Pathway 1 (**Figure 14**) is a commercial route that involves two-steps: the CO interaction with methanol to produce methyl formate and its hydrolysis to formic acid. **Pathway 2** is based on two-step oxidation of methanol and **Pathway 3** is related to the production of formic acid from biomass. The direct catalytic hydrogenation of CO_2, **Pathway 4**, is beneficial but not simple (Bulushev & Ross, 2018).

Direct formation of formic acid from carbon dioxide and hydrogen is not thermodynamically favorable (Bulushev & Ross, 2018) (**Eq. 7**):

$$CO_2(g) + H_2(g) \rightarrow HCOOH(l) \qquad \Delta G^{\circ}_{298} = 32.9\ kJ\ mol^{-1} \qquad \textbf{(Eq. 7)}$$

High thermodynamic stability of CO_2 molecule is often challenging (Qiyan Wang et al., 2021a). The unfavorable thermodynamics requires introduction of a solvent in a liquid phase, a base and either high pressures (>2 MPa) that can make this process favorable (Bulushev & Ross, 2018; Mazari et al., 2021). The selection of catalyst as well the solvent for the CO_2 hydrogenation play an important role to overcome the thermodynamic barrier (Mazari et al., 2021). The thermodynamic stability of formic acid relative to the gaseous starting materials can be also improved in the presence of a base such as ammonia, an amine or an alkali (Bulushev & Ross, 2018).

The main role of the base can be associated with the thermodynamic stabilization of the product by its conversion into formates or adducts (**Eq. 8**), for example: amines form adducts with formic acid and ammonia forms ammonium formate (Bulushev & Ross, 2018; Rohmann et al., 2016).

$$H_2 + CO_2 + Base \leftrightarrow CHOO^- + HBase^+ \qquad \Delta G^\circ < 0 \qquad \textbf{(Eq. 8)}$$

The presence of bases, in stoichiometric amounts acting as co-reagents, like tertiary amines, alkali hydroxides or carbonates, is able to shift the equilibrium of the reaction toward the stable formats (Rohmann et al., 2016; Qiyan Wang et al., 2021a). Some studies showed that the yield of formic acid reaches a high value in the presence of triethylamine (Hao et al., 2011). In particular, the amine bases can also perform a positive effect on the reaction rate, due to the possible involvement in the catalytic cycle by assisting the heterolytic hydrogen splitting for hydrogenolysis of the Metal-O bond in metal–formate intermediates (Rohmann et al., 2016; Schaub & Paciello, 2011a).

Based on the hypothesis that hydrogen bonding would play an important role for the stabilization of formic acid, water and dimethyl sulfoxide (DMSO) can be considered as favorable solvents for CO_2 hydrogenation (**Eq. 9**) (Rohmann et al., 2016; Schaub & Paciello, 2011b).

$$H_2 + CO_2 + Solvent \leftrightarrow CHOOH \cdots Solvent \ \Delta G^\circ < 0 \qquad \textbf{(Eq. 9)}$$

The CO_2 reduction to formic acid may take place through a stepwise mechanism: the hydrogen atom abstraction by CO_2 to form a formate intermediate and capturing of another hydrogen atom to produce formic acid (Heshmat, 2020; Maihom et al., 2013; Mazari et al., 2021). Water can be often involved in the reaction mechanism by the formation of carbonate species with hydrogen transfer for the synthesis of formate (Qiyan Wang et al., 2021a). For some homogeneous catalysts, the CO_2 hydrogenation can be performed in a water-free conditions, using organic solvents such as DMSO and THF. However for heterogenous catalysts, the water-free conditions may not be favorable since high concentrations of bases can undermine the activity and stability of these catalysts (Qiyan Wang et al., 2021a).

If the formic acid is produced with an objective of hydrogen storage or production, the separation of formic acid and the base used is not needed. When the target product is the formic acid itself, the separation process occurs normally by the thermal decomposition of the ammonium formate or by hydrolysis of the adducts, in the case of amines. In some cases, these separations process can face some obstacles. The ammonia can be retained as adsorbed species on the metal active sites of the catalyst and even deactivate it (Bulushev & Ross, 2018). Depending on the amine used, the separation procedure does not occur easily, then it is recommended use a high-boiling-temperature amine, that can be separated by distillation (Bulushev & Ross, 2018; Schaub & Paciello, 2011a). Note that the CO_2 hydrogenation is not thermodynamically feasible in some pure amine systems because the reaction enthalpy delivery by the amine protonation is too small (Schaub & Paciello, 2011a) and even the addition of a solvent such as water may not improve the formic acid formation (Schaub & Paciello, 2011a).

Higher CO_2 conversion in hydrogenation to formic acid and formates has been achieved using homogeneous catalysts that contain electron-donating ligands on the active metal centers (Bulushev & Ross, 2018; Qiyan Wang et al., 2021b). However, the application of homogeneous catalysts to this reaction have the difficulty to separate the product from the catalyst (Bulushev & Ross, 2018). The related economic factor of the separation of formic acid from the resulting adducts or complexes may prevent the industrial application of the process based in homogeneous catalysts and amines. Another factor is that, still, there is not a simple and efficient recycling of the precious metal catalyst (Bulushev & Ross, 2018). Heterogeneous catalysts may provide some advantages in comparison with the homogeneous ones: easier handling, separation and recovery (Bulushev & Ross, 2018; Qiyan Wang et al., 2021a).

Mechanism of CO_2 hydrogenation to formic acid

Based on theoretical and experimental studies, divalent transition metal species are the active components in the catalytic cycle (Hao et al., 2011). The reaction pathway is supposed to involve two steps: the formation of a metal-hydride intermediate from the reaction between hydrogen and the catalyst metal center followed by the generation of formate by the nucleophilic attack of the metal-hydride on CO_2 (Bulushev & Ross, 2018).

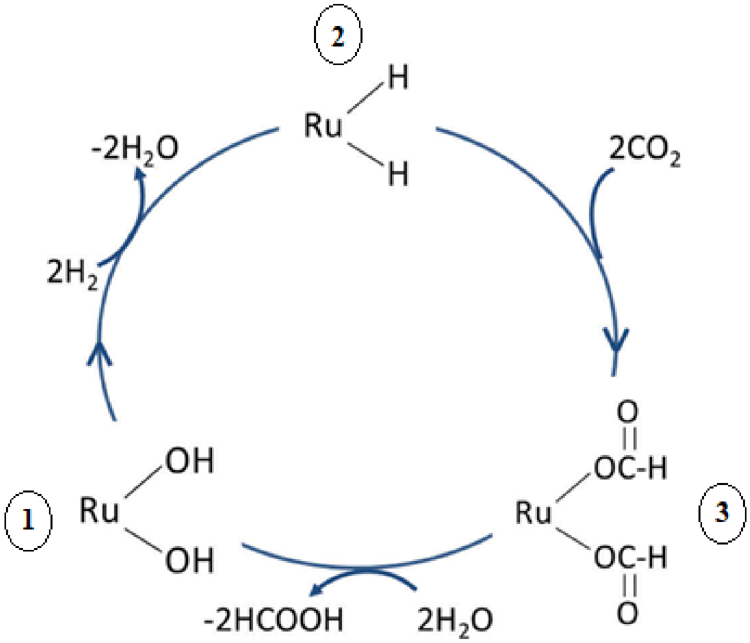

Figure 15. Catalytic scheme of CO_2 hydrogenation over Ru catalyst (Hao et al., 2011).

A plausible catalytic scheme for a supported ruthenium catalyst was proposed by Hao et al. (2011) (**Figure 15**). The authors assume that Ru-OH species (**1**) are the initial active species for the reaction, which will be hydrogenated to form the Ru hydride species (**2**). The Ru hydride reacts by the insertion of CO_2 into the ruthenium bond to generate the metal formate complex (**3**). As the reaction occurred in water phase, these formate species were substituted by hydroxide species to give formic acid, thus closing the catalytic cycle (Hao et al., 2011).

The generation of a metal formate complex or a metal carboxylic acid is normally considered as the rate-determined step of the reaction. It is suggested that $[Ru\text{-}OH_2]^{2+}$ is the initial ruthenium-water complex, which is hydrogenated to the ruthenium hydride species and so on the cycle continues (Bulushev & Ross, 2018).

Based on this, we may conclude that the presence of hydroxyl groups on the catalysts is really important for the formic acid formation. On the one hand, the interaction between the active ruthenium components with the hydroxyl groups through formation of Ru-OH species as the active species is crucial for the reaction. On the other hand, the formation of RuO_2 species can leads to lower catalytic activity (Hao et al., 2011).

Catalysts fo CO_2 hydrogenation to formic acid

In the last few decades, many catalysts, numerous homogeneous and heterogenous catalysts, were designed and examined for CO_2 hydrogenation/reduction (Betsy et al., 2020). The CO_2 hydrogenation to value-added products is a promising approach for the mitigation of CO_2, an abundant source that can lead to the production of hydrocarbons and oxygenates, besides the possible platform molecules that are important for the chemical industry(Jiang et al., 2020).

Significant advantages related to stability and recyclability can be achieved using heterogeneous catalysts, which make them a good industrial choice (Qiyan Wang et al., 2021b). Highly dispersed supported Pd, Au, Ru, and Ir catalysts have attracted attention of researchers as catalysts for the synthesis of formic acid and formates from CO_2 and hydrogen (Bulushev & Ross, 2018).

There are many materials that can be used as support for catalysts to CO_2 hydrogenation. The accessible pore structure, desired dimensions, distinct reactions and adsorption sites of porous materials have been extensively studied for catalysis and adsorption. Among these materials, we can highlight the zeolites, mesoporous silica, metal organic framework (MOFs) and covalent organic frameworks (COFs) (Betsy et al., 2020).

Catalysts using metal organic frameworks (MOFs) with different functionalities and metal complexes like Fe, Rh, Ru, Ir, Co and Re are attractive options for CO_2 hydrogenation (Mazari et al., 2021). Covalent organic frameworks (COFs) are materials, which are attracting attention due to their capability to accommodate homogeneous species through coordination bonds between the frameworks and the metal ions in organometallic complexes (Gunniya Hariyanandam et al., 2016).

The structures of COFs are capable to allow the passage and capture of CO_2 and H_2 gases and also others small molecules, such as formate. There are many COF's structures and compositions, the nitrogen-containing COFs present an additional advantage of forming coordination bonds with metal cations, which can result in the immobilization of organometallic complexes (Gunniya Hariyanandam et al., 2016).

Similarly, a variety of heterogeneous catalysts containing nitrogen atoms have been reported to improve the activity: N-heterocyclic carbenes, carbon nitride and amine-functionalized silica combined with both noble and non-noble metals such as Co, Ir, and Ru and bimetallic PdAg(Betsy et al., 2020). N-containing functional groups may facilitate anchoring of metal nanoparticles, stabilizing it as basic coordination sites to achieved higher activity (Z. Li & Xu, 2017).

Li & Xu (2017) showed that Pd nanoparticles immobilized onto reduced graphene oxide (rGO), that had diamine groups ligated to it, presented high activity for the formic acid dehydrogenation in comparison with the counterpart one without diamine groups. In this case, the diamine groups served as a proton scavenger, beneficiating the cleavage of the O-H bond in formic acid, which afford a Pd-formate intermediate and a $–[H_2NH]^+$ group in the initial reaction step. Following, the first one undergoes β-hydride elimination, affording CO_2 and a Pd-hydride species. Finally, the $-[H_2NH]^+$ group reacts with the Pd-hydride species to generate H_2 (Z. Li & Xu, 2017).

The catalytic reduction to formate/formic acid has some thermodynamic limitations, however among the strategies to overcome these limitations for the CO_2 hydrogenation in liquid phase is the use of suitable bases. However, Rohmann et al. (2016), reported an Ir complex that is capable to perform hydrogenation of CO_2 to formic acid in DMSO/water, without the presence of a base. The authors obtained a final concentration of 0.33 M of HCOOH(Rohmann et al., 2016).

Table 3 presents some examples of heterogeneous catalysts applied to CO_2 hydrogenation with hydrogen (Bulushev & Ross, 2018). The second part of the table contains several Ru-containing catalysts for CO_2 hydrogenation. The catalytic data and reaction conditions correspond to the catalysts of best performance among those studied in the correspondent paper.

Guynasekar et al. (2018) studied an strategy for heterogeneous catalysts capable to perform an recycable and highly efficient hydrogenation of CO_2 to formate. They demosntrated that a catalyst based on a $Ru(acac)_2$ complex supported on porous bipyridine-incorporated covalent triazine frameworks (bpy CTFs) showed an initial TOF of 22,700 h^{-1}, and produced the highest formate concentration of 1.8 M in 3 h (Gunasekar et al., 2018).

Table 3. Catalytic properties of heterogeneous catalysts containing metal nanoparticles, single atoms and metal complex as active sites in hydrogenation of CO_2 with hydrogen (Bulushev & Ross, 2018).

Catalyst, mean particle size	Base	T, °C	P_{total}, bar	Reaction time, h	TOF, h^{-1}	Reaction rate, $mol_{FA}\ g_{metal}^{-1}\ h^{-1}$	Reference
0.6% Pd/g-C_3N_4, 3.4 nm	(H_2O)	40	50	16	4.5	0.014	(H. Park et al., 2016)
1% Au/Al_2O3, 2.7 nm	NEt_3	70	40	20	120	0.264	(Filonenko et al., 2016)
1.5% Au/SiO_2 Schiff, 1.4 nm + single atoms	NEt_3	90	110	12	1444	6.1	(Q. Liu et al., 2017)
5.1% Pd 6.8% Ni/CNTs - graphene, 4 nm	(H_2O)	40	50	15	-	0.004	(Nguyen et al., 2015)
Catalyst, state of metal	**Base**	**T, °C**	**P_{total}, bar**	**Reaction time, h**	**TOF, h^{-1}**	**TON**	**Reference**
2% Ru/Al_2O_3, single atoms	NEt_3	80	135	1	-	91	(Hao et al., 2011)
0.4% Ru/LDH, single atoms	NaOH	100	20	24	29	698	(Mori et al., 2017)
1.7% Ru/bpyd-CTFs, metal complex	NEt_3	120	80	2	22700	6980	(Gunasekar et al., 2018)
2.4% Ir/CTFs, metal complex	$KHCO_3$	90	20	2	-	358	(Bavykina et al., 2016)
Ir/SBA-15, metal complex	NEt_3	60	40	20	880	2800	(Z. Xu et al., 2013)
0.9% Ir/COFs, metal complex	NEt_3	120	80	10	1500	6400	(Gunniya Hariyanandam et al., 2016)
4.7% Ir/COFs, metal complex	NEt_3	120	80	2	5300	5000	(K. Park et al., 2015)
0.68% Ir/CTFs, metal complex	NEt_3	120	80	15	16000	24300	(Gunasekar et al., 2017)

Single-atom catalysts for CO_2 hydrogenation to formic acid

Heterogeneous catalysts are stable even under relatively harsh reaction conditions and can be readily separated from reactants and products, dominating large-scale industrial processes.

Heterogeneous catalysis usually occurs at the surface of a solid catalyst, which ideally has a high surface area (A. Wang et al., 2018).

Smaller metal particles have a higher fraction of surface atoms than do larger metal particles and this fraction has an impact on the fraction of metal atoms that are catalytically active, besides, it has a substantial effect on selectivity. The metal atom utilization in homogeneous molecular catalysts can reach 100%, in the other hand, heterogeneous catalysts might feature a huge amount of non-uniform aggregates of metal atoms, but only a small fraction of this atoms are exposed to reactants (A. Wang et al., 2018).

In 2003, Flytzani-Stephanopoulos and co-workers (Fu et al., 2003) reported materials comprising cationic Au or Pt on CeO_2, heterogeneous catalysts for WGS reaction. Even though these smaller Au and Pt species are nonmetallic, they proved to be highly active in comparison with metallic Au and Pt NPs, that were catalytically inactive. The strong covalent bonding between single metal sites and the support was cited as the reason why supported Au NPs can be removed, while the isolated Au^{3+} ions remain in the CeO_2 support.

Heterogeneous catalysts with atomically dispersed metal atoms have been actively studied in the past several years (A. Wang et al., 2018). Such a catalyst is referred to as a single-atom catalyst (SAC), terminology that was first introduced in a 2011 report from Zhang, Li, Liu and coworkers (Qiao et al., 2011) describing the high CO oxidation activity of single Pt atoms dispersed on FeO_x. Such materials in which single metal atoms are dispersed on a support, are both atomically dispersed and heterogeneous. So on, a system in which many identical catalytically active sites are dispersed on a solid surface is defined as single-site heterogeneous catalyst (SSHC).

In general, SAC active sites are not necessarily uniform owing to the non-uniform nature of most solid supports, especially in practical industrial catalysts. SACs have maximal atom utilization efficiency and offer opportunities for tuning reaction rates and selectivities, providing a good platform for understanding structure-activity relationships on an atomic scale(A. Wang et al., 2018).

Moreover, the active sites of SACs are resistant to thermal sintering, due to the lower reduction potential, that is characteristic of SACs materials (Jones et al., 2016). Also, the absence of metal-metal bonds and the ionic nature of the isolated catalytic sites provide electronic properties and enable the complete atom utilization.

Zhang, Li, Liu and coworkers (Qiao et al., 2011) did not describe the interactions between the metal cations and the surface in detail, possibly owing to a lack of atomic-resolution technologies. The development of single-atom catalysis followed the recent advances in both atomic-resolution characterization techniques and theoretical modelling. Combined, these methods provide a clear picture of the dispersion of atoms, the bonding between single atoms and the support, and even in operando dynamics of single atoms during catalysis. Recent advances in electron microscopy techniques also enable the direct observation of single atoms (A. Wang et al., 2018).

Using aberration-corrected high-angle annular dark- field scanning transmission electron microscopy (AC-HAADF-STEM) it is possible to identify single metal atoms on supports (J. Liu, 2017). X-ray absorption spectroscopy (XAS) is also useful, and under either ex situ or in situ conditions, X-ray absorption near-edge structure (XANES) can provide information about metal oxidation states. The extended X- ray absorption fine structure (EXAFS), a complementary technique can provide information regarding the local coordination environment of central metal atoms as a weighted average (Ogino, 2017).

Other techniques that can be used to identify the SAC's structure include Fourier-transform infrared (FTIR) spectroscopy and scanning tunneling microscopy (STM). Also, density functional theory (DFT) is used to computational study the models of active sites. Considerable efforts have also been devoted to addressing important issues regarding SACs, such as how single atoms are stabilized on supports, the catalytic roles of the single atoms and the surrounding support atoms, and the dynamics and stability of active sites during catalysis (A. Wang et al., 2018).

Carbon-based materials and their potential for the design of CO and CO_2 hydrogenation catalysis

Research in nanotechnology and nanomaterials makes it possible for various chemical reactions at the nanoscale to be investigated, generating a new understanding of the processes involved and also, contributing to the development of tools that are fundamental for various applications (Zhichao Yang et al., 2019). The effects of nanoconfinement can be studied in different materials and in different ways, such as CNTs and simulations of molecular dynamics, enabling the improvement of processes and the results and reductions of reactions. The confinement effects in porous materials can strongly affect diffusion, phase transformations and catalytic properties, when these materials are applied as catalysts or supports for catalysts. The selectivity and activity of the catalyst in a reaction can also be influenced by the confinement environment, because this space generates changes in specific reactions due to differences in adsorption, selective absorption and changes in the potential energy surface, in addition to geometric restrictions (Mouarrawis et al., 2018).

Among these porous materials used for confinement, we can mention zeolites, CNTs (carbon nanotube), MOFs (metal organic framework) and COFs (covalent organic framework) (**Figure 16**). The porous materials are often and successfully used as support for catalysts, and we will focus on CNTs and COFs in the next sections.

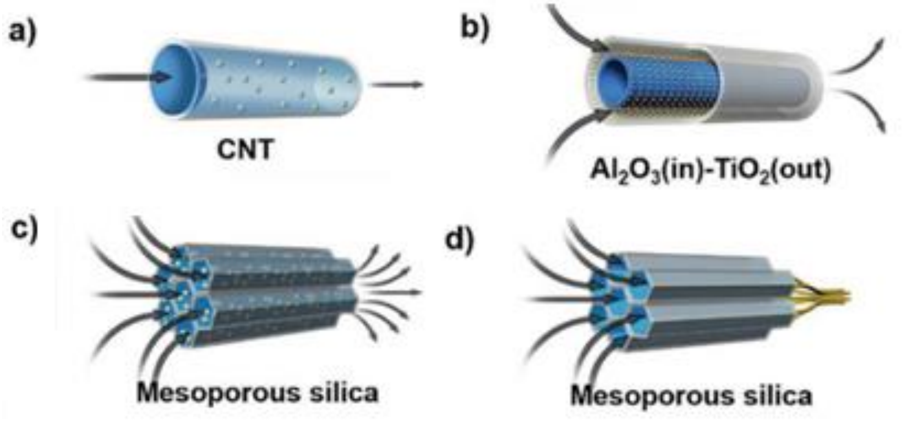

Figure 16. Schematic illustration of nanoconfined catalysis in 1D a) CNT nanochannels; b) tubular nanochannels with multiple metal–oxide interfaces with inner Ni-loaded Al_2O_3 layer and outer Pt-loaded TiO_2 layer; c) channels of mesoporous silica; d) nanochannel of fibrous PE (S. Liu et al., 2019).

An example of nanoconfinement using CNTs is FT synthesis catalyzed by Rh-based or Fe-based particles confined inside the channels of CNTs. The Rh-based catalyst was used to achieved enhanced catalytic activity for the conversion of syngas to ethanol (Pan et al., 2007). For its part, the Fe-based encapsulated inside the channels tended to form more iron carbides and showed improved reducibility due the nanoconfinement, which resulted in a higher activity and yield in

C_{5+} hydrocarbon synthesis in comparison with the counterpart one, the Fe-based located outside the channels of CTNs(S. Liu et al., 2019). Also PtRu nanoparticles confined in CNTs were used as a catalyst for selective hydrogenation of cinnamaldehyde to cinnamyl (Castillejos et al., 2009), the authors found that the particles confined within the channels presented improved activity and selectivity, showing the remarkable impact of the nanoconfinement of PtRu nanoparticles on catalytic performance. The hydrogenation of cinnamaldehyde was also analyzed using a Ni catalyst confined in the inner wall of Al_2O_3 nanotubes, and compared with the Ni located at the outer walls(Gao et al., 2015). The experiments showed that the confined one exhibited enhanced catalytic performance in comparison to the outside, which could be attributed to a larger interface and consequently a stronger Ni-Al_2O_3 interaction.

Carbon nanotubes

Carbon nanostructures (CNS) are robust, chemically inert and available in a wide variety of well-defined pore sizes and shapes. These characteristics make this material interesting for use as nanoreactors in a variety of different catalytic chemical reactions. CNS can act as reaction vessels and models for the formation of specific products and can also be used as a support for catalysts. It is possible to combine all the advantages of nanoreactors with the advantages inherent to heterogeneous catalysis by immobilizing metal nanoparticles in the CNS. In addition to controlling the size and shape of the reaction volume, CNS offers greater stability and recyclability of the metallic nanoparticles (Aygün et al., 2017).

Multi-walled carbon nanotubes (MWCNTs) are applied in catalytic chemical reactions such as nanoscale reaction vessels and flow reactors. Its hollow structure facilitates the encapsulation of metallic nanoparticles inside the nanotubes and ends up providing the perfect environment for reactions to take place within a strictly controlled nanoscale volume. There may be a significant increase in catalytic performance in some reactions for catalysts inserted in MWCNTs, as a result of the confinement and enrichment of the concentration of reagents inside the nanotubes, due to stronger interactions between the molecules and the inner surface of the carbon nanostructures. The size and shape of the nanotube channel can improve the stability and selectivity of confined nanoparticle catalysts. This allows strict control of the size, functionality and reactivity of the nanoparticles, providing stabilization for the nanoparticles and preventing aggregation into larger particles and bulk metal (Aygün et al., 2017).

Carbon nanotubes (CNTs) exhibit a well-defined tubular morphology, not planar hybridized with sp^2, and some properties such as good electrical conductivity, mechanical resistance and thermal stability which end up making CNTs potential supports for catalysts (W. Chen et al., 2007). CNTs can be distinguished according to the number of graphene beds that form their tubular structure: single wall carbon nanotubes (SWCNTs), double wall carbon nanotubes (DWCNTs) and multiple wall carbon nanotubes (MWCNTs) (**Figure 17**) (Pan & Bao, 2011).

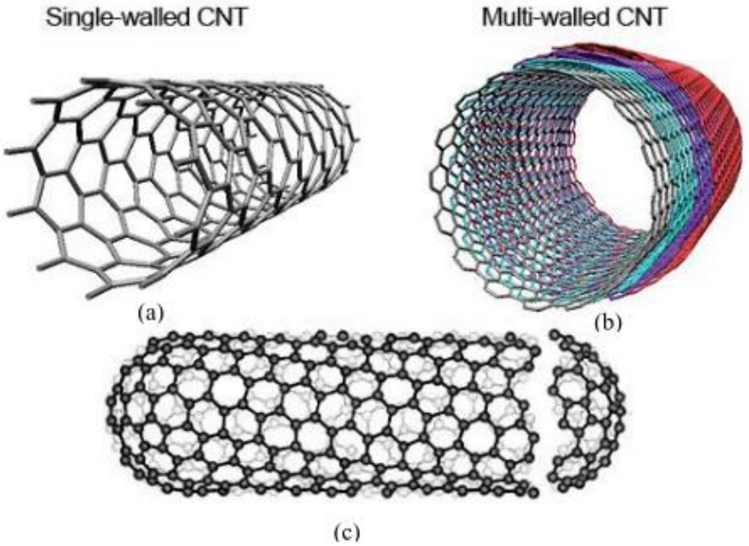

Figure 17. (a) SWCNT. (b) MWCNT (c) SWCNT with closed end(Porto, 2013).

SWCNT is ideally a monoatomic polyaromatic layer made of a hexagonal display of sp^2 hybridized carbon atoms with which genuine graphite is constructed, rolled into a cylinder and closed by two lids (semi-fullerenes). That is, the SWCNT is made of a perfect graphene sheet. The DWCNT is made of two layers of graphene sheet and the MWCNT of several dozen graphene sheets. The MWCNT can be considered as a SWCNT with an increasing diameter and coaxially arranged, where the concentric walls are regularly spaced. As the MWCNTs production process involves the presence of metallic particles, these can be found in the internal cavities of the MWCNTs (Serp et al., 2003).

When compared to others materials, used for supports in catalysis, carbon nanotubes distinguish themselves from other carbon materials, e.g., activated carbon, graphite and carbon nanofibers, due to its morphology, specific adsorption properties and for have graphene layers with semiconducting or metallic characteristics (W. Chen et al., 2008; Serp et al., 2003; Tessonnier et al., 2009).

The electron-deficient interior surface and the electron enriched exterior surface of the CNTs could influence the structure and electronic properties of substances in contact with either surface. According with theoretical studies, this electron difference between the surfaces is due to the deviation of the graphene layers from planarity, which causes π-electron density to shift from the concave inner surface to the convex outer surface (W. Chen et al., 2008; C. Wang et al., 2010).

With regard to bonding sites, magnetic moments, and charge-transfer directions, the interaction of transition metal atoms with CNTs walls differs significantly from their interaction with graphite layers. The values of magnetic moments of metal atoms on the nanotube's wall could be affected significantly by the curvature, as well as the charge transfer direction between the metal and carbon that could be inverted. Besides the application in catalysis, this effect could leads CNTs for potential applications in many fields such as magnetic materials, gas sensors and field emission (W. Chen et al., 2008; Serp et al., 2003).

The produced CNTs does not possess a high number of functional groups on its surface and the defects present on the surface can be considered as anchoring sites for metals. The surface defects could play a role in the interaction between the metal and the CNTs may be affecting the final metal dispersion (Serp et al., 2003).

Surface oxygen functionalities such as carboxylic groups can be introduced on the outer and possibly inner walls of the CNTs by nitric acid treatments, it is the most common method for the more or less pronounced surface oxidation. The main significant structural modification in MWNT may occurs on the nanotubes tip and can results in their opening, being able to form edges and steps on the graphene sheets. Others oxidative agents could be used to prepare functionalized CNTs, beyond the classical nitric acid treatment, such as concentrated sulfuric acid, aqua regia, HF-BF_3, aqueous OsO_4 and $KMnO_4$ (acid/alkali) solutions (Serp et al., 2003).

The employment of the CNTs channels as nanoreactors for catalysis may provide opportunities for the development of new heterogeneous catalysts, the possible confinement effect of CNTs makes them attractive materials as supports or catalysts (Z. Chen et al., 2011). In studies using CNTs as a support for FT iron catalysts, the iron was dispersed on the CNT outer walls, and the main focus was on the effect of additives such as copper and potassium and the catalyst preparation methods (W. Chen et al., 2008).

The confinement inside CNTs could facilitate the reduction of a series of metal oxides such as iron, ruthenium and cobalt. And also, compared with their counterparts located on the outer walls of CNTs, the oxidation of metallic iron could be retarded. This could be attributed to the spatial restriction on the particle aggregation under reaction conditions and interactions of the confined materials with the interior surface (Zhiqiang Yang et al., 2011).

Chen et al. studied the encapsulation of Pt nanoparticles in CNTs for heterogeneous asymmetric hydrogenations. Their results showed that the high activity and enantioselectivity are attributed mainly to the unique properties of the nanochannels of the CNTs and that them act as highly efficient nanoreactors (Z. Chen et al., 2011).

Chen et al. have found that the properties of Fe_2O_3 were modified significantly when the particles were encapsulated in CNTs and, particularly, the auto reduction of Fe_2O_3 was facilitated within the CNTs channels compared to that of those particles located on the CNTs outer walls. Besides that, they found that the reduction temperature decreases monotonically with the inner diameter of CNTs. This could be very significantly for many catalytic reactions that dependent on the redox state of the active components, it is a way to modify the redox properties of the confined substances (W. Chen et al., 2008).

Wang et al confined iron particles in CNTs channels and used for the direct synthesis of light olefins from syngas. They also founded that by introducing metal nanoparticles inside CNT channels the redox behavior of metal nanoparticles was modified, besides that, those CNT-confined catalysts exhibit different performance from those with metal particles dispersed on the outside of CNTs. These channels that enable encapsulation of nanomaterials are tubular structure formed by rolled-up graphene layers. The channels are well defined and their channel diameter could range from less than 1 to 100 nm (C. Wang et al., 2010).

It is important to consider that some of the CNTs characteristics such as purity, porosity and surface area may be significantly affected by the preparation processes, even it seems clear that oxidative surface treatments of the supports improve the dispersion of the metallic phase, it may not happen (Serp et al., 2003; Tessonnier et al., 2009).

For the synthesis of metal nanoparticles selectively localized inside or outside of carbon nanotubes, it is already known that two main synthesis routes could be suggested, the deposition on CNTs of various diameters and the asymmetric functionalization. For the first one, may have a variation of the catalytic behavior, but no curvature/confinement effects can be deduced from the catalytic behavior, once that by varying the tube diameter, both the curvature and the size of the inner cavity are changed. For de second one, the functionalization deeply modifies the surface properties of the CNTs, but there is no effects on supported metal nanoparticles reported (Tessonnier et al., 2009).

There are different efficient synthetic routes at the disposal of chemists to prepare supported metal catalysts on CNTs. To prepare carbon nanotubes supported catalysts several methods have been used: incipient wetness impregnation, ion-exchange, organometallic grafting, electron beam evaporation and deposition/precipitation (Serp et al., 2003).

The technique used for catalysts preparation that usually leads to a homogeneous metal deposition, with a good dispersion and a narrow particle size distribution is the incipient wetness impregnation. This well-known technique consists basically of a solid catalyst support brought in contact with a solution containing the metal precursor. To totally fill the pores of the solid, the volume of this solution is adjusted according to the porous volume of the solid. This leads to the external surface almost dry and it is expected that most of the formed metal nanoparticles will be inside the nanotube, once most of the solution is located in the pores during the impregnation process (Tessonnier et al., 2009).

Covalent Organic Frameworks

The environmentally benign and economically beneficial applications of porous materials in industrial catalysis, adsorption, and ion-exchange processes drive a continuing effort into the research of their fundamental properties and manipulation of their structures and function to enhance the performance. Beyond the traditional porous materials, the great tunability of covalent organic frameworks (COFs) gives this new type of porous material with high potential in catalysis, which displays advantageous features of both molecular and heterogeneous systems (Song et al., 2019).

Attracting wide attention in the past decades, the covalent organic frameworks (COFs) are an emerging class of crystalline porous materials (CPMs) integrated by the linkage of organic building blocks through covalent bonds (Babu et al., 2019). A COF framework consists of two different modules: linkers (building units) and linkages (bonds formed between those units upon reticulation) that control the pore size. The building units must possess specific geometries and rigid structures, then, based on the reticulation of these building units, they are joined together into an extended framework (Cao et al., 2019).

The work of Yaghi and co-workers, led by the exploration for tunable 2D polymers, make possible the synthesis of the first examples of COF: boroxine and boronate-based crystalline COFs, also known as COF-1 and COF-5(Côté, Benin, Ockwig, O'Keeffe, Matzger, Yaghi, et al., 2005), respectively (See **Figure 18**).

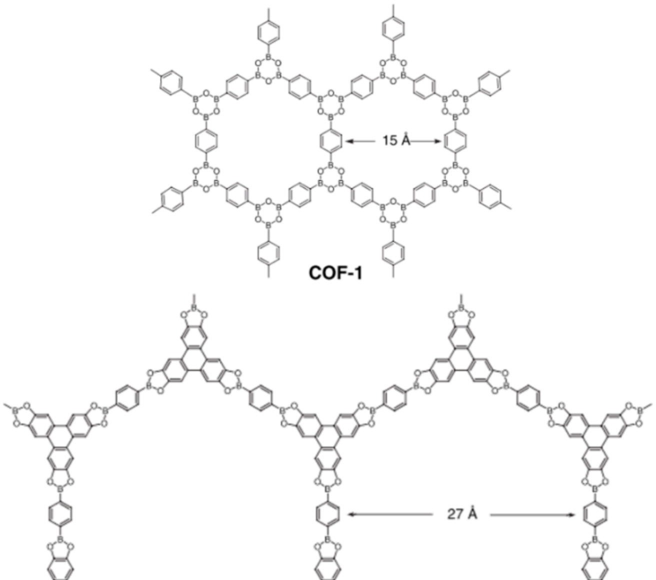

Figure 18. COFs structures (a) COF-1 and (b)COF-5, adapted from (Côté, Benin, Ockwig, O'Keeffe, Matzger, Yaghi, et al., 2005).

Many COFs can be formed by a variety of linkages: B−O (boronate ester, boroxine, borosilicate and spiroborate); B−N (borazine); C−C, C−N (imine, hydrazine, imide, ketoenamine, azine, triazine, melamine, amide, phenazine, squaraine and viologen); and N−N (azodioxide) (See linkages in **Figure 19**).

The reversible formation of imine bonds (-C=N-) is the basis of reactions by which several COFs with new networks are synthesized. Reversible reactions provide the COF systems with a self-healing ability that can repair structural defects, which is critical for the formation of highly ordered frameworks (Cao et al., 2019). The imine-linked frameworks, constructed from condensation of amine and aldehyde linkers, often result in chemically stable materials. However, the presence of water can potentially reverse the imine formation and consequently causing hydrolysis and collapse of the framework. Banerjee and co-workers (G. Das et al., 2014; Kandambeth et al., 2012) developed an strategy to overcome this undesired process. Their work is based on replacing hydrolysable imine bonding by robust b-ketoenamine linkages, taking advantage of the irreversible imine–enamine tautomerism. Interestingly, the replacing imine by b-ketoenamine linkages might result in structural variations of the framework, thereby playing a key role in the ultimate properties of the material (Romero-Muñiz et al., 2020).

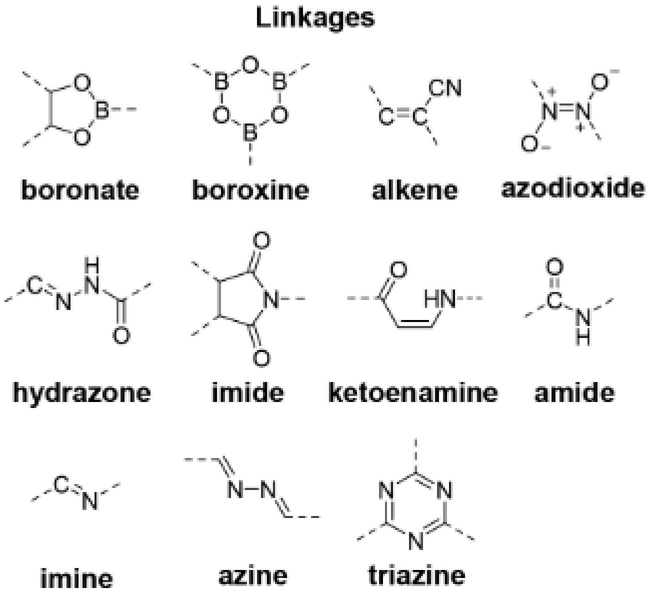

Figure 19. Some of the representative linkages in COFs synthesis.

COFs with boroxine and boronate–ester linkages exhibit high crystallinities and porosities, but they are unstable in the presence of water or protic solvents. By contrast, COFs based on imine, hydrazone, triazine, phenazine and azine linkages show improved stability, but they usually have low crystallinities and limited porosities. Despite significant efforts in the synthesis of these materials, stability, crystallinity and porosity can still be dificult to find together in a single COF material (H. Xu et al., 2015).

The already known synthesis of COF are the solvothermal methods, ionothermal synthesis, microwave heating. Another method that was explored is the sublimation of the building unit and the COFs grew onto a crystalline metal surface, forming COF monolayers or films by reactions on substrates (Cao et al., 2019).

Synthesis of COFs under solvothermal conditions starts placing the reactive material into a Pyrex tube and a degassing treatment is applied. The tube is then sealed and heated at the pre-set condition of temperature that normally is between 80 to 120 °C and the reaction times often takes 2 to even 9 days. The precipitate form is collected, washed using suitable solvents and dried under vacuum to obtain solid powder COFs. Although this method is widely applied in the synthesis of COFs, the temperature, pressure and long reaction time of this method cannot be applied to large-scale production. Peng et al. explore a room temperature batch and continuous flow synthesis of water-stable COFs, with high space–time yields, which provide the possibility of achieving large-scale production of COFs (Peng et al., 2016).

The COF synthesis is dynamic, the disordered polymers at initial reaction time evolve to porous crystalline frameworks at the end of synthesis. It is the reversible nature of the COF linkages that allows the starting disordered structures to reorganize into crystalline stable forms, and is exactly the intrinsic flexibility of COFs one of their most unique and yet underexplored structural features (Romero-Muñiz et al., 2020). On the other hand, due to the reversible nature of COFs synthesis, it may be difficult to obtain a stable crystalline porous framework that is robust against harsh conditions and environments, such as humidity, acidity and basicity. This remains the major issue that prevents the practical implementation of COFs (H. Xu et al., 2015).

As COFs are composed of lightweight elements (binding units or blocks) connected by stable covalent linkages that have an ordered π-structure, these materials are superiors in comparison to other porous materials due to its properties: high porosity and surface area, low density and chemical stability (Cao et al., 2019), which makes COFs having widely applications in the energy and environmental fields, such as gas adsorption and separation, water treatment, catalysis, electrochemistry, optoelectronics, sensing and photoconductive devices, energy storage and conversion (Cao et al., 2019; Côté, Benin, Ockwig, O'Keeffe, Matzger, & Yaghi, 2005; Romero-Muñiz et al., 2020; Saihua Wang et al., 2019).

According to the reticular chemistry theory, COF materials may be constructed from rigid organic building units with varying structural configurations, and can be classified according to the building unit dimensions: one-dimensional (1D), two-dimensional (2D) and three-dimensional (3D) COFs(Cao et al., 2019).

In 2007, Côté and co-workers (Côté et al., 2007) synthesized 2D COFs that have micro- and mesopores based on C_2O_2B rings, which formed layered eclipsed structures that were periodically aligned. The charge carrier transport could be facilitated via the ordered columns in 2D COFs, which means that it can be used as a photo-functional material for optoelectronics and photovoltaics. Also in 2007, the first synthesis of the 3D COF materials appeared (El-Kaderi et al., 2007). Although the yields are lower than the 2D COFs, the 3D COFs exhibit better physicochemical properties and are perfect containers for gas store, due to its high specific surface area, multiple open positions and low density.

The COFs-based catalysts can be organized into four different structural origins: skeleton design, pore surface engineering, pore confinement and systematic organization (Guo & Jiang, 2020). These catalysts have been designed with different principles and applied for different types of transformations.

- Catalysts based on π-skeletons or side walls: the catalytic activity is based on the aligned π columns to enhance light absorption, exciton migration, and electron transport and the coordinated sites on side walls may offer two different ways to explore specific interactions between the walls and reactants. The cooperation between π columns and catalytic sites to the framework is crucial for catalysis based on the skeleton. Using different walls to integrate different catalysts is a challenging goal where the synergistic effects between walls may play a key role in catalyzing multistep transformations (Guo & Jiang, 2020).

- Catalysts based on pore surface engineering: this approach allows the integration of catalytic sites into the channels without any coordinative monomers, synthetizing COFs with reactive sites on pore walls which enables the integration of various molecular catalysts that cannot be introduced via direct polymerization. The balance of the catalytic sites and pore size make possible the construction oh heterogeneous catalytic systems with exceptional activity and enantioselectivity (Guo & Jiang, 2020).

- Catalysts based on pore confinement: with precise shape, clear edges and corners and predesignable pore size, from micro- to mesoporous, the 1D channels of COFs allow the access of guest molecules and offer an ultimate pathway for mass transport. The combination of these all these features in one framework, creates a unique and unlimited potential, however, the elaboration of the pore wall in order to create an interface that controls confinement, spatially and dynamically, is challenging (Guo & Jiang, 2020).

In comparison with MOFs, COFs are a relatively new class of materials. The difference is that COFs are constructed by forming covalent (reversible) bonds, instead of coordination chemistry, having rigid structures that can be adjusted by the directionality of the covalent bonds used (Mouarrawis et al., 2018). COFs have more abundant π-π conjugated structures and functional groups such as hydroxyl, amino groups and oxygenated groups (Saihua Wang et al., 2019). The layered structure and the 1D channels that constitute COFs are sustained by intralayer π-π interactions (Guo & Jiang, 2020).

There are some studies with 3D COFs and their applications in catalysis, and these materials showed high size selectivity and also good recycling capacity (Mouarrawis et al., 2018). Fang et al.(Fang et al., 2014b) synthesized two microporous COFs with 3D-based functionality and applied it in Knoevenagel condensation reactions with a variety of substrates. Considering their unique structures and properties, the rational design and synthesis of 3D COFs with specific functions are highly demanding (H. Ding et al., 2018).

COFs offer an emerging molecular platform for designing stable heterogeneous catalysts and have greatly changed the research direction towards the control of kinetics and dynamics interactions, which provide the determination of the catalytic activity, selectivity, and efficiency. Owing to a rich diversity of building blocks, COFs have a great probability of developing nanoreactors that can greatly surpass the activity, selectivity, and durability of molecular catalysts (Guo & Jiang, 2020).

Nitrogen-enriched COF materials are ideal candidates for binding catalytic metals, from single sites to few-atom clusters and bigger nanoparticles. However, understanding the local nature of metal species loaded into COF frameworks under catalysis conditions still remains under debate (Romero-Muñiz et al., 2020). In imine-linked COFs, the C=N bond is polarized to yield partially positively charged carbon and negatively charged nitrogen. In a hexagonal 2D COF, each macrocycle consists of 12 polarized C=N segments; the aggregation of a large number of charged groups causes electrostatic repulsion and may destabilize the layered structure (H. Xu et al., 2015).

Post-synthetic modification of COFs is one of the alternative approaches to obtain active catalytic COFs, and this technique introduces metal sites in the structure of COFs. Ding et al. (S. Ding et al., 2011) carried out the incorporation of $Pd(OAc)_2$ in a COF bound to the imine to generate Pd/COF-LZU1. The authors used the Pd/COF-LZU1 structure for a coupling reaction and obtained superior catalytic results in relation to the activity, compared with other porous crystalline materials (MOFs and zeolites). An alternative also for asymmetric organic reactions is chiral COFs, which demonstrate efficiency in heterogeneous catalysis and also recyclability (Mouarrawis et al., 2018).

A huge hindrance to the further development and application of COFs is the low chemical stabilities, especially in acid and base, and the limitation to the currently linkages in available COFs. In high acid or base concentrations, in harsh chemical environments, these materials do not survive. Although the structural stabilities of some COFs can be improved, the stability under extreme conditions still remains a major challenge in the design and preparation of a new class of robust COFs for practical applications (Guan et al., 2019).

Objectives of this thesis

Hydrogenation of CO and CO_2 holds paramount importance in the realms of both industrial and environmental sustainability. These reactions are pivotal in the production of a wide range of valuable chemicals and fuels, including synthetic hydrocarbons, methanol, and aldehydes. Notably, the FT process, which utilizes CO and hydrogen to create hydrocarbons, plays a fundamental role in the production of synthetic fuels and waxes. Furthermore, the conversion of CO_2 into formic acid, driven by hydrogenation, has garnered significant attention as a means of mitigating greenhouse gas emissions. By harnessing the potential of CO and CO_2 hydrogenation, we can simultaneously meet industrial demands and contribute to a more sustainable and environmentally conscious future. Due to the chemical inertness of carbon dioxide and high energy barrier, the conversion of carbon dioxide into high value-added chemicals is still facing huge challenges. Formic acid produced from CO_2 hydrogenation is an important biodegradable sustainable feedstock. Anhydrous formic acid possesses energy density comparable to that of liquefied hydrogen, making it suitable for both hydrogen storage and generation.

Several challenges still remain in FT synthesis. The selectivity for certain products, the desired chain growth probability that is delimited by the ASF distribution, the catalytic activity and the stability of the catalysts used are still the main challenges to be overcome in order to have a wide industrial application of FT synthesis catalysts.

Formic acid is currently produced by a multistage high pressure and high temperature process. It involves the use of methanol and toxic carbon monoxide in the presence of corrosive sodium methoxide and it is accompanied by numerous by-products. The design of new catalysts for low temperature highly selective process is extremely demanding. Recent years have witnessed a spectacular growth of single atom catalysts (SACs) (L. Liu & Corma, 2018; Ma et al., 2023; Qiao et al., 2011; Qiyan Wang et al., 2021a; X.-F. Yang et al., 2013; Zhuang & Wang, 2023) as a conceptual bridge filling the gap (Iemhoff et al., 2023; T. Luo et al., 2023) between homogenous and heterogenous catalysis. SACs have several advantages relative to the conventional homogeneous and heterogeneous systems, such as a maximum atom utilization efficiency, absence of any metal–metal bonds and unique tunable active sites compared to homogeneous organometallic complexes. Their well-defined active sites can be downsized to nanoscale and sub-nanoscale. Very few information has been available (S. K. Das et al., 2020;

Ghosh et al., 2019; X. Yang et al., 2023) about the catalytic performance of SACs supported by COF in thermocatalytic reactions.

This thesis has a double objective

- to explore the potential of different carbon-based supports for meditation iron, copper and ruthenium dispersion;

-to evaluate the effects of the synergy of metal species with the support material on their catalytic performance in FT synthesis leading hydrocarbons and in low temperature CO_2 hydrogenation producing formic acid.

References

Abbaslou, R. M. M., Soltan, J., & Dalai, A. K. (2010). Effects of nanotubes pore size on the catalytic performances of iron catalysts supported on carbon nanotubes for Fischer-Tropsch synthesis. *Applied Catalysis A: General*, *379*(1–2), 129–134. https://doi.org/10.1016/j.apcata.2010.03.006

Abednatanzi, S., Najafi, M., Gohari Derakhshandeh, P., & Van Der Voort, P. (2022). Metal- and covalent organic frameworks as catalyst for organic transformation: Comparative overview and future perspectives. *Coordination Chemistry Reviews*, *451*, 214259. https://doi.org/10.1016/j.ccr.2021.214259

Abelló, S., & Montané, D. (2011). Exploring iron-based multifunctional catalysts for fischer-tropsch synthesis: A review. *ChemSusChem*, *4*(11), 1538–1556. https://doi.org/10.1002/cssc.201100189

Adesina, A. A. (1996). Hydrocarbon synthesis via Fischer-Tropsch reaction: Travails and triumphs. *Applied Catalysis A: General*, *138*(2), 345–367. https://doi.org/10.1016/0926-860X(95)00307-X

Al-Dossary, M., Fierro, J. L. G., & Spivey, J. J. (2015). Cu-promoted Fe2O3/MgO-based Fischer-Tropsch catalysts of biomass-derived syngas. *Industrial and Engineering Chemistry Research*, *54*(3), 911–921. https://doi.org/10.1021/ie504473a

Al-Salem, S. M., Lettieri, P., & Baeyens, J. (2009). Recycling and recovery routes of plastic solid waste (PSW): A review. *Waste Management*, *29*(10), 2625–2643. https://doi.org/10.1016/j.wasman.2009.06.004

Alakangas, E. (2011). European Standards for Fuel Specification and Classes of Solid Biofuels. In *Grammelis, P. (eds) Solid Biofuels for Energy. Green Energy and Technology* (Vol. 28, pp. 197–217). Springer. https://doi.org/10.1007/978-1-84996-393-0_2

An, Y., Lin, T., Yu, F., Yang, Y., Zhong, L., Wu, M., & Sun, Y. (2017). Advances in direct production of value-added chemicals via syngas conversion. *Science China Chemistry*, *60*(7), 887–903. https://doi.org/10.1007/s11426-016-0464-1

Arrigo, R., Teresi, R., Gambarotti, C., Parisi, F., Lazzara, G., & Dintcheva, N. T. (2018). Sonication-induced modification of carbon nanotubes: Effect on the rheological and thermo-oxidative behaviour of polymer-based nanocomposites. *Materials*, *11*(3), 1–14. https://doi.org/10.3390/ma11030383

Aygün, M., Stoppiello, C. T., Lebedeva, M. A., Smith, E. F., Gimenez-Lopez, M. D. C., Khlobystov, A. N., & Chamberlain, T. W. (2017). Comparison of alkene hydrogenation in carbon nanoreactors of different diameters: Probing the effects of nanoscale confinement on ruthenium nanoparticle catalysis. *Journal of Materials Chemistry A*, *5*(40), 21467–21477. https://doi.org/10.1039/c7ta03691d

B. H. Davis, M. L. O. (2009). *Advances in Fischer-Tropsch Synthesis, Catalysts, and Catalysis* (1st Editio). CRC Press.

Babu, H. V., Bai, M. G. M., & Rajeswara Rao, M. (2019). Functional π-Conjugated Two-Dimensional Covalent Organic Frameworks. *ACS Applied Materials and Interfaces*, *11*(12), 11029–11060. https://doi.org/10.1021/acsami.8b19087

Bagheri, A. R., Aramesh, N., Sher, F., & Bilal, M. (2021). Covalent organic frameworks as robust materials for mitigation of environmental pollutants. *Chemosphere*, *270*, 129523. https://doi.org/10.1016/j.chemosphere.2020.129523

Bahome, M. C., Jewell, L. L., Hildebrandt, D., Glasser, D., & Coville, N. J. (2005). Fischer-Tropsch synthesis over iron catalysts supported on carbon nanotubes. *Applied Catalysis A: General*, *287*(1), 60–67. https://doi.org/10.1016/j.apcata.2005.03.029

Banhart, F. (2009). Interactions between metals and carbon nanotubes: At the interface between old and new materials. *Nanoscale*, *1*(2), 201–213. https://doi.org/10.1039/b9nr00127a

Barrios Medina, A. J. (2023). *Direct Synthesis of Light Olefins Using CO and CO2 Hydrogenation Reactions* [Centrale Lille Institut; Universiteit Gent.]. https://theses.hal.science/tel-03987841

Basu, P. (2018a). Biomass characteristics. In *Biomass Gasification, Pyrolysis and Torrefaction: Practical Design and Theory*. https://doi.org/10.1016/B978-0-12-812992-0.00003-0

Basu, P. (2018b). Economic issues of biomass energy conversion. In *Biomass Gasification, Pyrolysis and Torrefaction: Practical Design and Theory* (pp. 29–47). https://doi.org/10.1016/B978-0-12-812992-0.00002-9

Batakliev, T., Petrova-Doycheva, I., Angelov, V., Georgiev, V., Ivanov, E., Kotsilkova, R., Casa, M., Cirillo, C., Adami, R., Sarno, M., & Ciambelli, P. (2019). Effects of Graphene Nanoplatelets and Multiwall Carbon Nanotubes on the Structure and Mechanical Properties of Poly(lactic acid) Composites: A Comparative Study. *Applied Sciences*, *9*(3), 469. https://doi.org/10.3390/app9030469

Bavykina, A. V., Rozhko, E., Goesten, M. G., Wezendonk, T., Seoane, B., Kapteijn, F., Makkee, M., & Gascon, J. (2016). Shaping Covalent Triazine Frameworks for the Hydrogenation of Carbon Dioxide to Formic Acid. *ChemCatChem*, *8*(13), 2217–2221. https://doi.org/10.1002/cctc.201600419

Behera, B. K., & Prasad, R. (2020). Greenhouse gas capture and conversion. In *Environmental Technology and Sustainability* (pp. 41–71). Elsevier Inc. https://doi.org/10.1016/b978-0-12-819103-3.00002-0

Beiramar, J. M. F. (2013). *Etude de la promotion des catalyseurs CuZnAl pour la production d'alcools supérieurs à partir du biosyngaz*. Université Lille 1 – Sciences et Technologies Thèse.

Betsy, K. J., Lazar, A., Pavithran, A., & Vinod, C. P. (2020). CO2 Hydrogenation to Formate by Palladium Nanoparticles Supported on N-Incorporated Periodic Mesoporous Organosilica. *ACS Sustainable Chemistry and Engineering*, *8*, 14765–14774. https://doi.org/10.1021/acssuschemeng.0c03860

Biesinger, M. C. (2017). Advanced analysis of copper X-ray photoelectron spectra. *Surface and Interface Analysis*, *49*(13), 1325–1334. https://doi.org/10.1002/sia.6239

Biesinger, M. C., Lau, L. W. M., Gerson, A. R., & Smart, R. S. C. (2010). Resolving surface chemical states in XPS analysis of first row transition metals, oxides and hydroxides: Sc, Ti, V, Cu and Zn. *Applied Surface Science*, *257*(3), 887–898. https://doi.org/10.1016/j.apsusc.2010.07.086

Biloen, P., Helle, J. N., & Sachtler, W. M. H. (1979). Incorporation of surface carbon into hydrocarbons during Fischer-Tropsch synthesis: Mechanistic implications. *Journal of Catalysis*, *58*(1), 95–107. https://doi.org/10.1016/0021-9517(79)90248-3

Blyholder, G., & Emmett, P. H. (1959). Fischer-Tropsch synthesis mechanism studies. The addition of radioactive ketene to the synthesis gas. *Journal of Physical Chemistry*, *63*(6), 962–965. https://doi.org/10.1021/j150576a044

Broicher, C., Foit, S. R., Rose, M., Hausoul, P. J. C., & Palkovits, R. (2017). A Bipyridine-Based Conjugated Microporous Polymer for the Ir-Catalyzed Dehydrogenation of Formic Acid. *ACS Catalysis*, *7*(12), 8413–8419. https://doi.org/10.1021/acscatal.7b02425

Bulushev, D. A., & Ross, J. R. H. (2018). Heterogeneous catalysts for hydrogenation of CO 2 and bicarbonates to formic acid and formates. *Catalysis Reviews*, *60*(4), 566–593. https://doi.org/10.1080/01614940.2018.1476806

Butt, J. B. (1991). Carbide phases on iron-based Fischer-Tropsch synthesis catalysts part I: Characterization studies. *Catalysis Letters*, *7*(1–4), 61–81. https://doi.org/10.1007/BF00764492

Cai, M. (2015). *Design of novel hybrid catalysts for direct synthesis of Dimethyl ether from syngas*. Université des Sciences et Technologies de Lille.

Cao, S., Li, B., Zhu, R., & Pang, H. (2019). Design and synthesis of covalent organic frameworks towards energy and environment fields. *Chemical Engineering Journal*, *355*(July 2018), 602–623. https://doi.org/10.1016/j.cej.2018.08.184

Carberry, J. J. (1987). Physico-Chemical Aspects of Mass and Heat Transfer in Heterogeneous Catalysis. In J. R. Anderson & M. Boudart (Eds.), *Catalysis* (vol 8, pp. 131–171). Springer Berlin Heidelberg. https://doi.org/10.1007/978-3-642-93278-6_3

Cargnello, M. (2019). Colloidal Nanocrystals as Building Blocks for Well-Defined Heterogeneous Catalysts. In *Chemistry of Materials* (Vol. 31, Issue 3, pp. 576–596). American Chemical Society. https://doi.org/10.1021/acs.chemmater.8b04533

Castillejos, E., Debouttière, P.-J., Roiban, L., Solhy, A., Martinez, V., Kihn, Y., Ersen, O., Philippot, K., Chaudret, B., & Serp, P. (2009). An Efficient Strategy to Drive Nanoparticles into Carbon Nanotubes and the Remarkable Effect of Confinement on Their Catalytic Performance. *Angewandte Chemie*, *121*(14), 2567–2571. https://doi.org/10.1002/ange.200805273

Centi, G., & Perathoner, S. (2004). Heterogeneous catalytic reactions with CO2: Status and perspectives. *Studies in Surface Science and Catalysis*, *153*, 1–8. https://doi.org/10.1016/s0167-2991(04)80212-x

Chambrey, S., Fongarland, P., Karaca, H., Piché, S., Griboval-Constant, A., Schweich, D., Luck, F., Savin, S., & Khodakov, A. Y. (2011). Fischer-Tropsch synthesis in milli-fixed bed reactor: Comparison with centimetric fixed bed and slurry stirred tank reactors. *Catalysis Today*, *171*(1), 201–206. https://doi.org/10.1016/j.cattod.2011.04.046

Chen, W., Fan, Z., Pan, X., & Bao, X. (2008). Effect of confinement in carbon nanotubes on the activity of Fischer-Tropsch iron catalyst. *Journal of the American Chemical Society*, *130*(29), 9414–9419. https://doi.org/10.1021/ja8008192

Chen, W., Pan, X., & Bao, X. (2007). Tuning of redox properties of iron and iron oxides via encapsulation within carbon nanotubes. *Journal of the American Chemical Society*, *129*(23), 7421–7426. https://doi.org/10.1021/ja0713072

Chen, X., Deng, D., Pan, X., & Bao, X. (2015). Iron catalyst encapsulated in carbon nanotubes for CO hydrogenation to light olefins. *Chinese Journal of Catalysis*, *36*(9), 1631–1637. https://doi.org/10.1016/S1872-2067(15)60882-8

Chen, Z., Guan, Z., Li, M., Yang, Q., & Li, C. (2011). Enhancement of the performance of a platinum nanocatalyst confined within carbon nanotubes for asymmetric hydrogenation. *Angewandte Chemie - International Edition*, *50*(21), 4913–4917. https://doi.org/10.1002/anie.201006870

Cheng, K. (2015). *Novel Fischer-Tropsch Catalysts Based on Mesoporous Zeolites and Carbon Materials for the Production of Gasoline-range Hydrocarbons and Lower Olefins*. Université Lille 1, Sciences et Technologies and Xiamen University Novel.

Cheng, K., Kang, J., King, D. L., Subramanian, V., Zhou, C., Zhang, Q., & Wang, Y. (2017). Advances in Catalysis for Syngas Conversion to Hydrocarbons. In *Advances in Catalysis* (1st ed., Vol. 60, pp. 125–208). Elsevier Inc. https://doi.org/10.1016/bs.acat.2017.09.003

Cheng, K., Ordomsky, V. V., Legras, B., Virginie, M., Paul, S., Wang, Y., & Khodakov, A. Y. (2015). Sodium-promoted iron catalysts prepared on different supports for high temperature Fischer-Tropsch synthesis. *Applied Catalysis A: General*, *502*, 204–214. https://doi.org/10.1016/j.apcata.2015.06.010

Cheng, Q., Tian, Y., Lyu, S., Zhao, N., Ma, K., Ding, T., Jiang, Z., Wang, L., Zhang, J., Zheng, L., Gao, F., Dong, L., Tsubaki, N., & Li, X. (2018). Confined small-sized cobalt catalysts stimulate carbon-chain growth reversely by modifying ASF law of Fischer–Tropsch synthesis. *Nature Communications*, *9*(1), 3250. https://doi.org/10.1038/s41467-018-05755-8

Cheng, Y., Lin, J., Xu, K., Wang, H., Yao, X., Pei, Y., Yan, S., Qiao, M., & Zong, B. (2016). Fischer-Tropsch Synthesis to Lower Olefins over Potassium-Promoted Reduced Graphene Oxide Supported Iron Catalysts. *ACS Catalysis*, *6*(1), 389–399. https://doi.org/10.1021/acscatal.5b02024

Chernyak, S. A., Corda, M., Dath, J. P., Ordomsky, V. V., & Khodakov, A. Y. (2022). Light olefin synthesis from a diversity of renewable and fossil feedstocks: state-of the-art and outlook. *Chemical Society Reviews*, *51*(18), 7994–8044. https://doi.org/10.1039/d1cs01036k

Chinthakuntla, A., Venkateswara Rao, K., Ashok, C., Rao, Kv., & Shilpa Chakra, C. (2014). Structural Analysis of CuO Nanomaterials prepared by Novel Microwave Assisted Method. *J. Atoms and Molecules*, *4*(5), 803–806. www.jamonline.in

Chonco, Z. H., Lodya, L., Claeys, M., & Van Steen, E. (2013). Copper ferrites: A model for investigating the role of copper in the dynamic iron-based Fischer-Tropsch catalyst. *Journal of Catalysis*, *308*, 363–373. https://doi.org/10.1016/j.jcat.2013.08.012

Cicco, A. Di, Aquilanti, G., Minicucci, M., Principi, E., Novello, N., Cognigni, A., & Olivi, L. (2009). Novel XAFS capabilities at ELETTRA synchrotron light source. *Journal of Physics: Conference Series*, *190*, 012043. https://doi.org/10.1088/1742-6596/190/1/012043

COSTA, S., BOROWIAK-PALEN, E., KRUSZYŃSKA, M., BACHMATIUK, A., & KALEŃCZUK, R. J. (2008). Characterization of carbon nanotubes by Raman spectroscopy. *Materials Science-Poland*, *26*(2), 433–441. https://doi.org/10.1016/j.carbon.2011.01.059

Côté, A. P., Benin, A. I., Ockwig, N. W., O'Keeffe, M., Matzger, A. J., & Yaghi, O. M. (2005). Porous, Crystalline, Covalent Organic Frameworks. *Science*, *310*(5751), 1166–1170. https://doi.org/10.1126/science.1120411

Côté, A. P., Benin, A. I., Ockwig, N. W., O'Keeffe, M., Matzger, A. J., Yaghi, O. M., Côté, A. P., Benin, A. I., Ockwig, N. W., O'Keeffe, M., Matzger, A. J., & Yaghi, O. M. (2005). Porous , Crystalline , Covalent Organic Frameworks. *Science*, *310*(November), 1166–1171. https://doi.org/10.1126/science.1120411

Côté, A. P., El-Kaderi, H. M., Furukawa, H., Hunt, J. R., & Yaghi, O. M. (2007). Reticular synthesis of microporous and mesoporous 2D covalent organic frameworks. *Journal of the American Chemical Society*, *129*(43), 12914–12915. https://doi.org/10.1021/ja0751781

Das, D., Ravichandran, G., & Chakrabarty, D. K. (1997). Conversion of syngas to light olefins over silicalite-1 supported iron and cobalt catalysts: Effect of manganese addition. *Catalysis Today*, *36*(3), 285–293. https://doi.org/10.1016/S0920-5861(96)00227-1

Das, G., Balaji Shinde, D., Kandambeth, S., Biswal, B. P., & Banerjee, R. (2014). Mechanosynthesis of imine, β-ketoenamine, and hydrogen-bonded imine-linked covalent organic frameworks using liquid-assisted grinding. *Chemical Communications*, *50*(84), 12615–12618. https://doi.org/10.1039/c4cc03389b

Das, S. K., Krishna Chandra, B., Molla, R. A., Sengupta, M., Islam, S. M., Majee, A., & Bhaumik, A. (2020). CuO grafted triazine functionalized covalent organic framework as an efficient catalyst for C-C homo coupling reaction. *Molecular Catalysis*, *480*, 110650. https://doi.org/10.1016/j.mcat.2019.110650

Davis, B. H. (2009). Fischer-Tropsch Synthesis: Reaction mechanisms for iron catalysts. *Catalysis Today*, *141*(1–2), 25–33. https://doi.org/10.1016/j.cattod.2008.03.005

De Smit, E., & Weckhuysen, B. M. (2008). The renaissance of iron-based Fischer-Tropsch synthesis: On the multifaceted catalyst deactivation behaviour. *Chemical Society Reviews, 37*(12), 2758–2781. https://doi.org/10.1039/b805427d

Ding, H., Li, J., Xie, G., Lin, G., Chen, R., Peng, Z., Yang, C., Wang, B., Sun, J., & Wang, C. (2018). An AIEgen-based 3D covalent organic framework for white light-emitting diodes. *Nature Communications*, *9*(1), 1–7. https://doi.org/10.1038/s41467-018-07670-4

Ding, S., Gao, J., Wang, Q., Zhang, Y., Song, W., Su, C., & Wang, W. (2011). Construction of Covalent Organic Framework for Catalysis : Pd / COF-LZU1 in Suzuki À Miyaura Coupling Reaction. *Journal of the American Chemical Society*, *133*, 19816–19822. https://doi.org/10.1021/ja206846p

Dong, X., Jia, Y., Zhang, M., Ji, S., Leng, L., Hugh Horton, J., Xu, C., He, C., Tan, Q., Zhang, J., & Li, Z. (2023). Molten salt-induction of geometrically deformed ruthenium single atom catalysts with high performance for aerobic oxidation of alcohols. *Chemical Engineering Journal*, *451*, 138660. https://doi.org/10.1016/j.cej.2022.138660

El-Kaderi, H. M., Hunt, J. R., Mendoza-Cortés, J. L., Côté, A. P., Taylor, R. E., O'Keeffe, M., & Yaghi, O. M. (2007). Designed Synthesis of 3D Covalent Organic Frameworks. *Science*, *316*(April), 268–272. https://doi.org/10.1126/science.1139915

Elvins, O. C., & Nash, A. W. (1926). The Reduction of Carbon Monoxide. *Nature*, *118*(2961), 154–155. https://doi.org/10.1038/118154a0

Eriksson, L. (2008). Modeling and Control of TC SI and DI enignes. *Oil & Gas Science and Technology*, *63*(1), 9–19. https://doi.org/10.2516/ogst

Fang, Q., Gu, S., Zheng, J., Zhuang, Z., Qiu, S., & Yan, Y. (2014a). 3D microporous base-functionalized covalent organic frameworks for size-selective catalysis. *Angewandte Chemie - International Edition*, *53*(11), 2878–2882. https://doi.org/10.1002/anie.201310500

Fang, Q., Gu, S., Zheng, J., Zhuang, Z., Qiu, S., & Yan, Y. (2014b). 3D Microporous Base-Functionalized Covalent Organic Frameworks for Size-Selective Catalysis. *Angew. Chem. Int. Ed.*, *53*(11), 2878–2882. https://doi.org/10.1002/anie.201310500

Feng, L., Zhang, C., Gao, G., & Cui, D. (2012). Facile synthesis of hollow Cu2O octahedral and spherical nanocrystals and their morphology-dependent photocatalytic properties. *Nanoscale Research Letters*, *7*(1), 1. https://doi.org/10.1186/1556-276X-7-276

Filonenko, G. A., Van Putten, R., Schulpen, E. N., Hensen, E. J. M., & Pidko, E. A. (2014). Highly efficient reversible hydrogenation of carbon dioxide to formates using a ruthenium PNP-pincer catalyst. *ChemCatChem*, *6*(6), 1526–1530. https://doi.org/10.1002/cctc.201402119

Filonenko, G. A., Vrijburg, W. L., Hensen, E. J. M., & Pidko, E. A. (2016). On the activity of supported Au catalysts in the liquid phase hydrogenation of CO2 to formates. *Journal of Catalysis*, *343*, 97–105. https://doi.org/10.1016/j.jcat.2015.10.002

Fiorio, J. L., Garcia, M. A. S., Gothe, M. L., Galvan, D., Troise, P. C., Conte-Junior, C. A., Vidinha, P., Camargo, P. H. C., & Rossi, L. M. (2023). Recent advances in the use of nitrogen-doped carbon materials for the design of noble metal catalysts. *Coordination Chemistry Reviews*, *481*, 215053. https://doi.org/10.1016/j.ccr.2023.215053

Fischer, F., & Tropsch, H. (1926). The Synthesis of Petroleum at Atmospheric Pressures from Gasification Products of Coal. *Brennstoff-Chemie*, *7*, 97–104.

Fraenkel, D., & Gates, B. C. (1980). Shape-Selective Fischer-Tropsch Synthesis Catalyzed by Zeolite-Entrapped Cobalt Clusters. *Journal of the American Chemical Society*, *102*(7), 2478–2480. https://doi.org/10.1021/ja00527a067

Fu, Q., Saltsburg, H., & Flytzani-Stephanopoulos, M. (2003). Active nonmetallic Au and Pt species on ceria-based water-gas shift catalysts. *Science*, *301*(5635), 935–938. https://doi.org/10.1126/science.1085721

Galvis, H. M. T., Bitter, J. H., Davidian, T., Ruitenbeek, M., Dugulan, A. I., Jong, K. P. de, Torres Galvis, H. M., Bitter, J. H., Davidian, T., Ruitenbeek, M., Dugulan, A. I., De Jong, K. P., Galvis, H. M. T., Bitter, J. H., Davidian, T., Ruitenbeek, M., Dugulan, A. I., Jong, K. P. de, Torres Galvis, H. M., … De Jong, K. P. (2012). Iron particle size effects for direct production of lower olefins from synthesis gas. *Journal of the American Chemical Society*, *134*(39), 16207–16215. https://doi.org/10.1021/ja304958u

Galvis, H. M. T., Bitter, J. H., Khare, C. B., Ruitenbeek, M., Dugulan, A. I., & Jong, K. P. de. (2012). Supported Iron Nanoparticles as Catalysts for Sustainable Production of Lower Olefins. *Science*, *335*(6070), 835–838. https://doi.org/10.1126/science.1215614

GANESAN, P. (1978). Particle size distribution function of supported metal catalysts by X-ray diffraction. *Journal of Catalysis*, *52*(2), 310–320. https://doi.org/10.1016/0021-9517(78)90145-8

Gao, Z., Dong, M., Wang, G., Sheng, P., Wu, Z., Yang, H., Zhang, B., Wang, G., Wang, J., & Qin, Y. (2015). Multiply Confined Nickel Nanocatalysts Produced by Atomic Layer Deposition for Hydrogenation Reactions. *Angewandte Chemie - International Edition*, *54*(31), 9006–9010. https://doi.org/10.1002/anie.201503749

Garba, M. D., Usman, M., Khan, S., Shehzad, F., Galadima, A., Ehsan, M. F., Ghanem, A. S., & Humayun, M. (2021). CO2towards fuels: A review of catalytic conversion of carbon dioxide to hydrocarbons. *Journal of Environmental Chemical Engineering*, *9*(2), 104756. https://doi.org/10.1016/j.jece.2020.104756

García-Sánchez, J. T., Valderrama-Zapata, R., Acevedo-Córdoba, L. F., Pérez-Martínez, D., Rincón-Ortiz, S., & Baldovino-Medrano, V. G. (2023). Calculation of Mass Transfer Limitations for a Gas-Phase Reaction in an Isothermal Fixed Bed Reactor: Tutorial and Sensitivity Analysis. *ACS Catalysis*, *13*(10), 6905–6918. https://doi.org/10.1021/acscatal.3c01282

Geng, K., He, T., Liu, R., Dalapati, S., Tan, K. T., Li, Z., Tao, S., Gong, Y., Jiang, Q., & Jiang, D. (2020). Covalent Organic Frameworks: Design, Synthesis, and Functions. *Chemical Reviews*, *120*(16), 8814–8933. https://doi.org/10.1021/acs.chemrev.9b00550

Ghosh, S., Molla, R. A., Kayal, U., Bhaumik, A., & Islam, S. M. (2019). Ag NPs decorated on a COF in the presence of DBU as an efficient catalytic system for the synthesis of tetramic acids via CO 2 fixation into propargylic amines at atmospheric pressure. *Dalton Transactions*, *48*(14), 4657–4666. https://doi.org/10.1039/C9DT00017H

Gracia, J. M., Prinsloo, F. F., & Niemantsverdriet, J. W. (2009). Mars-van krevelen-like mechanism of CO hydrogenation on an iron carbide surface. *Catalysis Letters*, *133*(3–4), 257–261. https://doi.org/10.1007/s10562-009-0179-5

Grommet, A. B., Feller, M., & Klajn, R. (2020). Chemical reactivity under nanoconfinement. *Nature Nanotechnology*, *15*(4), 256–271. https://doi.org/10.1038/s41565-020-0652-2

Gu, B. (2019). *Design of Metal Catalysts for Carbon Monoxide Hydrogenation with High Activity, Selectivity and Stability*. University of Lille.

Gu, B., Bahri, M., Ersen, O., Khodakov, A., & Ordomsky, V. V. (2019). Self-Regeneration of Cobalt and Nickel Catalysts Promoted with Bismuth for Non-deactivating Performance in Carbon Monoxide Hydrogenation. *ACS Catalysis*, *9*(2), 991–1000. https://doi.org/10.1021/acscatal.8b03991

Gu, B., He, S., Peron, D. V., Strossi Pedrolo, D. R., Moldovan, S., Ribeiro, M. C., Lobato, B., Chernavskii, P. A., Ordomsky, V. V., & Khodakov, A. Y. (2019). Synergy of nanoconfinement and promotion in the design of efficient supported iron catalysts for direct olefin synthesis from syngas. *Journal of Catalysis*, *376*, 1–16. https://doi.org/10.1016/j.jcat.2019.06.035

Gu, B., Ordomsky, V. V., Bahri, M., Ersen, O., Chernavskii, P. A., Filimonov, D., & Khodakov, A. Y. (2018). Effects of the promotion with bismuth and lead on direct synthesis of light olefins from syngas over carbon nanotube supported iron catalysts. *Applied Catalysis B: Environmental*, *234*, 153–166. https://doi.org/10.1016/j.apcatb.2018.04.025

Guan, X., Li, H., Ma, Y., Xue, M., Fang, Q., Yan, Y., Valtchev, V., & Qiu, S. (2019). Chemically stable polyarylether-based covalent organic frameworks. *Nature Chemistry*, *11*(6), 587–594. https://doi.org/10.1038/s41557-019-0238-5

Gunasekar, G. H., Jung, K.-D., & Yoon, S. (2019). Hydrogenation of CO2 to Formate using a Simple, Recyclable, and Efficient Heterogeneous Catalyst. *Inorganic Chemistry*, *58*, 3717–3723. https://doi.org/10.1021/acs.inorgchem.8b03336

Gunasekar, G. H., Park, K., Ganesan, V., Lee, K., Kim, N.-K., Jung, K.-D., & Yoon, S. (2017). A Covalent Triazine Framework, Functionalized with Ir/N- Heterocyclic Carbene Sites, for the Efficient Hydrogenation of CO2 to Formate. *Chemistry of Materials*, *29*, 6740–6748. https://doi.org/10.1021/acs.chemmater.7b01539

Gunasekar, G. H., Shin, J., Jung, K.-D., Park, K., & Yoon, S. (2018). Design Strategy toward Recyclable and Highly Efficient Heterogeneous Catalysts for the Hydrogenation of CO2 to Formate. *ACS Catalysis*, *8*, 4346–4353. https://doi.org/10.1021/acscatal.8b00392

Gunniya Hariyanandam, G., Hyun, D., Natarajan, P., Jung, K. D., & Yoon, S. (2016). An effective heterogeneous Ir(III) catalyst, immobilized on a heptazine-based organic framework, for the hydrogenation of CO2 to formate. *Catalysis Today*, *265*, 52–55. https://doi.org/10.1016/j.cattod.2015.10.037

Guo, J., & Jiang, D. (2020). Covalent Organic Frameworks for Heterogeneous Catalysis: Principle, Current Status, and Challenges. *ACS Central Science*, *6*(6), 869–879. https://doi.org/10.1021/acscentsci.0c00463

HALL, W. K., KOKES, R. J., & EMMET, P. H. (1957). Mechanism Studies of the Fischer-Tropsch Synthesis. The Addition of Radioactive Methanol, Carbon Dioxide and Gaseous Formaldehyde. *JOURNAL OF THE AMERICAN CHEMICAL SOCIETY*, *79*(12), 2983–2989. https://doi.org/10.1021/ja01569a001

Hall, W. K., Kokes, R. J., & Emmett, P. H. (1960). Mechanism Studies of the Fischer-Tropsch Synthesis: The Incorporation of Radioactive Ethylene, Propionaldehyde and Propanol. *Journal of the American Chemical Society*, *82*(5), 1027–1037. https://doi.org/10.1021/ja01490a005

Hao, C., Wang, S., Li, M., Kang, L., & Ma, X. (2011). Hydrogenation of CO2 to formic acid on supported ruthenium catalysts. *Catalysis Today*, *160*(1), 184–190. https://doi.org/10.1016/j.cattod.2010.05.034

He, Q., Yang, X., Ren, X., Koel, B. E., Ramaswamy, N., Mukerjee, S., & Kostecki, R. (2011). A novel CuFe-based catalyst for the oxygen reduction reaction in alkaline media. *Journal of Power Sources*, *196*(18), 7404–7410. https://doi.org/10.1016/j.jpowsour.2011.04.016

He, S., Wang, W., Shen, Z., Li, G., Kang, J., Liu, Z., Wang, G.-C., Zhang, Q., & Wang, Y. (2019). Carbon nanotube-supported bimetallic Cu-Fe catalysts for syngas conversion to higher alcohols. *Molecular Catalysis*, *479*(September), 110610. https://doi.org/10.1016/j.mcat.2019.110610

Heise, H. M., Kuckuk, R., Ojha, A. K., Srivastava, A., Srivastava, V., & Asthana, B. P. (2009). Characterisation of carbonaceous materials using Raman spectroscopy: A comparison of carbon nanotube filters, single- And multi-walled nanotubes, graphitised porous carbon and graphite. *Journal of Raman Spectroscopy*, *40*(3), 344–353. https://doi.org/10.1002/jrs.2120

Henrici-Olivé, G., & Olivé, S. (1976). The Fischer-Tropsch Synthesis: Molecular Weight Distribution of Primary Products and Reaction Mechanism. *Angewandte Chemie International Edition in English*, *15*(3), 136–141. https://doi.org/10.1002/anie.197601361

Heshmat, M. (2020). Alternative Pathway of CO2 Hydrogenation by Lewis-Pair- Functionalized UiO-66 MOF Revealed by Metadynamics Simulations. *The Journal of Physical Chemistry C*, *124*, 10951−10960. https://doi.org/10.1021/acs.jpcc.0c01088

Hong, J. (2009). *Novel preparation techniques and reactivity of cobalt metal nanoparticles for synthesis of clean fuels using Fischer-Tropsch reaction*. Université des Sciences et Technologies de Lille and Sichuan University.

Huff, G. A., & Satterfield, C. N. (1984). Intrinsic kinetics of the Fischer-Tropsch synthesis on a

Reduced Fused-Magnetite Catalyst. *Industrial and Engineering Chemistry Process Design and Development*, *23*(4), 696–705. https://doi.org/10.1021/i200027a012

IEA. (2023). *Greenhouse Gas Emissions from Energy Data Explorer*. https://www.iea.org/data-and-statistics/data-tools/greenhouse-gas-emissions-from-energy-data-explorer

Iemhoff, A., Vennewald, M., & Palkovits, R. (2023). Single-Atom Catalysts on Covalent Triazine Frameworks: at the Crossroad between Homogeneous and Heterogeneous Catalysis. *Angewandte Chemie International Edition*, *62*(7). https://doi.org/10.1002/anie.202212015

Ismail, A. S. M., Casavola, M., Liu, B., Gloter, A., Van Deelen, T. W., Versluijs, M., Meeldijk, J. D., Stéphan, O., De Jong, K. P., & De Groot, F. M. F. (2019). Atomic-Scale Investigation of the Structural and Electronic Properties of Cobalt-Iron Bimetallic Fischer-Tropsch Catalysts. *ACS Catalysis*, *9*(9), 7998–8011. https://doi.org/10.1021/acscatal.8b04334

Jacobs, G., Patterson, P. M., Zhang, Y., Das, T., Li, J., & Davis, B. H. (2002). Fischer-Tropsch synthesis: Deactivation of noble metal-promoted Co/Al2O3 catalysts. *Applied Catalysis A: General*, *233*(1–2), 215–226. https://doi.org/10.1016/S0926-860X(02)00147-3

Jian, L., Xiuling, J., Dairong, C., & Wei, L. (2009). Solvothermal synthesis and characterization of Fe3O4 and γ-Fe2O3 nanoplates. *Journal of Physical Chemistry C*, *113*(10), 4012–4017. https://doi.org/10.1021/jp810583e

Jiang, X., Nie, X., Guo, X., Song, C., & Chen, J. G. (2020). Recent Advances in Carbon Dioxide Hydrogenation to Methanol via Heterogeneous Catalysis. *Chemical Reviews*, *120*(15), 7984–8034. https://doi.org/10.1021/acs.chemrev.9b00723

Jones, J., Xiong, H., DeLaRiva, A. T., Peterson, E. J., Pham, H., Challa, S. R., Qi, G., Oh, S., Wiebenga, M. H., Hernández, X. I. P., Wang, Y., & Datye, A. K. (2016). Thermally stable single-atom platinum-on-ceria catalysts via atom trapping. *Science*, *353*(6295), 150–154. https://doi.org/10.1126/science.aaf7720

Jong, K. P. de. (2009). *Synthesis of Solid Catalysts* (K. P. de Jong (ed.)). WILEY-VCH Verlag GmbH & Co. KGaA.

Kandambeth, S., Mallick, A., Lukose, B., Mane, M. V., Heine, T., & Banerjee, R. (2012). Construction of Crystalline 2D Covalent Organic Frameworks with Remarkable Chemical (Acid/Base) Stability via a Combined Reversible and Irreversible Route. *Journal of the American Chemical Society*, *134*, 19524−19527. https://doi.org/10.1021/ja308278w

Khodakov, A. Y., Chu, W., & Fongarland, P. (2007). Advances in the development of novel cobalt Fischer-Tropsch catalysts for synthesis of long-chain hydrocarbons and clean fuels. *Chemical Reviews*, *107*(5), 1692–1744. https://doi.org/10.1021/cr050972v

Kowalczuk, P. B., & Drzymala, J. (2016). Physical meaning of the Sauter mean diameter of spherical particulate matter. *Particulate Science and Technology*, *34*(6), 645–647. https://doi.org/10.1080/02726351.2015.1099582

Kummer, J. T., & Emmett, P. H. (1953). Fischer-Tropsch Synthesis Mechanism Studies. The

Addition of Radioactive Alcohols to the Synthesis Gas. *Journal of the American Chemical Society*, *75*(21), 5177–5183. https://doi.org/10.1021/ja01117a008

Kummer, J. T., Podgurski, H. H., W. B. Spencer, & Emmett, P. H. (1951). Mechanism Studies of the Fischer-Tropsch Synthesis. The Addition of Radioactive Alcohol. *Journal of the American Chemical Society*, *73*(2), 564–569. https://doi.org/10.1021/ja01146a018

Kuznetsov, V. L., Bokova-Sirosh, S. N., Moseenkov, S. I., Ishchenko, A. V., Krasnikov, D. V., Kazakova, M. A., Romanenko, A. I., Tkachev, E. N., & Obraztsova, E. D. (2014). Raman spectra for characterization of defective CVD multi-walled carbon nanotubes. *Physica Status Solidi (B) Basic Research*, *251*(12), 2444–2450. https://doi.org/10.1002/pssb.201451195

Lee, S. (1996). *Alternative Fuels* (1st editio). CRC Press. https://doi.org/10.1201/9781315137179

Li, F., & Fan, L. S. (2008). Clean coal conversion processes - Progress and challenges. *Energy and Environmental Science*, *1*(2), 248–267. https://doi.org/10.1039/b809218b

Li, Z., & Xu, Q. (2017). Metal-Nanoparticle-Catalyzed Hydrogen Generation from Formic Acid. *Accounts of Chemical Research*, *50*(6), 1449–1458. https://doi.org/10.1021/acs.accounts.7b00132

Liu, J. (2017). Aberration-corrected scanning transmission electron microscopy in single-atom catalysis: Probing the catalytically active centers. *Cuihua Xuebao/Chinese Journal of Catalysis*, *38*(9), 1460–1472. https://doi.org/10.1016/S1872-2067(17)62900-0

Liu, L., & Corma, A. (2018). Metal Catalysts for Heterogeneous Catalysis: From Single Atoms to Nanoclusters and Nanoparticles. *Chemical Reviews*, *118*(10), 4981–5079. https://doi.org/10.1021/acs.chemrev.7b00776

Liu, Q., Yang, X., Li, L., Miao, S., Li, Y., Li, Y., Wang, X., Huang, Y., & Zhang, T. (2017). Direct catalytic hydrogenation of CO2 to formate over a Schiff-base-mediated gold nanocatalyst. *Nature Communications*, *8*(1), 1407. https://doi.org/10.1038/s41467-017-01673-3

Liu, S., Zhang, X., & Jiang, L. (2019). 1D Nanoconfined Ordered-Assembly Reaction. *Advanced Materials Interfaces*, *6*(8), 1–9. https://doi.org/10.1002/admi.201900104

Liu, Y., Chen, J. F., & Zhang, Y. (2015). Effects of pretreatment on iron-based catalysts for forming light olefins via Fischer–Tropsch synthesis. *Reaction Kinetics, Mechanisms and Catalysis*, *114*(2), 433–449. https://doi.org/10.1007/s11144-014-0821-0

Londoño-Calderon, A., Ponce, A., Santiago, U., Mejia, S., & José-Yacamán, M. (2017). Controlling the Number of Atoms on Catalytic Metallic Clusters. In *Studies in Surface Science and Catalysis* (Vol. 177). https://doi.org/10.1016/B978-0-12-805090-3.00006-1

Lu, J., Yang, L., Xu, B., Wu, Q., Zhang, D., Yuan, S., Zhai, Y., Wang, X., Fan, Y., & Hu, Z. (2014). Promotion effects of nitrogen doping into carbon nanotubes on supported iron fischer-tropsch catalysts for lower olefins. *ACS Catalysis*, *4*(2), 613–621.

https://doi.org/10.1021/cs400931z

Lu, Q., & Jiao, F. (2016). Electrochemical CO2 reduction: Electrocatalyst, reaction mechanism, and process engineering. *Nano Energy*, *29*, 439–456. https://doi.org/10.1016/j.nanoen.2016.04.009

Lu, Y., Zhang, R., Cao, B., Ge, B., Tao, F. F., Shan, J., Nguyen, L., Bao, Z., Wu, T., Pote, J. W., Wang, B., & Yu, F. (2017). Elucidating the Copper-Hägg Iron Carbide Synergistic Interactions for Selective CO Hydrogenation to Higher Alcohols. *ACS Catalysis*, *7*(8), 5500–5512. https://doi.org/10.1021/acscatal.7b01469

Luk, H. T., Mondelli, C., Mitchell, S., Siol, S., Stewart, J. A., Curulla Ferré, D., & Pérez-Ramírez, J. (2018). Role of Carbonaceous Supports and Potassium Promoter on Higher Alcohols Synthesis over Copper-Iron Catalysts. *ACS Catalysis*, *8*(10), 9604–9618. https://doi.org/10.1021/acscatal.8b02714

Luo, Q. X., Guo, L. P., Yao, S. Y., Bao, J., Liu, Z. T., & Liu, Z. W. (2019). Cobalt nanoparticles confined in carbon matrix for probing the size dependence in Fischer-Tropsch synthesis. *Journal of Catalysis*, *369*, 143–156. https://doi.org/10.1016/j.jcat.2018.11.002

Luo, T., Gilmanova, L., & Kaskel, S. (2023). Advances of MOFs and COFs for photocatalytic CO2 reduction, H2 evolution and organic redox transformations. *Coordination Chemistry Reviews*, *490*, 215210. https://doi.org/10.1016/j.ccr.2023.215210

Ma, M., Cheng, X., Shi, Z., Zhang, C., Li, Y., Yang, Y., Gong, C., Zhang, Z., Fei, H., Zhu, C., He, Y., & Xie, E. (2022). Role of N in Transition-Metal-Nitrides for Anchoring Platinum-Group Metal Atoms toward Single-Atom Catalysis. *Small Methods*, *6*(7), 2200295. https://doi.org/10.1002/smtd.202200295

Ma, M., Gong, C., An, X., Shi, Z., Liu, Z., & He, Y. (2023). The emergence of single-atom-layer catalysis. *Materials Today Catalysis*, *1*, 100004. https://doi.org/10.1016/j.mtcata.2023.100004

Maihom, T., Wannakao, S., Boekfa, B., & Limtrakul, J. (2013). Production of Formic Acid via Hydrogenation of CO2 over a Copper- Alkoxide-Functionalized MOF: A Mechanistic Study. *The Journal of Physical Chemistry C*, *117*, 17650−17658. https://doi.org/10.1021/jp405178p

Masters, C. (1979). The Fischer-Tropsch Reaction. *Advances in Organometallic Chemistry*, *17*(C), 61–103. https://doi.org/10.1016/S0065-3055(08)60321-4

Matsubu, J. C., Yang, V. N., & Christopher, P. (2015). Isolated metal active site concentration and stability control catalytic CO2 reduction selectivity. *Journal of the American Chemical Society*, *137*(8), 3076–3084. https://doi.org/10.1021/ja5128133

Mazari, S. A., Hossain, N., Basirun, W. J., Mubarak, N. M., Abro, R., Sabzoi, N., & Shah, A. (2021). An overview of catalytic conversion of CO2 into fuels and chemicals using metal organic frameworks. *Process Safety and Environmental Protection*, *149*, 67–92. https://doi.org/10.1016/j.psep.2020.10.025

Mears, D. E. (1971). Diagnostic criteria for heat transport limitations in fixed bed reactors. *Journal of Catalysis*, *20*(2), 127–131. https://doi.org/10.1016/0021-9517(71)90073-X

Modak, A., Ghosh, A., Bhaumik, A., & Chowdhury, B. (2021). CO2 hydrogenation over functional nanoporous polymers and metal-organic frameworks. *Advances in Colloid and Interface Science*, *290*, 102349. https://doi.org/10.1016/j.cis.2020.102349

Morales, J., Espinos, J. P., Caballero, A., Gonzalez-Elipe, A. R., & Mejias, J. A. (2005). XPS study of interface and ligand effects in supported Cu2O and CuO nanometric particles. *Journal of Physical Chemistry B*, *109*(16), 7758–7765. https://doi.org/10.1021/jp0453055

Mori, K., Taga, T., & Yamashita, H. (2017). Isolated Single-Atomic Ru Catalyst Bound on a Layered Double Hydroxide for Hydrogenation of CO2 to Formic Acid. *ACS Catalysis*, *7*, 3147−3151. https://doi.org/10.1021/acscatal.7b00312

Mouarrawis, V., Plessius, R., van der Vlugt, J. I., & Reek, J. N. H. (2018). Confinement effects in catalysis using well-defined materials and cages. *Frontiers in Chemistry*, *6*(DEC), 1–20. https://doi.org/10.3389/fchem.2018.00623

Moulder, J. F., Stickle, W. F., E.'Sobol, P., & Bomben, K. D. (1992). *Handbook of X-ray Photoelectron Spectroscopy: A Reference Book of Standard Spectra for Identification and Interpretation of XPS Data* (J. Chastain (ed.)). Physical Electronics Division, Perkin-Elmer Corporation.

Muetterties, E. L., & Stein, J. (1979). Mechanistic Features of Catalytic Carbon Monoxide Hydrogenation Reactions. *Chemical Reviews*, *79*(6), 479–490. https://doi.org/10.1021/cr60322a001

Navarro-Jaén, S., Virginie, M., Bonin, J., Robert, M., Wojcieszak, R., & Khodakov, A. Y. (2021). Highlights and challenges in the selective reduction of carbon dioxide to methanol. *Nature Reviews Chemistry*, *5*(8), 564–579. https://doi.org/10.1038/s41570-021-00289-y

Nguyen, L. T. M., Park, H., Banu, M., Kim, J. Y., Youn, D. H., Magesh, G., Kim, W. Y., & Lee, J. S. (2015). Catalytic CO2 hydrogenation to formic acid over carbon nanotube-graphene supported PdNi alloy catalysts. *RSC Advances*, *5*(128), 105560–105566. https://doi.org/10.1039/c5ra21017h

Ogino, I. (2017). X-ray absorption spectroscopy for single-atom catalysts: Critical importance and persistent challenges. *Cuihua Xuebao/Chinese Journal of Catalysis*, *38*(9), 1481–1488. https://doi.org/10.1016/S1872-2067(17)62880-8

Ordomsky, V. V., Legras, B., Cheng, K., Paul, S., & Khodakov, A. Y. (2015). The role of carbon atoms of supported iron carbides in Fischer-Tropsch synthesis. *Catalysis Science and Technology*, *5*(3), 1433–1437. https://doi.org/10.1039/c4cy01631a

Ordomsky, Vitaly V., Dros, A.-B., Schwiedernoch, R., & Khodakov, A. Y. (2017). Challenges and Role of Catalysis in CO2 Conversion to Chemicals and Fuels. In B. Sels & M. Van de Voorde (Eds.), *Nanotechnology in Catalysis: Applications in the Chemical Industry, Energy Development, and Environment* (First Edit, pp. 805–849). WILEY-VCH Verlag GmbH &

Co. KGaA.

Ordomsky, Vitaly V., Luo, Y., Gu, B., Carvalho, A., Chernavskii, P. A., Cheng, K., & Khodakov, A. Y. (2017). Soldering of iron catalysts for direct synthesis of light olefins from syngas under mild reaction conditions. *ACS Catalysis*, *7*(10), 6445–6452. https://doi.org/10.1021/acscatal.7b01307

Ou, M., Tu, W., Yin, S., Xing, W., Wu, S., Wang, H., Wan, S., Zhong, Q., & Xu, R. (2018). Amino-Assisted Anchoring of CsPbBr 3 Perovskite Quantum Dots on Porous g-C 3 N 4 for Enhanced Photocatalytic CO 2 Reduction . *Angewandte Chemie*, *130*(41), 13758–13762. https://doi.org/10.1002/ange.201808930

Pan, X., & Bao, X. (2011). The effects of confinement inside carbon nanotubes on catalysis. *Accounts of Chemical Research*, *44*(8), 553–562. https://doi.org/10.1021/ar100160t

Pan, X., Fan, Z., Chen, W., Ding, Y., Luo, H., & Bao, X. (2007). Enhanced ethanol production inside carbon-nanotube reactors containing catalytic particles. *Nature Materials*, *6*(7), 507–511. https://doi.org/10.1038/nmat1916

Park, H., Lee, J. H., Kim, E. H., Kim, K. Y., Choi, Y. H., Youn, D. H., & Lee, J. S. (2016). A highly active and stable palladium catalyst on a g-C3N4 support for direct formic acid synthesis under neutral conditions. *Chemical Communications*, *52*(99), 14302–14305. https://doi.org/10.1039/c6cc07401d

Park, K., Gunasekar, G. H., Prakash, N., Jung, K. D., & Yoon, S. (2015). A Highly Efficient Heterogenized Iridium Complex for the Catalytic Hydrogenation of Carbon Dioxide to Formate. *ChemSusChem*, *8*(20), 3410–3413. https://doi.org/10.1002/cssc.201500436

Peña, D., Jensen, L., Cognigni, A., Myrstad, R., Neumayer, T., van Beek, W., & Rønning, M. (2018). The Effect of Copper Loading on Iron Carbide Formation and Surface Species in Iron-Based Fischer–Tropsch Synthesis Catalysts. *ChemCatChem*, *10*(6), 1300–1312. https://doi.org/10.1002/cctc.201701673

Peng, Y., Wong, W. K., Hu, Z., Cheng, Y., Yuan, D., Khan, S. A., & Zhao, D. (2016). Room Temperature Batch and Continuous Flow Synthesis of Water-Stable Covalent Organic Frameworks (COFs). *Chemistry of Materials*, *28*(14), 5095–5101. https://doi.org/10.1021/acs.chemmater.6b01954

Phaahlamohlaka, T. N., Kumi, D. O., Dlamini, M. W., Jewell, L. L., & Coville, N. J. (2016). Ruthenium nanoparticles encapsulated inside porous hollow carbon spheres: A novel catalyst for Fischer–Tropsch synthesis. *Catalysis Today*, *275*, 76–83. https://doi.org/10.1016/j.cattod.2015.11.034

Pham, T. H., Duan, X., Qian, G., Zhou, X., & Chen, D. (2014). CO activation pathways of fischer-tropsch synthesis on χ-Fe 5C2 (510): Direct versus hydrogen-assisted CO dissociation. *Journal of Physical Chemistry C*, *118*(19), 10170–10176. https://doi.org/10.1021/jp502225r

Philippe, R., Lacroix, M., Dreibine, L., Pham-Huu, C., Edouard, D., Savin, S., Luck, F., &

Schweich, D. (2009). Effect of structure and thermal properties of a Fischer-Tropsch catalyst in a fixed bed. *Catalysis Today*, *147*(SUPPL.). https://doi.org/10.1016/j.cattod.2009.07.058

Philippe, R., Lacroix, M., Dreibine, L., Pham-Huu, C., Edouard, D., Savin, S., Luck, F., & Schweich, D. (2011). Erratum: Effect of structure and thermal properties of a Fischer-Tropsch catalyst in a fixed bed (Catalysis Today (2009) 147 (S305-S312)). *Catalysis Today*, *160*(1), 255–256. https://doi.org/10.1016/j.cattod.2010.03.032

Pichler, H., & Schulz, H. (1970). Neuere Erkenntnisse auf dem Gebiet der Synthese von Kohlenwasserstoffen aus CO und H2. *Chemie Ingenieur Technik*, *42*(18), 1162–1174. https://doi.org/10.1002/cite.330421808

Pichler, Helmut. (1952). Twenty-five Years of Synthesis of Gasoline by Catalytic Conversion of Carbon Monoxide and Hydrogen. *Advances in Catalysis*, *4*, 271–341. https://doi.org/10.1016/S0360-0564(08)60617-3

Podgurski, H. H., Kummer, J. T., DeWitt, T. W., & Emmett, P. H. (1950). Preparation, Stability and Adsorptive Properties of the Carbides of Iron. *Journal of the American Chemical Society*, *72*(12), 5382–5388. https://doi.org/10.1021/ja01168a006

Porto, A. B. (2013). *Modelagem de processos de oxidação de nanotubos de carbono de carbono de parede única em meio ácido*. Universidade Federal de Juiz de Fora.

Qiao, B., Wang, A., Yang, X., Allard, L. F., Jiang, Z., Cui, Y., Liu, J., Li, J., & Zhang, T. (2011). Single-atom catalysis of CO oxidation using Pt1/FeOx. *Nature Chemistry*, *3*(8), 634–641. https://doi.org/10.1038/nchem.1095

Ramaraj, H., Madiga, J., Elangovan, H., Haridoss, P., & Sharma, C. P. (2017). Homogenization for Dispersion and Reduction in Length of Carbon Nanotubes. *Transactions of the Indian Institute of Metals*, *70*(10), 2629–2639. https://doi.org/10.1007/s12666-017-1123-9

Ravel, B., & Newville, M. (2005). ATHENA , ARTEMIS , HEPHAESTUS : data analysis for X-ray absorption spectroscopy using IFEFFIT. *Journal of Synchrotron Radiation*, *12*(4), 537–541. https://doi.org/10.1107/S0909049505012719

Rennhofer, H., & Zanghellini, B. (2021). Dispersion state and damage of carbon nanotubes and carbon nanofibers by ultrasonic dispersion: A review. *Nanomaterials*, *11*(6). https://doi.org/10.3390/nano11061469

Richard, A. R., & Fan, M. (2017). Low-Pressure Hydrogenation of CO2 to CH3OH Using Ni-In-Al/SiO2 Catalyst Synthesized via a Phyllosilicate Precursor. *ACS Catalysis*, *7*(9), 5679–5692. https://doi.org/10.1021/acscatal.7b00848

Rohmann, K., Kothe, J., Haenel, M. W., Englert, U., Hölscher, M., & Leitner, W. (2016). Hydrogenation of CO2to Formic Acid with a Highly Active Ruthenium Acriphos Complex in DMSO and DMSO/Water. *Angewandte Chemie - International Edition*, *55*(31), 8966–8969. https://doi.org/10.1002/anie.201603878

Romero-Muñiz, I., Mavrandonakis, A., Albacete, P., Vega, A., Briois, V., Zamora, F., & Platero-

Prats, A. E. (2020). Unveiling the Local Structure of Palladium Loaded into Imine-Linked Layered Covalent Organic Frameworks for Cross-Coupling Catalysis. *Angewandte Chemie - International Edition*, *59*(31), 13013–13020. https://doi.org/10.1002/anie.202004197

Saib, A. M., Moodley, D. J., Ciobîc, I. M., Hauman, M. M., Sigwebela, B. H., Weststrate, C. J., Niemantsverdriet, J. W., & Van De Loosdrecht, J. (2010). Fundamental understanding of deactivation and regeneration of cobalt Fischer-Tropsch synthesis catalysts. *Catalysis Today*, *154*(3–4), 271–282. https://doi.org/10.1016/j.cattod.2010.02.008

Santos, R. G. dos, & Alencar, A. C. (2019). Biomass-derived syngas production via gasification process and its catalytic conversion into fuels by Fischer Tropsch synthesis: A review. *International Journal of Hydrogen Energy*, *xxxx*. https://doi.org/10.1016/j.ijhydene.2019.07.133

Schaub, T., & Paciello, R. A. (2011a). A process for the synthesis of formic acid by CO2 hydrogenation: Thermodynamic aspects and the role of CO. *Angewandte Chemie - International Edition*, *50*(32), 7278–7282. https://doi.org/10.1002/anie.201101292

Schaub, T., & Paciello, R. A. (2011b). A Process for the Synthesis of Formic Acid by CO2 Hydrogenation: Thermodynamic Aspects and the Role of CO. *Angewandte Chemie International Edition*, *50*(32), 7278–7282. https://doi.org/10.1002/anie.201101292

Serp, P., Corrias, M., & Kalck, P. (2003). Carbon nanotubes and nanofibers in catalysis. *Applied Catalysis A: General*, *253*(2), 337–358. https://doi.org/10.1016/S0926-860X(03)00549-0

Sesis, A., Hodnett, M., Memoli, G., Wain, A. J., Jurewicz, I., Dalton, A. B., Carey, J. D., & Hinds, G. (2013). Influence of Acoustic Cavitation on the Controlled Ultrasonic Dispersion of Carbon Nanotubes. *Journal of Physical Chemistry B, 117*, 15141–15150. https://doi.org/10.1021/jp410041y

Shao, X., Xu, J., Huang, Y., Su, X., Duan, H., Wang, X., & Zhang, T. (2016). Pd@C3N4 Nanocatalyst for Highly Efficient Hydrogen Storage System Based on Potassium Bicarbonate/Formate. *AIChE Journal*, *62*(7), 2410–2418. https://doi.org/10.1002/aic.15218

Shi, D., Yang, Q., Peterson, C., Lamic-Humblot, A. F., Girardon, J. S., Griboval-Constant, A., Stievano, L., Sougrati, M. T., Briois, V., Bagot, P. A. J., Wojcieszak, R., Paul, S., & Marceau, E. (2019). Bimetallic Fe-Ni/SiO2 catalysts for furfural hydrogenation: Identification of the interplay between Fe and Ni during deposition-precipitation and thermal treatments. *Catalysis Today*, *334*(July 2018), 162–172. https://doi.org/10.1016/j.cattod.2018.11.041

Shroff, M. D., Kalakkad, D. S., Coulter, K. E., Kohler, S. D., Harrington, M. S., Jackson, N. B., Sault, A. G., & Datye, A. K. (1995). Activation of Precipitated Iron Fischer-Tropsch Synthesis Catalysts. *Journal of Catalysis, 156*(2), 185–207. https://doi.org/10.1006/jcat.1995.1247

Singh, V., Jang, S., Vishwakarma, N. K., & Kim, D. P. (2018). Intensified synthesis and post-synthetic modification of covalent organic frameworks using a continuous flow of microdroplets technique. *NPG Asia Materials*, *10*(1). https://doi.org/10.1038/am.2017.209

Smit, B., & Maesen, T. L. M. (2008). Towards a molecular understanding of shape selectivity. *Nature*, *451*(7179), 671–678. https://doi.org/10.1038/nature06552

Song, Y., Sun, Q., Aguila, B., & Ma, S. (2019). Opportunities of Covalent Organic Frameworks for Advanced Applications. *Advanced Science*, *6*(2), 1801410. https://doi.org/10.1002/advs.201801410

Subramanian, V., Cheng, K., Lancelot, C., Heyte, S., Paul, S., Moldovan, S., Ersen, O., Marinova, M., Ordomsky, V. V., & Khodakov, A. Y. (2016). Nanoreactors: An Efficient Tool to Control the Chain-Length Distribution in Fischer-Tropsch Synthesis. *ACS Catalysis*, *6*(3), 1785–1792. https://doi.org/10.1021/acscatal.5b01596

Sun, R., Liao, Y., Bai, S. T., Zheng, M., Zhou, C., Zhang, T., & Sels, B. F. (2021). Heterogeneous catalysts for CO2hydrogenation to formic acid/formate: From nanoscale to single atom. *Energy and Environmental Science*, *14*(3), 1247–1285. https://doi.org/10.1039/d0ee03575k

Suresh, S., Karthikeyan, S., & Jayamoorthy, K. (2016). FTIR and multivariate analysis to study the effect of bulk and nano copper oxide on peanut plant leaves. *Journal of Science: Advanced Materials and Devices*, *1*(3), 343–350. https://doi.org/10.1016/j.jsamd.2016.08.004

Tao, F. (Feng). (2012). Design of an in-house ambient pressure AP-XPS using a bench-top X-ray source and the surface chemistry of ceria under reaction conditions. *Chemical Communications*, *48*(32), 3812. https://doi.org/10.1039/c2cc17715c

Tavasoli, A., Trépanier, M., Malek Abbaslou, R. M., Dalai, A. K., & Abatzoglou, N. (2009). Fischer-Tropsch synthesis on mono- and bimetallic Co and Fe catalysts supported on carbon nanotubes. *Fuel Processing Technology*, *90*(12), 1486–1494. https://doi.org/10.1016/j.fuproc.2009.07.007

Tessonnier, J. P., Ersen, O., Weinberg, G., Pham-Huu, C., Su, D. S., & Schlögl, R. (2009). Selective deposition of metal nanoparticles inside or outside multiwalled carbon nanotubes. *ACS Nano*, *3*(8), 2081–2089. https://doi.org/10.1021/nn900647q

Tsakoumis, N. E., Rønning, M., Borg, Ø., Rytter, E., & Holmen, A. (2010). Deactivation of cobalt based Fischer-Tropsch catalysts: A review. *Catalysis Today*, *154*(3–4), 162–182. https://doi.org/10.1016/j.cattod.2010.02.077

Vannice, M. A. (1976). The Catalytic Synthesis of Hydrocarbons from Carbon Monoxide and Hydrogen. *Catalysis Reviews: Science and Engineering*, *14*(1), 153–191. https://doi.org/10.1080/03602457608073410

Védrine, J. C. (2019). Metal Oxides in Heterogeneous Oxidation Catalysis: State of the Art and Challenges for a More Sustainable World. *ChemSusChem*, *12*(3), 577–588. https://doi.org/10.1002/cssc.201802248

Wang, A., Li, J., & Zhang, T. (2018). Heterogeneous single-atom catalysis. *Nature Reviews Chemistry*, *2*(6), 65–81. https://doi.org/10.1038/s41570-018-0010-1

Wang, C., Pan, X., & Bao, X. (2010). Direct production of light olefins from syngas over a carbon nanotube confined iron catalyst. *Chinese Science Bulletin*, *55*(12), 1117–1119. https://doi.org/10.1007/s11434-010-0076-8

Wang, J. (2012). *Design of efficient catalysts for hydrogenation of carbon oxides to alcohols and olefins*. Université des Sciences et Technologies de Lille and Xiamen University.

Wang, Qiang, Chen, Y., & Li, Z. (2019). Research Progress of Catalysis for Low-Carbon Olefins Synthesis Through Hydrogenation of CO 2 . *Journal of Nanoscience and Nanotechnology*, *19*(6), 3162–3172. https://doi.org/10.1166/jnn.2019.16586

Wang, Qiyan, Santos, S., Urbina-Blanco, C. A., Hernández, W. Y., Impéror-Clerc, M., Vovk, E. I., Marinova, M., Ersen, O., Baaziz, W., Safonova, O. V., Khodakov, A. Y., Saeys, M., & Ordomsky, V. V. (2021a). Solid micellar Ru single-atom catalysts for the water-free hydrogenation of CO2 to formic acid. *Applied Catalysis B: Environmental*, *290*(November 2020), 120036. https://doi.org/10.1016/j.apcatb.2021.120036

Wang, Qiyan, Santos, S., Urbina-Blanco, C. A., Hernández, W. Y., Impéror-Clerc, M., Vovk, E. I., Marinova, M., Ersen, O., Baaziz, W., Safonova, O. V., Khodakov, A. Y., Saeys, M., & Ordomsky, V. V. (2021b). Solid micellar Ru single-atom catalysts for the water-free hydrogenation of CO2 to formic acid. *Applied Catalysis B: Environmental*, *290*(November 2020), 1–9. https://doi.org/10.1016/j.apcatb.2021.120036

Wang, Saihua, Niu, H., Cao, D., & Cai, Y. (2019). Covalent-organic frameworks as adsorbent and matrix of SALDI-TOF MS for the enrichment and rapid determination of fluorochemicals. *Talanta*, *194*(October 2018), 522–527. https://doi.org/10.1016/j.talanta.2018.10.071

Wang, Shengping, Hou, S., Wu, C., Zhao, Y., & Ma, X. (2019). RuCl3 anchored onto post-synthetic modification MIL-101(Cr)-NH2 as heterogeneous catalyst for hydrogenation of CO2 to formic acid. *Chinese Chemical Letters*, *30*(2), 398–402. https://doi.org/10.1016/j.cclet.2018.06.021

Weisz, P. B., & Prater, C. D. (1954). Interpretation of Measurements in Experimental Catalysis. *Advances in Catalysis*, *6*, 143–196. https://doi.org/10.1016/S0360-0564(08)60390-9

Wu, X., Qian, W., Ma, H., Zhang, H., Liu, D., Sun, Q., & Ying, W. (2019). Li-decorated Fe-Mn nanocatalyst for high-temperature Fischer–Tropsch synthesis of light olefins. *Fuel*, *257*(August), 116101. https://doi.org/10.1016/j.fuel.2019.116101

Xiao, J., Pan, X., Guo, S., Ren, P., & Bao, X. (2015). Toward fundamentals of confined catalysis in carbon nanotubes. *Journal of the American Chemical Society*, *137*(1), 477–482. https://doi.org/10.1021/ja511498s

Xiao, S., Zhang, Y., Gao, P., Zhong, L., Li, X., Zhang, Z., Wang, H., Wei, W., & Sun, Y. (2017). Highly efficient Cu-based catalysts via hydrotalcite-like precursors for CO2 hydrogenation to methanol. *Catalysis Today*, *281*, 327–336. https://doi.org/10.1016/j.cattod.2016.02.004

Xu, H., Gao, J., & Jiang, D. (2015). Stable, crystalline, porous, covalent organic frameworks as a platform for chiral organocatalysts. *Nature Chemistry*, *7*(11), 905–912. https://doi.org/10.1038/nchem.2352

Xu, R., Tan, Z., Fan, G., Ji, G., Xiong, D. B., Guo, Q., Su, Y., Li, Z., & Zhang, D. (2018). High-strength CNT/Al-Zn-Mg-Cu composites with improved ductility achieved by flake powder metallurgy via elemental alloying. *Composites Part A: Applied Science and Manufacturing*, *111*(May), 1–11. https://doi.org/10.1016/j.compositesa.2018.05.012

Xu, Z., Mcnamara, N. D., Neumann, G. T., Schneider, W. F., & Hicks, J. C. (2013). Catalytic hydrogenation of CO2 to formic acid with silica-tethered iridium catalysts. *ChemCatChem*, *5*(7), 1769–1771. https://doi.org/10.1002/cctc.201200839

Yang, C., Zhao, H., Hou, Y., & Ma, D. (2012). Fe 5 C 2 Nanoparticles: A Facile Bromide-Induced Synthesis and as an Active Phase for Fischer–Tropsch Synthesis. *Journal of the American Chemical Society*, *134*(38), 15814–15821. https://doi.org/10.1021/ja305048p

Yang, G., Kuwahara, Y., Mori, K., Louis, C., & Yamashita, H. (2021a). Pd–Cu Alloy Nanoparticles Confined within Mesoporous Hollow Carbon Spheres for the Hydrogenation of CO 2 to Formate. *The Journal of Physical Chemistry C*, *125*, 3961−3971. https://doi.org/10.1021/acs.jpcc.0c10962

Yang, G., Kuwahara, Y., Mori, K., Louis, C., & Yamashita, H. (2021b). PdAg alloy nanoparticles encapsulated in N-doped microporous hollow carbon spheres for hydrogenation of CO2 to formate. *Applied Catalysis B: Environmental*, *283*(June 2020), 119628. https://doi.org/10.1016/j.apcatb.2020.119628

Yang, H., Zhang, C., Gao, P., Wang, H., Li, X., Zhong, L., Wei, W., & Sun, Y. (2017). A review of the catalytic hydrogenation of carbon dioxide into value-added hydrocarbons. *Catalysis Science and Technology*, *7*(20), 4580–4598. https://doi.org/10.1039/c7cy01403a

Yang, J., Ma, W., Chen, D., Holmen, A., & Davis, B. H. (2014). Fischer-Tropsch synthesis: A review of the effect of CO conversion on methane selectivity. *Applied Catalysis A: General*, *470*, 250–260. https://doi.org/10.1016/j.apcata.2013.10.061

Yang, L., He, J., Zhang, Q., & Wang, Y. (2010). Copper-catalyzed propylene epoxidation by oxygen: Significant promoting effect of vanadium on unsupported copper catalyst. *Journal of Catalysis*, *276*(1), 76–84. https://doi.org/10.1016/j.jcat.2010.09.002

Yang, X.-F., Wang, A., Qiao, B., Li, J., Liu, J., & Zhang, T. (2013). Single-Atom Catalysts: A New Frontier in Heterogeneous Catalysis. *Accounts of Chemical Research*, *46*(8), 1740–1748. https://doi.org/10.1021/ar300361m

Yang, X., Lan, X., Zhang, Y., Li, H., & Bai, G. (2023). Rational design of MoS2@COF hybrid composites promoting C-C coupling for photocatalytic CO2 reduction to ethane. *Applied Catalysis B: Environmental*, *325*, 122393. https://doi.org/10.1016/j.apcatb.2023.122393

Yang, Z. Z., Zhang, H., Yu, B., Zhao, Y., Ji, G., & Liu, Z. (2015). A Tröger’s base-derived microporous organic polymer: Design and applications in CO2/H2 capture and hydrogenation of CO2 to formic acid. *Chemical Communications*, *51*(7), 1271–1274.

https://doi.org/10.1039/c4cc08295h

Yang, Zhichao, Qian, J., Yu, A., & Pan, B. (2019). Singlet oxygen mediated iron-based Fenton-like catalysis under nanoconfinement. *Proceedings of the National Academy of Sciences of the United States of America*, *116*(14), 6659–6664. https://doi.org/10.1073/pnas.1819382116

Yang, Zhiqiang, Guo, S., Pan, X., Wang, J., & Bao, X. (2011). FeN nanoparticles confined in carbon nanotubes for CO hydrogenation. *Energy and Environmental Science*, *4*(11), 4500–4503. https://doi.org/10.1039/c1ee01428e

Yang, Zhiqiang, Pan, X., Wang, J., & Bao, X. (2012). FeN particles confined inside CNT for light olefin synthesis from syngas : Effects of Mn and K additives. *Catalysis Today*, *186*(1), 121–127. https://doi.org/10.1016/j.cattod.2011.11.034

Yu, L., Li, W. X., Pan, X., & Bao, X. (2012). In- and out-dependent interactions of iron with carbon nanotubes. *Journal of Physical Chemistry C*, *116*(31), 16461–16466. https://doi.org/10.1021/jp302311r

Yue, H., Zhao, Y., Zhao, S., Wang, B., Ma, X., & Gong, J. (2013). A copper-phyllosilicate core-sheath nanoreactor for carbon-oxygen hydrogenolysis reactions. *Nature Communications*, *4*, 1–7. https://doi.org/10.1038/ncomms3339

Zhang, C. H., Yang, Y., Teng, B. T., Li, T. Z., Zheng, H. Y., Xiang, H. W., & Li, Y. W. (2006). Study of an iron-manganese Fischer-Tropsch synthesis catalyst promoted with copper. *Journal of Catalysis*, *237*(2), 405–415. https://doi.org/10.1016/j.jcat.2005.11.004

Zhang, Q., Cheng, K., Kang, J., Deng, W., & Wang, Y. (2014). Fischer-tropsch catalysts for the production of hydrocarbon fuels with high selectivity. *ChemSusChem*, *7*(5), 1251–1264. https://doi.org/10.1002/cssc.201300797

Zhang, W., Yang, Y., Li, Y., Li, F., & Luo, M. (2023). Recent progress on integrated CO2 capture and electrochemical upgrading. *Materials Today Catalysis*, *2*, 100006. https://doi.org/10.1016/j.mtcata.2023.100006

Zhao, D., Tu, C. M., Hu, X. J., & Zhang, N. (2017). Notable in situ surface transformation of Cu2O nanomaterials leads to dramatic activity enhancement for CO oxidation. *RSC Advances*, *7*(60), 37596–37603. https://doi.org/10.1039/c7ra05950g

Zhao, Z., Lu, W., Yang, R., Zhu, H., Dong, W., Sun, F., Jiang, Z., Lyu, Y., Liu, T., Du, H., & Ding, Y. (2018). Insight into the Formation of Co@Co2C Catalysts for Direct Synthesis of Higher Alcohols and Olefins from Syngas. *ACS Catalysis*, *8*(1), 228–241. https://doi.org/10.1021/acscatal.7b02403

Zheng, Q., Williams, J., Mantle, M. D., Sederman, A. J., Baart, T. A., Guédon, C. M., & Gladden, L. F. (2020). Experimental Determination of H2 and CO Diffusion Coefficients in a Wax Mixture Confined in a Porous Titania Catalyst. *The Journal of Physical Chemistry B*, *124*, 10971−10982. https://doi.org/10.1021/acs.jpcb.0c07440

Zhou, W., Cheng, K., Kang, J., Zhou, C., Subramanian, V., Zhang, Q., & Wang, Y. (2019). New horizon in C1 chemistry: Breaking the selectivity limitation in transformation of syngas and hydrogenation of CO2 into hydrocarbon chemicals and fuels. *Chemical Society Reviews*, *48*(12), 3193–3228. https://doi.org/10.1039/c8cs00502h

Zhou, Y., Sadia Traore, A., Peron, D. V., Barrios, A. J., Chernyak, S. A., Corda, M., Safonova, O. V., Iulian Dugulan, A., Ersen, O., Virginie, M., Ordomsky, V. V., & Khodakov, A. Y. (2023). Promotion effects of alkali metals on iron molybdate catalysts for CO2 catalytic hydrogenation. *Journal of Energy Chemistry*, *85*, 291–300. https://doi.org/10.1016/j.jechem.2023.06.019

Zhuang, J., & Wang, D. (2023). Recent advances of single-atom alloy catalyst: Properties, synthetic methods and electrocatalytic applications. *Materials Today Catalysis*, *2*, 100009. https://doi.org/10.1016/j.mtcata.2023.100009

Experimental Section and Characterization Analysis

Catalyst preparation

CNTs pre-treatment

Multi-walled CNTs (Iolitec nanomaterial, 95 %, length: 5-15 µm, outer diameter 20–40 nm) used in this work were pretreated with (34 wt.%) HNO_3 at 383 K under refluxing conditions to remove the remaining metals and other impurities. This pretreatment creates defect sites on the surface of CNTs, these surface defects can be considered as anchoring sites for metals. In addition, the hydrophobic nature of CNTs is reduced. The polar functional groups on the surfaces of CNTs during acid treatment, make the surface more accessible to aqueous solutions (Serp et al., 2003). Another pretreatment was used for opening of CNT. Opening of CNT was enabled (Gu, He, et al., 2019; Pan et al., 2007) by treating CNT (3.0 g) in concentrated HNO_3 (68%, 210 mL) for 14 h at 413 K under reflux. The treated CNTs samples were then filtered, washed with distilled water and dried overnight in the oven.

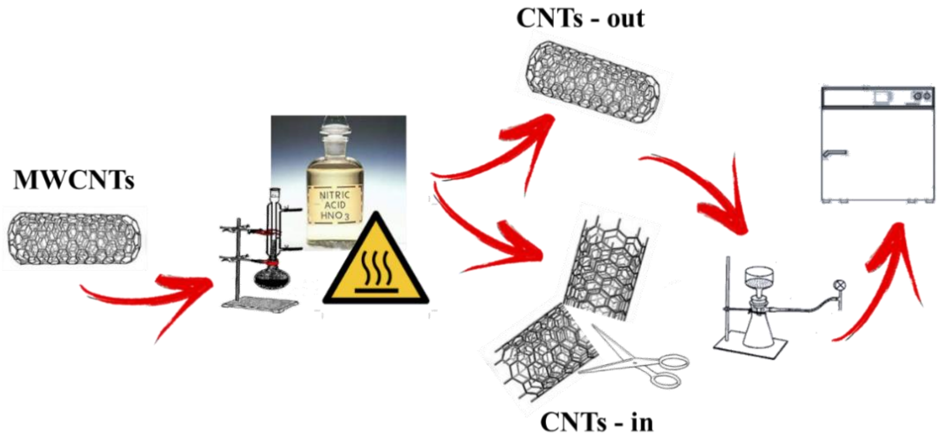

Figure 1. Scheme of pretreatment of CNTs.

Preparation of iron and copper-based catalysts

The CNTs-supported metals catalysts were fabricated by impregnation with a single metal (Fe or Cu), co-impregnation with two metals (Fe and Cu together) and sequential impregnation (first, copper and then, iron or first, iron and then, copper). The impregnation with a single metal was performed using either open or closed CNTs. For deposition of metal species inside the CNT channels, the open CNTs with the aqueous solution of the metal nitrate were placed for 1 h in a ultrasonicator. On the outer surface of the closed CNT, the metal salt was deposited directly by impregnation with the metal nitrate without any pretreatment with ultrasound. For the co-impregnation method, powdery open CNTs (1.0 g) were first added into a mixed aqueous solution (40 mL) simultaneously containing copper (1.75 mmol) and iron (1.99 mmol) nitrates, followed by stirring for 3 h at room temperature. The CNT support and impregnating solution were placed for 1 h in an ultrasonicator. The mixture was left for 2 h and then placed in a water bath at 80 °C with stirring until the solution evaporates. The slurry was then dried at 80 °C overnight in an oven and then calcined at 400 °C in the nitrogen flow for 4 h.

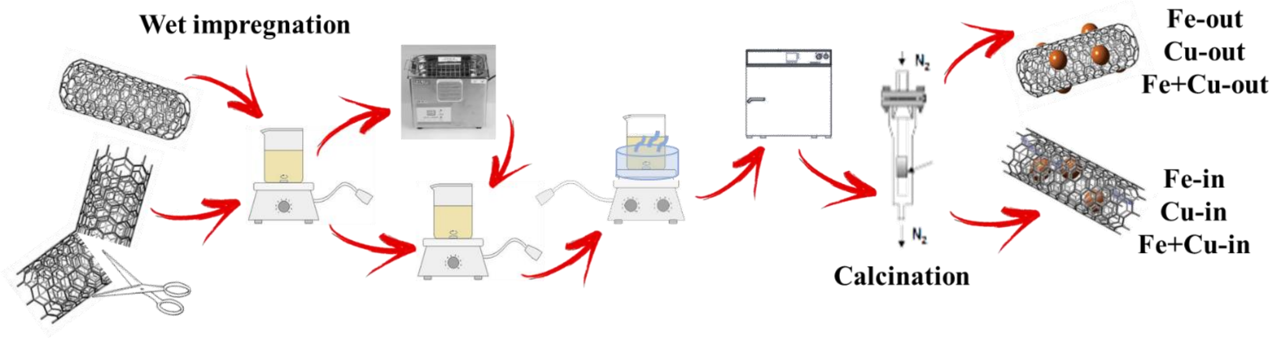

Figure 2. Scheme of impregnation and calcination of catalysts.

The sequential impregnation was used to depose the first metal (Fe or Cu) inside the CNT channels, while the second metal on the CNT outer surface. CNTs were added to the solution of the first metal. The solution was then placed in the ultrasonicator, agitated in a water bath and subsequently dried in an oven. The catalyst was then calcined in nitrogen flow at 400 °C for 4 h. The same catalyst sample was used for the impregnation with the second metal in the same sequence (agitation, rest, overflow in a water bath, drying, calcination in nitrogen).

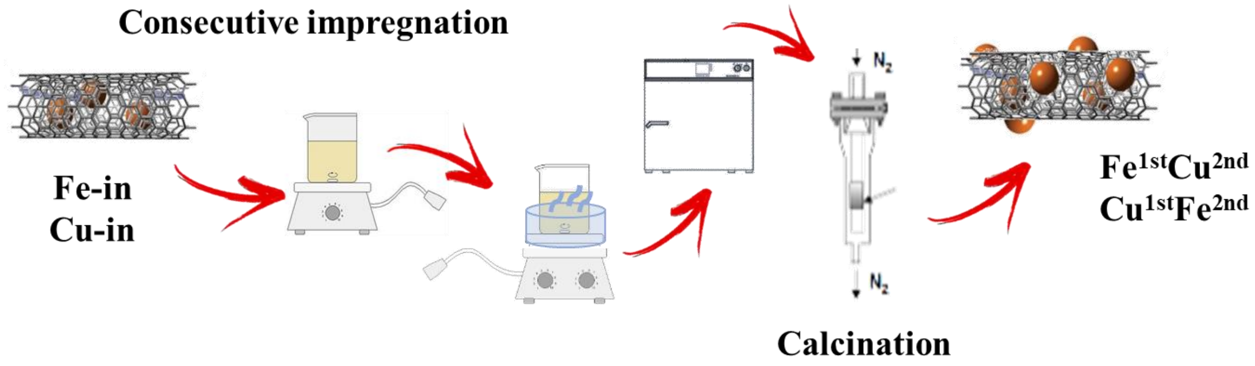

Figure 3. Scheme of consecutive impregnation and calcination of catalysts.

In order to evaluate the influence of exposure to the second step of impregnation on the stability of CNT, Fe-in sample was additionally impregnated with pure deionized water (pH ~ 3, same pH as metal nitrate solution used for impregnation). The sample was then dried and calcined using the same procedure as for bimetallic catalyst prepared using two-step impregnation. The relevant sample is labeled Fe-in^{2nd}. The targeted Cu and Fe theoretical contents were 10 wt. % for each metal in all the catalysts.

Preparation of COFs

Materials: 1,3,5-triformylphloroglucinol (Tp) (Sigma Aldrich); Benzene-1,3,5-tricarboxaldehyde (TFB) (TCI products); hydrazine (Hz) (Sigma Aldrich); *p*-phenylenediamine (Pa-1); o-Tolidine (o-Tol) (Sigma Aldrich); 1,3,5-Tris(4-aminophenyl)benzene (TAB) (TCI products); methanol (Sigma Aldrich); tetrahydrofuran (THF) (Sigma Aldrich); acetone; 1,4-dioxane (Sigma Aldrich), acetic acid (Sigma Aldrich); mesitylene (Sigma Aldrich); dichloromethane; triethylamine (Sigma Aldrich); $RuCl_3 \cdot H_2O$ (Sigma-Aldrich)

Synthesis of COF Tp Pa-1 and COF Tp o-Tol: Initially, a mixture of Tp (0.2 mmol) and dioxane (1 mL) was sonicated for 10 min to get a homogenous dispersion. Then, PDA or o-Tol (0.3 mmol) was added to this mixture and sonicated for another minute. Following by the addition of acetic acid 3M (0.35 mL), the mixture was sealed and left reacting for 3 days at room temperature. After 72 h of reaction, we collected the precipitate by centrifugation and washed it. 3 cycles of washing and centrifugation with THF, followed by 3 steps with acetone and 3 steps of solvent exchange with methanol (T = 80°C, 1 h) were carried out. The powder was dried at 120°C for 12 h, under vacuum.

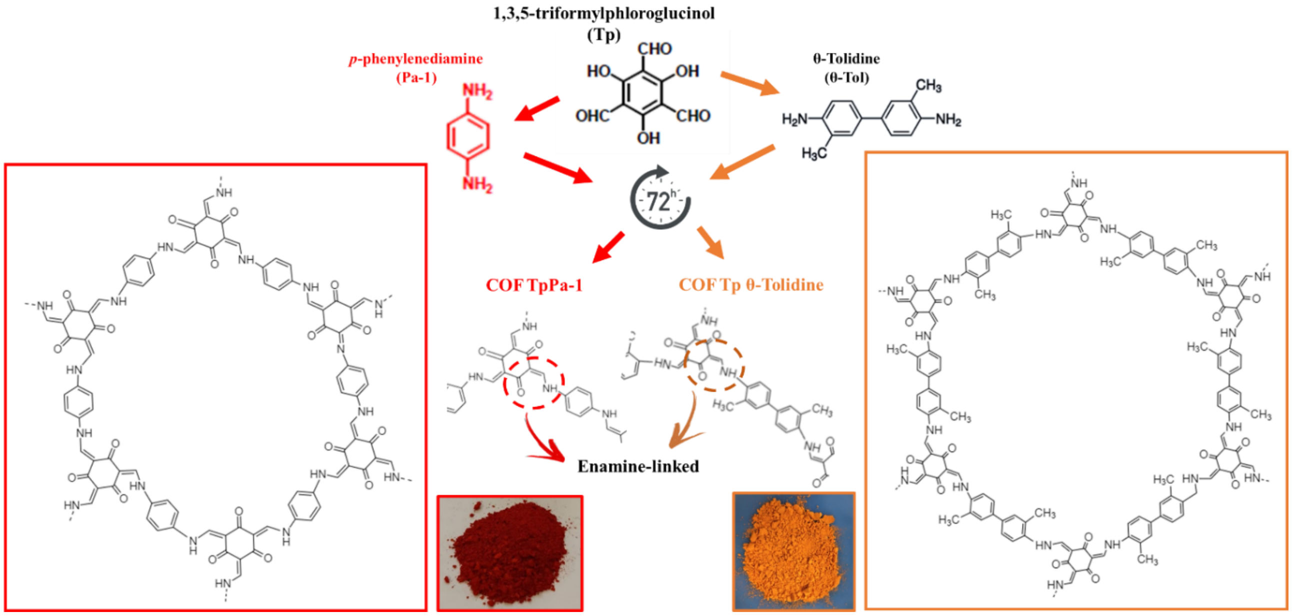

Figure 4. Scheme of synthesis of Tp-COFs.

Synthesis of COF TFB Hz: A mixture of TFB (0.1 mmol) and 2 mL of mesitylene/dioxane (1:1, v/v) was sonicated for 10 min to get a clear solution. Hz (0.15 mmol) was added and the mixture was sonicated for more 20 min. Then, we added 2 ml of acetic acid, sealed the mixture and left it reacting for 3 days, at room temperature. After 3 days of reaction, we collected the precipitate by centrifugation. 3 cycles of washing and centrifugation with THF, followed by 3 steps with acetone, 3 steps with dichloromethane, and 3 steps of solvent exchange with methanol (T = 80°C, 1 h) were performed. The collected powder was dried for 12 h at 120°C, under vacuum.

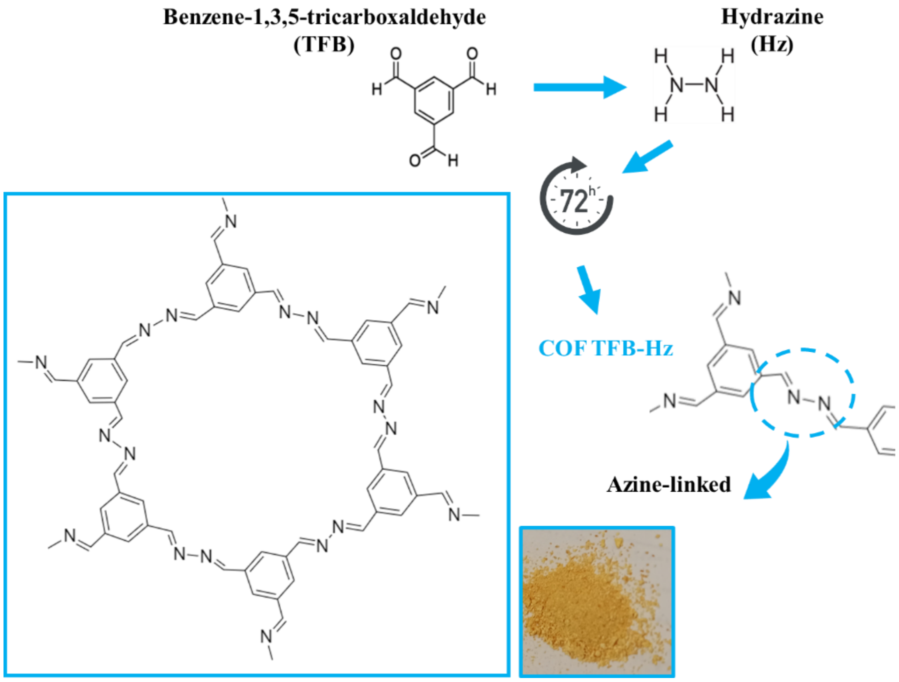

Figure 5. Scheme of synthesis of COF TFB-Hz.

Synthesis of COF TFB o-Tol and COF TFB TAB: A mixture of TFB (0.2 mmol or 0.3 mmol) and 1 mL of dioxane was sonicated for 10 min to get a clear solution. o-Tol (0.3 mmol) or TAB (0.2 mmol) was added to this mixture and sonicated for another additional minute. Acetic acid 3M (0.35 mL) was added to the mixture, sealed and letting react for 3 days at room temperature. After the reaction time, we collected the precipitate by centrifugation and washed it. 3 cycles of washing and centrifugation with THF, followed by 3 steps with acetone, 3 steps with dichloromethane, and 3 steps of solvent exchange with methanol (T = 80 °C, 1 h) were carried out. The powder was dried at 120 °C for 12 h, under vacuum.

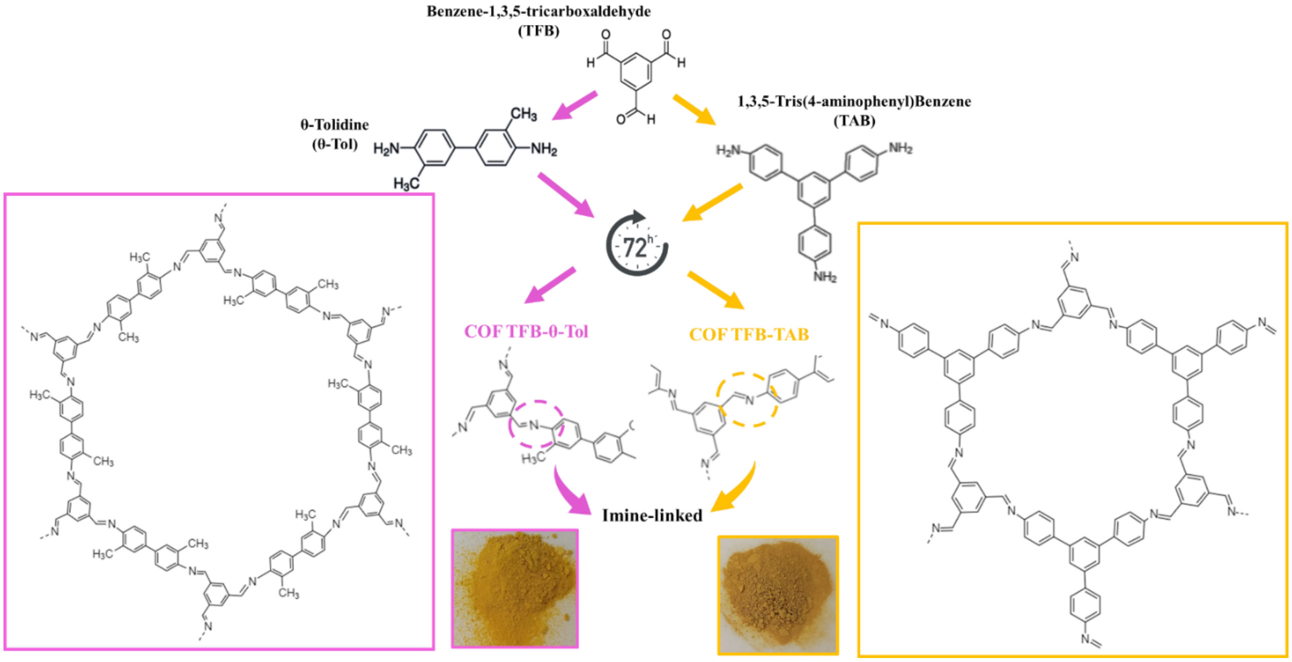

Figure 6. Scheme of synthesis of TFB-COFs.

Preparation of Ru based catalysts

All the Ru/COF catalysts were prepared by wetness impregnation of synthetized COF using a solution of ruthenium chloride in methanol/water mixture (v/v=1/1) followed by evaporation in oil bath at 80°C in a fume hood and then drying in oven at 80°C for 2 h.

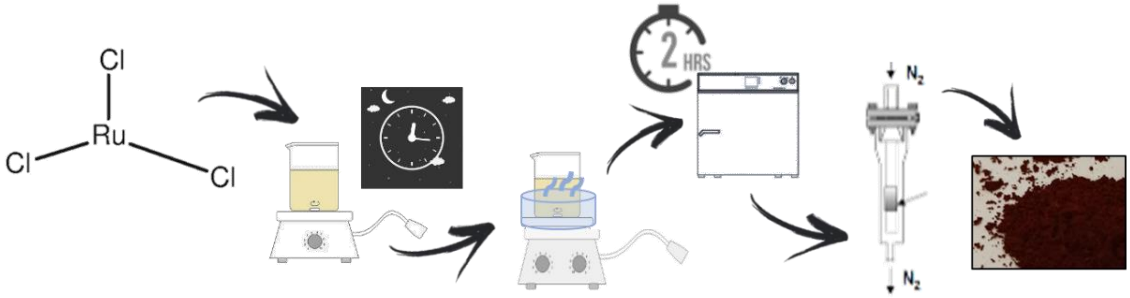

Figure 7. Scheme of preparation of Ru/COF catalysts.

The calcination under inert atmosphere was the last step to obtain the Ru/COF catalysts. The proposed arrangement of the catalyst is presented below.

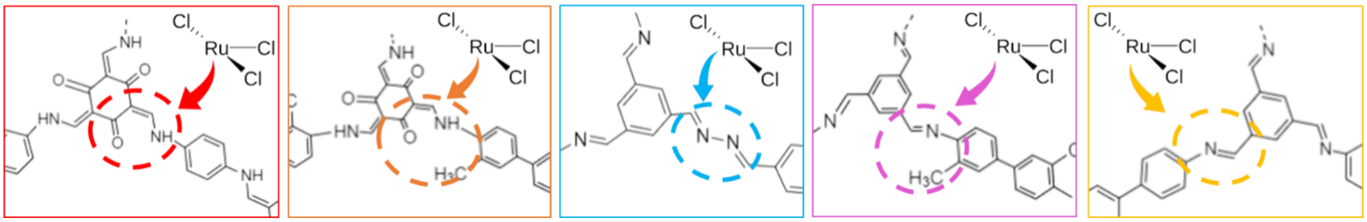

Figure 8. Scheme of proposed arrangement of Ru/COF catalysts.

Catalytic performance

FT synthesis setup: continuous flow reactor

The catalytic conversion of syngas was performed in a fixed-bed reactor with an inner diameter of 8.0 mm. 0.2 g of fresh catalyst was loaded into the reactor. Prior to the reaction, the catalyst was activated under the CO gas flow (50 mL min^{-1}) at atmospheric pressure and 623 K for 10 h (at a rate of 2 °C min^{-1}). For the Cu-in and Cu-out catalysts, the activation was under H_2 gas flow (50 mL min^{-1}) at atmospheric pressure and 573 K for 5 h (at a rate of 2 °C min^{-1}).

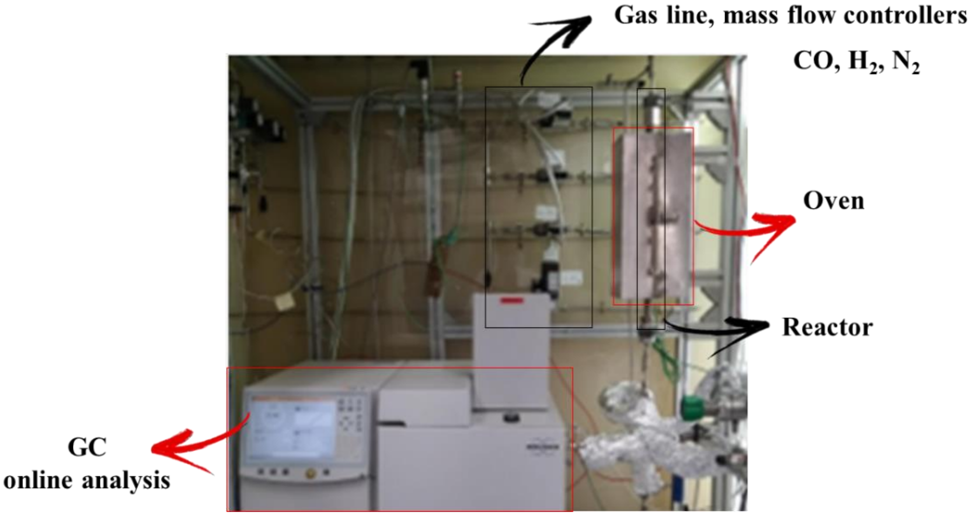

Figure 9. FT synthesis catalytic set-up.

The reactor was cooled down to 453 K and a syngas flow with a H_2/CO ratio of 1/1 was introduced into the reactor. Nitrogen with a flow of 1 mL min^{-1} in the syngas was used as an internal standard for the calculation of CO conversion. The pressure of syngas was typically regulated to 10 bar. After collecting bypass, the temperature started to increase with a heating rate of 1 K min^{-1} until the temperature of 623 K to start the reaction.

The reaction products were analyzed online by a gas chromatograph (Bruker GC-450). N_2, CO, CO_2, and CH_4 were separated by a packed CTR-1 column and were analyzed by a thermal conductivity detector (TCD). The produced C_1 to C_9 hydrocarbons and alcohols were separated by a Rt-Q-PLOT capillary column and analyzed by a flame ionization detector (FID). The catalytic performance at 20 h of reaction was used for catalyst comparison. Further details of catalytic experiments are available in **2.3.1.**

CO_2 conversion: batch reactor

The CO_2 hydrogenation to formic acid was performed in a 40 ml stainless-steel autoclave batch reactor equipped with a pressure gauge. For the reaction, 10 mg of catalyst was added to the reactor with 6 g of water and 0.9 g of TEA. The reactor was then sealed and pressurized to 40 bar with CO_2 and H_2 (1:1; 1:3) and accoupled in the heating plate to stirring during the reaction time (1 h or 15 h) at 90 °C or 120 °C. After cooling to room temperature, the pressure was released and the reacted solution was filtered and collected to analyze the product concentration by ^{1}H NMR, using as internal standards, the signals from water and TEA. The gaseous phase was analyzed using gas-chromatography. No CO or methane were detected.

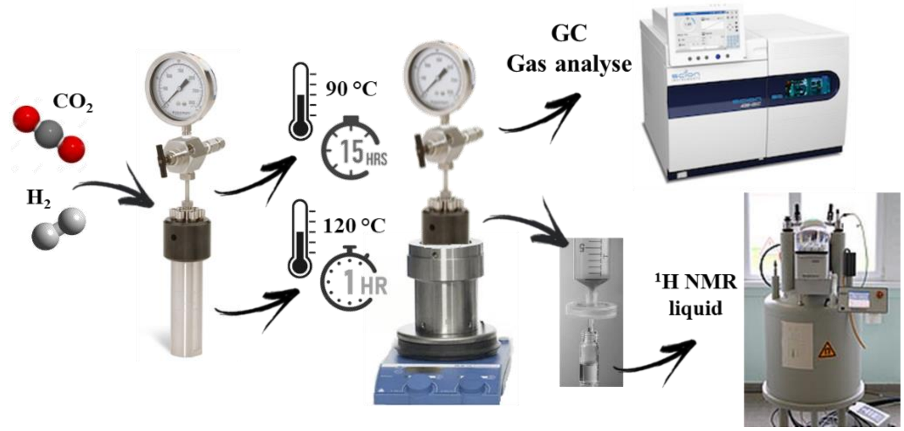

Figure 10. Scheme of CO_2 hydrogenation and gaseous and liquid products analysis.

Analytical methods

CO conversion and selectivities

The CO conversion was calculated from molar flows of CO in and out of the reactor:

$$\mathrm{CO_{conversion}(\%\ mol) = (1 - \left(\frac{CO_{out}\ mol/h}{CO_{in}\ mol/h}\right))}$$

The formulas used to calculate the selectivities are given below:

$$\mathrm{CO_{2}}_{\mathrm{selectivity}} = \frac{\mathrm{CO_{2}}_{\mathrm{out}}\mathrm{mol/h}}{\mathrm{CO_{in}}\frac{\mathrm{mol}}{\mathrm{h}} - \mathrm{CO_{out}}\frac{\mathrm{mol}}{\mathrm{h}}}$$

$$\mathrm{CH_{4}}_{\mathrm{selectivity}}\mathrm{in\ CH} = \frac{\mathrm{CH_{4}}_{\mathrm{selectivity}}\ \mathrm{in\ C}}{1 - \mathrm{CO_{2}}_{\mathrm{selectivity}}}$$

$$C_2^{=} - C_4^{=}{}_{selectivity}in\ CH = \frac{C_2^{=} - C_4^{=}{}_{selectivity}in\ C}{1 - CO_{2}{}_{selectivity}}$$

$$\mathrm{C_2^0 - C_4^0}{}_{\mathrm{selectivity}}\mathrm{in\ CH} = \frac{\mathrm{C_2^0 - C_4^0}{}_{\mathrm{selectivity}}\mathrm{in\ C}}{1 - \mathrm{CO_{2}}_{\mathrm{selectivity}}}$$

$$\mathrm{C_{5+}}_{\mathrm{selectivity}}\mathrm{in\ CH} = \frac{\mathrm{C_{5+}}_{\mathrm{selectivity}}\ \mathrm{in\ C}}{1 - \mathrm{CO_{2}}_{\mathrm{selectivity}}}$$

The calculated carbon balance was defined as the molar ratio between carbon in products and carbon in consumed reactants and was ≥90%:

$$\mathrm{Balance} = \frac{\sum \mathrm{Products}}{\sum \mathrm{Consumed\ CO}}\ 100\%$$

The absence of intraparticle transport limitations was checked by the Weisz-Prater criterion(Weisz & Prater, 1954) (N_{W-P}).

$$\mathrm{N_{W-P}} = \frac{\mathrm{Rr_p^2}}{\mathrm{D_{eff}C_S}} \leq 0.3$$

where R is observed reaction rate (mol_{CO} cm^{-3} s^{-1}), r_p is catalyst particle radius (m), D_{eff} is effective diffusivity (cm^2 s^{-1}), C_S is gas concentration of CO at the external surface of the catalyst (mol cm^{-3}). In the case of a cylindrical particle (CNTs), the equivalent diameter can be obtained as follow(García-Sánchez et al., 2023):

$$d_p = (d_c l_c + \frac{1}{2} d_c^2)^{1/2}$$

Where l_c is the length of the cylinder and d_c is the diameter. The packed density of catalyst bed filled with CNT of 0.3 cm^3 g^{-1}. The pressure was 10 bar and the R reaction rate was calculated from the measured FTY of 4.05*10^{-4} mol_{CO} g_{Fe}^{-1} s^{-1} for the most active $Cu^{1st}Fe^{2nd}$ catalysts. C_S was estimated as 2.23 10^{-4} mol cm^{-3} at zero CO conversion and 4.5 10^{-5} mol cm^{-3} for the CO conversion of 79.9%. In saturated porous media, D_{eff} is related to the molecular diffusion coefficient:

$$D_{eff} = \frac{\varepsilon_p}{\tau_p} D_m$$

where D_m is the CO molecular diffusion coefficient(Zheng et al., 2020) in hydrocarbon mixture, $\varepsilon_p = 0.6$ is the catalyst internal porosity and $\tau_p = 3$ is the tortuosity. D_m at 350°C was evaluated from the literature gives 1.38 10^{-4} cm^2 s^{-1}. The N_{W-P} value at zero CO conversion was 3.12*10^{-10}. Even at the CO conversion of 79.9%, the N_{W-P} was 5.63*10^{-5}, which is still lower than 0.3. This suggests a low contribution of diffusion to the apparent reaction rate.

The external diffusion limitations were evaluated using the Carberry number(Carberry, 1987) (C_a).

$$C_a = \frac{r}{a k_f C_b} \leq 0.05$$

Where r is observed reaction rate (mol_{CO} cm^{-3} s^{-1}), a is the specific external surface of the catalyst particle (m^{-1}), k_f is the mass transfer coefficient (m s^{-1}), C_b is the concentration in the bulk (mol cm^{-3}). k_f=101.5 m s^{-1}, C_b= 92.1 mol m^{-3}, for the most active $Cu^{1st}Fe^{2nd}$ catalysts the C_a was 2.22*10^{-11}.

TOF of iron-based catalysts

The iron time yield (FTY), defined as moles of CO converted per gram of total iron per second, was calculated for all samples using the following formula:

$$\mathrm{FTY}\left(\frac{\mathrm{mol\ CO}}{\mathrm{g_{Fe}\ s}}\right) = \mathrm{GHSV}\left(\frac{\mathrm{L}}{\mathrm{g_{cat}h}}\right) * \mathrm{CO_{molar\ fraction_{in}}} * \left(\frac{\mathrm{1mol\ CO}}{\mathrm{24{,}055L}} * \frac{\mathrm{1h}}{\mathrm{3600s}}\right) * \frac{\mathrm{1g_{cat}}}{\mathrm{g_{Fe}}} * \mathrm{X_{CO}}$$

The apparent turnover frequency (TOF) was calculated using the particle size measured by TEM. The TOF calculation method was similar to that described in the paper of de Jong's group(Galvis, Bitter, Davidian, et al., 2012), which takes into consideration FTY of the catalyst, diameter of iron carbide particles in the used catalysts, density of iron carbide ($\rho = 7.57\ \mathrm{g\ cm^{-3}}$) and assumes the surface density of 14 Fe atoms $\mathrm{nm^{-2}}$ in iron carbide nanoparticles. Note that measuring reaction rates at higher conversion may require detailed information about the reaction kinetics and TOFs extracted directly from carbon monoxide conversion can be underestimated.

CO2 hydrogenation: TON and TOF

The amount of formic acid produced was calculated using the results from ^{1}H NMR liquid, using the signals of TEA and formic acid, according to the equation bellow:

$$\mathrm{Formic\ acid\ (mg)} = \frac{\mathrm{g_{TEA}} * (\mathrm{1000mg/1g}) * 9\ \mathrm{protons}(3 * \mathrm{H_3}) * \mathrm{A_{formic\ acid}} * \mathrm{MW_{formic\ acid}}}{\mathrm{MW_{TEA}} * \mathrm{A_{TEA}} * 1\ \mathrm{proton}(1 * \mathrm{H})}$$

where:

$g_{TEA} = \mathrm{g\ of\ TEA\ used\ in\ the\ reaction} = 0.9\ \mathrm{g}$

$MW_{TEA} = 101.19\ \mathrm{g/mol}$

$\mathrm{MW_{formic\ acid}} = 46.03\ \mathrm{g/mol}$

$\mathrm{A_{TEA}} =$ area from peak integration TEA 1 ppm

$\mathrm{A_{formic\ acid}} =$ area from peak integration formic acid 8.3 ppm $=$ 1 (normalized)

The concentration of formic acid was determined as follow:

$$\text{Concentration of Formic acid } (\mu\text{mol/ml}) = \frac{\left(\frac{\text{Formic acid (mg)}}{46.03\text{ g/mol}}\right)}{7.2397\text{ ml} * 1000\text{ mg}}$$

where:

$$\text{Solution TEA} + H_2O\text{ (ml) used in the reaction} = 0.9\text{g TEA} + 6\text{g}H_2O = \left(\frac{0.9\text{g}}{0.726\frac{\text{g}}{\text{mL}}}\right) + \left(\frac{6\text{g}}{\frac{1\text{g}}{\text{ml}}}\right)$$

$$= 7.2397\text{ ml}$$

The turnover number (TON) was calculated using the amount of formic acid produced and the amount of ruthenium used for the reaction.

$$\text{TON} = \frac{\text{n moles of formic acid}}{\text{n moles of Ru}}$$

where:

$$\text{n moles of Ru used in the reaction (in 10 mg of catalyst)}$$
$$= \frac{\text{metal loading wt\%} * 10\text{ mg (catalyst)}}{100\% * 1000\text{ mg} * 101.07\text{ g/mol}}$$

$$\text{n moles of formic acidproduced} = \frac{\text{Formic acid (mg)}}{1000\text{ mg} * 46.03\text{ g/mol}}$$

The apparent turnover frequency (TOF) is obtained with the TON over the reaction time.

$$\text{TOF} = \frac{\text{TON}}{\text{time of reaction}}$$

Cycling tests

The cycling tests were performed in order to evaluate the recyclability of the catalysts. After each cycle, the catalyst was recuperated by filtration, washed with distilled water and dried at 60°C. The amount of catalyst recuperated was weighted before to be use in the next cycle of reaction, in order to obtain the exact amount of formic acid produced by grams of catalyst in each cycle per hour of reaction.

$$rate\ of\ HCOOH = \frac{mg_{formic\ acid}}{g_{catalyst} * h_{reaction}}$$

Characterization Analysis

Nitrogen Physisorption

The nitrogen physisorption measurements were carried out using a Micromeritics Tristar II PLUS Surface Area and Porosimetry analyzer (**Figure 1**). Prior to the N_2 adsorption, the CNTs samples were degassed at 250 °C for 2 h, and the COFs samples were degassed at 150 °C for 12 h. The N_2 adsorption-desorption isotherms were measured at −196 °C. The specific surface area of the sample was calculated by the BET method from the isotherms between $P/P_0 = 0.05$ and 0.3, and the average pore volume was estimated using the Barrett−Joyner−Halenda (BJH) method.

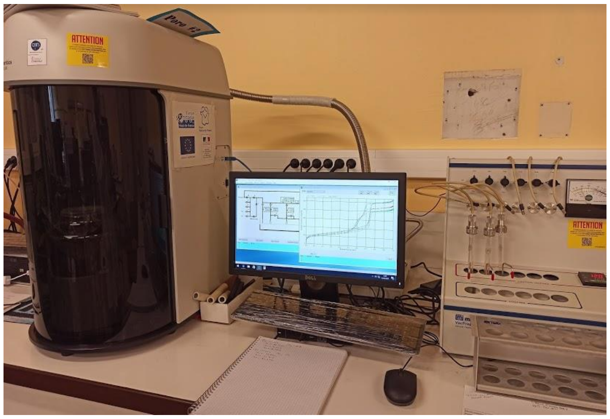

Figure 1. Micromeritics Tristar II PLUS Surface Area and Porosimetry analyzer.

Thermogravimetric analysis

To determine the thermal stability of the COFs samples, the thermogravimetric analysis was performed using an SDT Q600 V20.9 Build 20 Thermogravimetric Analyzer (TGA) & Differential Scanning Calorimeter (DSC) with 2.5 mg of sample (**Figure 2**). The temperature ramp was 10 °Cmin^{-1} up to 800 °C under N_2 (100 mLmin^{-1}). Also, TGA was carried out under air conditions (100 mLmin^{-1}), at the heating rate of 10 °Cmin^{-1} up to 800 °C.

Figure 2. SDT Q600 V20.9 Build 20 Thermogravimetric Analyzer.

Temperature Programmed Reduction

The reduction behavior of the catalysts was examined by the H_2 temperature-programmed reduction (H_2-TPR) using the AutoChem II 2920 apparatus (Micromeritics) (**Figure 3**). 100 mg of the CNTs samples were reduced in a flow of H_2/Ar (5 vol. % H_2) stream (50 mL min^{-1}). The temperature was increased up to 900 °C at the rate of 10 °C min^{-1}.

Figure 3. Micrometrics Auto Chem II 2920 equipment.

X-Ray Diffraction

A Bruker AXS D8 diffractometer (**Figure 4**) with Cu Kα radiation (λ = 0.153 nm) was used for the X-ray powder diffraction (XRD) measurements of the CNTs samples. The XRD patterns were collected in the 5−90 ° (2θ) range, with the 0.02 ° step size and 0.5 s step time. The identification was carried out by comparison with the database from the EVA software. The average crystallite size of the metal nanoparticles was calculated using the diffraction peaks according to the Scherrer equation.

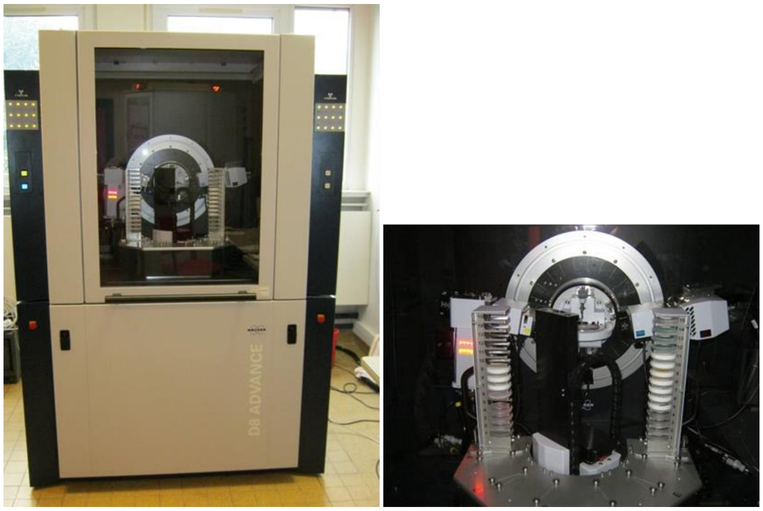

Figure 4. Bruker AXS D8 diffractometer.

The XRD of COFs samples was conducted using a X-ray Diffractometer Smart Lab Guidance Rigaku (**Figure 5**), 200 mA,45 kV (9kW), with Cu $K\alpha_1$ radiation ($\lambda = 0.15406$ nm), rotating anode, parallel beam, was used for the X-ray diffraction (XRD) measurements. The XRD patterns were collected in the 2−40 ° (2θ) range, with the 0.01 ° step size and 0.07 s step time.

Figure 5. X-ray Diffractometer Smart Lab Guidance Rigaku.

X-Ray Fluorescence

The X-ray fluorescence (XRF) spectroscopy was used to measure the elemental catalyst compositions. The XRF measurements were performed with an energy dispersive micro-X-Ray Fluorescence spectrometer M4 TORNADO (Bruker) (**Figure 6**), equipped with 2 anodes a Rhodium X-ray tube 50 kV/600 mA (30 W) and a Tungsten X-Ray tube 50 kV/700 mA (35 W). A Silicon-Drift-Detector Si(Li) with <145 eV resolution at 100000 cps (Mn Kα) was used as a detector and cooled with a Peltier cooling (253K). The measurements were done under vacuum (20 mbar) and for each sample 36 points (of 200 μm) were analyzed.

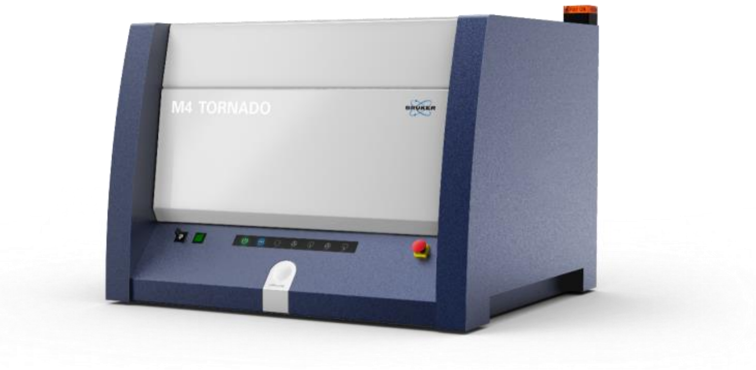

Figure 6. Micro-X-Ray Fluorescence spectrometer M4 TORNADO (Bruker).

Raman Spectroscopy

The Raman spectroscopy was performed in Horiba XploRA plus spectrometer (**Figure 7**), equipped with CCD high-sensitive detector cooled by the Peltier effect, 2 laser sources: 532 nm, 785 nm, 4 networks: 600,1200,1600 and 2400 lines mm^{-1}, xyz motorized stage and fiber optical. The Raman spectra were carried out at the excitation wavelength of 785 nm, the objective 100, the filter at 1%, the source 1200 and the step of 120 s^{-1}, in the spectral range from 100 to 1800 cm^{-1}. The Raman spectra have been registered in two spectral regions: D (disorder-induced) and G (graphene) bands.

Figure 7. Horiba XploRA plus spectrometer.

Fourier-Transform Infrared Spectroscopy

The chemical functional groups and linked-bonds that are present in the catalyst were identified by FT-IR using a Nicolet iS50 FTIR Spectrometer (Thermo Scientific) equipped with a DTGS-ATR detector (**Figure 8**), a diamond ATR window, a KBr beam splitter for the range of 4000-525 cm^{-1} and a solid substrate beam splitter for the range of 1800-80 cm^{-1}, scan number of 128 cm^{-1}, respectively, and resolution of 2 cm^{-1}.

Figure 8. Nicolet iS50 FTIR Spectrometer.

Nuclear Magnetic Ressonance

The local structure of the COFs was inestigated using Nuclear Magnetic Resonance (NMR), solid state, performed in the 400MHz Bruker AVANCE III Spectrometer (**Figure 9**), equipped with 4 mm standard probe for ^{1}H and ^{13}C, DEPTH and CPMAS, Ro=12.5KHz and 100.6 MHz, respectively, and the chemical shiFT synthesis for protons are reported in part per million (ppm).

Figure 9. Bruker Avance III 400MHz Spectrometer.

For analyze the catalytic results the Nuclear Magnetic resonance in liquid-state was performed in the 300MHz Bruker AVANCE III HD (**Figure 10**), equipped with BBFO 5 mm probe, gradient Z, and sample changer Xpress 60 positions for 5 mm tubes.

Figure 10. 300 MHz Bruker AVANCE III HD spectrometer.

X-Ray Photoelectron Spectroscopy

The X-ray photoelectron spectroscopy (XPS) was carried out with a Kratos Axis Ultra DLD spectrometer equipped with a monochromatized Al-K X-ray source (1486.6 eV) operating at 180 W (**Figure 11**).

For CNTs samples: Fe 2p, Cu 2p, C 1s and O 1s core level spectra were recorded using a 40 eV Pass Energy. The Binding Energies (BEs) were corrected with respect to C1s fixed at 284.6 eV for the CNT contribution. Relative surface atomic quantification was calculated after the removal of a Shirley type background on each spectrum.

For COFs samples: the Pass Energy used to record all the core level spectra of C1s, O1s, N1s and Ru 3p was 40 eV. The correction of the Binding Energies (BEs) was done with respect to C1s fixed at 284.6 eV. The Shirley type background was used in each spectrum to calculate the relative surface atomic concentrations.

Figure 11. Kratos Axis Ultra DLD spectrometer.

Near-Ambient Pressure X-Ray Photoelectron Spectroscopy

NAP-XPS was performed in Prague using a spectrometer custom-built by SPECS Surface Nano Analysis, GmbH Germany (**Figure 12**). An ultrahigh vacuum (UHV) system equipped with a PHOIBOS 150 Hemispheric Energy Analyser and an Al *Kα* monochromatized X-ray source of high intensity (excitation energy of 1486.6 eV) was employed to perform X-ray photoelectron spectroscopy (XPS) measurements (Tao, 2012). The *in-situ* reaction cell was set in the analysis chamber allowing XPS measurements in the presence of gases with pressure up to 10 mbar and at high temperature. Typically, the catalyst (~20 mg) was pressed into a tungsten mesh and together with a K-type thermocouple spot welded to a stainless-steel sample holder. The measurements were performed in presence of carbon monoxide or syngas (1 mbar) at temperature ranging from ambient to 350 ºC (See detailed scheme of the experimental set-up in **Figure 13**). The XPS spectra were analyzed by fitting the Shirley-type function with the Casa XPS software.

Figure 12. Near Ambient Pressure X-Ray Photoelectron Spectroscopy at Charles University.

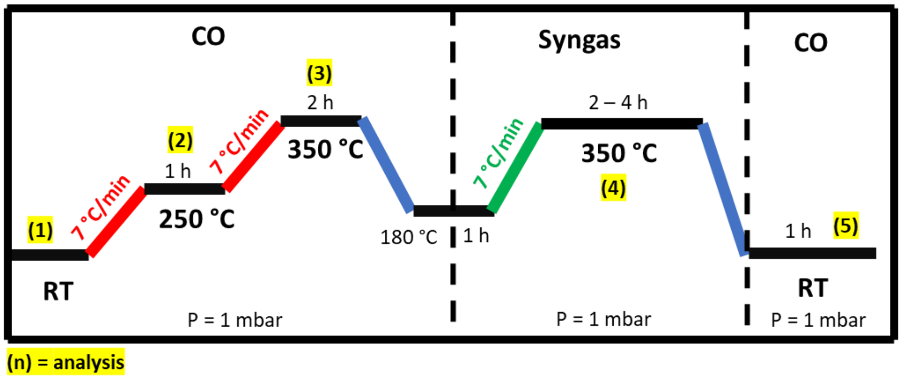

Figure 13. Scheme of *in-situ* experimental setup.

X-Ray Absorption Spectroscopy

The *ex-situ* X-ray absorption spectra were recorded at the XAFS beamline station of the Elettra Sincrotrone (Trieste, Italy)(Cicco et al., 2009) (**Figure 14**) and SuperXAS beamline in Swiss Light Source (SLS, Villigen, Switzerland) (**Figure 15**). In Elettra, the X-ray beam was vertically collimated silicon ingot with Pt-coating mirror positioned at 3.0 mrad with respect to the direct beam. The beam was monochromatized by a fixed-exit double cam double crystal monochromator, using a pair of Si (111) crystals. The monochromatic beam is high 1.2 mm in vertical and horizontally variable according to the size of the sample inside the capillary. The beam energy was calibrated using metallic Ru (K edge at 22117 eV). In the SLS synchrotron, the incident photon beam was selected by a Si (111) channel-cut monochromator from the polychromatic beam coming from 2.9 T superbend magnet. The rejection of higher harmonics and the collimation were achieved by a platinum-coated collimating mirror at 2.5 mrad located before the monochromator, while focusing was achieved by a platinum-coated torroidal mirror at 2.5 mrad. Ru (K edge at 22117 eV). The samples were measured in transmission mode using 15 cm long ionization chambers filled with 1 bar of Ar and 1 bar of N_2. The size of the X-ray beam on the sample was about 1.5 mm in horizontal and 0.5 mm in vertical directions.

Elettra Sincrotrone Trieste

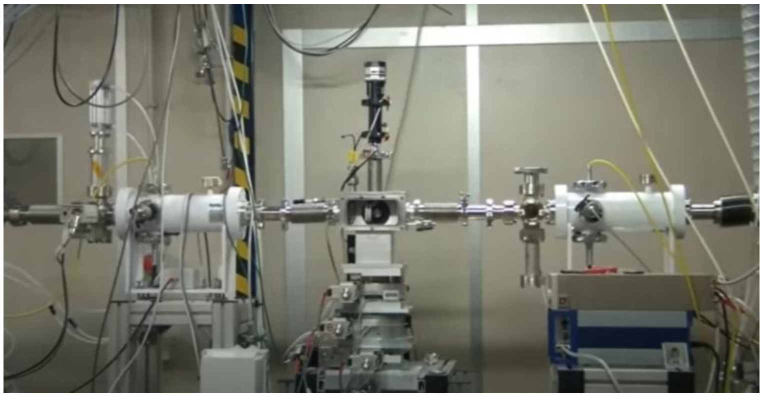

Figure 14. X-Ray absorption spectroscopy at Ellettra Sincrotone, Italy.

PAUL SCHERRER INSTITUT
PSI

Figure 15. X-Ray absorption spectroscopy at Swiss Light Source, Switzerland.

In-situ X-Ray Absorption Spectroscopy

The *in-situ* Ru K-edge X-ray absorption spectra during the CO_2 hydrogenation were measured at beamline CLÆSS of the ALBA synchrotron (Barcelona, Spain) 5 **Figure 16-**. The X-ray energy range at Ru K-absorption edge was covered, using pairs of Si(111) and Si(311) crystals. The current signals from the ionization chambers were collected, amplified and converted to output voltage by the ALBA Electrometer. For the *in-situ* XANES and EXAFS measurements, the sample was loaded in a 2 mm quartz capillary. The schema of *in-situ* experimental setup is given in **Figure 17**. The *XAS* measurements at Ru K-edge were performed in the flow of aqueous solution of triethylamine (TEA), which was used as formic acid scavenger. The aqueous solution was added to the capillary using a syringe pump. The measurements were performed in a gasflow of He (P=10 bar) and in a flow of H_2/CO=3 mixture (P=10 Bar) at temperatures ranging from ambient to 120 ºC. The liquid samples downstream of the capillary was collected and analyzed by ^{1}H NMR for the presence of formic acid. For the NMR analysis, the sample (0.5 ml) was mixed with 0.1 ml solution DMSO in D_2O (1:2000 vol). All obtained EXAFS spectra were analyzed using the Demeter software package(Ravel & Newville, 2005).

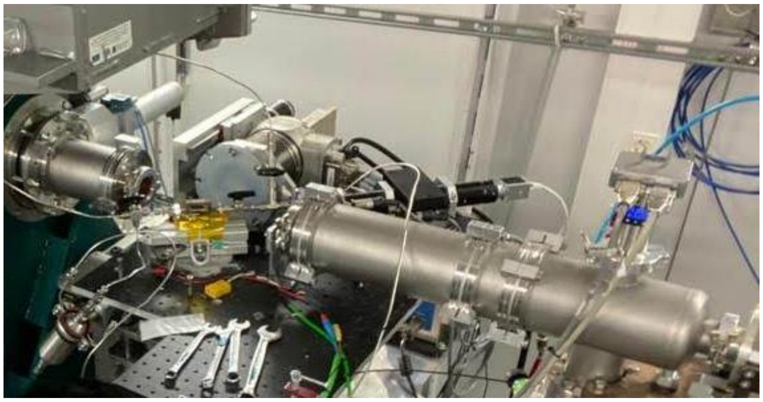

Figure 16. X-Ray absorption spectroscopy at CLÆSS - ALBA synchrotronm, Spain.

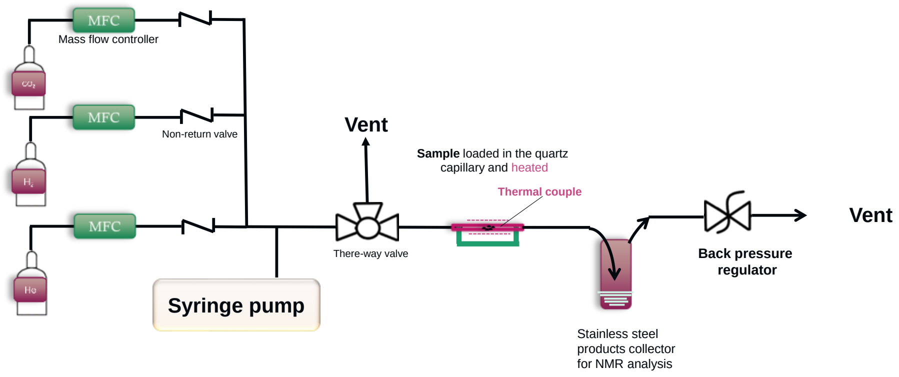

Figure 17. Scheme of *in-situ* XAS experimental setup used for CO_2 hydrogenation to formic acid.

Transmission Electron Microscopy

The transmission electron microscopy (TEM) and energy-dispersive X-ray spectroscopy (EDS) characterizations for CNTs samples were done using a Thermo Fisher Talos F200X, a FEI Tecnai G2 (**Figure 18**) and a Thermofisher Titan Themis microscope (**Figure 19**), operated at 200 and 300 kV, respectively. The sample was dispersed in ethanol and a droplet of solution was deposited onto a 400-mesh carbon-coated nickel (or copper) grid. The counting and measurement of the particle size and inner and outer diameters of CNTs follow the same procedure for all samples. A line tool of software Gatan Digital Micrograph was used in order to obtain the values of metal particle size and CNTs diameters. In the case of bimetallic catalysts, we measured three kinds of particles: iron-only, copper-only and interacting iron-copper particles. For each sample, we plotted a histogram of the measurements, the distribution of the particles size and CNTs diameters. The particle sizes were calculated using the Sauter mean diameter equation (Kowalczuk & Drzymala, 2016).

Figure 18. TEM FEI Tecnai G2-20 twin.

The transmission electron microscopy (TEM) and energy-dispersive X-ray spectroscopy (EDS) measurements for COFs samples were done using a FEI Tecnai G2 and a Thermofisher Titan Themis microscope, operating at 200 and 300 kV, respectively. The sample was deposited onto a 400-mesh carbon-coated copper grid.

Figure 19. TEM FEI Tecnai G2-20 twin.

TEM, STEM and Spectroscopy Techniques

Electron microscopy is one of the main characterization techniques in catalysis and has played a central role in the structural characterization of materials. Since its first commercial implementations, the resolution of transmission electron microscopy (TEM) has improved by more than three orders of magnitude. Both in conventional TEM and in the most recent models of scanning electron microscopes (STEMs), it was possible not only to improve the resolution in TEM and STEM, but also to achieve sub-Angstrom resolution(Londoño-Calderon et al., 2017).

In order to be able to identify the structure close to the interface of two metallic species, high-resolution transmission electron microscopy (HRTEM) can be used to achieve the resolution of the structure on nanocrystals. Scanning transmission electron microscopy images in a high angle annular dark field (HAADF-STEM) is an excellent technique for identifying elements present in a sample of a metallic system. The HAADF-STEM images are able to collect a large amount of elastic dispersed electrons, and the intensity of the signal collected by the detector will depend on the cross section of the dispersion and the atomic number of the atoms in the sample, called the Z contrast, in which the intensity is proportional to the atomic number Z. That is, for a single atom the distribution of scattered electrons is more or less like a Gaussian function (Rutherford scattering)(Londoño-Calderon et al., 2017).

With the resolution in the picometer range in the spherical aberration correction area achieved by electron microscopy, it is possible to study from single atoms to clusters and, finally, nanoparticles. However, some problems can significantly complicate the absorption of catalysts, such as the damage caused by the radiation of the electron beam, which may end up modifying the structure of the catalyst; the substrate may have an influence on reducing the contrast of nanoparticles as the particles may be in different positions than the focal length of the microscope; the contrast will be very low if the difference in electron scattering distribution between nanoparticles and substrate is very small(Londoño-Calderon et al., 2017).

HAADF-STEM of Bimettalic Catalysts

STEM is a particularly important technique in the study of nanoalloys because it is useful for determining the local chemical composition of the sample. The technique is based on the elastic dispersion of electrons across the sample at relatively large angles, where the electron beam is rasterized through a thin sample. This technique is also known as the Z contrast image, because the elastic dispersion is strongly dependent on the atomic number of atoms present in the sample and the intensity also depends on Z. The HAADF-STEM technique, or scanning transmission electron microscopy in the dark field high-angle ring is when a high-angle detector is used. In this case, an annular dark-field detector is used to collect the elastically dispersed electrons(Londoño-Calderon et al., 2017).

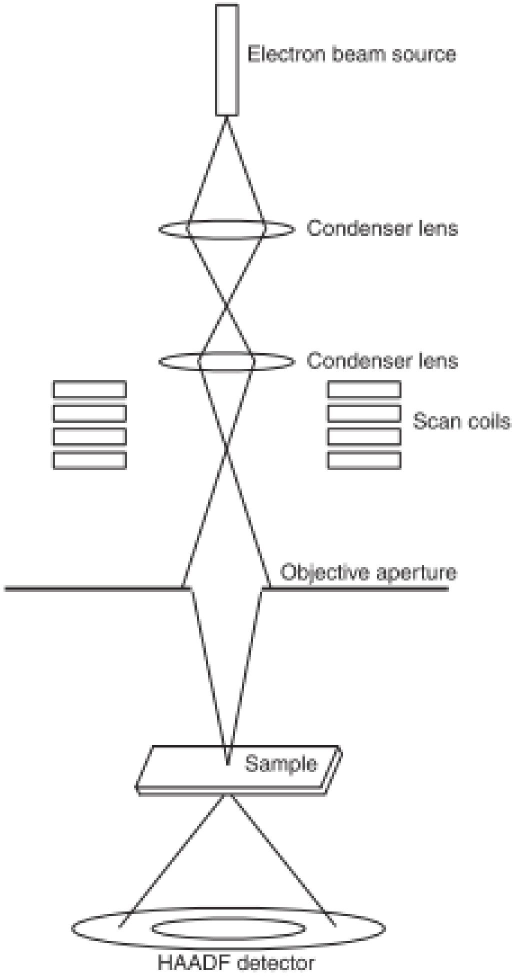

Figure 20. Schematic representation of the working principle of HAADF-STEM(Londoño-Calderon et al., 2017).

The HAADF-STEM principle can be seen briefly in **Figure 20**. Due to the Rutherford dispersion, the beam carries information about the electron's mass, so that the intensity signal is like Zn (the value of n is predicted to be 1.4). Due to the contrast of the atomic number, and because it is particularly useful for the discrimination of heavy atoms, the HAADF-STEM technique seems very suitable for studying bimetallic catalysts. However, some factors must be taken into consideration, such as the fact that the difference in the atomic number of the elements should be meaningful and that the HAADF-STEM contrast depends not only on Z, but also the thickness.

Even in the case of a single metal, the thickness effects are very important and are not easy to separate from the Z contrast(Londoño-Calderon et al., 2017).

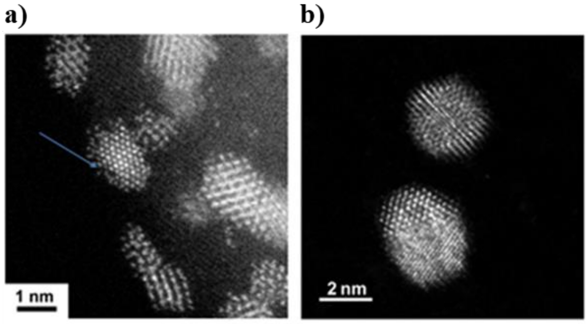

Figure 21. a) Z-contrast image of Au/Ir bimetallic catalysts. The nanoparticle marked by an arrow shows contrast variations not due to atomic number(Londoño-Calderon et al., 2017); **b)** HAADF-STEM image of Au-Pd nanoparticles. The particle at the bottom has a higher concentration of gold than the one on the top of the micrograph(Londoño-Calderon et al., 2017).

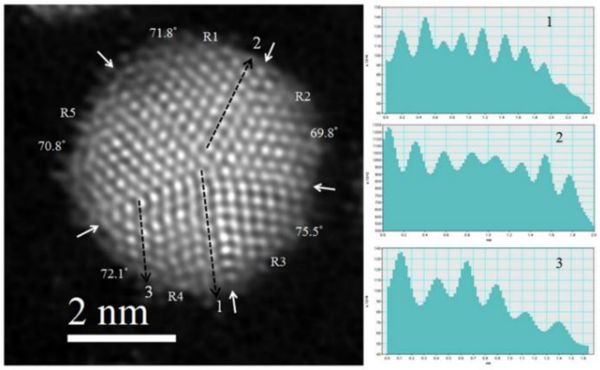

Figure 22. Left: STEM micrograph of decahedral Au-Co nanoparticle with an inhomogeneous distribution of the atomic species. **Right**: intensity profiles corresponding to the lines marked at the micrograph(Londoño-Calderon et al., 2017).

After a few atoms of thickness, the relationship between thickness and intensity may not be linear. In **Figure 21a** it is possible to see a practical example of this, an Au/Ir bimetallic cluster. Due to variations in thickness, there is a variation in intensity in the contrast of the atomic column. To determine the shape or composition of the clusters, it is reliable to use the Z contrast only when the clusters are less than five atoms thick.

There are other, more formal methods of counting atoms, in addition to the use of Z contrast. In **Figure 21b** is shown the micrograph of two AuPd nanoparticles of homogeneous alloy, where the particle at the top seems slightly less intense than the one at the bottom, which shows a higher concentration of gold on the bottom particle(Londoño-Calderon et al., 2017).

A detailed description of the composition and ordering of metals in a nanoparticle is provided by the high-resolution Z STEM contrast micrographs. The HAADF-STEM image was used, together with the mapping by dispersive energy spectroscopy (EDS), for the structural characterization of Au/Co nanoparticles. In the micrograph of the **Figure 22**, it is possible to notice that some of the atomic columns appear relatively brighter than the others, which may denote the high presence of gold in these columns. The tendency of gold atoms to concentrate on adjacent columns of the double-bounded planes indicates a non-homogeneous alloy. Even though the small particle size avoids the appearance of displacements and other defects, distortions are observed in the atomic lines that make the particle strained internally, which may be due to the lattice incompatibility between gold and copper being relatively high (about 14%)(Londoño-Calderon et al., 2017).

Using high resolution TEM and STEM it is possible to investigate the roughness on the surface of the nanoparticles. Using the HAADF image mode in an aberration-corrected STEM / TEM, it is possible to compare the experimental and model intensity profiles, and thus highlight the appearance of high index surfaces in the particles, which can play an important role in the catalytic activity of the system(Londoño-Calderon et al., 2017).

HAADF-STEM of Supported Metallic Catalysts

The HAADF-STEM technique clearly overcomes some of the contrast problems in the digitalized transmission images of samples of noble metals supported on high-area ceramics. The image is formed by scanning the electron beam and recording the intensity, as the signal intensity depends on the atomic number, the difference in Z results in a high contrast image, with the catalyst particles appearing as bright spots (**Figure 23. Left**). As no strong contrast from the support is produced, the background noise in the image is due to the amorphous character of the support, which can be easily eliminated by filtering images (**Figure 23. Right**). In this case, the structure of the clusters can be observed and the average particle size determined.

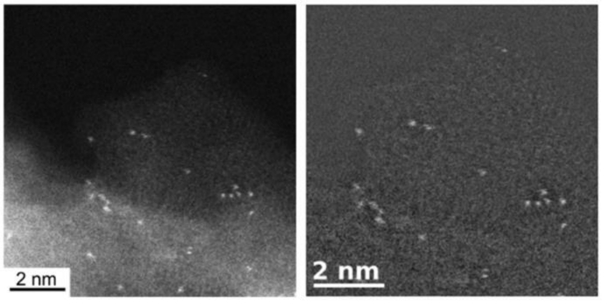

Figure 23. Left: Pt nanoparticles supported on alumina are shown using the HAADF-STEM tech- nique. The particles appear as bright spots. **Right**: Images of Pt clusters on a g0Al2O3 support. The size of the clusters is ~0.17 nm (Londoño-Calderon et al., 2017).

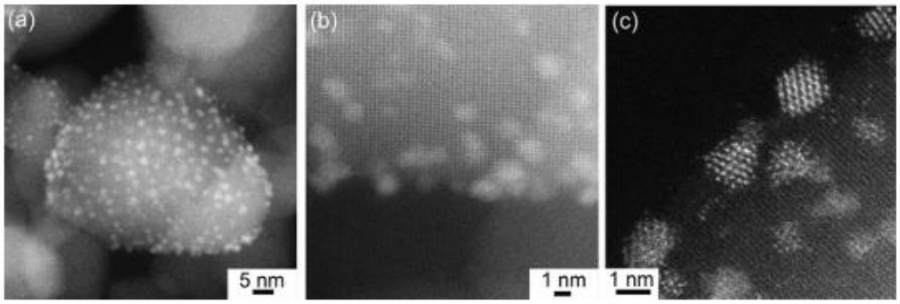

Figure 24. Images of Ir supported on TiO_2 (rutile) support **(A)** low-magnification STEM image. **(B)** STEM image focusing on the substrate with the Ir particles out of focus. The lattice from the support is visible and **(C)** HAADF-STEM image. The Ir is present as nanoparticles and single atoms(Londoño-Calderon et al., 2017).

In case the substrate is crystalline, the situation is different, for example, a noble metal (Ir) in TiO_2 (**Figure 24 A, B, C**). First (**Figure 24 A**), a low magnification image of the catalyst where the metal appears as bright spots. Second (**Figure 24 B**), the crystalline structure of the substrate is revealed and the clusters are slightly out of contrast due to the focus conditions, this is because, because the focal length is relatively short from the STEM and the clusters are three-dimensional, the focus on the substrate ends up producing a blur in the particle image. Third (**Figure 24 C**), a high magnification of the sample, where it is possible to observe, in addition to the nanoparticles, unique atoms. In the case of the crystalline substrate, the nanoparticles can grow in different ways, since the growth is determined by the geometry between the substrate and the nanoparticles (epitaxial growth)(Londoño-Calderon et al., 2017).

Yang et al.(Zhichao Yang et al., 2019) in their work with iron oxide confined in CNTs, they used some imaging techniques and others techniques to better understand and determine the behavior of this catalyst in Fenton reaction. The authors used representative images from the dark field scanning transmission electron microscopy (HADDF-STEM) with elementary mapping by X-ray dispersive energy spectroscopy (EDX) (**Figures 25** and **26**) to demonstrate how the nanoparticles are randomly distributed in the direction of the CNT for the Fe_2O_3/FCNT-L sample, and for the Fe_2O_3@FCNT-H sample, the distribution of the nanoparticles is dictated by the center of the CNTs (indicated by the red arrows). The (311) crystalline lattice of the Fe_2O_3 nanoparticles can also be seen in the high-resolution transmission electron microscopy (HRTEM) images for the two samples(Zhichao Yang et al., 2019).

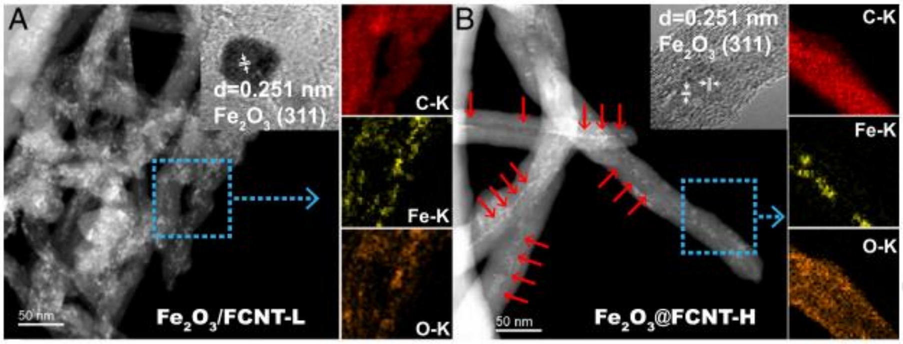

Figure 25. (A and B) Representative HADDF-STEM images of Fe_2O_3/FCNT-L and Fe_2O_3@FCNT-H (Insets) HRTEM images of the Fe_2O_3 nanoparticles; dexter figures show the EDX elemental mappings of the selected area(Zhichao Yang et al., 2019).

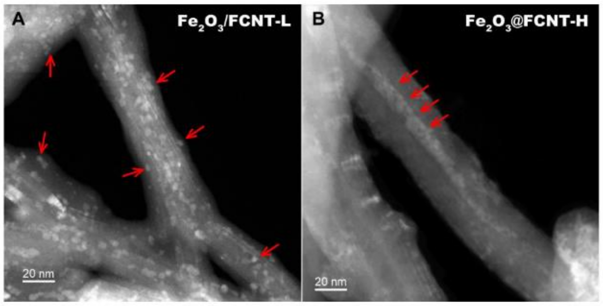

Figure 26. STEM-HADDF images of **(A)** Fe_2O_3/FCNT-L and **(B)** Fe_2O_3@FCNT-H(Zhichao Yang et al., 2019).

Core-Schell Nanoparticles

Core-shell is a structure composed of more than one material and in this type of configuration, two or more phases can be differentiated by their chemical composition and order, usually starting with a central material in the internal structure, surrounded by a shell on the outside of a different composition. Core-shell structures can be found from several different combinations of organic and inorganic materials. Core-shell metallic nanoparticles are generally highly functional materials and have different properties than their isolated counterparts. If a second or third material is added to the surface of these structures, reactivity and stability will be affected, although properties that are more related to volume can be conserved(Londoño-Calderon et al., 2017).

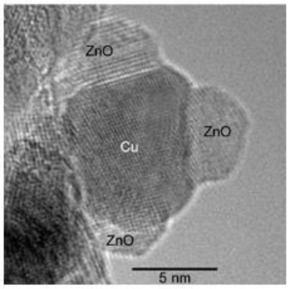

Figure 29. Metallic Cu particle partially covered by ZnO. The catalyst was prepared by coprecipitation with a molar ratio of Cu/Zn/Al of about 60:30:10(Jong, 2009).

References

Carberry, J. J. (1987). Physico-Chemical Aspects of Mass and Heat Transfer in Heterogeneous Catalysis. In J. R. Anderson & M. Boudart (Eds.), *Catalysis* (vol 8, pp. 131–171). Springer Berlin Heidelberg. https://doi.org/10.1007/978-3-642-93278-6_3

Cicco, A. Di, Aquilanti, G., Minicucci, M., Principi, E., Novello, N., Cognigni, A., & Olivi, L. (2009). Novel XAFS capabilities at ELETTRA synchrotron light source. *Journal of Physics: Conference Series*, *190*, 012043. https://doi.org/10.1088/1742-6596/190/1/012043

Galvis, H. M. T., Bitter, J. H., Davidian, T., Ruitenbeek, M., Dugulan, A. I., Jong, K. P. de, Torres Galvis, H. M., Bitter, J. H., Davidian, T., Ruitenbeek, M., Dugulan, A. I., De Jong, K. P., Galvis, H. M. T., Bitter, J. H., Davidian, T., Ruitenbeek, M., Dugulan, A. I., Jong, K. P. de, Torres Galvis, H. M., … De Jong, K. P. (2012). Iron particle size effects for direct production of lower olefins from synthesis gas. *Journal of the American Chemical Society*, *134*(39), 16207–16215. https://doi.org/10.1021/ja304958u

García-Sánchez, J. T., Valderrama-Zapata, R., Acevedo-Córdoba, L. F., Pérez-Martínez, D., Rincón-Ortiz, S., & Baldovino-Medrano, V. G. (2023). Calculation of Mass Transfer Limitations for a Gas-Phase Reaction in an Isothermal Fixed Bed Reactor: Tutorial and Sensitivity Analysis. *ACS Catalysis*, *13*(10), 6905–6918. https://doi.org/10.1021/acscatal.3c01282

Gu, B., He, S., Peron, D. V., Strossi Pedrolo, D. R., Moldovan, S., Ribeiro, M. C., Lobato, B., Chernavskii, P. A., Ordomsky, V. V., & Khodakov, A. Y. (2019). Synergy of nanoconfinement and promotion in the design of efficient supported iron catalysts for direct olefin synthesis from syngas. *Journal of Catalysis*, *376*, 1–16. https://doi.org/10.1016/j.jcat.2019.06.035

Jong, K. P. de. (2009). *Synthesis of Solid Catalysts* (K. P. de Jong (ed.)). WILEY-VCH Verlag GmbH & Co. KGaA.

Kowalczuk, P. B., & Drzymala, J. (2016). Physical meaning of the Sauter mean diameter of spherical particulate matter. *Particulate Science and Technology*, *34*(6), 645–647. https://doi.org/10.1080/02726351.2015.1099582

Londoño-Calderon, A., Ponce, A., Santiago, U., Mejia, S., & José-Yacamán, M. (2017). Controlling the Number of Atoms on Catalytic Metallic Clusters. In *Studies in Surface Science and Catalysis* (Vol. 177). https://doi.org/10.1016/B978-0-12-805090-3.00006-1

Pan, X., Fan, Z., Chen, W., Ding, Y., Luo, H., & Bao, X. (2007). Enhanced ethanol production inside carbon-nanotube reactors containing catalytic particles. *Nature Materials*, *6*(7), 507–511. https://doi.org/10.1038/nmat1916

Ravel, B., & Newville, M. (2005). ATHENA , ARTEMIS , HEPHAESTUS : data analysis for X-ray absorption spectroscopy using IFEFFIT. *Journal of Synchrotron Radiation*, *12*(4), 537–541. https://doi.org/10.1107/S0909049505012719

Serp, P., Corrias, M., & Kalck, P. (2003). Carbon nanotubes and nanofibers in catalysis. *Applied Catalysis A: General*, *253*(2), 337–358. https://doi.org/10.1016/S0926-860X(03)00549-0

Tao, F. (Feng). (2012). Design of an in-house ambient pressure AP-XPS using a bench-top X-ray source and the surface chemistry of ceria under reaction conditions. *Chemical Communications*, *48*(32), 3812. https://doi.org/10.1039/c2cc17715c

Weisz, P. B., & Prater, C. D. (1954). Interpretation of Measurements in Experimental Catalysis. *Advances in Catalysis*, *6*, 143–196. https://doi.org/10.1016/S0360-0564(08)60390-9

Yang, Z., Qian, J., Yu, A., & Pan, B. (2019). Singlet oxygen mediated iron-based Fenton-like catalysis under nanoconfinement. *Proceedings of the National Academy of Sciences of the United States of America*, *116*(14), 6659–6664. https://doi.org/10.1073/pnas.1819382116

Zheng, Q., Williams, J., Mantle, M. D., Sederman, A. J., Baart, T. A., Guédon, C. M., & Gladden, L. F. (2020). Experimental Determination of H2 and CO Diffusion Coefficients in a Wax Mixture Confined in a Porous Titania Catalyst. *The Journal of Physical Chemistry B, 124*, 10971−10982. https://doi.org/10.1021/acs.jpcb.0c07440

Iron and copper nanoparticles inside and outside carbon nanotubes: Nanoconfinement, migration, interaction and catalytic performance in Fischer-Tropsch synthesis

Introduction

The goal of this work is to evaluate the effect of catalyst preparation, activation and catalytic reaction on the localization, confinement and mobility of iron and copper nanoparticles inside and outside of CNT in bimetallic and monometallic catalysts. The characterization results, which were obtained using a combination of techniques: X-ray diffraction (XRD), conventional X-ray photoelectron spectroscopy (XPS), Near-ambient pressure X-ray photoelectron spectroscopy (NAP-XPS), Raman, Scanning Transmission Electron Microscopy (STEM) are discussed together with the catalytic data measured in a higher-pressure fixed-bed reactor.

Results and Discussion

Characterization of calcined catalysts

The XRF, XRD, TPR, and nitrogen adsorption data for the monometallic and bimetallic catalysts are presented in **Table 1**. The catalysts with non-confined and confined iron and/or copper nanoparticles do not present similar iron and copper contents measured by XRF. At the same time, the targeted value should be around 10 wt.% for all of them. In the confined catalysts, the metal content is higher than in non-confined counterparts. Note that the metals were deposited over the catalysts using impregnation followed by evaporation of the impregnating solution. Some amount of the deposited metal species can be removed during the washing step. **Table 1** also shows textural properties of the CNTs supports without acid treatment (commercial form) and CNT with open and closed channels, for confined particles (in) and non-confined particles (out), and also for the catalysts containing iron and copper nanoparticles located either outside (non-confined) or inside the CNTs tubes (confined).

Table 1. Physical properties of supports and supported Cu and Fe catalysts.

Sample	S_{BET}[a] (m²/g)	V_{tot}[b] (cm³/g)	D_{meso}[c] (nm)	$D_{crystallite}$[d] (nm)	Total H_2 consumption[e] (mmol/g)	Cu or Fe content[f] (wt%)
CNTs commercial	76.9	0.19	14.1	-	-	-
CNTs out	88.3	0.21	13.5	-	-	-
CNTs in	157.1	0.38	11.4	-	-	-
Fe-in	154.4	0.35	10.7	Fe_2O_3: 27	2.3	Fe: 8.2
Fe-out	104.5	0.26	11.6	Fe_2O_3: 30	2.1	Fe: 4.5
Cu-in	136.1	0.38	11.1	CuO: 14	1.9	Cu: 2.8
Cu-out	106.2	0.23	11.6	CuO: 26	1.8	Cu: 1.3
$Fe^{1st}Cu^{2nd}$	130.2	0.28	11.2	Fe_2O_3: 25 CuO: 23	5.2	Fe: 6.5 Cu: 6.6
$Cu^{1st}Fe^{2nd}$	152.4	0.34	10.7	Fe_2O_3: 18 CuO: 23	4.8	Fe: 6.9 Cu: 5.2
Fe+Cu-in	133.9	0.35	11.3	$CuFe_2O_2$/CuO: 10	3.9	Fe: 5.4 Cu: 5.2
Fe+Cu-out	91.1	0.23	10.6	$CuFe_2O_2$/CuO: 21	3.8	Fe: 3.7 Cu: 3.3

[a] BET Surface Area

[b] BJH Desorption cumulative volume of pores between 17.000 Å and 3,000.000 Å

[c] BJH Desorption average pore width (4V/A)

[d] Size of crystallites by XRD (Scherrer equation)

[e] The total H_2 consumption from TPR analysis

[f] The Fe and Cu content from XRF analysis

The surface area of CNTs increases after the acid treatments. As expected, the severe acid treatment used to open the channels, produces a higher impact on the surface area and pore volume, while the mild acid treatment has a much lower impact. CNTs with open tubes (CNTs-in) exhibit a larger pore volume compared with CNTs with closed tubes (CNTs-out). After the impregnation with iron and copper, the surface area decreases for the catalysts with the metal particles presumably located inside of the tubes and increases for the catalysts with the metal particles outside CNT. The addition of iron and copper to CNT leading to the Fe-in and Cu-in samples results in a decrease in the surface area of CNTs from 157.1 to 154.4 and 136.1 m^2 g^{-1}, respectively. He et al. (S. He et al., 2019) also observed that both surface area values and pore volume values decreased after a severe acid treatment followed by the impregnation with iron and copper. Similar effect was also observed by Chen et al.(Z. Chen et al., 2011) who used CNTs as a support for preparation of platinum nanocatalysts. Gu et al.(Gu, He, et al., 2019) observed that the impregnation with iron produced only a very small impact on the pore volume of CNT with closed tubes. However, when the metal particles are located inside the CNTs tubes, a very significant decrease was observed.

For the $Fe^{1st}Cu^{2nd}$, Cu^{1st} Fe^{2nd}, Fe+Cu-in and Fe+Cu-out bimetallic catalysts, the surface area decreases to 130.2, 152.4, 133.9 and 91.1 m^2 g^{-1}, respectively. The decrease in the surface area and pore volume of open CNT after impregnation with the iron or copper precursors can be due to two phenomena. First, the introduction of metals may result in the effect of “dilution” of CNTs, reducing the weight normalized surface area. Second, the impregnation can lead to blocking of CNT inner channels with metal species (Gu et al., 2018). Note however, that some increase in the BET surface area from 88.3 to 104.5 and 106.2 m^2 g^{-1} was observed for the Fe-out and Cu-out catalysts compared to their corresponding support (CNTs-out). CNT with closed channels does not have a highly developed mesoporosity. Introduction of metals can generate some defects on the surface of closed CNT and favor CNT redispersion. This could result in some surface area increase.

Figure 1 a, b, c and **d** displays XRD profiles of the calcined supported catalysts. The detailed assignment of XRD peaks in the calcined catalysts is given in **Table S1, Appendix**. For all monometallic and bimetallic calcined catalysts, the XRD patterns show diffraction peaks at 26.4° and 42.9° attributed to the (0 0 2) and (1 0 0) reflections of the CNTs supports(Abbaslou et al., 2010; Y. Cheng et al., 2016; S. He et al., 2019; Ismail et al., 2019; J. Lu et al., 2014; V. V. Ordomsky et al., 2015) (#PDF 01-0646). This indicates that the crystal structure of CNTs is maintained after the acid treatments and metal impregnation (Ismail et al., 2019). Interestingly, the relative intensity peak of copper oxide relative to the CNT peak is higher for non-confined copper monometallic catalyst in comparison with the confined one. This could be due to the higher difference between the copper oxide particle size, which in the case of non-confined copper monometallic catalyst is 1.8 times higher than the copper oxide particle size for the confined counterpart.

The peaks in the XRD patterns of the Fe-in, Fe-out, $Fe^{1st}Cu^{2nd}$ and Cu^{1st} Fe^{2nd} samples at 33.1, 35.6, 40.8, 49.5, 54, 62.4 and 64.1° are assignable to the hematite phase (Fe_2O_3)(Abbaslou et al., 2010; Y. Cheng et al., 2016; Ismail et al., 2019; J. Lu et al., 2014) (#PDF 01-1053), while the peaks at 30, 35.5, 43, 53.5, 57, 62.5 and 74.1 ° can be attributed to the magnetite phase (Fe_3O_4) (Abbaslou et al., 2010; S. He et al., 2019; Ismail et al., 2019; J. Lu et al., 2014; V. V. Ordomsky et al., 2015) (#PDF 01-1111). In the iron containing catalysts, calcined at 400 °C in nitrogen atmosphere, the iron species exist as a mixture of Fe_2O_3 and Fe_3O_4 (J. Lu et al., 2014).

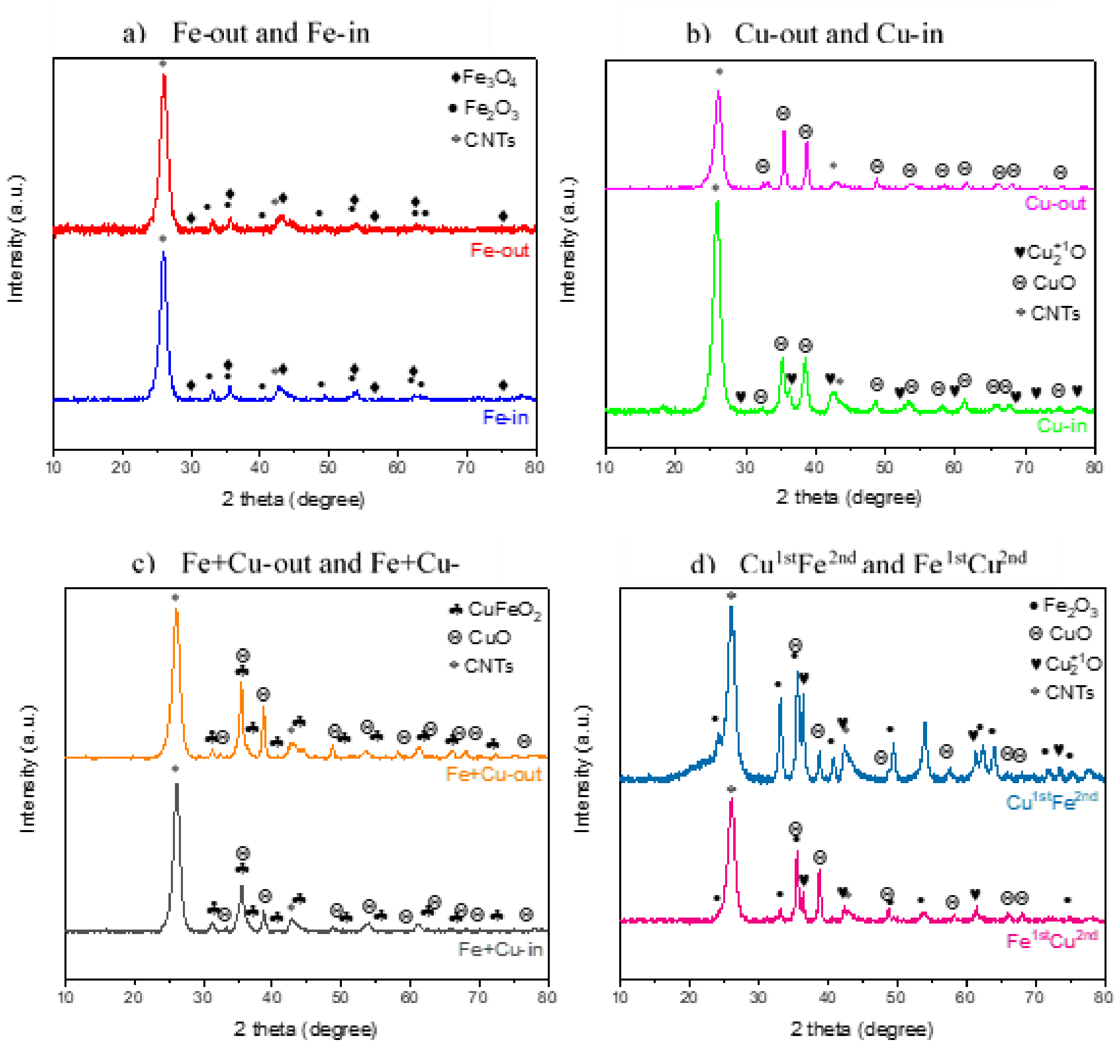

Figure 1. XRD patterns of calcined catalysts.

The calcined copper-containing catalysts exhibit peaks attributed to the CuO tenorite and Cu_2O cuprite phases. For the Cu-in, Cu-out monometallic catalysts and $Fe^{1st}Cu^{2nd}$, Cu^{1st} Fe^{2nd}, Fe+Cu-in and Fe+Cu-out bimetallic samples, the peaks at 32.5, 35.4, 38.6, 48.8, 53.4, 58.3, 61.6, 66.2, 68.1 and 75.1 ° can be attributed to the (1 1 0), (0 0 2), (1 1 1), (-2 0 2), (0 2 0), (2 0 2), (-1 1 3), (-3 1 1), (2 2 0) and (0 0 4) reflections of tenorite phase (CuO)(Chinthakuntla et al., 2014; S. He et al., 2019; Suresh et al., 2016; S. Xiao et al., 2017; D. Zhao et al., 2017)(#PDF 05-0661), respectively (**Table S1, Appendix**). For the Cu-in catalyst, the peaks at 29.5, 36.3, 42.4, 52.5, 61.3, 69.5, 73.5 and 77.2° could be assigned to the (1 1 0), (1 1 1), (2 0 0), (2 1 1), (2 2 0), (3 1 0), (3 1 1) and (2 2 2) reflections of cubic cuprite phase (Cu_2O)(Feng et al., 2012; S. Xiao et al., 2017; L. Yang et al., 2010; D. Zhao et al., 2017)(#PDF 05-0667). For the bimetallic catalyst Fe+Cu-in and Fe+Cu-out, the peaks at 31.3, 34.5, 35.6, 40.2, 43.4, 47.7, 55.2, 61, 64.8 and 70° can be attributed to the (0 0 6), (1 0 1), (0 1 2), (1 0 4), (0 1 5), (0 0 9), (0 1 8), (1 1 0), (1 0 10) and (0 1 11) reflections of delafossite phase ($CuFeO_2$) (#PDF 03-0870).

The crystallite sizes of iron and copper oxides were calculated from the XRD peak broadening using the Scherrer equation (**Table S2, Appendix**). The crystallite sizes measured by XRD were in the range from 20 to 30 nm for both copper and iron species, with the exception for Cu-in. In this sample, XRD detected smaller copper oxide crystallites of 5-14 nm. Note that measuring sizes of crystallites from the half-width of the diffraction profile could slightly overestimate (GANESAN, 1978) the crystallite diameters. In addition, some very small metal oxide particles could be missed by XRD, because of significant XRD line broadening, while others can adopt an elongated shape in the pores.

In order to provide further information about the sizes and localization of metal oxide nanoparticles, the catalysts and CNT supports were characterized by TEM. First, we measured inner and outer diameter distributions for the CNT supports (**Figure S1, Appendix)**. The size distribution is broad, with the internal average diameter of 8.4-9.9 nm, and the outer average diameter of 42.7-43.9 nm for both CNTs-in and CNTs-out (See **Table S3, Appendix**).

Figure 2 displays TEM micrographs of the freshly calcined CNT-supported catalysts. Several hundreds of nanoparticles were taken for calculating nanoparticle size histograms and evaluation of the localization of iron and copper nanoparticles inside and outside CNT. Note that HAADF-STEM and Z-contrast alone do not allow the identification of the chemical composition of copper and iron nanoparticles. That was the reason, why for the bimetallic catalysts, EDS was applied for identification of the chemical particle composition. We considered the largest diameter of nanoparticles in the particle size measurements.

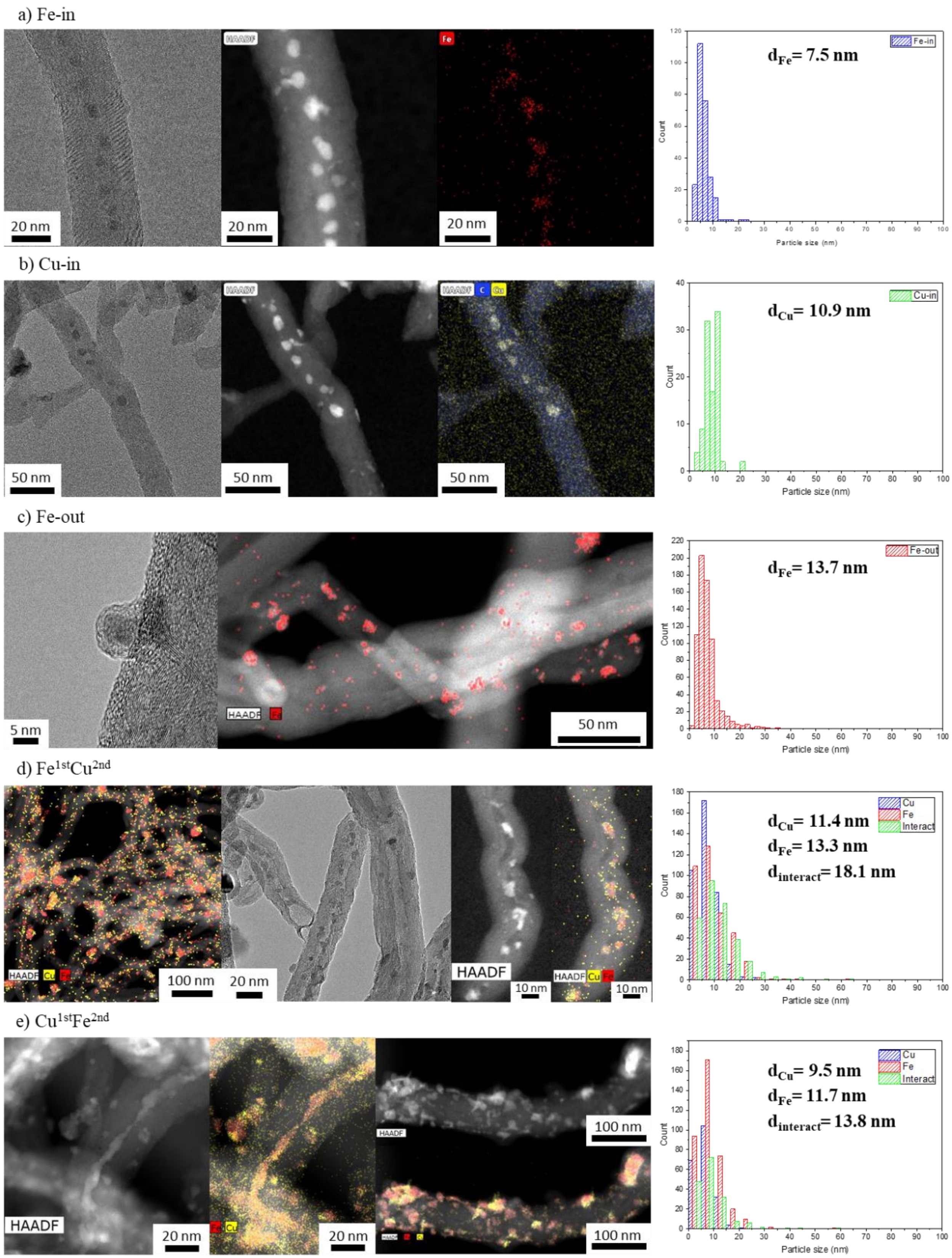

Figure 2. TEM micrographs for the freshly calcined supported catalysts.

Moreover, TEM images also allowed identification of the nanoparticle localization either inside or outside of CNTs. For each analyzed catalyst, we built histograms of copper, iron individual, and interacting metal nanoparticle distribution localized inside and outside of CNT. The average particle size for Cu, Fe, and interacting particles were calculated from the histograms using the Sauter equation. The average (Sauter) particle sizes calculated from TEM images are presented in **Table 2**. We detected three types of metal oxide nanoparticles in the CNT supported catalysts: isolated copper oxide nanoparticles, isolated iron oxide nanoparticles and interacting copper-iron oxide nanoparticles. The particles are considered "interacting", if the TEM images clearly show their close intimate contact. The distribution of copper, iron and interacting particles inside and outside of CNT is given in **Table 3**.

Table 2. Average particle size of the catalysts before and after reaction.

Before reaction		After reaction	
Sample	Sauter D (nm)	Sample	Sauter D (nm)
Fe-in	7.5	Fe-in used	15.1
Fe-out	13.7	Fe-out used	18.8
Cu-in	10.9	Cu-in used	14.0
Fe^{1st}Cu^{2nd}	Cu: 11.4 Fe: 13.3 Interacting: 18.1	Fe^{1st}Cu^{2nd} used	Cu: 27.2 Fe: 18.3 Interacting: 34.7
Cu^{1st}Fe^{2nd}	Cu: 9.5 Fe: 11.7 Interacting: 13.8	Cu^{1st}Fe^{2nd} used	Cu: 18.3 Fe: 20.7 Interacting: 23.3

The TEM images for the freshly calcined Fe-in catalyst exhibit iron oxide particles with an average size of 8.8 nm and a narrow particle size distribution. The fresh Cu-in catalyst also presents an average size of 10.9 nm. TEM images clearly confirm the presence of a larger fraction of iron and copper nanoparticles inside the CNTs tubes (83% for Fe-in and 78% for Cu-in, **Table 3**). The iron and copper localization inside open CNT is due to the tubular morphology of CNTs, which can induce capillary forces to absorb the Fe or Cu nitrate solutions into the tubes during the impregnation (Pan & Bao, 2011). Due to their confinement inside the tubes, the nanoparticle growth seems to be limited by the inner walls of the CNTs (Q. Cheng et al., 2018; Gu, He, et al., 2019; C. Wang et al., 2010). Our results are consistent with the data of Chen et al.(W. Chen et al., 2007) who observed that the size of confined iron oxide nanoparticles changed according to the inner diameter. The larger is the internal diameter of the CNTs, the larger is the confined particle.

Table 3. Particle location inside and outside CNT before and after reaction.

<table>
<tr><th rowspan="2">Catalyst</th><th colspan="3">Before reaction</th><th colspan="3">After reaction</th></tr>
<tr><th colspan="2">% of particles in</th><th>% of particles out</th><th colspan="2">% of particles in</th><th>% of particles out</th></tr>
<tr><td>Fe-in</td><td colspan="2">78.0</td><td>22.0</td><td colspan="2">72.2</td><td>27.8</td></tr>
<tr><td>Fe-out</td><td colspan="2">7.5</td><td>92.5</td><td colspan="2">12.6</td><td>87.4</td></tr>
<tr><td>Cu-in</td><td colspan="2">83.0</td><td>17.0</td><td colspan="2">58.2</td><td>41.8</td></tr>
<tr><td></td><td>% of Interacting particles</td><td>% of particles in</td><td>% of particles out</td><td>% of Interacting particles</td><td>% of particles in</td><td>% of particles out</td></tr>
<tr><td>$Fe^{1st}Cu^{2nd}$</td><td>39.8</td><td>Cu: 33.6
Fe: 36.8
Int: 40.8</td><td>Cu: 66.4
Fe: 63.2
Int: 59.2</td><td>7.8</td><td>Cu: 11.9
Fe: 25.5
Int: 5.6</td><td>Cu: 88.1
Fe: 74.5
Int: 94.4</td></tr>
<tr><td>$Cu^{1st}Fe^{2nd}$</td><td>29.4</td><td>Cu: 32.4
Fe: 20.2
Int: 36.3</td><td>Cu: 67.6
Fe: 79.8
Int: 63.7</td><td>23.7</td><td>Cu: 49.1
Fe: 54.8
Int: 30.4</td><td>Cu: 50.9
Fe: 45.2
Int: 69.6</td></tr>
</table>

The metal particles are larger, when the metal species are deposited on the outer surface of closed CNT. For the Fe-out catalyst, the particle size distribution is broad with the average size of 13.7 nm (**Figure 2**, **Table 2**). Note that 92.5 % iron particles in Fe-out are located outside CNT (**Table 3**).

In the bimetallic $Fe^{1st}Cu^{2nd}$ and $Cu^{1st}Fe^{2nd}$ catalysts, the sizes of iron, copper and interacting nanoparticles are in the range from 9.5 to 14.0 nm. The calcined $Fe^{1st}Cu^{2nd}$ and $Cu^{1st}Fe^{2nd}$ catalysts were prepared from Fe-in and Cu-in with subsequent impregnation with respectively, copper or iron nitrate. Interestingly, the second impregnation significantly modifies the distribution of metal oxide nanoparticles introduced during the first impregnation. After the first impregnation, most of iron or copper nanoparticles are located inside the CNT channels. After the second impregnation, it seems that a major fraction of metal nanoparticles migrates from inside CNT to the outer surface. Most of isolated monometallic or interacting nanoparticles are located on the CNT outer surface.

TEM suggests considerable migration of metal nanoparticles in the catalysts prepared by sequential two-step impregnation. It can be suggested that the acid treatment in the support and also the impregnation method can damage CNTs and facilitate the mobility of the metal nanoparticles. Note that the ultrasonication can contribute to the defects in CNTs. Both longer sonication time and use of high frequency can result in cutting of carbon nanotubes into shorter lengths (Arrigo et al., 2018; Ramaraj et al., 2017; Rennhofer & Zanghellini, 2021; Sesis et al., 2013). Ultrasonicate can also contribute to the migration and redispersion of metals.

To confirm this hypothesis, Raman spectroscopic measurements were performed for all the catalysts. It has been shown(Heise et al., 2009) that Raman spectroscopy can be particularly sensitive to the microstructure of the carbon. This technique provides therefore a nondestructive control of structural and electronic characteristics of carbon materials(Kuznetsov et al., 2014). **Figure S2, Appendix** shows the Raman spectra of the commercial CNTs (in grey), CNTs after severe acid treatment (CNTs-in) and CNTs after the mild acid treatment (CNTs-out). The bands D (~1350 cm^{-1}) and G- (~1580 cm^{-1}) reveal the presence of defects in the graphite layer(R. Xu et al., 2018). A good indicator of the quality of bulk CNT samples is the ratio of the intensities of D and G bands: if these intensities are similar, it indicates a high quantity of structural defects (COSTA et al., 2008).

The Raman spectra of calcined catalysts are presented in **Figure 3**. The ratios of D and G bands (I_D/I_G) are shown in **Table S4, Appendix**. A smaller intensity ratio of D- and G-bands (**I_D/I_G**) indicates a higher degree of graphitization and less damage of CNTs(R. Xu et al., 2018). **Table S4, Appendix** shows that sequential two-step impregnation provokes more damages in the CNTs structures than the co-impregnation (Fe+Cu-in and Fe+Cu-out) and single-step impregnation (Fe-in, Fe-out, Cu-in and Cu-out).

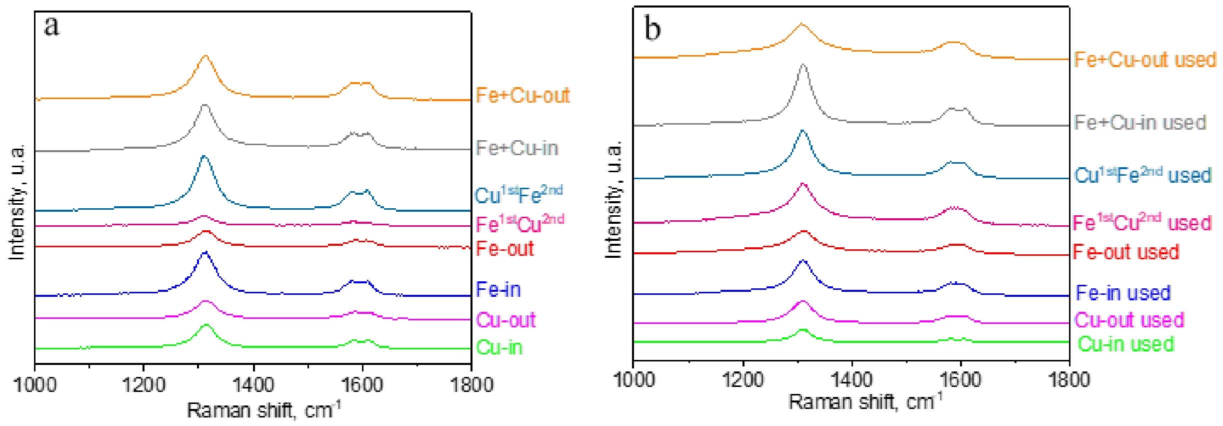

Figure 3. Raman spectra of calcined and used catalysts (excitation wavelength of 785 nm).

In addition to the variation of the intensities, a high frequency shift of the G bands is observed. This shift is possibly related to the structural defects or residual strains in CNTs(R. Xu et al., 2018). The high frequency shift, especially for the G band, could be attributed to disentanglement and dispersion of the CNTs bundles. This deformation on CNTs could result in a change in C-C bond vibrations, which in turn, leads to a change in the vibrational frequencies of the normal modes and thus to Raman band shiFT synthesis (Batakliev et al., 2019). The I_D/I_G ratio increases with the number of impregnation steps. This indicates formation of defect CNT structure, which reduces the efficient length of CNT and creates orifices. The information obtained by Raman spectroscopy is also consistent with the TEM data. **Figure S3, Appendix** allows visualization of the defects provoked by the second step of impregnation in used catalysts. In the left images, it is possible to observe longer CNTs and also it is possible to view better the channel limits.

In contrast, in the images on the right, the CNTs are shorter and the channel limits are not that easy to see anymore. These visual observations are consistent with the Raman results, that show higher concentration of defects in the catalysts prepared with two steps of impregnation, comparing with the other catalysts prepared by only one impregnation. The presence of numerous defects in the $Fe^{1st}Cu^{2nd}$ and $Cu^{1st}Fe^{2nd}$ catalysts prepared by successive impregnation could possibly explain facile migration of metal nanoparticles. In order to evaluate the effect of impregnation on the structure of the Fe-in monometallic catalyst, this catalyst was impregnated with deionized water (pH ~ 3 adjusted by nitric acid, same pH as in metal nitrate solution). The impregnation with acid water also results in the modification of the Raman spectra (**Figure S3, Appendix**) and in the increase in the **I_D/I_G** intensity ratio to the value observed for the bimetallic $Fe^{1st}Cu^{2nd}$ and $Cu^{1st}Fe^{2nd}$ samples (**Table S4, sample Fe-in 2nd, Appendix)**. This suggests that each impregnation step (even exposure to pure water) decreases the ordering of CNT.

FT synthesis may involve iron carbide phase (Abelló & Montané, 2011). The improved iron reducibility can favor the formation of more iron carbides under reaction conditions. The reduction of iron oxides and iron carbidisation are therefore, essential for the activation of iron catalysts (Gu, He, et al., 2019). H_2-TPR analyzes were performed for all catalysts (**Figure 4**). The monometallic Fe-in and Fe-out iron catalysts exhibit similar profiles, with 3 main groups of hydrogen consumption peaks referring to the multistep reduction from hematite to metallic Fe (Gu et al., 2018; Gu, He, et al., 2019): $Fe_2O_3 \rightarrow Fe_3O_4 \rightarrow FeO \rightarrow Fe$ (Abbaslou et al., 2010). The extent of the reduction of metal is defined as the ratio between the actual H_2 amount consumed during the H_2-TPR process (from room temperature to 900 °C) and theoretical amount of H_2 required for the complete reduction of metal oxides (Abbaslou et al., 2010). The TPR peaks of iron catalysts are broad, this may be due to broad iron particle size distribution and/or metal-support interactions. The first peak can be related to the reduction of Fe_2O_3 to Fe_3O_4 (~250–420 °C) (Y. Liu et al., 2015; Shi et al., 2019), the second peak can be ascribed to the reduction of Fe_3O_4 to FeO and the third peak can be assigned to the reduction of FeO to Fe (~600–700 °C) (Gu et al., 2018; Gu, He, et al., 2019; Y. Liu et al., 2015). There is a tail, after 650 °C, due to the gasification of CNTs(Abbaslou et al., 2010; J. Lu et al., 2014). The copper catalysts (Cu-in and Cu-out) exhibit a broad peak (~100-280 °C), referring to the reduction of CuO to metallic Cu (Y. Liu et al., 2015; L. Yang et al., 2010; D. Zhao et al., 2017) and another large and weak peak referring to the gasification of CNT supports. The Cu-in catalyst exhibited a shoulder in the mean peak (~226 °C), this could be due to the reduction of CuO to metallic Cu proceeding through intermediate Cu^+ species (S. Xiao et al., 2017; Yue et al., 2013). The bimetallic $Cu^{1st}Fe^{2nd}$, $Fe^{1st}Cu^{2nd}$, Fe+Cu-in, Fe+Cu-out catalysts had similar profiles, being a junction of the profiles of iron catalysts and copper catalysts, with two large and separate peaks. The TPR peaks attributed to the reduction to iron metallic phase shift from 615-640 °C (**Figure 4a**), in monometallic iron catalysts to 453-535 °C in the bimetallic counterparts (**Figure 4 c** and **d**). If we compare the profiles of monometallic iron catalysts with the bimetallic catalysts, the catalyst reduction is accomplished at lower temperatures for the bimetallic catalysts. This suggests that the presence of copper may facilitate the reduction of iron. The CuO reduction occurs at lower temperatures than Fe_xO_y reduction. This nucleation of copper metal nanoparticles can provide dissociation sites for H_2 and therefore can increase the concentration of atomic hydrogen on the surface of the catalyst, which assists the reduction of iron oxides (Peña et al., 2018).

The broad peaks at 450-660°C can be due to the gasification of CNTs, which usually happens at temperatures higher than 600 °C(Abbaslou et al., 2010). In the profiles of bi-metallic catalysts, the peaks at this temperature range are larger and shifted by 100 to 200 °C to lower temperatures compared to the monometallic copper catalysts. This suggests that the presence of both iron and copper may lead to the CNT gasification at temperatures below 600 °C. This observation is consistent with the data of Serp et al.(Serp et al., 2003) who showed that the gasification of the CNTs could be catalyzed by metal nanoparticles.

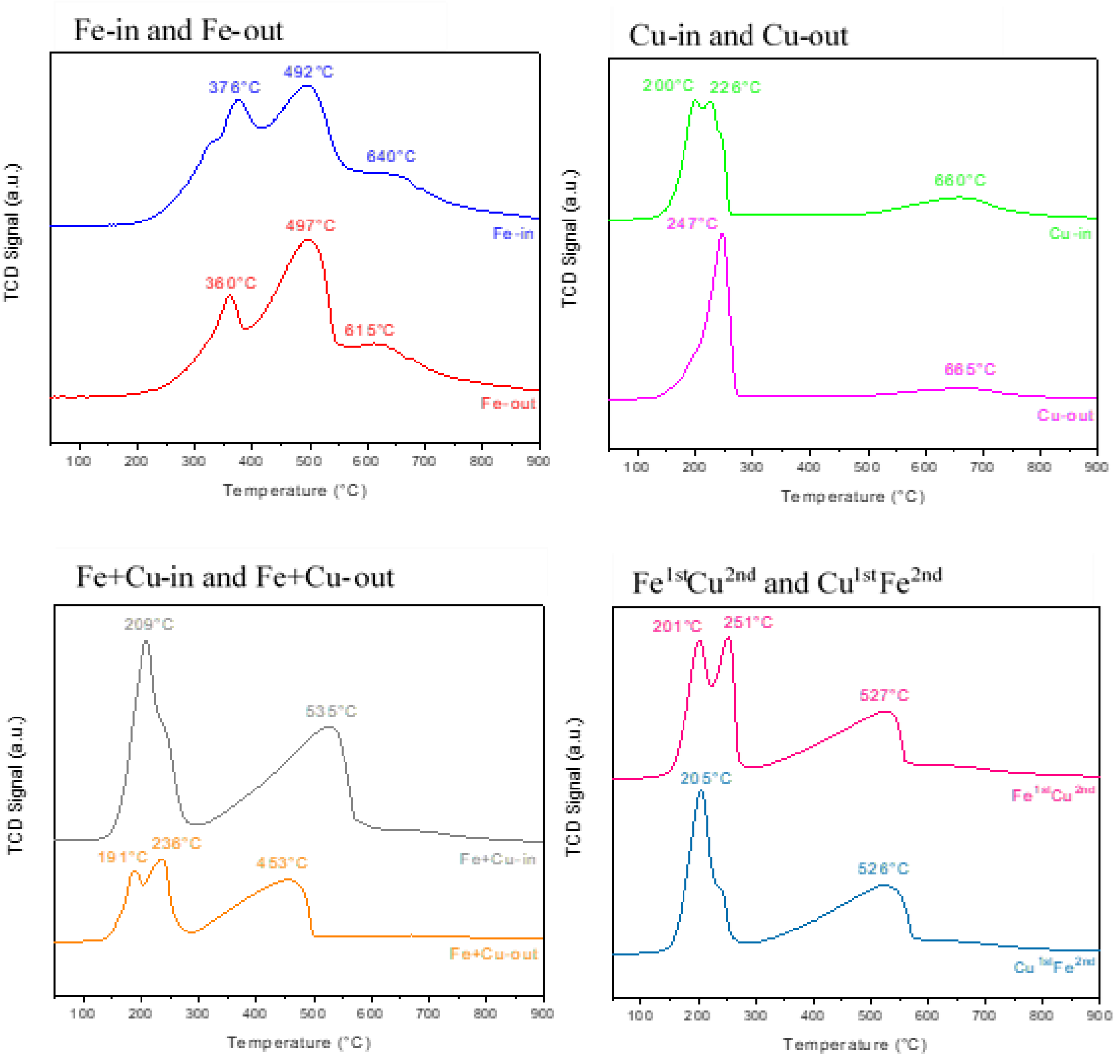

Figure 4. TPR profiles of the catalysts.

Further information about the reducibility of supported iron and copper species can be obtained through the total amount of hydrogen consumed during TPR experiments (**Table 1**). The bimetallic catalysts show higher hydrogen consumption in the following sequence: Fe^{1st}Cu^{2nd} > Cu^{1st}Fe^{2nd} >Fe+Cu-in>Fe+Cu-out, compared to the monometallic catalysts. The amount of H_2 consumed for Fe-in catalyst was a bit larger when comparing to Fe-out catalyst (**Table 1**). The theoretical value required for the complete reduction of Fe_2O_3 to Fe is 2.686 mmol/g. This suggests that the extent of reduction for the Fe-in catalyst was 85% and for Fe-out catalyst was 79%. This can be attributed to a different interaction of iron oxide with inner surface of CNT. For the Cu-in and Cu-out catalysts, the amount of H_2 consumed was 1.9 and 1.8 mmol/g, respectively. Then, the extent of reduction for the Cu-in and Cu-out catalysts is 122% and 115%, respectively. The TPR peaks were observed at lower temperatures for Cu-in catalyst than in Cu-out catalyst. Higher extent of reduction of iron and copper species located inside CNT is consistent with previous results of the group of Pan and Bao (Abbaslou et al., 2010). Pan et al.(Pan & Bao, 2011) revealed that the reduction of Fe_2O_3 particles was facilitated, when the particles are confined within MWCNTs in relation to the particles located on the outside. The reduction was facilitated by narrowing the channels of the CNTs. Not only the location of the nanoparticles, but also the metal loading and the dispersion of the nanoparticles may also influence in the extent of reduction. The higher the metal loading, the higher is the consumption of hydrogen.

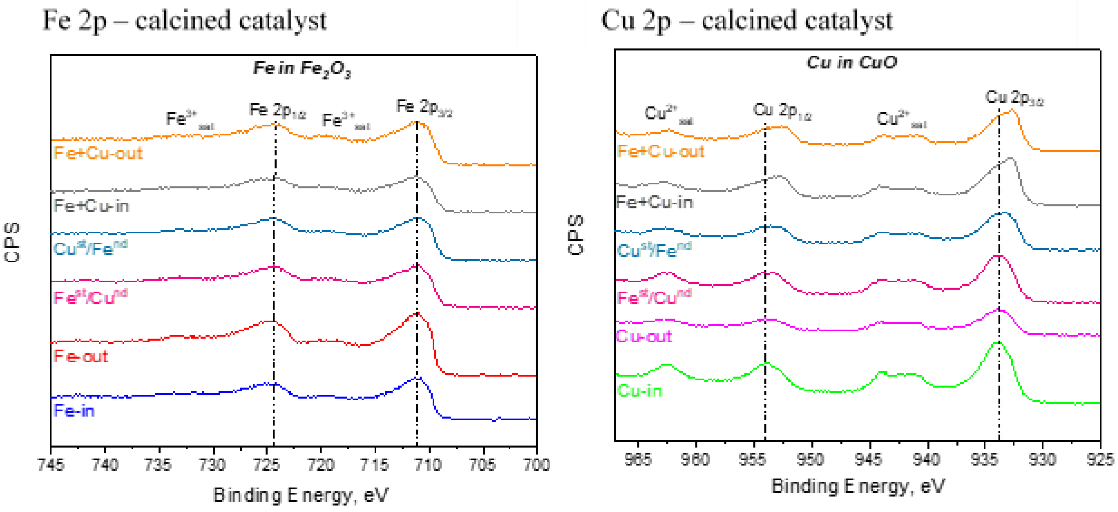

Figure 5. XPS results for the calcined catalysts.

We performed conventional *ex-situ* XPS measurements for the calcined catalysts in order to get the information about the chemical states and concentration of Cu and Fe on the catalyst surfaces. The XPS spectra in the Fe 2 p region are shown in **Figure 5a**. The binding energies (BEs) for the $Fe2p_{3/2}$ and $2p_{1/2}$ main peaks were around 711 and 724.5 eV, respectively (**Table S5, Appendix**), for all iron containing monometallic and bimetallic catalysts. The peaks for the $Fe2p_{3/2}$ and $Fe2p_{1/2}$ core levels with BEs of ~711 and ~724.5 eV, respectively, combined with the satellite peak at ~719 eV, which is characteristic of Fe^{3+}, are related to the Fe_2O_3 (Y. Cheng et al., 2016; S. He et al., 2019; Jian et al., 2009; Morales et al., 2005; Moulder et al., 1992; L. Yang et al., 2010). Note that the Fe^{3+} $2p_{3/2}$ peak of $Cu^{1st}Fe^{2nd}$ catalyst appears at 711.0 eV, which is a little higher in energy than the standard peak at 710.9 eV for Fe_2O_3. This may indicate the existence of a small amount of Fe_3O_4 species in $Cu^{1st}Fe^{2nd}$, since the Fe^{3+} $2p_{3/2}$ peak for Fe^3O^4 at 711.4 eV is about 0.5 eV higher than that for Fe_2O_3 at 710.9 eV(J. Lu et al., 2014).

Table 4. XPS **s**urface concentration of the calcined and used catalysts.

Sample		% Mass conc	% At conc	Ratio area, %	XPS atom ratio, %
Fe-in	Fe 2p	4.8	1.1	Fe/C = 1.05	Fe/C = 1.05
Fe-out	Fe 2p	7.3	1.7	Fe/C = 1.61	Fe/C = 1.61
Cu-in	Cu 2p	5.9	1.2	Cu/C = 1.23	Cu/C = 1.23
Cu-out	Cu 2p	2.6	0.5	Cu/C = 0.46	Cu/C = 0.46
Cu^{1st}/Fe^{2nd}	Fe 2p	7.0	1.7	Fe/C = 1.66	Fe/C = 1.66
	Cu 2p	4.8	1.0	Cu/C = 1.06	Cu/C = 1.06
Fe^{1st}/Cu^{2nd}	Fe 2p	5.8	1.4	Fe/C = 1.48	Fe/C = 1.48
	Cu 2p	4.9	1.0	Cu/C = 1.11	Cu/C = 1.11
Fe+Cu-in	Fe 2p	5.0	1.2	Fe/C = 1.17	Fe/C = 1.17
	Cu 2p	4.5	0.9	Cu/C = 0.94	Cu/C = 0.94
Fe+Cu-out	Fe 2p	4.8	1.1	Fe/C = 1.12	Fe/C = 1.12
	Cu 2p	3.1	0.6	Cu/C = 0.67	Cu/C = 0.67
Sample		% Mass conc	% At conc	Ratio area	XPS atom ratio
Fe-out used	Fe 2p	1.6	0.4	Fe/C = 0.32	Fe/C = 0.32
Cu-in used	Cu 2p	1.9	0.4	Cu/C = 0.34	Cu/C = 0.34
Cu-out used	Cu 2p	0.9	0.2	Cu/C = 0.20	Cu/C = 0.20
Cu^{1st}/Fe^{2nd} used	Fe 2p	1.3	0.3	Fe/C = 0.42	Fe/C = 0.42
	Cu 2p	1.3	0.3	Cu/C = 0.29	Cu/C = 0.29
Fe^{1st}/Cu^{2nd} used	Fe 2p	1.2	0.3	Fe/C = 0.29	Fe/C = 0.29
	Cu 2p	1.2	0.2	Cu/C = 0.22	Cu/C = 0.22
Fe+Cu-out used	Fe 2p	1.2	0.3	Fe/C = 0.39	Fe/C=0.39
	Cu 2p	1.6	0.3	Cu/C = 0.34	Cu/C=0.34

The BEs of $Cu2p_{3/2}$ and $Cu2p_{1/2}$ were around 933 eV and 953 eV, respectively (**Figure 5b, Table S5, Appendix**). According to the Moulder et al. (Moulder et al., 1992), the BE values for $Cu2p_{3/2}$ between 932 and 933 eV indicate the presence of Cu_2O, while the values between 933 and 934 eV suggest CuO(D. Zhao et al., 2017). The standard binding energy for the $Cu2p_{3/2}$ for Cu in CuO is 933.6 eV. This is the case for the Cu-in and Cu-out catalysts that show BE of 933.8 eV.

The BE values of Cu $2p_{3/2}$ were observed at 932.8 eV and 932.7 eV for the Fe+Cu-in and Fe+Cu-out catalysts and can be attributed to the Cu^{+} species(Q. He et al., 2011), but while the presence of a the strong satellite peak at ~ 942 eV is characteristic of Cu^{2+} species(Q. He et al., 2011). The Cu KLL Auger peaks (**Figure S5, Table S5, Appendix**) have thus been examined for Fe+Cu-in and Fe+Cu-out catalysts and showed a main peak with Kinetic Energies (KEs) 917.0 eV and 917.5 eV respectively.

The Cu 2p photopeak BE along with the Cu KLL Auger peak KE allows the determination of the modified Auger Parameter (AP') and correspond to 1849.3 eV and 1850.2 eV respectively. The AP' energy for both catalysts is characteristic of Cu^{+} species. This means that both Cu oxide species are present in this samples, also, the major copper species in the Fe+Cu-in catalyst are Cu^{+} (Biesinger, 2017).

The copper and iron atomic and mass relative concentrations calculated from XPS, are presented in **Table 4**. The XPS data provide information about Cu/Fe ratio on the surface. Rather similar bulk and surface Cu/Fe ratios measured by XRF and XPS indicate uniform distribution and similar dispersion of copper and iron in the calcined bimetallic catalysts.

Catalytic performance

The FT catalytic data for the confined and non-confined catalysts are displayed in **Table 5**, **S7** and **S8**, **Appendix**. Methane, light olefins, light paraffins, C_{5+} hydrocarbons, oxygenates and CO_2 were detected as major reaction products. The catalysts exhibit very high selectivity to CO_2 (between 29 and 44 %), which is probably produced by an almost stoichiometric reaction of CO with the produced water: $CO+H_2O=CO_2+H_2$. At 350 °C, the catalysts show higher selectivity to the C_2-C_4 olefins, while the selectivity to the C_{5+} hydrocarbons was between 30 and 47%. Only trace amounts of oxygenates (methanol and ethanol) were observed.

Figure 6 shows the CO conversion over the catalysts during FT synthesis as a function of the reaction time, while **Figure S6, Appendix** displays the time-dependent variation of the selectivities. Some variation of the CO conversion is observed during the first 5 h of reaction. But after that, the values become stable. The copper catalysts showed extremely low activity under these conditions with the CO conversion well below 5%. The conversion of monometallic iron catalysts strongly depends on the localization of iron. Interestingly, when iron nanoparticles are located inside CNT, the reaction rate was 20% higher compared to the Fe-out catalysts with iron species situated outside of CNT. These results are consistent with previous works showing higher activity of the catalysts containing iron nanoparticles inside CNT (W. Chen et al., 2007, 2008; X. Chen et al., 2015; Gu, He, et al., 2019; J. Xiao et al., 2015; Zhiqiang Yang et al., 2011). Previously, Pan et al.(Pan & Bao, 2011) studied the effect of confinement on the FT synthesis by comparing external iron (Fe-out) and internal iron (Fe-in). According to their TEM analyses, more than 70% of the Fe particles were distributed within the CNT channels for the confined Fe-in catalyst. For Fe-out, almost all the Fe particles were on the outside of CNTs. In this work, the behavior was similar to the work of Pan et al. (Pan & Bao, 2011). The Fe-in catalyst shows almost 80% of the Fe particles within CNTs, and its counterpart Fe-out present ~93% of Fe particles out of channels. However, differently from Pan et al. (Pan & Bao, 2011) that obtained favored CO conversion and formation of long-chain hydrocarbons with the confined catalyst Fe-in. In the present work, only the CO conversion was favored by the confinement of Fe particles, whereas the formation of C_{5+} hydrocarbons was favored in the Fe-out catalyst (**Table 5** and **S7, Appendix**). Higher activity of Fe-in could be attributed to the confinement inside CNTs, which may prevent iron particles from severe sintering and facilitate the reduction of iron oxide to form iron carbides (Pan & Bao, 2011).

Table 5. Catalytic results for the catalysts. Reaction conditions: T= 350°C, 10 bar, H_2/CO= 1, GHSV= 6.6 L/ g h, $t_{reaction}$= 20 h.

Catalyst	FTY 10^{-4} (molCO /g_{Fe} s)	CO conv (%)	CO_2 selec (%)	Hydrocarbon Selectivity (%)					Ratio CH_2-CH_4=/ CH_2-H_4°	TOF (s^{-1})
				CH_4	Olefins CH_2-CH_4=	Paraffins CH_2-H_4°	Alcohols (CH_3OH. C_2H_5OH)	C_{5+}		
Fe-in	2.37	53.4	44.4	19.5	26.6	15.2	0.3	38.4	1.75	1.05
Fe-in 2nd	-	54.2	45.0	20.0	28.3	14.5	0.8	36.4	1.95	-
Fe-out	1.97	19.0	29.0	19.4	21.3	11.5	0.0	47.8	1.85	1.09
Cu^{1st}Fe^{2nd}	4.05	79.9	49.5	25.7	24.9	18.9	0.4	30.1	1.32	2.47
Fe^{1st}Cu^{2nd}	3.35	50.2	42.8	20.3	24.0	14.4	0.5	40.8	1.67	1.81
Fe+Cu-in	2.47	37.7	38.7	19.9	22.0	13.8	1.8	42.5	1.59	-
Fe+Cu-out	3.16	33.0	37.2	20.3	19.4	15.4	1.9	43.0	1.26	-

On the bimetallic catalysts, the CO conversion strongly depends on the catalyst preparation method. Moderate catalytic activity is observed over the catalyst prepared by co-impregnation over both closed and open CNT. The bimetallic catalysts prepared by sequential impregnation exhibit higher catalytic performance. The $Cu^{1st}Fe^{2nd}$ catalyst prepared using first impregnation with copper followed impregnation with iron showed the higher FT reaction rate. Only relatively small effect of the promotion and catalyst preparation method was observed on the hydrocarbon selectivity.

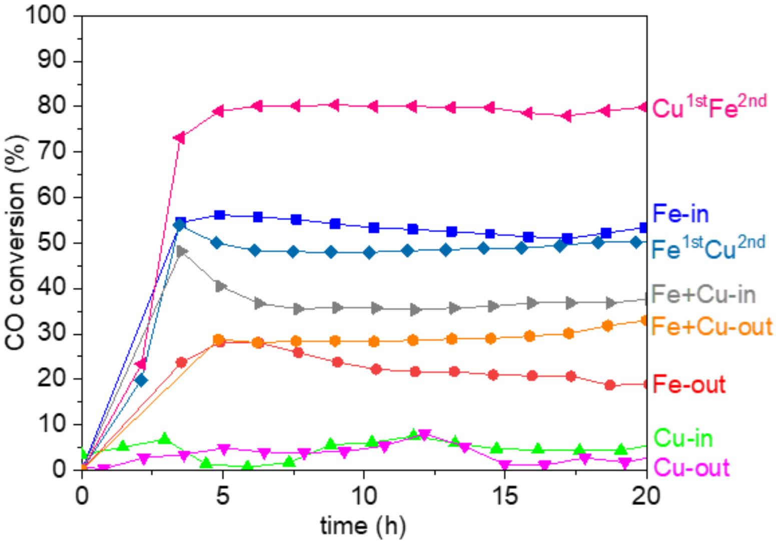

Figure 6. Carbon monoxide conversion over monometallic and bimetallic catalysts as function of reaction time. Reaction conditions: H_2/CO=1, P=10 bar, T=350°C.

Water Gas Shift (WGS) is an important side reaction that occurs during FT synthesis, over iron catalysts. **Table 5** suggests that the WGS-activity was significantly lower for the non-confined than for confined Fe monometallic catalyst. On the other hand, for Fe-in and bimetallic catalysts, the higher selectivity of CO_2 may be due to the higher rate of WGS reaction, and also to higher CO conversion. This behavior repeat itself even at the same CO conversion of 20% (**Table S7, Appendix**).

The chain growth probability was in the range of 0.48 to 0.59. According to the Anderson-Schulz- Flory (ASF) distribution, this value of alpha is related to the maximum selectivity for C_2-C_4 range: ~ 58 %. Higher C_2-C_4 selectivity of ~ 44% was obtained for the $Cu^{1st}Fe^{2nd}$ catalyst. The selectivities to alpha- and internal-C4 olefins are given in **Table S8, Appendix.** The selectivity effects are consistent with previous report by Coville et al (Bahome et al., 2005), who also observed the effect of copper on the catalytic activity and not on the selectivity over iron catalysts supported by CNT.

Characterization of spent catalysts

The XRD profiles of the catalysts after reaction are displayed in **Figure 7**. Both Fe-in used and Fe-out used catalysts present a broad peak around 44° related to iron carbide (X. Chen et al., 2015; Y. Cheng et al., 2016). No XRD peaks attributed to metallic iron were detected.

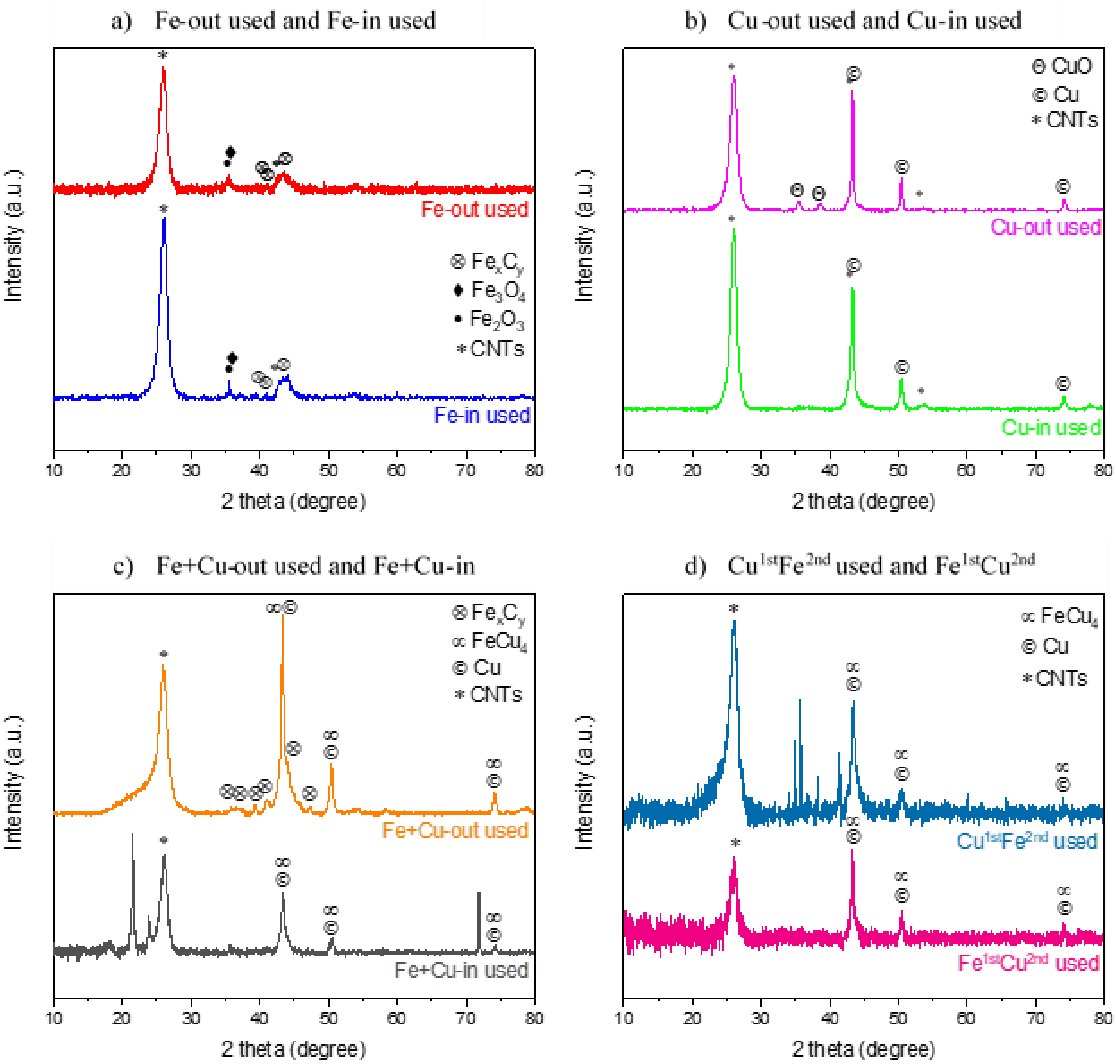
a) Fe-out used and Fe-in used

b) Cu -out used and Cu-in used

c) Fe+Cu-out used and Fe+Cu-in

d) $Cu^{1st}Fe^{2nd}$ used and $Fe^{1st}Cu^{2nd}$

Figure 7. XRD results for the used catalysts.

This broad peak may correspond to the superposition of the most intense diffraction peaks of several iron carbides, very likely Fe_5C_2 (Hägg-carbide) and Fe_3C (cementite) (W. Chen et al., 2008; X. Chen et al., 2015). The formation of iron carbides occurs as result of the interaction of metallic iron with carbon from the dissociation of CO at high temperatures (W. Chen et al., 2008). Both iron carbides have been considered active in FT synthesis. Higher concentration of iron carbide could lead to a much higher FT reaction rate (W. Chen et al., 2008; X. Chen et al., 2015; K. Cheng et al., 2015). Note that iron carbide crystallite sizes determination and even the precise identification of the specific carbide phases from the XRD patterns are not possible because of the overlapping of the peaks and their broad shape (Gu et al., 2018). The Hägg carbide is generally acknowledged as active phase for FT synthesis (Y. Cheng et al., 2016; Galvis, Bitter, Khare, et al., 2012).

The XRD patters of used Cu-in and Cu-out catalysts (**Figure 7**) show metallic Cu and CuO tenorite. Note that the copper oxide was not present in the used Cu-in sample, when the Cu particles were confined in the CNTs. The confinement therefore prevents oxidation of the metal particles. The XRD patterns of used Fe+Cu-in and Fe+Cu-out showed the metallic Cu, alloy $FeCu_4$ and Hägg-carbide-Fe_5C_2 phases. The peaks at 43.3°, 50.4°, and 74.1° in the XRD patterns of used Fe+Cu-in and $Fe^{1st}Cu^{2nd}$, and can be assigned to (1 1 1), (2 0 0), and (2 2 0) reflections of cubic metallic copper (S. He et al., 2019; S. Xiao et al., 2017; L. Yang et al., 2010; Yue et al., 2013).

The crystallinity of Fe/CNT was also evaluated using Raman spectroscopy. **Table S4, Appendix** shows further increase in the **I_D/I_G** ratio after conducting FT synthesis. The higher decrease in CNT disordering and a higher concentration of defects are observed in the $Fe^{1st}Cu^{2nd}$ and $Cu^{1st}Fe^{2nd}$ prepared using the sequential two-step impregnation.

Figure 8 shows the TEM micrographs of the used catalysts and relevant particle size distribution. The TEM images of the Fe-out spent catalyst reveal that some of the iron carbide particles were covered by a carbon layer (K. Cheng et al., 2015; Ismail et al., 2019). This covering layer is due to carbon deposition during reaction, which is favored at low H_2/CO ratios and high temperatures (Y. Cheng et al., 2016). The TEM analysis of the used catalyst after conducting FT reaction also exhibit a large number of defects (**Figure S4, Appendix**). These results are consistent with the Raman data and indicate damage of the CNT structure after the second impregnation. The effect is even more pronounced after exposing the catalysts to FT reaction.

a) Fe-in used

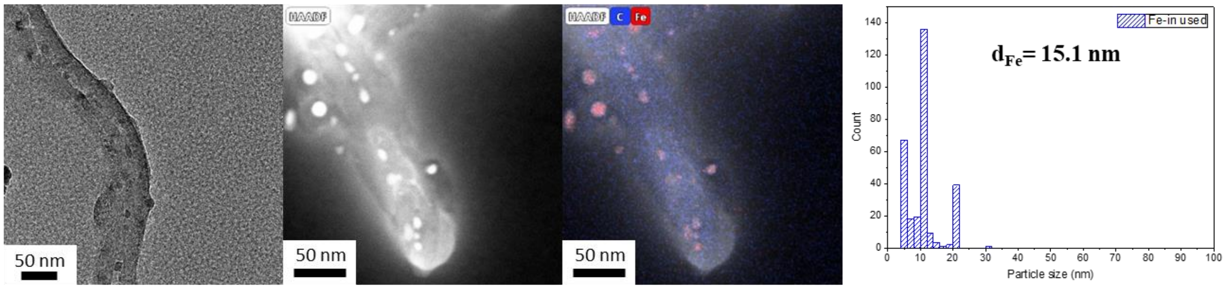

b) Cu-in used

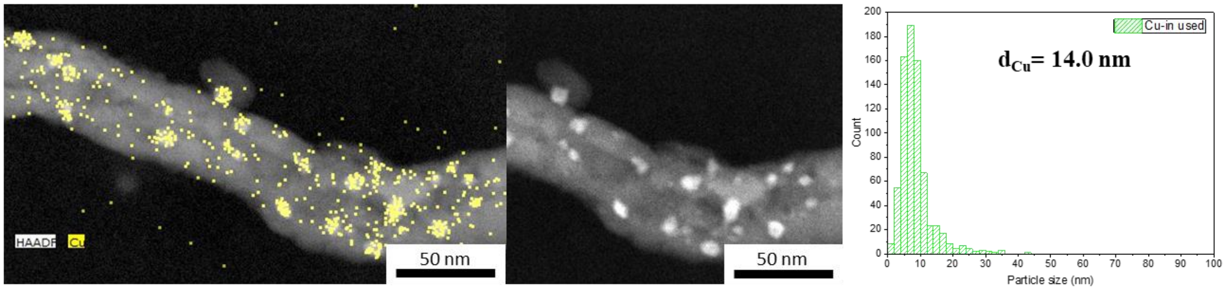

c) Fe-out used

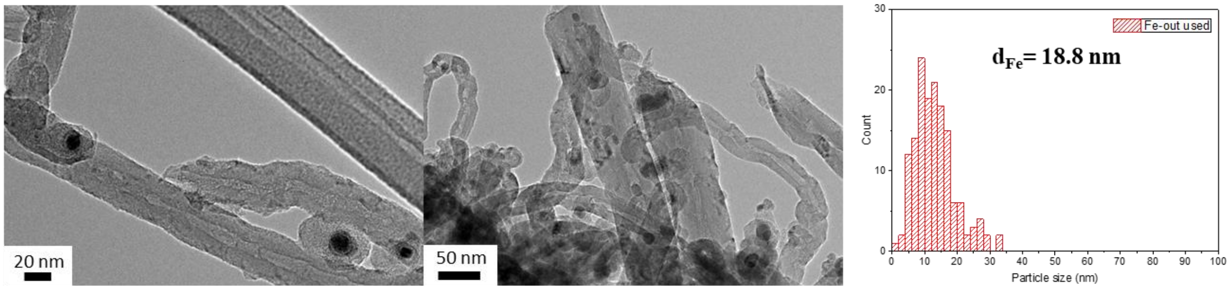

d) $Fe^{1st}Cu^{2nd}$ used

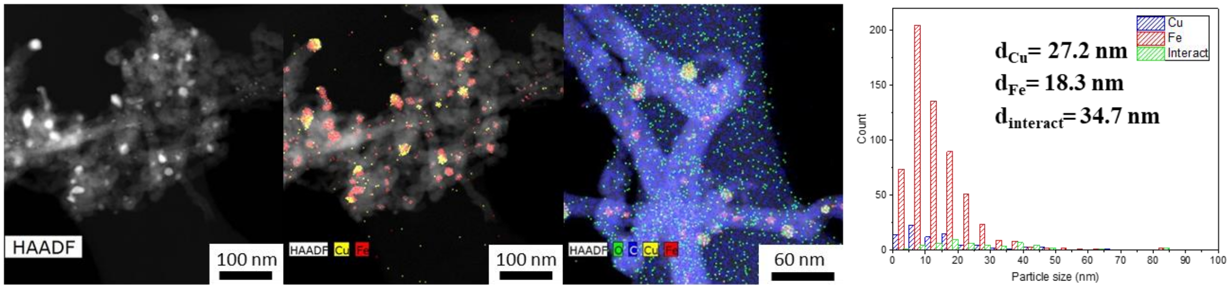

e) $Cu^{1st}Fe^{2nd}$ used

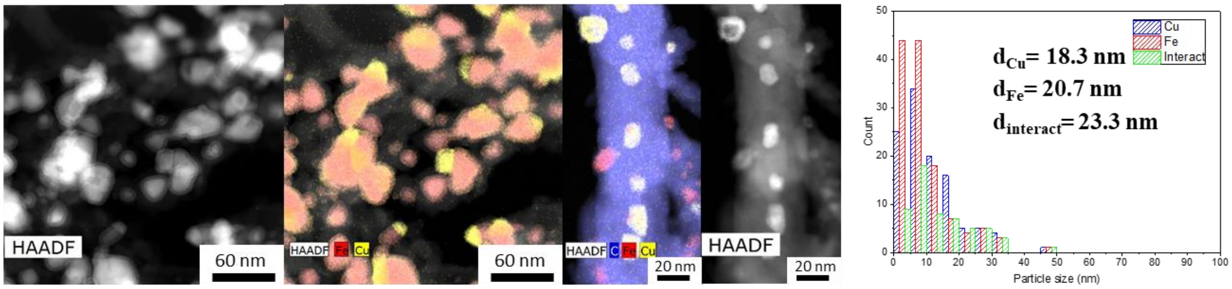

Figure 8. TEM micrographs of the used catalysts.

The TEM images for the Fe-in used catalyst present iron particles with the average size of around 16 nm with a broad particle size distribution. For the Fe-out used catalyst, the particle size distribution is also broad with the average size of 19.0 nm. As could be observed in **Table 2**, for all the catalysts, the particle sizes after reaction were larger than before reaction, except for the Cu particles in Cu^{1st}Fe^{2nd} catalyst.

In the Fe-in catalyst, iron particle size increases from 8.8 nm to 16.1 nm after reaction and seems to be limited by CNT inner diameter. The inner diameters of CNT were evaluated in the range from 8.4 to 9.9 nm using TEM analysis (**Table S3, Appendix**). Note that growth of iron nanoparticle can result in their elongated shape and can also expand to some extent the CNT inner channels. For comparison, the size of the outside particles in Fe-out grew from 13.7 nm to 19.0 nm after the reaction tests (**Table 2**). This indicates that particle sintering was effectively prevented inside CNTs under the reaction conditions due to the spatial restriction of the CNT channels(W. Chen et al., 2008). STEM-EDX analysis shows that the distribution of iron nanoparticles between inner CNT channels and outer surface does not change very much after conducting the catalytic reaction (**Table 3**). In the used bimetallic catalysts, significant modification of the distribution of copper and iron nanoparticles between inner channels and outer surface of CNT and reduction in the number of interacting copper and iron nanoparticles were observed. The fraction of interacting nanoparticles is getting clearly higher in Cu^{1st}Fe^{2nd} sample compared to the Fe^{1st}Cu2nd counterpart.

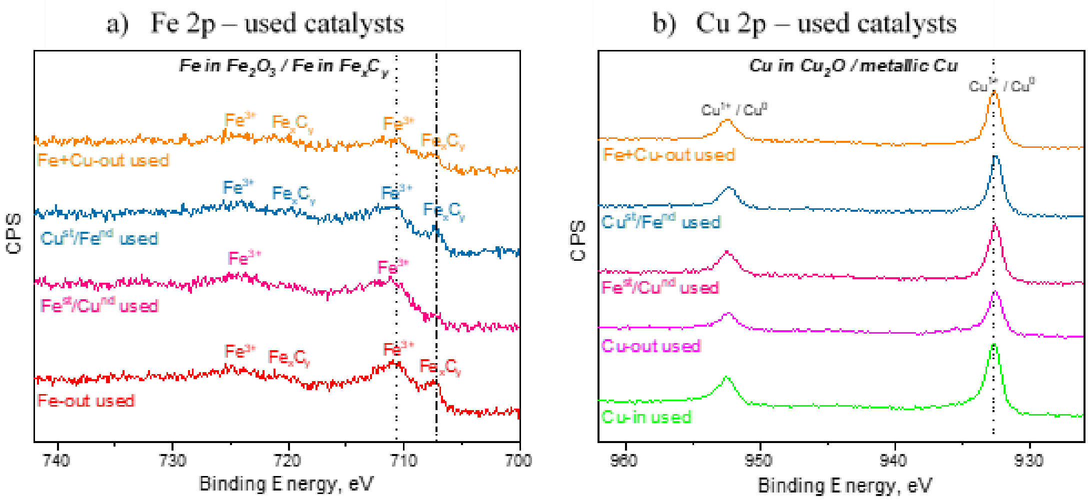

Figure 9. XPS spectra of the used catalysts.

The *ex-situ* XPS spectra of the used catalyst are displayed in **Figure 9**. In addition to hematite, a broad shoulder with the binding energy of 707.3 eV assignable to iron carbide (Butt, 1991; C. Yang et al., 2012) was detected. The Cu Auger spectra and calculation of the Auger parameter (**Figure S7, Appendix**) show the presence of mostly Cu^+ species. This is consistent with the formation of iron carbide during catalyst activation and FT synthesis. Iron carbide in the used catalysts was also observed by XRD. A major decrease in the relative Fe/C and Cu/C atomic concentrations is observed after the catalytic tests (**Table 4**). This is indicative of sintering and increase in the size of both iron and copper nanoparticle under the reaction conditions. The sintering of copper and iron species during FT reaction was also observed by TEM (**Table 2**).

In-situ investigation of the catalyst sub-surface layer by NAP-XPS

Iron carbide and copper metallic nanoparticles are sensitive to the presence of air and can be oxidized after their withdrawal for the reactor. The nanoparticle surface can be even more affected by oxidation. In order to obtain information about the evolution of surface and sub-surface layer in the bimetallic copper-iron catalysts in CO or syngas at different temperatures, we conducted NAP-XPS experiments following the experimental procedure shown in **Figure S8, Appendix**. The freshly calcined samples were first loaded into the NAP-XPS spectrometer and exposed to CO at room temperature. Then, the temperature was increased subsequently from room temperature to 250°C and to 350°C. After the exposure to 350°C in CO, the sample was cooled down to 180°C for 1 h. Then, CO was switched to syngas (H_2/CO=1) and the temperature was increased to 350°C. The sample was maintained in syngas at this temperature and then cooled back again to room temperature. At different steps of the in-situ catalyst treatment under about 1 mbar of CO or syngas, the position, shape and intensity of Fe 2p, Cu 2p and C 1s peaks were thoroughly analyzed by XPS.

The Fe 2p and Cu 2p NAP-XPS spectra of the $Fe^{1st}Cu^{2nd}$, $Cu^{1st}Fe^{2nd}$ and Fe-Cu- in catalysts are presented in **Figures 10, 11** and **S9, Appendix**. Similar to the conventional XPS, the Cu2p XPS spectra of calcined catalysts (**Figures 10a** and **11 a**) suggest the possible presence of CuO and Cu_2O, which were detected by the peak at 934-935 eV(Q. He et al., 2011; Moulder et al., 1992; D. Zhao et al., 2017), spin-orbital splitting and satellites. The Fe 2p NAP-XPS spectra (**Figures 10b** and **11b**) of the calcined catalysts also exhibit the peaks at ~711.0 eV ($Fe2p_{3/2}$) and ~724.6 eV (Fe $2p_{1/2}$) with a shakeup satellite peak at ~719.2 eV. The spectra and binding energies distinctly indicate the presence of Fe^{3+} species(Shroff et al., 1995). This observation is consistent with the results of XRD and conventional XPS and indicates the presence of iron and copper oxides in the fresh samples.

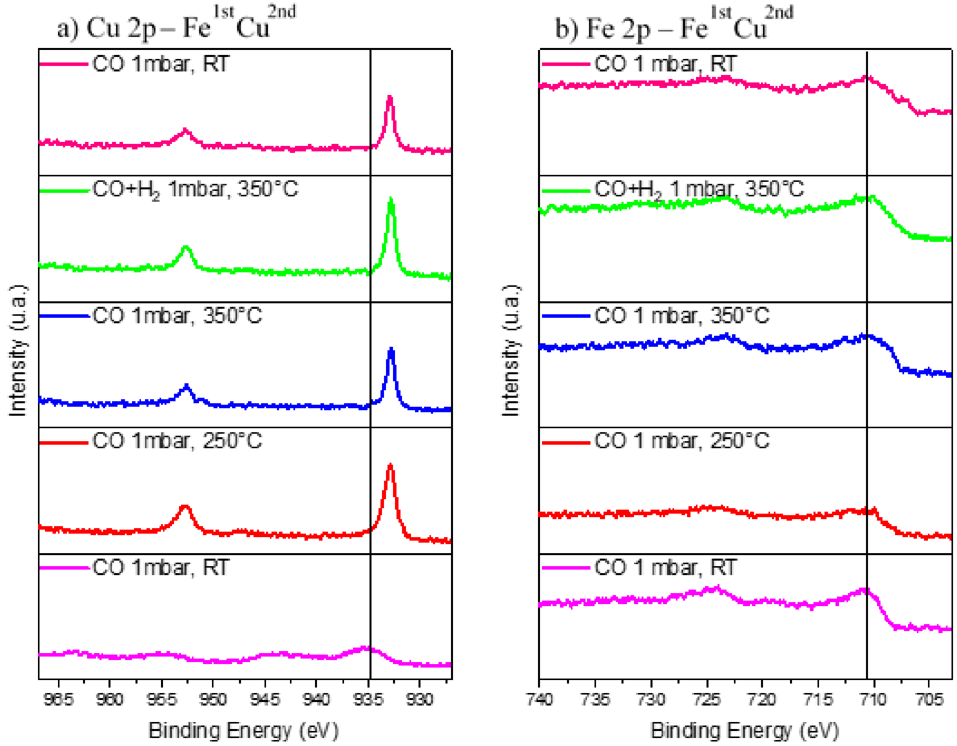

Figure 10. NAP-XPS spectra of the $Fe^{1st}Cu^{2nd}$ catalyst.

After the temperature increase in CO to 250 and then to 350 °C, the Cu 2p peaks (**Figures 10a** and **11a**) shift to lower energy. The low energy shift is indicative of copper reduction. The copper metal phase was identified in the XPS spectra by binding energies (Cu2p3/2=932.9 eV(Biesinger et al., 2010)), spin-orbital splitting and line shape. The exposure of the catalysts to CO also leads to a broad shoulder in the Fe 2p XPS region with the binding energy of 707 eV assignable to iron carbide (Butt, 1991; C. Yang et al., 2012). Further treatment of the catalysts in syngas results in an increase in the intensity of this feature and correspondingly a higher fraction of iron carbide. The NAP-XPS results for both $Fe^{1st}Cu^{2nd}$ and $Cu^{1st}Fe^{2nd}$ suggest the almost complete reduction of copper to the metallic state in CO at 250°C, while only a relatively small amount of iron carbide has been produced even after extended catalyst treatment in CO at 350°C.

The oxidation state of both copper and iron do not change after subsequent cooling down the catalysts to room temperature.

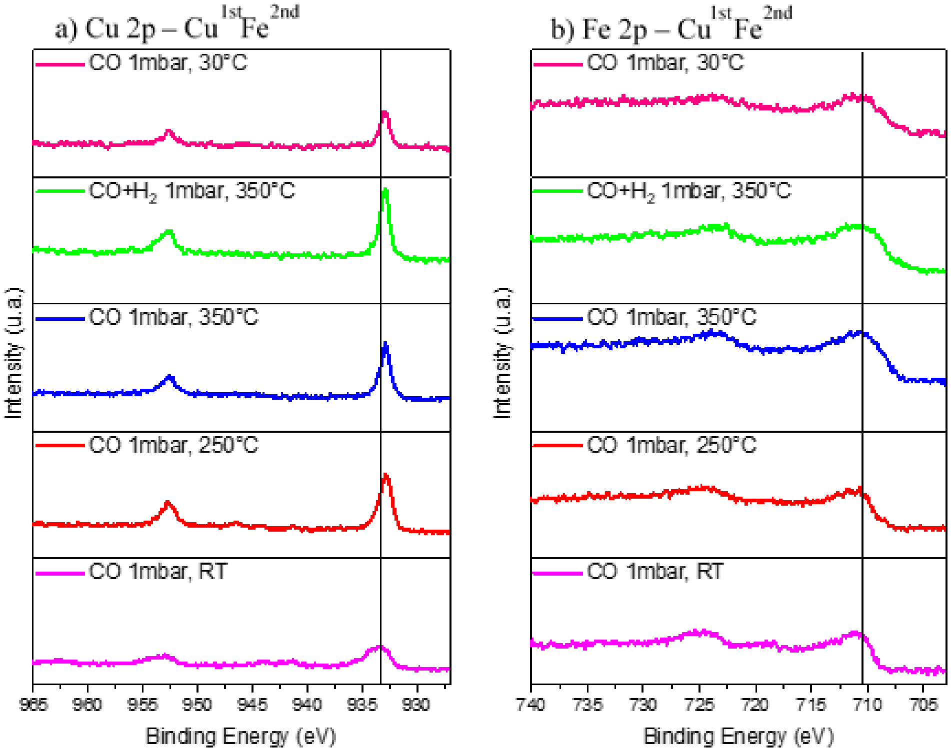

Figure 11. NAP-XPS spectra of the Cu^{1st}Fe^{2nd} catalyst.

Since the catalysts were supported by CNT, we consider that the intensity of C 1s peak does not change during the experiments. The C 1s intensity was used therefore, as a reference in order to evaluate the variation of the relative intensity of Fe 2p XPS peaks during the treatments in CO and syngas at high temperatures. The relative intensities and atomic concentrations (normalized to carbon) measured by NAP-XPS are displayed in **Table 6**. Both Fe/C and Cu/C ratios are higher in Cu^{1st}Fe^{2nd} sample compared to Fe^{1st}Cu^{2nd}. This is consistent with the conventional XPS results (**Table 4**) and also indicates a smaller size of copper and iron nanoparticles in the Cu^{1st}Fe^{2nd} sample measured by TEM (**Table 2**).

The increase in the temperature results in the decrease in both Fe/C and Cu/C atomic ratios for both catalysts. This decrease may correspond to lower concentration of metals in the subsurface layer due to the nanoparticle sintering. The decrease in the surface concentration of copper in CO between 250°C and 350°C is much more pronounced compared to iron (**Table 6** and **Table S6, Appendix**). Interestingly, this temperature range also corresponds to copper reduction.

Table 6. Relative intensities of peaks and atomic concentrations measured in the presence of hydrogen and syngas in the NAP-XPS experiments.

Sample	Gas	Temperature, °C	Fe/C area ratio, %	Cu/C area ratio, %	Fe/C atom ratio, %	Cu/C atom ratio, %
$Fe^{1st}Cu^{2nd}$	CO	RT	2.36	1.61	2.32	1.74
	CO	250	2.36	2.44	2.46	2.46
	CO	350	1.93	0.73	1.83	0.76
	CO+H_2	350	2.20	0.86	2.17	0.87
	CO	40	1.56	0.63	1.61	0.65
$Cu^{1st}Fe^{2nd}$	CO	RT	3.32	1.74	3.39	1.75
	CO	250	3.16	1.88	3.08	1.83
	CO	350	2.63	1.06	2.67	1.11
	CO+H_2	350	3.49	1.80	3.49	1.80
	CO	30	2.52	0.78	2.53	0.77

This suggests that both copper migration and sintering proceed during the reduction. The Cu/C ratio also drops more than three-times in $Fe^{1st}Cu^{2nd}$, while a much smaller decrease was observed for the $Cu^{1st}Fe^{2nd}$ sample. These results are consistent with TEM, which indicates a more significant increase in the copper particle size in $Fe^{1st}Cu^{2nd}$ (**Table 2**) and major migration of copper nanoparticles from inside to outside of CNT (**Table 3**). The copper particle size increases from 11.4 to 27.1 nm in $Fe^{1st}Cu^{2nd}$ and the fraction of copper outside CNT increases from 66.4 to 88.1 %. Exposure of the $Cu^{1st}Fe^{2nd}$ catalyst to syngas at 350°C leads to the increase in the intensity of both Fe and Cu XPS signals, which may correspond to migration and restructuring the metallic and carbide species during the FT reaction.

Cooling down the catalysts after exposure to syngas at 350°C to 30-40°C is accompanied by a decrease in Fe/C and Cu/C ratio (**Table 6**). TEM-EDS shows (**Figure 8**) the presence of a shell of carbon around metal nanoparticles in the spent catalysts. It can be suggested that after the exposure to syngas this carbon shell could reduce the intensity of the XPS signal for both iron and copper.

Mobility, nanoconfinement and interaction of copper and iron nanoparticles in CNT and their influence on the catalytic performance

The catalyst characterization indicates several important phenomena occurring with iron and iron-copper catalysts supported over CNT during the catalyst synthesis, activation and catalytic reaction. First, we must emphasize the major differences between monometallic and bimetallic catalysts. As could be expected, in the iron or copper monometallic catalysts, if CNTs are closed, more than 90% of metal nanoparticles are located on the CNT outer surface. Only small fraction of metal nanoparticles (about 10%) can possibly penetrate the CNT channels, because of the presence of defects. When the CNTs were open by treatment with concentrated nitric acid, introduction of either iron or copper results in the preferential localization of these species inside carbon nanotubes. TEM-EDX shows that about 80% of these metals are confined in the CNTs (**Table 3**). Note that the localization of iron or copper species in the monometallic copper or iron catalysts is relatively stable. Most of these species remain confined inside CNTs even after extensive exposure to syngas under FT reaction conditions. The fraction of iron nanoparticles inside CNT slightly decreases to 72% in the used catalysts, while for copper it drops to 58%.

The situation is very different for the bimetallic iron-copper samples prepared by sequential impregnation. TEM-EDX identified three types of nanoparticles in these samples: (i) monometallic iron nanoparticles, (ii) monometallic copper nanoparticles, (iii) interacting copper-iron nanoparticles, which are situated in close contact with each other. Note that we did not see bimetallic iron-copper nanoparticles in both samples. This is probably due to a very low mutual solubility (Luk et al., 2018) of copper and iron. In the calcined catalysts prepared by sequential impregnation, most iron, copper and interacting nanoparticles are localized outside CNTs. The fraction of the nanoparticles outside CNT is always higher than 50% (**Table 3**). The $Fe^{1st}Cu^{2nd}$ and $Cu^{1st}Fe^{2nd}$ samples are prepared from Fe-in and Cu-in samples by impregnation with respectively copper and iron. This suggests significant migration of the metal species introduced in the first impregnation step, which were initially confined inside CNTs. Note that we did not observe this migration in the monometallic catalysts. Our results suggest that the order of CNT impregnation with copper and iron does not affect to any noticeable extent the distribution of metal species between the channels and outer surface of CNTs.

There can be three driving forces for the mobility of metal nanoparticles from the inner to the outer CNT surface. The first driving force is due to the interaction energy between copper and iron nanoparticles with nanotubes. For CNTs, the contact to the metal can be an end-contact(Banhart, 2009), that involves bonds at the interface, or can be a side-contact, that involves a weakly bonded interface with the outer or inner surface of the tube. Yu(Yu et al., 2012) et al used density functional theory to calculate the interactions of Fe inside and outside CNTs and showed that for several Fe species, the bonding with the outside wall of the CNT could be stronger than that with the inside wall.

Second, the diffusion of metal particles to the outer surface of CNT may facilitate their sintering and thus minimization of surface energy. Indeed, inside CNT the nanoparticle sintering can be limited by the pore diameter. These steric constrains do not exist anymore, when the nanoparticles have moved to the CNT outer surface. Previously, diffusion of metal nanoparticles in porous supports to the outer surface during the exposure to the higher temperature and chemical agents has been observed in a number of publications.

The third driving force of particle diffusion can be the interaction between copper metallic and iron carbide nanoparticles. Because of less significant steric constrains, the strong interaction and proximity of copper and iron nanoparticles could be much easier to reach on the CNT outer surface than inside CNT channels.

The exposure of the catalysts prepared by sequential impregnation to CO and syngas further modifies the distribution of different types of metal nanoparticles (**Table 3**). Interestingly, the fraction of interacting nanoparticles in both $Cu^{1st}Fe2^{nd}$ and $Fe^{1st}Cu^{2nd}$ decreases after conducting FT synthesis. NAP-XPS suggests that noticeable migration of copper proceeds during its reduction to metallic state in CO at 250-350°C, while the migration of iron was less significant (**Table 6**). At the same time, we observed using TEM and Raman spectroscopy a decrease in CNT ordering and appearance of defects after the second impregnation step with copper or iron (**Figure S5, Appendix**). Note that even exposure of the Fe-in catalyst to acidified water (pH=3) without a metal precursor also damages the CNT structure. Exposure of the catalysts to FT reaction conditions further damages the CNT structure. At the same time, the impregnation of Fe-in with water with pH similar to that of the copper nitrate solution does not affect the catalytic performance (**Table 5**). This suggests that the dispersion and localization of iron nanoparticles have not been much affected by the second impregnation with water. This also suggests that the migration of iron and copper is not only due to the presence of the defects in the CNT structure, but is also related to the reduction/oxidation processes in the presence of CO and syngas and interaction between copper and iron.

NAP-XPS is indicative of further migration of iron and copper, which occurs in syngas and generally leads to some increase in their dispersion (**Table 6**). Our results also show that confinement, migration and interaction of copper and iron affect the catalytic performance in FT synthesis. The catalytic activity of monometallic copper catalyst with copper localized either inside (Cu-in) or outside (Cu-out) CNT was very low compared to the iron counterparts. The catalytic performance of the bimetallic iron-copper or monometallic iron catalysts can be therefore attributed to the surface sites associated with iron and not with copper. In agreement with numerous previous reports(Abelló & Montané, 2011), the catalytic activity of iron catalysts in high-temperature FT synthesis has been attributed to the iron carbide phase, which has been detected in the spent catalyst by XRD (**Figure 7**). At the same time, copper can be considered as a promoter, which enhances the activity of the iron active phase.

The iron time yield (FTY) and turnover frequency (TOF) are presented in **Table 5**. The calculated TOF values provided important information about the intrinsic activity of surface sites in the monometallic iron and bimetallic iron-copper catalysts. First, we observed that the intrinsic activity of iron sites (TOF) is not much affected by nanoconfinement. Indeed, TOFs calculated for Fe-in and Fe-out are almost the same (**Table 5**). The effect of nanoconfinement is therefore mostly relevant to the enhancement of iron dispersion inside CNT. The size of iron nanoparticles encapsulated inside CNT is smaller in Fe-in than Fe-out sample with nanoparticles located on the outer surface. Moreover, they remain much smaller in Fe-in after the catalytic test (**Table 2**). This result is consistent with the recent report by Gu(Gu, He, et al., 2019).

Second, the promotion with copper results in a noticeable increase in TOF from 1.05-1.09 s^{-1} in the monometallic iron catalysts to 1.81-2.47 s^{-1} in the bimetallic samples. Note that the higher TOF is observed in the $Cu^{1st}Fe^{2nd}$ catalyst. Characterization of this catalyst using STEM-EDX (**Table 3**) suggests the presence of a higher fraction of interacting iron copper nanoparticles than in $Fe^{1st}Cu^{2nd}$ (23.7% in $Cu^{1st}Fe^{2nd}$ versus 7.8% $Fe^{1st}Cu^{2nd}$). The catalytic performance in FT synthesis is an interplay of several phenomena occurring in monometallic iron and bimetallic copper-iron catalysts. First, the FT reaction rate depends on iron particle size and the number of active sites. Smaller iron nanoparticle size is generally obtained when iron species are localized inside CNT. The second parameter is the extent of iron carbidisation, which is also a function of iron particle size and promoter. Finally, the interaction between iron carbide and copper nanoparticles results in the increase of instinct activity of active sites. **Table 5** shows that the FT reaction rate (FTY) slightly increases when copper and iron are added together inside CNT compared to the monometallic Fe-in sample from 2.37 to 2.47x10^{-4} mol CO g_{Fe}^{-1} s^{-1}. This is consistent with previous reports, which emphasize the importance of copper and iron interaction(Chonco et al., 2013; S. He et al., 2019) for the enhanced catalytic performance of iron-copper bimetallic catalysts.

Thus, copper seems to be both as a structuring and an electronic promoter. On the one hand, copper improves iron reducibility and carbidisation compared to the monometallic iron catalysts. The facilitated iron reduction can be related to the hydrogen spillover effect on Cu, meanwhile producing a large number of active sites and then, increasing the CO conversion(Peña et al., 2018). On the other hand, a close localization of copper to iron results in a higher intrinsic activity of iron surface sites (TOF). The addition of Cu in iron based catalyst can increase the selectivity to CO_2 due to the positive effect of copper on the WGS reaction. (Al-Dossary et al., 2015) The geometry of Fe and Cu particles in interaction can play a crucial role in catalytic performance. Lu et al.(Y. Lu et al., 2017) performed a DFT calculation on a Cu^0-χ-Fe_5C_2 surface model to elucidate the synergistic interactions of Cu^0-χ-Fe_5C_2 catalysts for selective CO hydrogenation to higher alcohols. The authors showed that the atomic arrangement of the active sites can play a significant effect on the binding strength of the adsorbates. Their calculation results showed that only CO prefers the adsorption at the interface of Cu^0-χ-Fe_5C_2, CH_x (x=1-3) and H species prefer the adsorption at the top of Fe sites on Cu^0-χ-Fe_5C_2 surface. The CH_x (x=1-3) dissociation, hydrogenation and coupling to C_2-hydrocarbons occur preferentially at the Fe sites on Cu^0-χ-Fe_5C_2.

The amount of iron sites with enhanced activity situated in close proximity to copper nanoparticles depends on the catalyst preparation method and evolves during catalyst activation and reaction. Surprisingly, both copper and iron species remain extremely mobile in bimetallic catalysts, while in the monometallic catalysts, copper and iron nanoparticles seems to be relatively immobile within CNT during catalyst preparation, activation and reaction.

Conclusion

Remarkable mobility of both iron and copper species was observed in the bimetallic iron-copper catalysts. This mobility seems to be enhanced by the emergence of numerous defects in CNT caused by the second impregnation with acid solutions and results in the enhanced iron-copper interaction. The catalytic performance of bimetallic iron-copper catalysts is affected by the localization of iron species within CNT and their interaction with copper localized in the proximity. The number of these iron active sites interacting with copper is not much affected by the initial localization of these two species deposited over CNT during the impregnation but by the migration of iron and copper during the catalyst calcination, activation and catalytic reaction.

In the monometallic iron catalysts, the nanoconfinement results in localization and relative stability of iron nanoparticles inside CNT. The catalytic performance of monometallic iron catalysts is principally a function of iron dispersion, while the intrinsic activity of iron sites is not much influenced by the nanoconfinement inside CNT.

References

Abbaslou, R. M. M., Soltan, J., & Dalai, A. K. (2010). Effects of nanotubes pore size on the catalytic performances of iron catalysts supported on carbon nanotubes for Fischer-Tropsch synthesis. *Applied Catalysis A: General*, *379*(1–2), 129–134. https://doi.org/10.1016/j.apcata.2010.03.006

Abelló, S., & Montané, D. (2011). Exploring iron-based multifunctional catalysts for fischer-tropsch synthesis: A review. *ChemSusChem*, *4*(11), 1538–1556. https://doi.org/10.1002/cssc.201100189

Al-Dossary, M., Fierro, J. L. G., & Spivey, J. J. (2015). Cu-promoted Fe2O3/MgO-based Fischer-Tropsch catalysts of biomass-derived syngas. *Industrial and Engineering Chemistry Research*, *54*(3), 911–921. https://doi.org/10.1021/ie504473a

Arrigo, R., Teresi, R., Gambarotti, C., Parisi, F., Lazzara, G., & Dintcheva, N. T. (2018). Sonication-induced modification of carbon nanotubes: Effect on the rheological and thermo-oxidative behaviour of polymer-based nanocomposites. *Materials*, *11*(3), 1–14. https://doi.org/10.3390/ma11030383

Bahome, M. C., Jewell, L. L., Hildebrandt, D., Glasser, D., & Coville, N. J. (2005). Fischer-Tropsch synthesis over iron catalysts supported on carbon nanotubes. *Applied Catalysis A: General*, *287*(1), 60–67. https://doi.org/10.1016/j.apcata.2005.03.029

Banhart, F. (2009). Interactions between metals and carbon nanotubes: At the interface between old and new materials. *Nanoscale*, *1*(2), 201–213. https://doi.org/10.1039/b9nr00127a

Batakliev, T., Petrova-Doycheva, I., Angelov, V., Georgiev, V., Ivanov, E., Kotsilkova, R., Casa, M., Cirillo, C., Adami, R., Sarno, M., & Ciambelli, P. (2019). Effects of Graphene Nanoplatelets and Multiwall Carbon Nanotubes on the Structure and Mechanical Properties of Poly(lactic acid) Composites: A Comparative Study. *Applied Sciences*, *9*(3), 469. https://doi.org/10.3390/app9030469

Biesinger, M. C. (2017). Advanced analysis of copper X-ray photoelectron spectra. *Surface and Interface Analysis*, *49*(13), 1325–1334. https://doi.org/10.1002/sia.6239

Biesinger, M. C., Lau, L. W. M., Gerson, A. R., & Smart, R. S. C. (2010). Resolving surface chemical states in XPS analysis of first row transition metals, oxides and hydroxides: Sc, Ti, V, Cu and Zn. *Applied Surface Science*, *257*(3), 887–898. https://doi.org/10.1016/j.apsusc.2010.07.086

Butt, J. B. (1991). Carbide phases on iron-based Fischer-Tropsch synthesis catalysts part I: Characterization studies. *Catalysis Letters*, *7*(1–4), 61–81. https://doi.org/10.1007/BF00764492

Chen, W., Fan, Z., Pan, X., & Bao, X. (2008). Effect of confinement in carbon nanotubes on the activity of Fischer-Tropsch iron catalyst. *Journal of the American Chemical Society*, *130*(29), 9414–9419. https://doi.org/10.1021/ja8008192

Chen, W., Pan, X., & Bao, X. (2007). Tuning of redox properties of iron and iron oxides via encapsulation within carbon nanotubes. *Journal of the American Chemical Society*, *129*(23), 7421–7426. https://doi.org/10.1021/ja0713072

Chen, X., Deng, D., Pan, X., & Bao, X. (2015). Iron catalyst encapsulated in carbon nanotubes for CO hydrogenation to light olefins. *Chinese Journal of Catalysis*, *36*(9), 1631–1637. https://doi.org/10.1016/S1872-2067(15)60882-8

Chen, Z., Guan, Z., Li, M., Yang, Q., & Li, C. (2011). Enhancement of the performance of a platinum nanocatalyst confined within carbon nanotubes for asymmetric hydrogenation. *Angewandte Chemie - International Edition*, *50*(21), 4913–4917. https://doi.org/10.1002/anie.201006870

Cheng, K., Ordomsky, V. V., Legras, B., Virginie, M., Paul, S., Wang, Y., & Khodakov, A. Y. (2015). Sodium-promoted iron catalysts prepared on different supports for high temperature Fischer-Tropsch synthesis. *Applied Catalysis A: General*, *502*, 204–214. https://doi.org/10.1016/j.apcata.2015.06.010

Cheng, Q., Tian, Y., Lyu, S., Zhao, N., Ma, K., Ding, T., Jiang, Z., Wang, L., Zhang, J., Zheng, L., Gao, F., Dong, L., Tsubaki, N., & Li, X. (2018). Confined small-sized cobalt catalysts stimulate carbon-chain growth reversely by modifying ASF law of Fischer–Tropsch synthesis. *Nature Communications*, *9*(1), 3250. https://doi.org/10.1038/s41467-018-05755-8

Cheng, Y., Lin, J., Xu, K., Wang, H., Yao, X., Pei, Y., Yan, S., Qiao, M., & Zong, B. (2016). Fischer-Tropsch Synthesis to Lower Olefins over Potassium-Promoted Reduced Graphene Oxide Supported Iron Catalysts. *ACS Catalysis*, *6*(1), 389–399. https://doi.org/10.1021/acscatal.5b02024

Chinthakuntla, A., Venkateswara Rao, K., Ashok, C., Rao, Kv., & Shilpa Chakra, C. (2014). Structural Analysis of CuO Nanomaterials prepared by Novel Microwave Assisted Method. *J. Atoms and Molecules*, *4*(5), 803–806. www.jamonline.in

Chonco, Z. H., Lodya, L., Claeys, M., & Van Steen, E. (2013). Copper ferrites: A model for investigating the role of copper in the dynamic iron-based Fischer-Tropsch catalyst. *Journal of Catalysis*, *308*, 363–373. https://doi.org/10.1016/j.jcat.2013.08.012

COSTA, S., BOROWIAK-PALEN, E., KRUSZYŃSKA, M., BACHMATIUK, A., & KALEŃCZUK, R. J. (2008). Characterization of carbon nanotubes by Raman spectroscopy. *Materials Science-Poland*, *26*(2), 433–441. https://doi.org/10.1016/j.carbon.2011.01.059

Feng, L., Zhang, C., Gao, G., & Cui, D. (2012). Facile synthesis of hollow Cu2O octahedral and spherical nanocrystals and their morphology-dependent photocatalytic properties. *Nanoscale Research Letters*, *7*(1), 1. https://doi.org/10.1186/1556-276X-7-276

Galvis, H. M. T., Bitter, J. H., Khare, C. B., Ruitenbeek, M., Dugulan, A. I., & Jong, K. P. de. (2012). Supported Iron Nanoparticles as Catalysts for Sustainable Production of Lower Olefins. *Science*, *335*(6070), 835–838. https://doi.org/10.1126/science.1215614

GANESAN, P. (1978). Particle size distribution function of supported metal catalysts by X-ray diffraction. *Journal of Catalysis*, *52*(2), 310–320. https://doi.org/10.1016/0021-9517(78)90145-8

Gu, B., He, S., Peron, D. V., Strossi Pedrolo, D. R., Moldovan, S., Ribeiro, M. C., Lobato, B., Chernavskii, P. A., Ordomsky, V. V., & Khodakov, A. Y. (2019). Synergy of nanoconfinement and promotion in the design of efficient supported iron catalysts for direct olefin synthesis from syngas. *Journal of Catalysis*, *376*, 1–16. https://doi.org/10.1016/j.jcat.2019.06.035

Gu, B., Ordomsky, V. V., Bahri, M., Ersen, O., Chernavskii, P. A., Filimonov, D., & Khodakov, A. Y. (2018). Effects of the promotion with bismuth and lead on direct synthesis of light olefins from syngas over carbon nanotube supported iron catalysts. *Applied Catalysis B: Environmental*, *234*, 153–166. https://doi.org/10.1016/j.apcatb.2018.04.025

He, Q., Yang, X., Ren, X., Koel, B. E., Ramaswamy, N., Mukerjee, S., & Kostecki, R. (2011). A novel CuFe-based catalyst for the oxygen reduction reaction in alkaline media. *Journal of Power Sources*, *196*(18), 7404–7410. https://doi.org/10.1016/j.jpowsour.2011.04.016

He, S., Wang, W., Shen, Z., Li, G., Kang, J., Liu, Z., Wang, G.-C., Zhang, Q., & Wang, Y. (2019). Carbon nanotube-supported bimetallic Cu-Fe catalysts for syngas conversion to higher alcohols. *Molecular Catalysis*, *479*(September), 110610. https://doi.org/10.1016/j.mcat.2019.110610

Heise, H. M., Kuckuk, R., Ojha, A. K., Srivastava, A., Srivastava, V., & Asthana, B. P. (2009). Characterisation of carbonaceous materials using Raman spectroscopy: A comparison of carbon nanotube filters, single- And multi-walled nanotubes, graphitised porous carbon and graphite. *Journal of Raman Spectroscopy*, *40*(3), 344–353. https://doi.org/10.1002/jrs.2120

Ismail, A. S. M., Casavola, M., Liu, B., Gloter, A., Van Deelen, T. W., Versluijs, M., Meeldijk, J. D., Stéphan, O., De Jong, K. P., & De Groot, F. M. F. (2019). Atomic-Scale Investigation of the Structural and Electronic Properties of Cobalt-Iron Bimetallic Fischer-Tropsch Catalysts. *ACS Catalysis*, *9*(9), 7998–8011. https://doi.org/10.1021/acscatal.8b04334

Jian, L., Xiuling, J., Dairong, C., & Wei, L. (2009). Solvothermal synthesis and characterization of Fe3O4 and γ-Fe2O3 nanoplates. *Journal of Physical Chemistry C*, *113*(10), 4012–4017.

https://doi.org/10.1021/jp810583e

Kuznetsov, V. L., Bokova-Sirosh, S. N., Moseenkov, S. I., Ishchenko, A. V., Krasnikov, D. V., Kazakova, M. A., Romanenko, A. I., Tkachev, E. N., & Obraztsova, E. D. (2014). Raman spectra for characterization of defective CVD multi-walled carbon nanotubes. *Physica Status Solidi (B) Basic Research*, *251*(12), 2444–2450. https://doi.org/10.1002/pssb.201451195

Liu, Y., Chen, J. F., & Zhang, Y. (2015). Effects of pretreatment on iron-based catalysts for forming light olefins via Fischer–Tropsch synthesis. *Reaction Kinetics, Mechanisms and Catalysis*, *114*(2), 433–449. https://doi.org/10.1007/s11144-014-0821-0

Lu, J., Yang, L., Xu, B., Wu, Q., Zhang, D., Yuan, S., Zhai, Y., Wang, X., Fan, Y., & Hu, Z. (2014). Promotion effects of nitrogen doping into carbon nanotubes on supported iron fischer-tropsch catalysts for lower olefins. *ACS Catalysis*, *4*(2), 613–621. https://doi.org/10.1021/cs400931z

Lu, Y., Zhang, R., Cao, B., Ge, B., Tao, F. F., Shan, J., Nguyen, L., Bao, Z., Wu, T., Pote, J. W., Wang, B., & Yu, F. (2017). Elucidating the Copper-Hägg Iron Carbide Synergistic Interactions for Selective CO Hydrogenation to Higher Alcohols. *ACS Catalysis*, *7*(8), 5500–5512. https://doi.org/10.1021/acscatal.7b01469

Luk, H. T., Mondelli, C., Mitchell, S., Siol, S., Stewart, J. A., Curulla Ferré, D., & Pérez-Ramírez, J. (2018). Role of Carbonaceous Supports and Potassium Promoter on Higher Alcohols Synthesis over Copper-Iron Catalysts. *ACS Catalysis*, *8*(10), 9604–9618. https://doi.org/10.1021/acscatal.8b02714

Morales, J., Espinos, J. P., Caballero, A., Gonzalez-Elipe, A. R., & Mejias, J. A. (2005). XPS study of interface and ligand effects in supported Cu2O and CuO nanometric particles. *Journal of Physical Chemistry B*, *109*(16), 7758–7765. https://doi.org/10.1021/jp0453055

Moulder, J. F., Stickle, W. F., E.'Sobol, P., & Bomben, K. D. (1992). *Handbook of X-ray Photoelectron Spectroscopy: A Reference Book of Standard Spectra for Identification and Interpretation of XPS Data* (J. Chastain (ed.)). Physical Electronics Division, Perkin-Elmer Corporation.

Ordomsky, V. V., Legras, B., Cheng, K., Paul, S., & Khodakov, A. Y. (2015). The role of carbon atoms of supported iron carbides in Fischer-Tropsch synthesis. *Catalysis Science and Technology*, *5*(3), 1433–1437. https://doi.org/10.1039/c4cy01631a

Pan, X., & Bao, X. (2011). The effects of confinement inside carbon nanotubes on catalysis. *Accounts of Chemical Research*, *44*(8), 553–562. https://doi.org/10.1021/ar100160t

Peña, D., Jensen, L., Cognigni, A., Myrstad, R., Neumayer, T., van Beek, W., & Rønning, M. (2018). The Effect of Copper Loading on Iron Carbide Formation and Surface Species in

Iron-Based Fischer–Tropsch Synthesis Catalysts. *ChemCatChem*, *10*(6), 1300–1312. https://doi.org/10.1002/cctc.201701673

Ramaraj, H., Madiga, J., Elangovan, H., Haridoss, P., & Sharma, C. P. (2017). Homogenization for Dispersion and Reduction in Length of Carbon Nanotubes. *Transactions of the Indian Institute of Metals*, *70*(10), 2629–2639. https://doi.org/10.1007/s12666-017-1123-9

Rennhofer, H., & Zanghellini, B. (2021). Dispersion state and damage of carbon nanotubes and carbon nanofibers by ultrasonic dispersion: A review. *Nanomaterials*, *11*(6). https://doi.org/10.3390/nano11061469

Serp, P., Corrias, M., & Kalck, P. (2003). Carbon nanotubes and nanofibers in catalysis. *Applied Catalysis A: General*, *253*(2), 337–358. https://doi.org/10.1016/S0926-860X(03)00549-0

Sesis, A., Hodnett, M., Memoli, G., Wain, A. J., Jurewicz, I., Dalton, A. B., Carey, J. D., & Hinds, G. (2013). Influence of Acoustic Cavitation on the Controlled Ultrasonic Dispersion of Carbon Nanotubes. *Journal of Physical Chemistry B, 117*, 15141–15150. https://doi.org/10.1021/jp410041y

Shi, D., Yang, Q., Peterson, C., Lamic-Humblot, A. F., Girardon, J. S., Griboval-Constant, A., Stievano, L., Sougrati, M. T., Briois, V., Bagot, P. A. J., Wojcieszak, R., Paul, S., & Marceau, E. (2019). Bimetallic Fe-Ni/SiO2 catalysts for furfural hydrogenation: Identification of the interplay between Fe and Ni during deposition-precipitation and thermal treatments. *Catalysis Today*, *334*(July 2018), 162–172. https://doi.org/10.1016/j.cattod.2018.11.041

Shroff, M. D., Kalakkad, D. S., Coulter, K. E., Kohler, S. D., Harrington, M. S., Jackson, N. B., Sault, A. G., & Datye, A. K. (1995). Activation of Precipitated Iron Fischer-Tropsch Synthesis Catalysts. *Journal of Catalysis*, *156*(2), 185–207. https://doi.org/10.1006/jcat.1995.1247

Suresh, S., Karthikeyan, S., & Jayamoorthy, K. (2016). FTIR and multivariate analysis to study the effect of bulk and nano copper oxide on peanut plant leaves. *Journal of Science: Advanced Materials and Devices*, *1*(3), 343–350. https://doi.org/10.1016/j.jsamd.2016.08.004

Wang, C., Pan, X., & Bao, X. (2010). Direct production of light olefins from syngas over a carbon nanotube confined iron catalyst. *Chinese Science Bulletin*, *55*(12), 1117–1119. https://doi.org/10.1007/s11434-010-0076-8

Xiao, J., Pan, X., Guo, S., Ren, P., & Bao, X. (2015). Toward fundamentals of confined catalysis in carbon nanotubes. *Journal of the American Chemical Society*, *137*(1), 477–482. https://doi.org/10.1021/ja511498s

Xiao, S., Zhang, Y., Gao, P., Zhong, L., Li, X., Zhang, Z., Wang, H., Wei, W., & Sun, Y. (2017). Highly efficient Cu-based catalysts via hydrotalcite-like precursors for CO2 hydrogenation to methanol. *Catalysis Today*, *281*, 327–336. https://doi.org/10.1016/j.cattod.2016.02.004

Xu, R., Tan, Z., Fan, G., Ji, G., Xiong, D. B., Guo, Q., Su, Y., Li, Z., & Zhang, D. (2018). High-strength CNT/Al-Zn-Mg-Cu composites with improved ductility achieved by flake powder metallurgy via elemental alloying. *Composites Part A: Applied Science and Manufacturing*, *111*(May), 1–11. https://doi.org/10.1016/j.compositesa.2018.05.012

Yang, C., Zhao, H., Hou, Y., & Ma, D. (2012). Fe 5 C 2 Nanoparticles: A Facile Bromide-Induced Synthesis and as an Active Phase for Fischer–Tropsch Synthesis. *Journal of the American Chemical Society*, *134*(38), 15814–15821. https://doi.org/10.1021/ja305048p

Yang, L., He, J., Zhang, Q., & Wang, Y. (2010). Copper-catalyzed propylene epoxidation by oxygen: Significant promoting effect of vanadium on unsupported copper catalyst. *Journal of Catalysis*, *276*(1), 76–84. https://doi.org/10.1016/j.jcat.2010.09.002

Yang, Z., Guo, S., Pan, X., Wang, J., & Bao, X. (2011). FeN nanoparticles confined in carbon nanotubes for CO hydrogenation. *Energy and Environmental Science*, *4*(11), 4500–4503. https://doi.org/10.1039/c1ee01428e

Yu, L., Li, W. X., Pan, X., & Bao, X. (2012). In- and out-dependent interactions of iron with carbon nanotubes. *Journal of Physical Chemistry C*, *116*(31), 16461–16466. https://doi.org/10.1021/jp302311r

Yue, H., Zhao, Y., Zhao, S., Wang, B., Ma, X., & Gong, J. (2013). A copper-phyllosilicate core-sheath nanoreactor for carbon-oxygen hydrogenolysis reactions. *Nature Communications*, *4*, 1–7. https://doi.org/10.1038/ncomms3339

Zhao, D., Tu, C. M., Hu, X. J., & Zhang, N. (2017). Notable in situ surface transformation of Cu2O nanomaterials leads to dramatic activity enhancement for CO oxidation. *RSC Advances*, *7*(60), 37596–37603. https://doi.org/10.1039/c7ra05950g

Appendix

Table S1. Assignment of XRD peaks in the calcined catalysts.

Sample	Compound	Reference	Peak positions (2Θ)
Fe-in	Fe_2O_3 Hematite	PDF 24-0072	33,1-35,6-41-49,5-54,2-62-64
	Fe_3O_4 Magnetite	PDF 11-0614	30-35,5-37-43-53,5-57-62,5
	C Graphite	PDF 01-0646	26-42,9
Fe-out	Fe_2O_3 Hematite	PDF 24-0072	33,1-35,6-41-49,5-54,2-62-64
	Fe_3O_4 Magnetite	PDF 11-0614	30-35,5-37-43-53,5-57-62,5
	C Graphite	PDF 01-0646	26-42,9
Cu-in	CuO Tenorite, syn	PDF 05-0661	32,7-35,5-38,75-48,8-53,4-58,3-61,8-66,2-68-75
	Cu_2O Cuprite, syn	PDF 05-0667	29,5-36,2-42,45-52,5-61,3-69,5-73,5-77,2
	C Graphite	PDF 01-0646	26-42,9
Cu-out	CuO Tenorite, syn	PDF 05-0661	32,7-35,5-38,75-48,8-53,4-58,3-61,8-66,2-68-75
	C Graphite	PDF 01-0646	26-42,9
$Fe^{1st}Cu^{2nd}$	Fe_2O_3 Hematite	PDF 24-0072	24,1-33,2-35,7-54-75,4
	CuO Tenorite, syn	PDF 05-0661	32,7-35,5-38,75-46,5-53,4-58,3-61,8-66,2-68-75
	Cu_2O Cuprite, syn	PDF 05-0667	36,2-42,45-61,3
	C Graphite	PDF 01-0646	26-42,9
$Cu^{1st}Fe^{2nd}$	Fe_2O_3 Hematite	PDF 01-1053	24,1-33,2-35,7-40,9-49,5-54-62,5-64-71,9-75,4
	CuO Tenorite, syn	PDF 05-0661	32,7-35,5-38,75-46,5-53,4-58,3-61,8-66,2-68-75
	Cu_2O Cuprite, syn	PDF 05-0667	36,2-42,45-61,3-73,5
	C Graphite	PDF 01-0646	26-42,9
Fe+Cu-in	CuO Tenorite, syn	PDF 05-0661	32,7-35,5-38,75-46,5-53,4-58,3-61,8-66,2-68-75
	$CuFeO_2$ Delafossite	PDF 39-0246	31,3-35,6-36,2-40,4-43,4-47,7-55,4-60,9-64,7-70,1
	C Graphite	PDF 01-0646	26-42,9
Fe+Cu-out	CuO Tenorite, syn	PDF 05-0661	32,7-35,5-38,75-46,5-53,4-58,3-61,8-66,2-68-75
	$CuFeO_2$ Delafossite	PDF 39-0246	31,3-35,6-36,2-40,4-43,4-47,7-55,4-60,9-64,7-70,1
	C Graphite	PDF 01-0646	26-42,9

Table S2. Scherrer crystallites size of the catalysts before and after reaction.

Before reaction				After reaction			
Sample	Compound	Peak position (2Θ)	crystallites size (nm)	Sample	Compound	Peak position (2Θ)	crystallites size (nm)
Fe-in	Fe_2O_3 Hem	33.1	27	Fe-in used	Fe_5C_2 Hägg	44	5
	Fe_3O_4 Mag	35.5	20				
Fe-out	Fe_2O_3 Hem	33.1	30	Fe-out used	Fe_5C_2 Hägg	44	5
	Fe_3O_4 Mag	35.5	21		Fe_2O_3	35.6	15
Cu-in	CuO	35.5	14	Cu-in used	Cu	43.3	22
	Cu_2O Cup	36.2	5				
Cu-out	CuO Ten	35.5	26	Cu-out used	CuO Ten	35.5	15
					Cu	43.3	34
Fe^{1st}Cu^{2nd}	Fe_2O_3 Hem	33.1	25	Fe^{1st}Cu^{2nd} used	Cu/ $FeCu_4$	43.3	24
	CuO Ten	38.8	23				
	Cu_2O Cup	36.2	27				
Cu^{1st}Fe^{2nd}	Fe_2O_3 Hem	33.1	18	Cu^{1st}Fe^{2nd} used	Cu/ $FeCu_4$	43.3	16
	CuO Ten	33.8	23				
	Cu_2O Cup	36.2	23				
Fe+Cu-in	CuO Ten/ $CuFe_2O_2$ Dela	35.6	10	Fe+Cu-in used	Cu/ $FeCu_4$	43.3	18
Fe+Cu-out	CuO Ten/ $CuFe_2O_2$ Dela	35.6	21	Fe+Cu-out used	Cu/ $FeCu_4$	43.3	24
					Fe_5C_2 Hägg	39.5	26
Fe-in 2nd	Fe_2O_3 Hem	33.1	26	Fe-in 2nd used	Fe_5C_2 Hägg	44	6

Table S3. Inner and outer diameters for both CNTs after acid treatment

Sample	SD (nm)	Sample	SD (nm)
ID-CNTs-in	9.4	OD-CNTs-in	32.8
ID-CNTs-out	8.9	OD-CNTs-out	34.2

Table S4. I_D/I_G ratios in the calcined and used catalysts.

Sample	**I_D/I_G**	**Sample**	**I_D/I_G**
CNTs	1.33		
CNTs-in	2.26		
CNTs-out	1.67		
Cu-in	2.36	Cu-in used	3.02
Cu-out	1.91	Cu-out used	2.55
Fe-in	2.40	Fe-in used	3.07
Fe-in 2nd	2.58		
Fe-out	2.02	Fe-out used	2.88
Fe^{1st}Cu^{2nd}	2.56	Fe^{1st}Cu^{2nd} used	3.61
Cu^{1st}Fe^{2nd}	2.56	Cu^{1st}Fe^{2nd} used	3.25
Fe+Cu-in	2.46	Fe+Cu-in used	2.98
Fe+Cu-out	2.14	Fe+Cu-out used	2.59

Table S5. Copper and iron binding energies in the calcined catalysts.

Samples	Cu-in	Cu-out	Fe-in	Fe-out	Fe^{1st}Cund	Cu^{1st}Fend	Fe+Cu-in	Fe+Cu-out
				Binding energy (eV)				
Cu2p$_{3/2}$	33.8	933.8	-	-	933.9	933.2	932.8	932.7
sat	42.4	942.6	-	-	942.5	942.4	942.3	941.4
Cu2p$_{1/2}$	53.9	954.0	-	-	953.6	953.5	952.7	952.8
sat	62.6	962.6	-	-	962.3	962.6	962.8	962.3
Fe2p$_{3/2}$		-	710.8	711.1	711.0	711.0	711.1	711.1
sat		-	718.3	718.5	718.5	718.8	719.4	719.1
Fe2p$_{1/2}$		-	724.6	724.6	724.5	724.7	724.4	724.5
sat		-	731.9	732.1	732.4	731.5	731.6	732.0

Table S6. Relative intensities of peaks and atomic concentrations measured in the presence of hydrogen and syngas in the NAP-XPS experiments with Fe+Cu-in sample.

Gas	Temperature, °C	Fe/C, %	Cu/C, %	Fe/C atom ratio, %	Cu/C atom ratio, %
CO	RT	1.50	1.13	1.43	1.21
CO	250	1.22	1.29	1.29	1.29
CO	350	1.33	0.73	1.28	0.75
CO+H_2	350	1.42	0.80	1.49	0.85
CO	40	1.38	0.56	1.38	0.53
UHV	RT	1.13	0.69	1.27	0.64

Table S.7 Selectivity results for the catalysts. Reaction conditions: T= 350°C, 10 bar, H_2/CO= 1, GHSV= 6.6 L/ g h (COconv fixed at 20% due to the lowest value for Fe-out catalyst).

Catalyst	CO Conv (%)	CO_2 selec (%)	Hydrocarbon Selectivity (%)					Ratio CH_2-CH_4=/ CH_2-H_4°
			CH_4	Olefins CH_2-CH_4=	Paraffins CH_2-H_4°	Alcohols (CH_3OH. C_2H_5OH)	C_{5+}	
Fe-in	20.0	30.6	15.1	21.5	12.2	0.1	51.1	1.8
Fe-in 2nd		32.2	16.0	23.8	12.2	0.3	47.7	1.3
Fe-out		26.5	16.9	18.8	10.1	0.3	53.9	1.9
Cu^{1st}Fe^{2nd}		37.4	17.4	17.7	13.5	0.1	51.3	1.3
Fe^{1st}Cu^{2nd}		35.9	16.0	21.3	10.7	0.4	51.7	2.0
Fe+Cu-in		35.0	17.3	19.1	13.9	1.0	48.7	1.4
Fe+Cu-out		33.4	18.8	18.0	14.8	1.4	47.0	1.2

Table S.8 Selectivities for a-olefins and olefins (Reaction conditions: T= 350°C, 10 bar, H_2/CO= 1, GHSV= 6.6 L/ g h, $t_{reaction}$=20 h).

Catalyst	C_4 α-olefins (%)	C_4 olefins (%)	Ratio α-olefins/olefins
Fe-in	2.27	2.56	0.89
Fe-in 2^{nd}	2.63	2.54	1.03
Fe-out	2.76	2.30	1.20
$Cu^{1st}Fe^{2nd}$	2.00	2.16	0.93
$Fe^{1st}Cu^{2nd}$	2.66	2.13	1.25
Fe+Cu-in	2.95	1.87	1.58
Fe+Cu-out	2.55	1.90	1.35

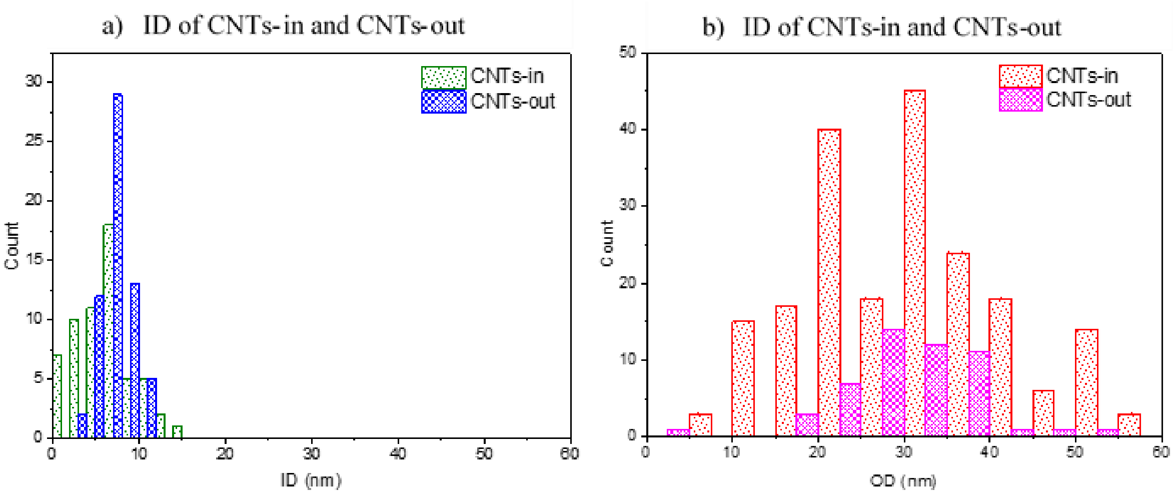

Fig. S1. Inner and outer diameter size distribution for the CNTs supports.

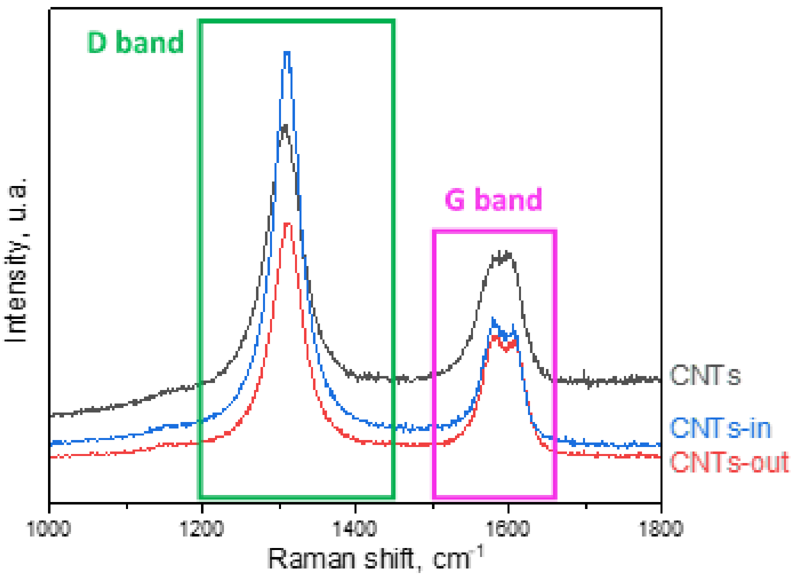

Figure S2. Raman spectra of commercial CNT, CNT after mild and severe treatments with nitric acid.

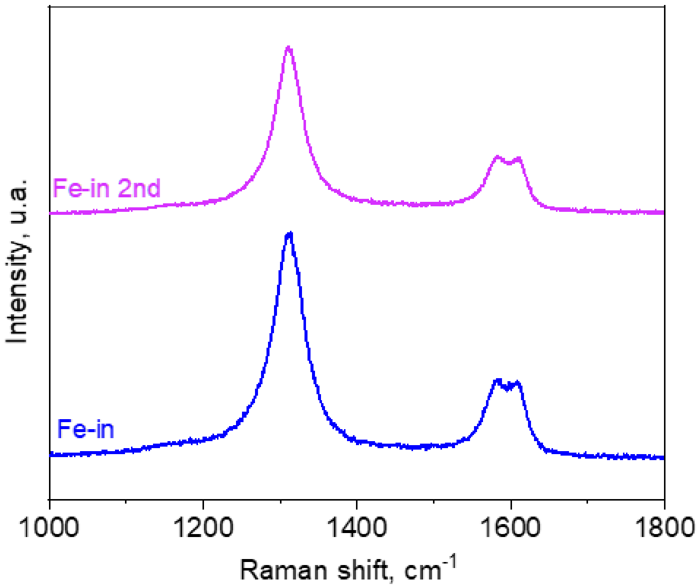

Figure S3. Raman spectra of Fe-in catalyst and Fe-in catalyst additionally impregnated with deionized water (Fe-in 2nd).

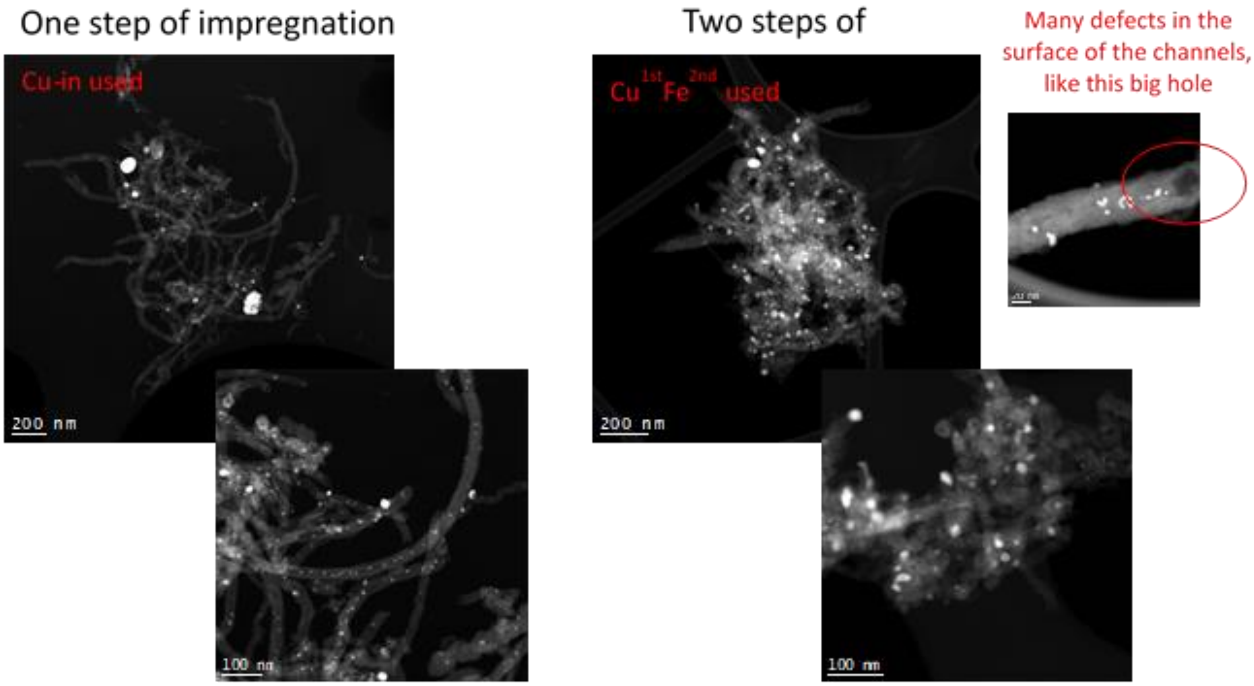

Figure S4. Comparison between Cu-in and Cu^{1st}Fe^{2nd} after reaction.

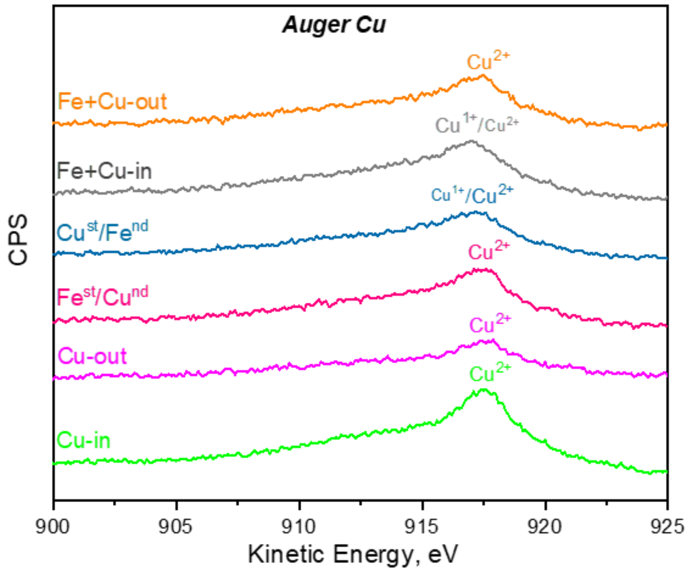

Figure S5. Auger spectra for the calcined catalysts.

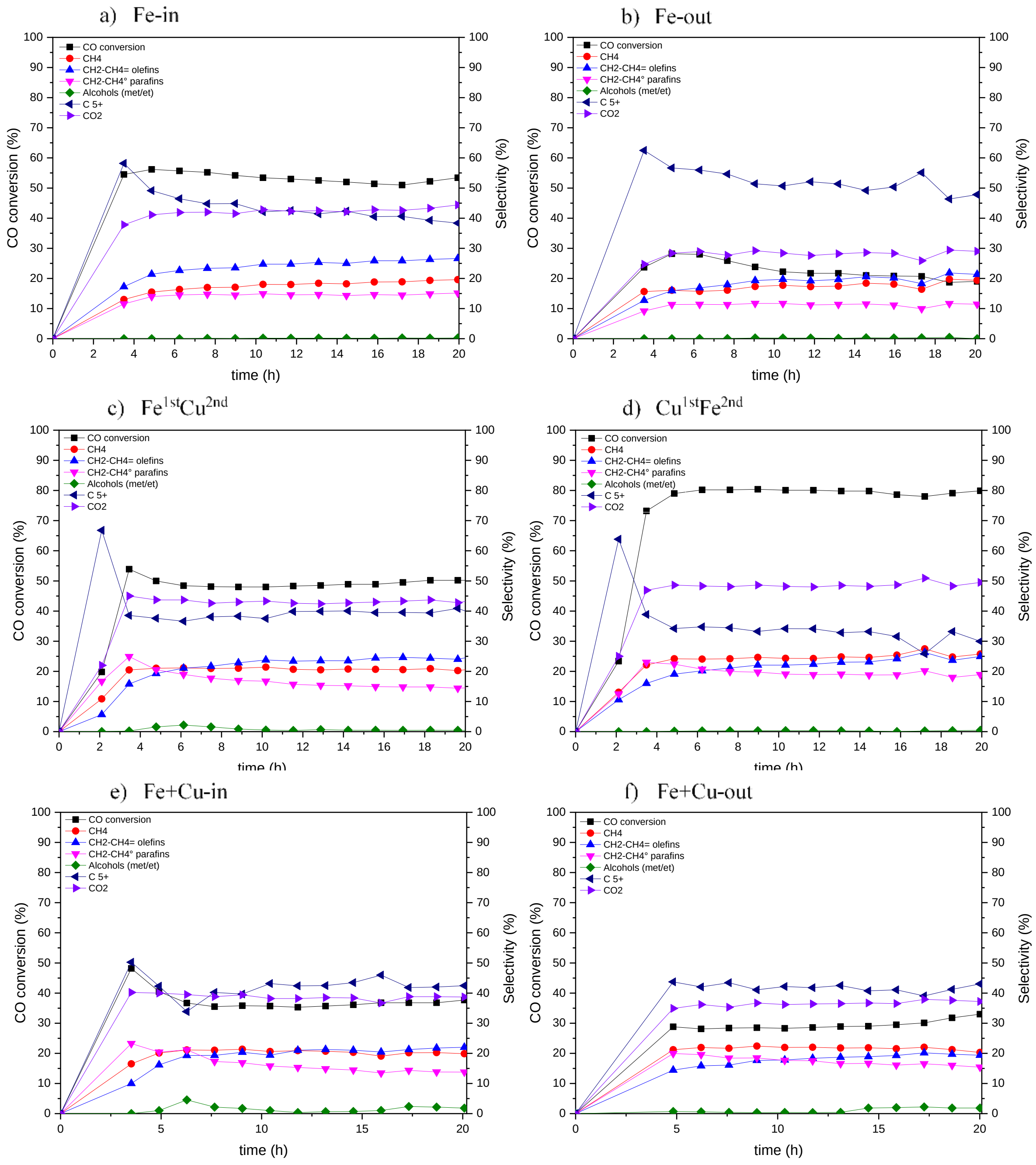

Fig. S6. Evolution of carbon monoxide conversion and selectivity to the reaction products as a function of time on-stream (Reaction conditions: H_2/CO = 1, P = 10 bar, T = 350 °C).

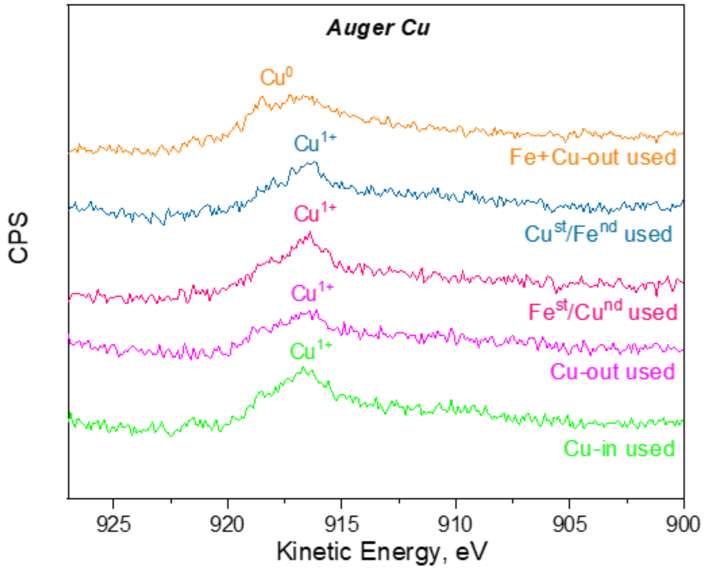

Figure S7. Auger spectra for the used catalysts.

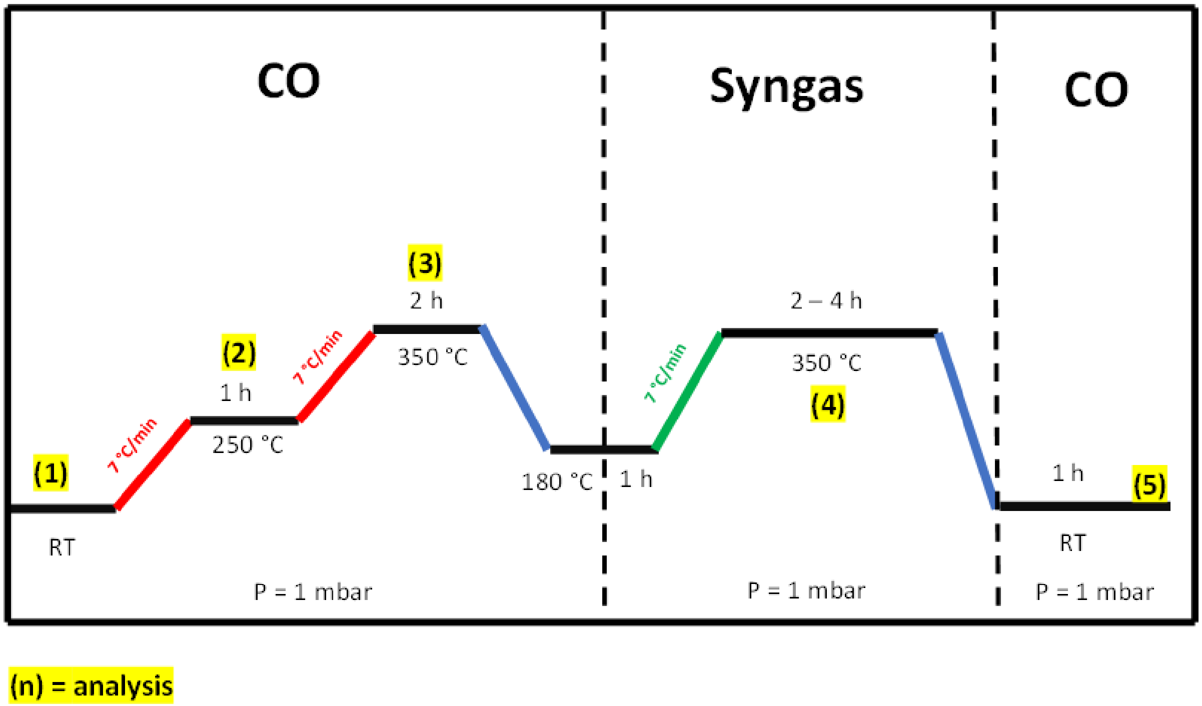

Figure S8. Experimental procedure used for NAP-XPS experiments.

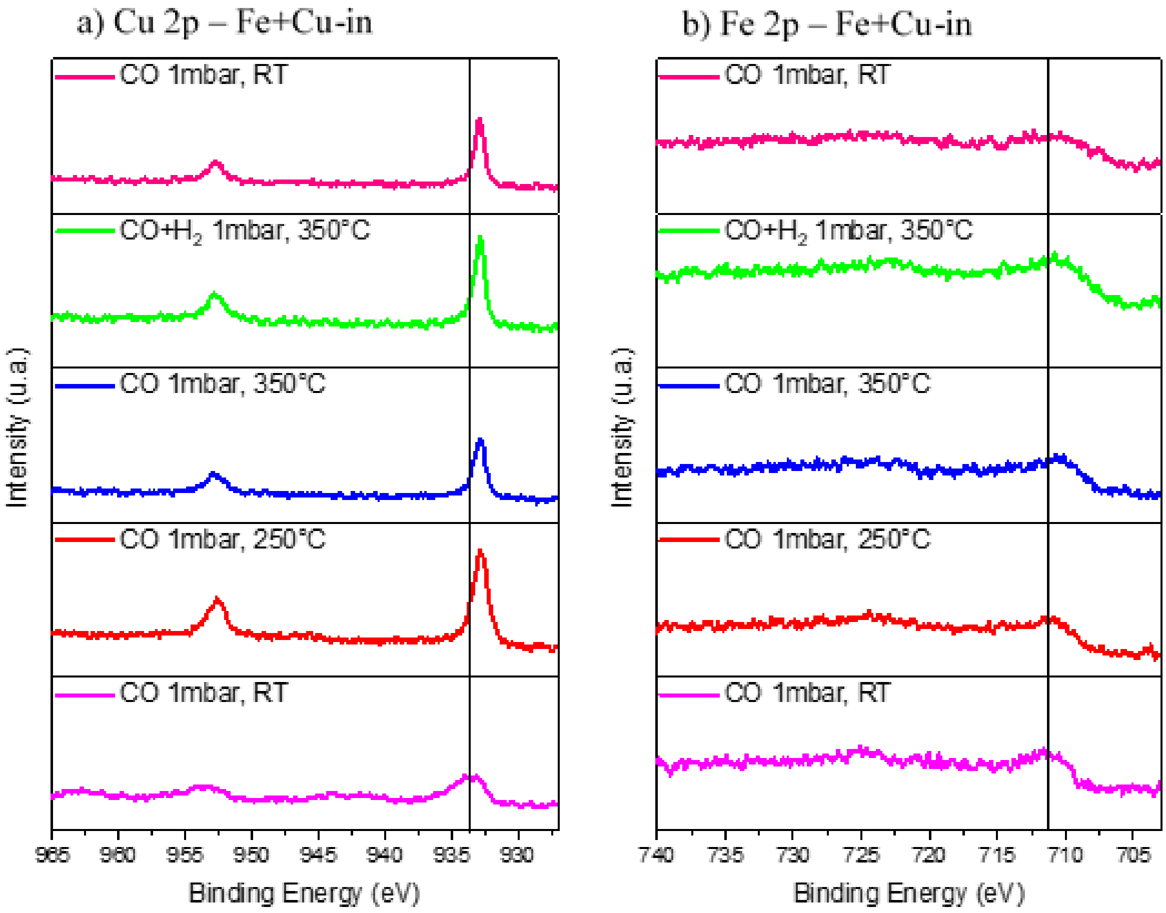

Figure S9. NAP-XPS spectra of the Fe+Cu-in catalyst.

Covalent Organic Frameworks for Mediation of ruthenium Dispersion for Low-Temperature CO2 hydrogenation to Formic acid

Introduction

Covalent organic frameworks (COFs) (Côté, Benin, Ockwig, O'Keeffe, Matzger, & Yaghi, 2005; Fang et al., 2014a; Geng et al., 2020) are dense porous polymers with definite 2D and 3D crystalline structures composed of light elements (B, N, C and O) linked via covalent bonds that exhibit many interesting characteristics, such as high surface area, porosity in a small mesopore range, presence of several functional groups and versatile chemistry. They have triggered significant research perspectives towards energy applications attributed to their unique physiochemical properties.

The current growing attention to global climate changes, growing energy demands and dwindling oil reserves have spurred major research efforts in academia and industry focused on the CO_2 capture and utilization technologies (Q. Lu & Jiao, 2016; Matsubu et al., 2015; Ou et al., 2018; Richard & Fan, 2017; W. Zhang et al., 2023). Using CO_2 as a cost-effective, non-toxic and renewable carbon source is not only an incentive to reduce greenhouse gas emissions, but also an exciting challenge to develop new concepts and new strategies in the chemical and fuel industries (Al-Salem et al., 2009; Centi & Perathoner, 2004; Chernyak et al., 2022; Navarro-Jaén et al., 2021; Y. Zhou et al., 2023). Formic acid produced from CO_2 hydrogenation is an important biodegradable sustainable feedstock. Anhydrous formic acid possesses energy density comparable to that of liquefied hydrogen, making it suitable for both hydrogen storage and generation.

In the present work, we propose a strategy to mediate ruthenium dispersion in COF of different structure and composition in order to prepare efficient catalysts for low temperature CO_2 hydrogenation to formic acid **(Figure 1)**. The catalysts were characterized using a combination of techniques including *operando* X-ray absorption spectroscopy. The density of nitrogen functional groups in the COF matrix was found to be a key factor affecting the performance of Ru/COF catalysts. The catalyst's performance was linked to ruthenium's capability to remain as single atoms and resist reduction to the metallic phase.

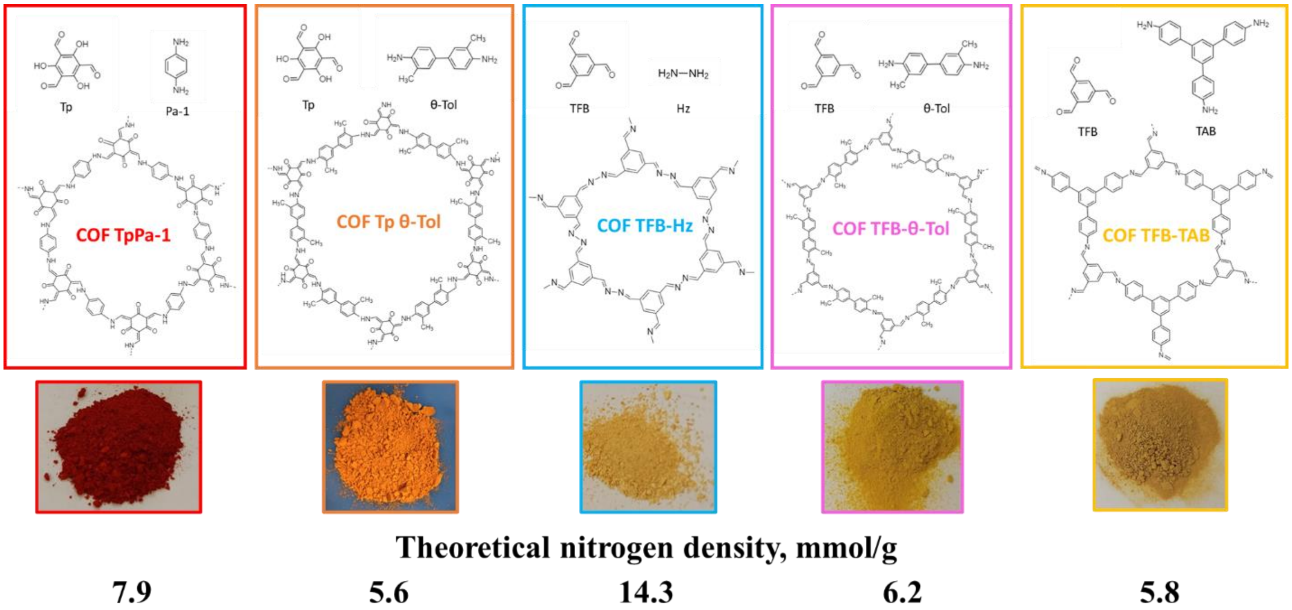

Figure 1. COFs synthesized in this work.

Results and Discussion

Ex-situ catalyst characterization

The synthesis procedures and detailed characterization of COF materials used in this work as catalytic supports are given in **SI**. The elemental composition of prepared Ru/COF samples measured by XRF analysis is shown in **Table S1, SI**. In addition to ruthenium, the catalysts contain carbon and nitrogen, which were already present in the parent COF materials. The higher concentration of nitrogen was detected in the Ru10% COF TFB Hz. The N/Ru molar ratios were calculated from the amounts of nitrogen and ruthenium measured by XRF (experimental N/Ru ratio in the fresh samples) and from the theoretic concentration of nitrogen calculated from the COF chemical formula and Ru experimental concentration (theoretic N/Ru ratio). Note that these theoretic and experimental N/Ru ratios are very close to each other and follow the same trend (**Table 1**). Interestingly, the experimental N/Ru values are somewhat lower than the theoretic ones. This can be attributed to the partial amorphization of the samples during their preparation, also observed by XRD.

Table 1. Elemental composition of Ru/COF catalysts measured by XRF.

Sample Identifier	Mass percent (%)				N/Ru molar ratio	
	Ru	Cl	C	N	Theor	Exp.
Ru 10% COF Tp Pa-1	9.5	28.3	48.5	8.2	8.4	6.2
Ru 10% COF Tp o-Tol	8.4	25.7	55.1	5.0	6.8	4.3
Ru 10% COF TFB Hz	4.8	28.2	45.1	15.6	30.1	23.5
Ru 10% COF TFB o-Tol	4.6	14.8	68.0	7.5	13.7	11.8
Ru 10% COF TFB TAB	3.4	16.6	68.5	7.0	17.4	14.9

The crystalline structure of COF is distinctly affected by introduction of ruthenium. Broadening of the XRD peaks was observed after impregnating COF with $RuCl_3$ (**Figure 2**). The $RuCl_3$ deposition can possibly block the pores and may result in less-effective π-π stacking interactions between adjacent layers. This may result in a lateral shift of the COF 2D sheets and reduce the crystallinity of COF (Singh et al., 2018).

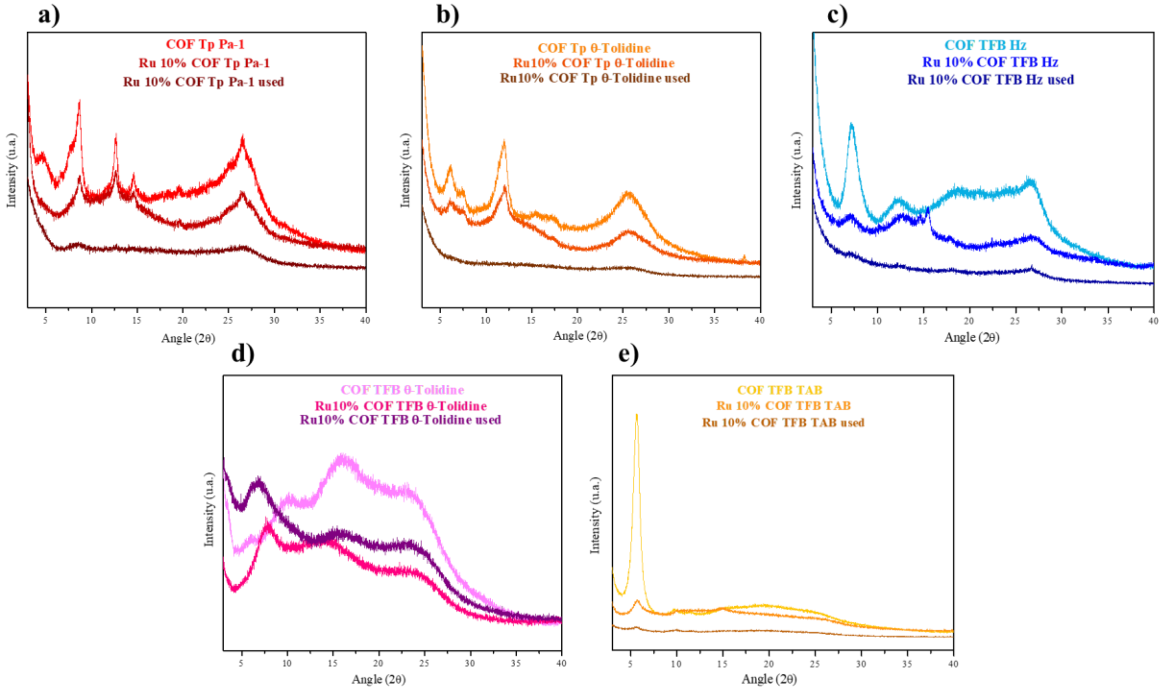

Figure 2. XRD patterns of COF and Ru/COF catalysts.

In addition to the crystallinity, the COF morphology undergoes a noticeable change after impregnation with ruthenium and during the CO_2 hydrogenation. The introduction of Ru and conducting CO_2 hydrogenation appear to alter the arrangement of the framework structures, causing misalignment and shifting of the 2D sheets. Additionally, the introduced metal species may create defects. This suggestion is consistent with nitrogen adsorption measurements. The BET surface areas of COF have been significantly modified by the impregnation with ruthenium chloride (**Figure 3 and Table 2**). Interestingly, the presence of $RuCl_3$ results either in an increase or in a decrease in the COF surface area. The observed increase in the Tp o-Tol and TFB Hz COF surface area after the $RuCl_3$ impregnation (**Table 2**) could be explained by modification of their film-like morphology and creation of interlayer voids after the impregnation.

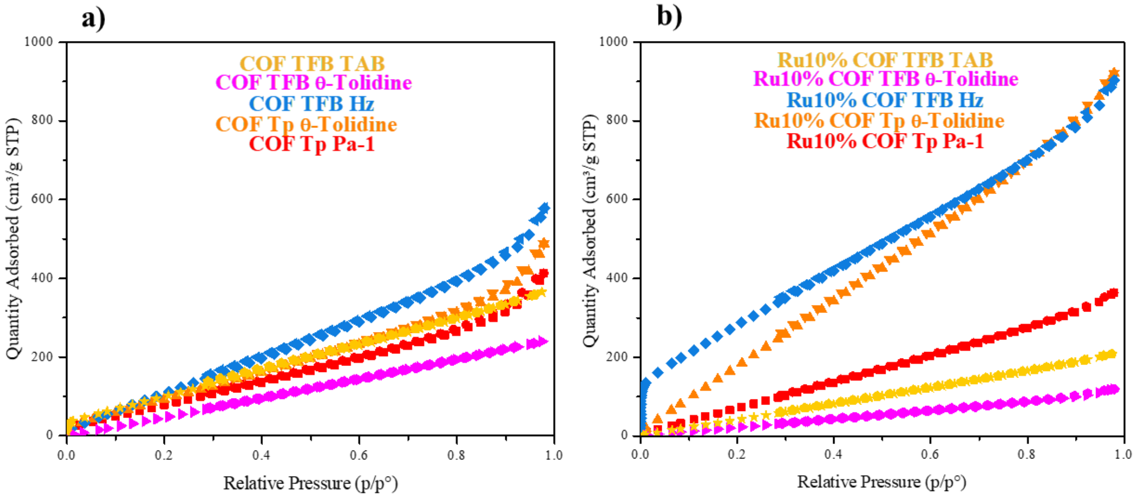

Figure 3. Nitrogen adsorption isotherms over COF (a) and Ru/COF catalysts (b).

The Ru/COF catalysts were characterized by TGA, ^{13}C NMR and ATR-FTIR (**Figures 4, 5 and 6**). In comparison with original COF, all characteristic peaks were preserved in fresh and spent Ru/COF. After the $RuCl_3$ impregnation, the FTIR bands at around 3210 and 3415 cm^{-1}, related to the free (N-H) and (hydrogen-bonded N-H) (Shengping Wang et al., 2019; Z. Z. Yang et al., 2015) groups lose their intensity, which could indicate their interaction with the introduced ruthenium species (Shengping Wang et al., 2019). The interaction between Ru and N-H groups seems to increase in the samples after the reaction. Note that a new FTIR band around 1940 cm^{-1} appears that could be assigned to the Ru-H stretching vibrations. This suggests that the Cl anions in the Ru coordination environment (from $RuCl_3$) have been replaced by hydride and N-H ligands (Gunasekar et al., 2019).

Table 2. Surface area and porosity of COF materials and Ru/COF catalysts.

Sample	COF TpPa-1	COF Tp o-Tol	COF TFB Hz	COF TFB o-Tol	COF TFB-TAB
S_{BET}^{a} (m^{2} g^{-1})	626	483	643	411	476
Pore Volume^{b} (cm^{3} g^{-1})	0.86	0.75	0.94	0.39	0.52
Pore size$_{BET}^{c}$ (nm)	5.0	5.8	5.1	3.5	4.6
Pore size$_{BJH}^{d}$ (nm)	5.9	6.7	6.3	5.2	5.3
Sample	Ru 10 COF TpPa-1	Ru 10 COF Tp-θ-Tol	Ru 10 COF TFB-Hz	Ru 10 COF TFB-θ-Tol	Ru 10 COF TFB-TAB
S_{BET}^{a} (m^{2} g^{-1})	495	1274	1172	165	319
Pore Volume^{b} (cm^{3} g^{-1})	0.6	1.5	1.22	0.19	0.34
Pore size$_{BET}^{c}$ (nm)	4.3	4.3	4.45	4.3	3.9
Pore size$_{BJH}^{d}$ (nm)	5.6	5.6	5.8	5.8	5.3

[a] BET Surface Area
[b] BJH Desorption cumulative volume of pores (between 1.7 nm and 300 nm width)
[c] Desorption average pore diameter (4V/A by BET)
[d] BJH Desorption average pore width (4V/A)

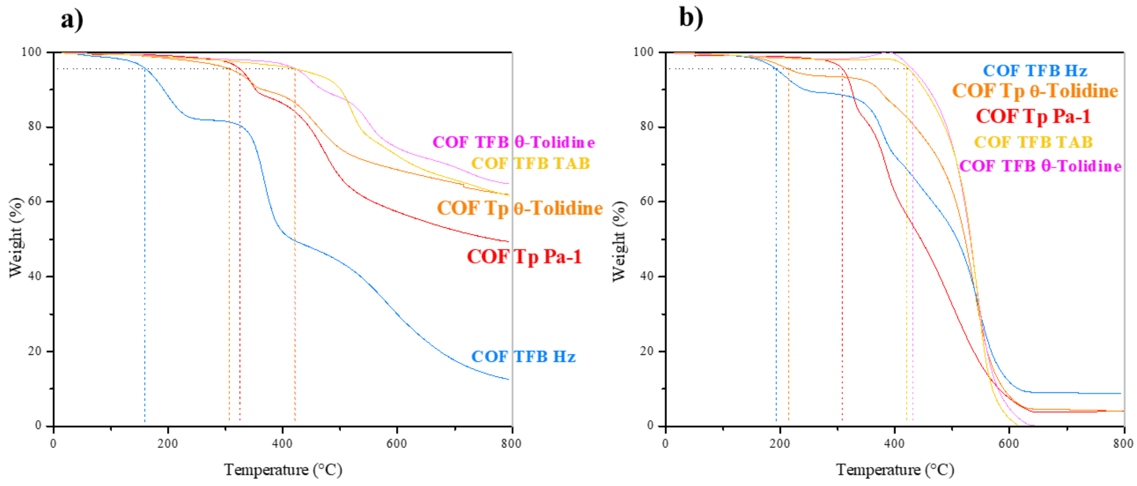

Figure 4. TGA curves of COF measured in nitrogen (a) and air (b).

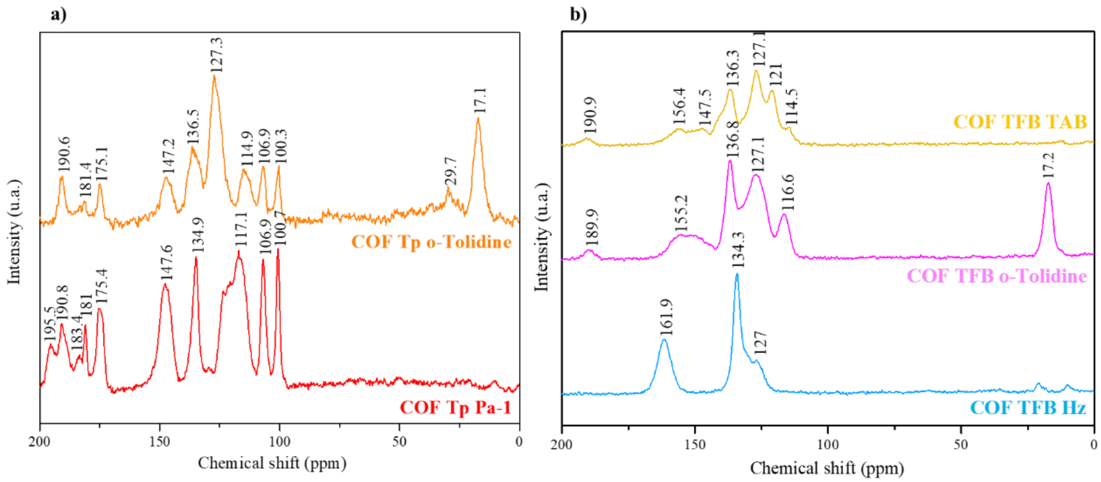

Figure 5. ^{13}C NMR spectra of COF materials.

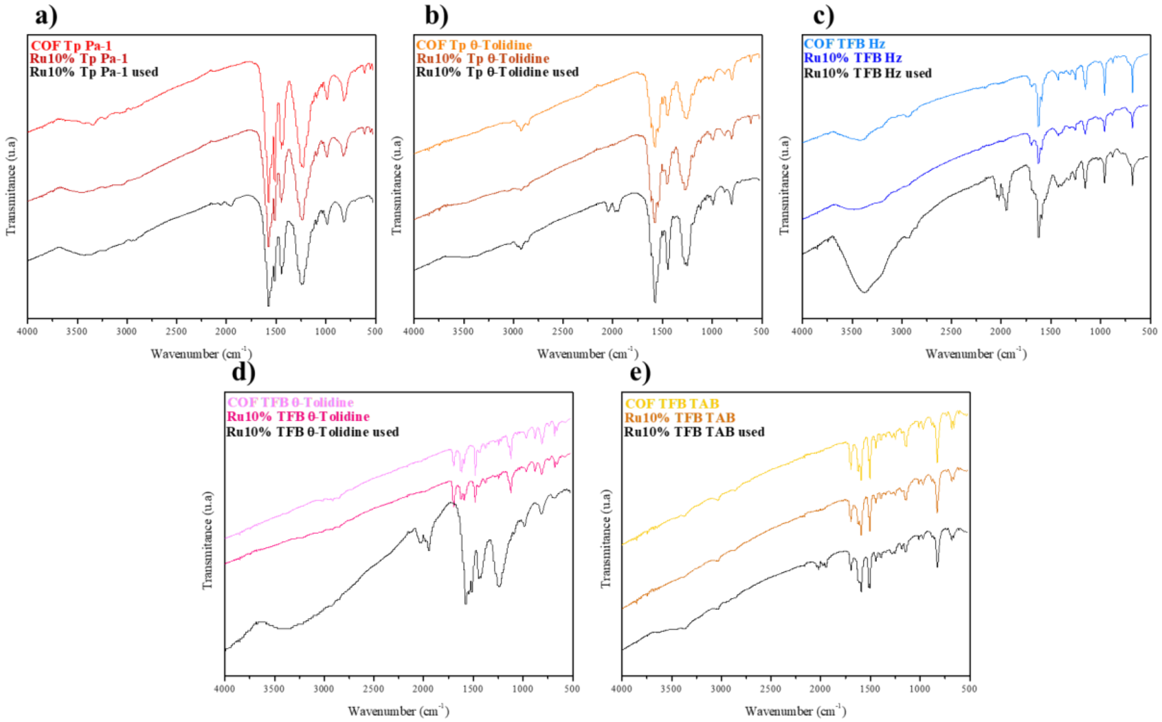

Figure 6. ATR-FTIR spectra of COF and Ru/COF catalysts.

The metal dispersion in COFs was examined by HAADF-TEM and TEM-EDS (**Figures 7** and **8**). TEM and EDS images did not reveal distinct Ru nanoparticles in the samples after impregnation, indicating high ruthenium dispersion. The Ru chemical maps overlap with the chemical maps of chlorine. This suggests that Ru could be mostly present in the form of chlorine containing species. This observation is consistent with a high chlorine content measured in the fresh Ru/COF catalysts (**Table 1**). The COF samples with larger spherical particles showed some enrichment of the surface layer with ruthenium. The formation of core-shell structures can be due to slow diffusion of ruthenium cations inside larger COF particles during the impregnation with $RuCl_3$.

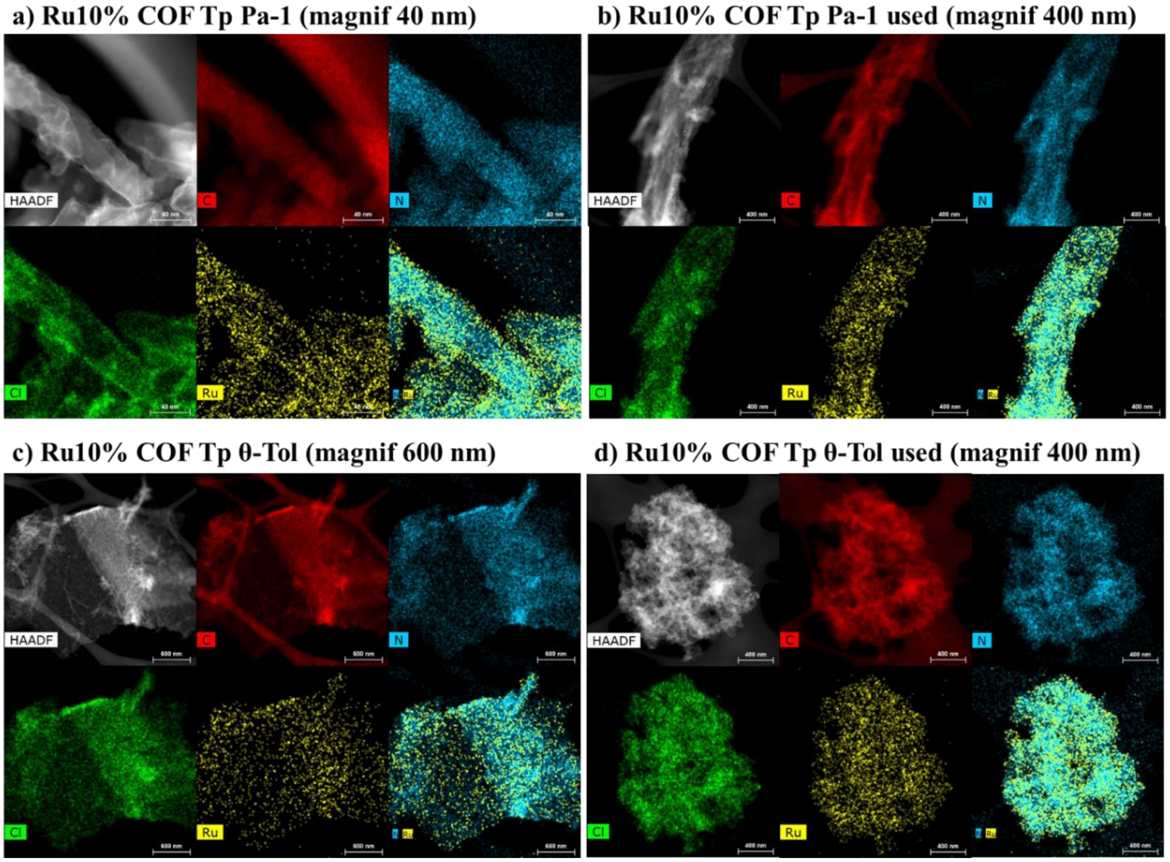
a) Ru10% COF Tp Pa-1 (magnif 40 nm)

b) Ru10% COF Tp Pa-1 used (magnif 400 nm)

c) Ru10% COF Tp θ-Tol (magnif 600 nm)

d) Ru10% COF Tp θ-Tol used (magnif 400 nm)

Figure 7. HAADF and EDS of the COFs before and after reaction. a) Ru 10% COF TpPa-1; b) Ru 10% COF TpPa-1 used; c) Ru 10% COF Tp o-Tolidine; d) Ru 10% COF Tp o-Tolidine used; (continuation at next page).

e) Ru10% COF TFB Hz (magnif 300nm) f) Ru10% COF TFB Hz used (magnif 40nm)

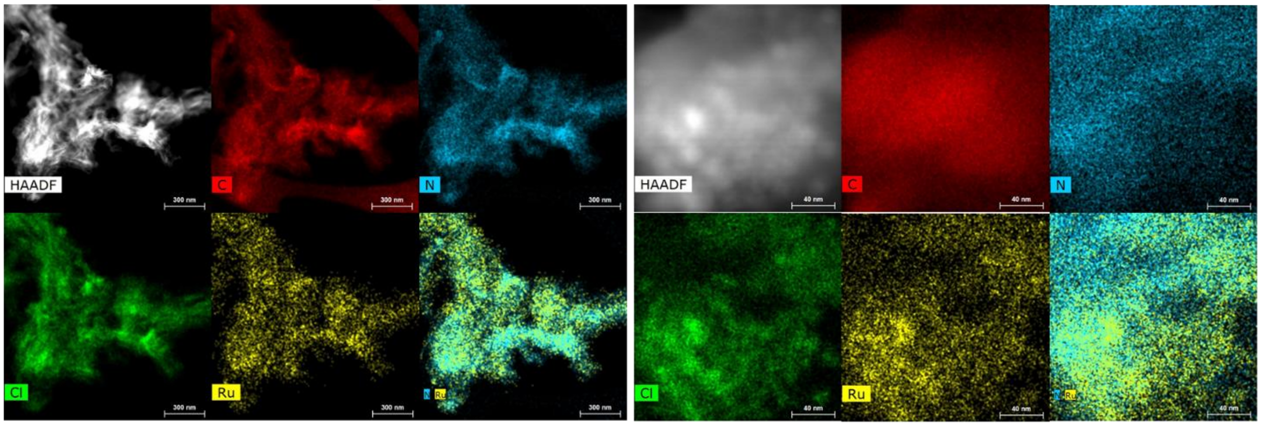

g) Ru10% COF TFB θ-Tol (magnif 1 µm) h) Ru10% COF TFB θ-Tol used (magnif 600 nm)

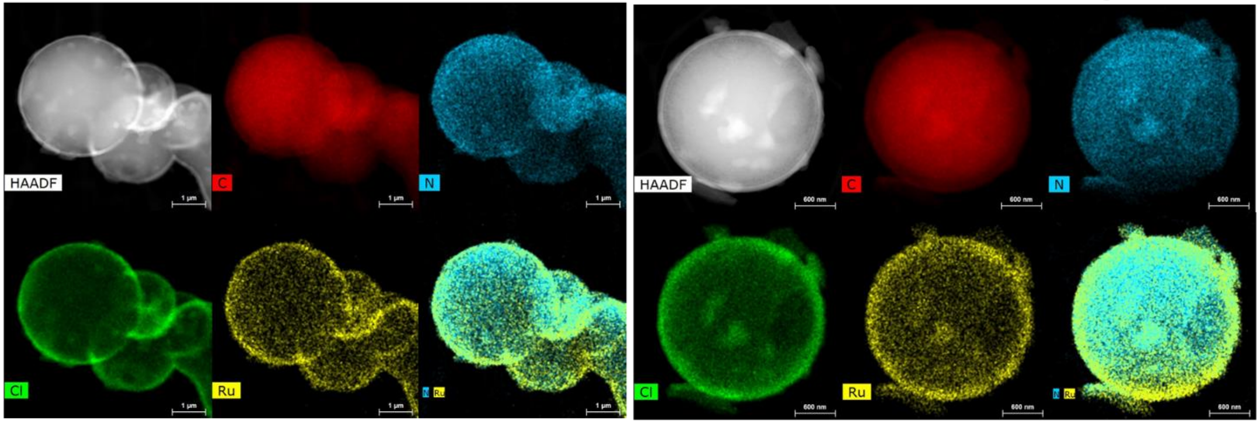

i) Ru10% COF TFB TAB (magnif 400 nm) j) Ru10% COF TFB TAB used (magnif 200 nm)

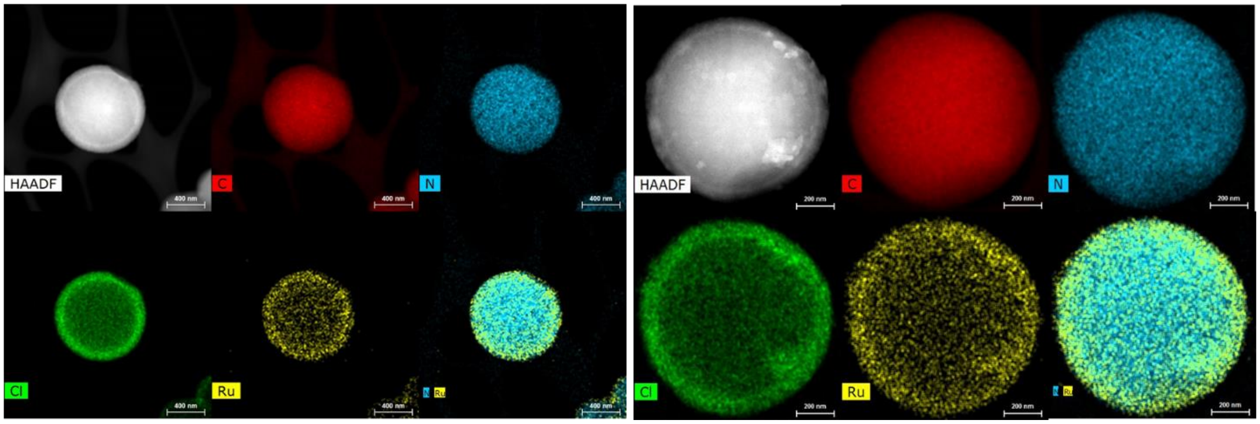

Figure 7 (continuation). HAADF and EDS of the COFs before and after reaction. e) Ru 10% COF TFB Hz; f) Ru 10% COF TFB Hz used; g) Ru 10% COF TFB o-Tolidine; h) Ru 10% COF TFB o-Tolidine used; i) Ru 10% COF TFB TAB; j) Ru 10% COF TFB TAB used.

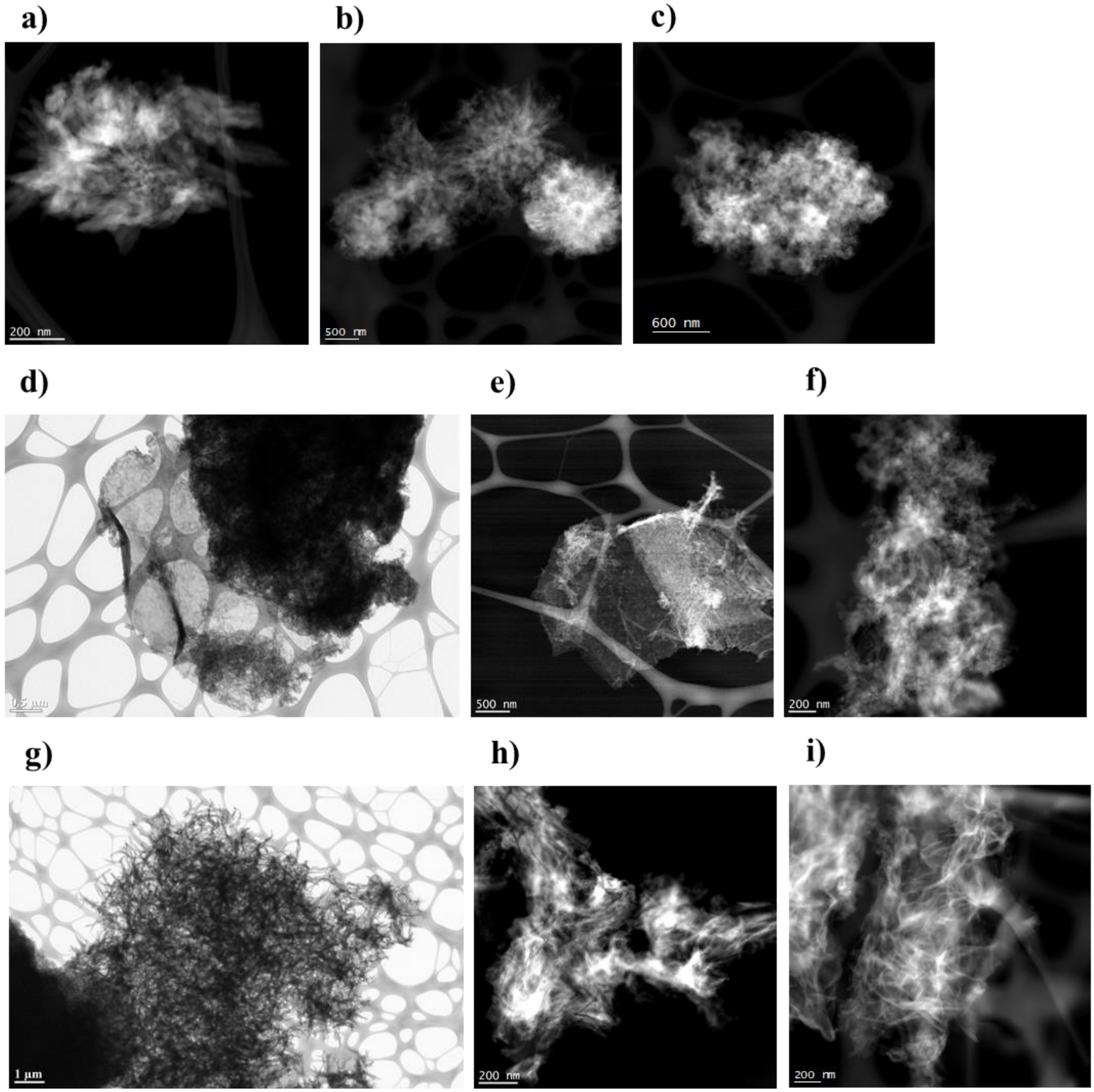

Figure 8. HAADF images of COF and Ru/COF catalysts: a) COF TpPa-1; b) Ru 10% COF TpPa-1; c) Ru 10% COF TpPa-1 used; d) COF Tp o-Tol; e) Ru 10% COF Tp o-Tol; f) Ru 10% COF Tp o-Tol used; g) COF TFB Hz; h) Ru 10% COF TFB Hz; i) Ru 10% COF TFB Hz used; (continuation at next page).

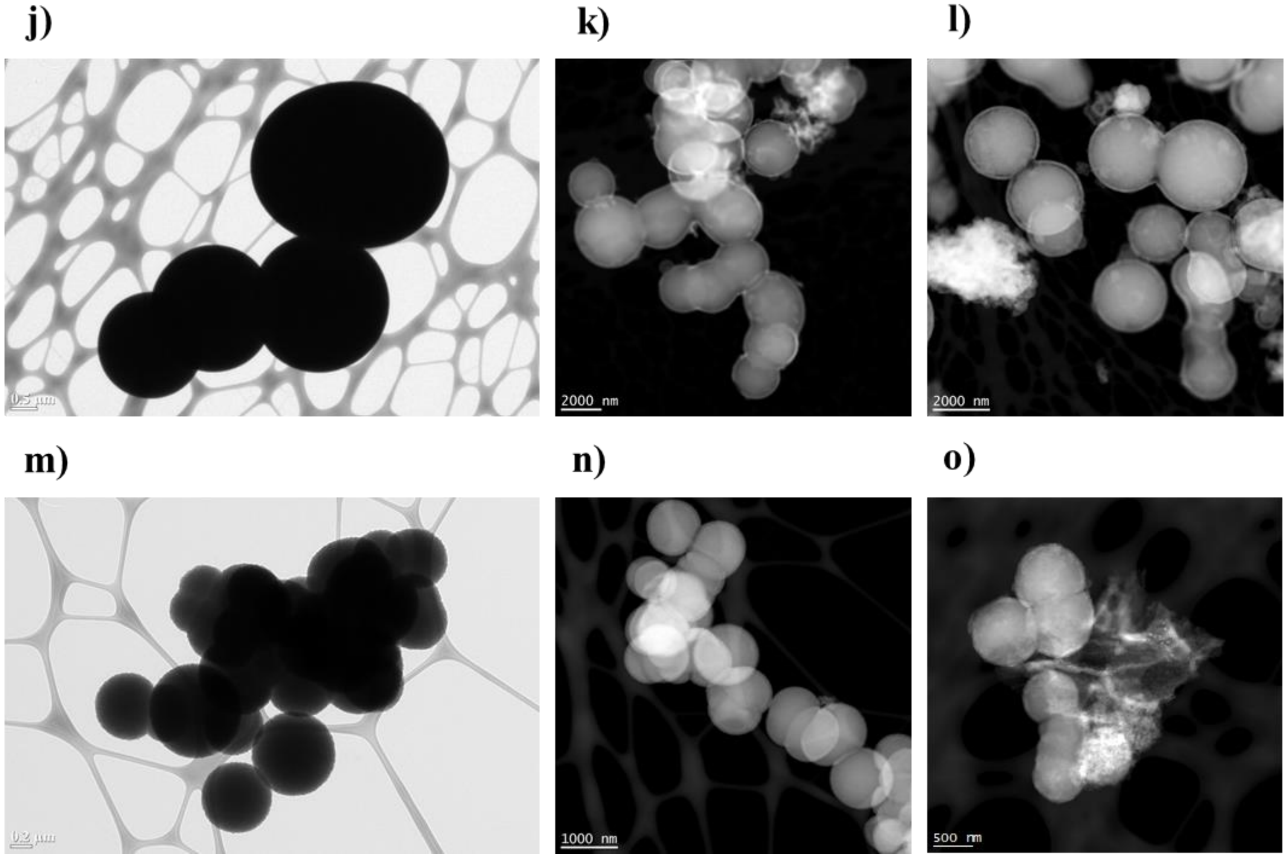

Figure 8 (continuation). HAADF images of COF and Ru/COF catalysts: j) COF TFB o-Tol; k) Ru 10% COF TFB o-Tol; l) Ru 10% COF TFB o-Tol used; m) COF TFB TAB; n) Ru 10% COF TFB TAB; o) Ru 10% COF TFB TAB used.

Interestingly, even after the reaction, no ruthenium clusters or agglomerates were observed in the catalysts. According to TEM analysis, all spent Ru-COF catalysts exhibit rather homogeneous ruthenium dispersion with particles smaller than 1 nm. Thus, no ruthenium sintering and formation of metallic ruthenium particles were observed by TEM. It's important to emphasize that ruthenium nanoparticles (≥1 nm) were not detected in either fresh or spent catalysts. We assume that Ru is mostly present in COF as single atom species.

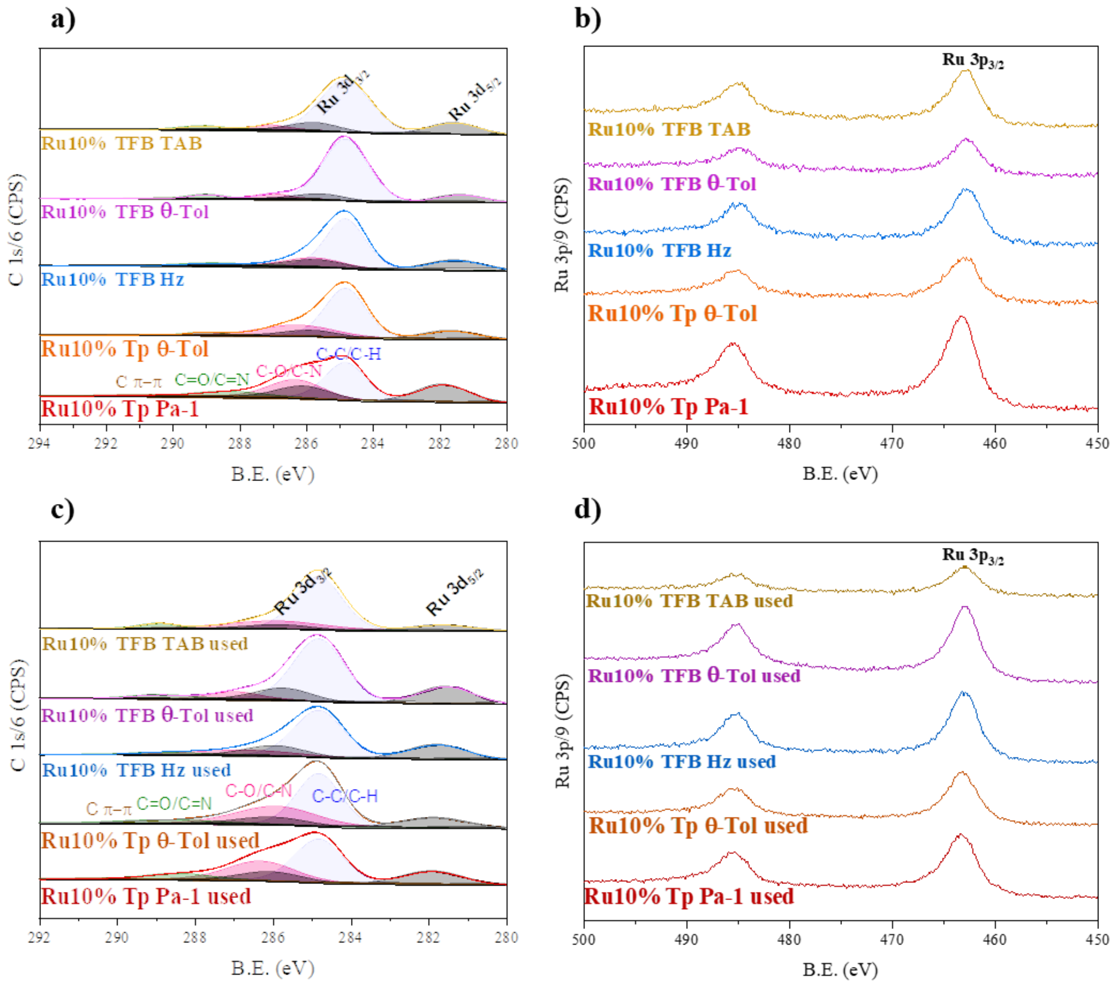

Figure 9. 3d and 3p Ru XPS spectra of fresh and spent Ru/COF catalysts.

Further information about Ru species in the fresh and spent catalysts was obtained using XPS and X-ray absorption. The Ru 3d and 3p XPS spectra of Ru/COF fresh and spent catalysts are shown in **Figure 9**. In the Ru/COF catalysts, the Ru 3d and Ru 3p XPS binding energies (BE) are 2eV higher relative to metallic Ru (**Tables 3** and **4). ** This is indicative of Ru oxidized state in the catalysts and absence of Ru metallic phase. In the Tp Pa-1 sample, Ru BEs are close to those measured for Ru acetylacetonate. It seems that in Ru/COFs, the ruthenium species can be coordinated by the C=O groups of Tp-derived COFs. For TFB-derived COFs, BEs are closer to the values of RuO_2 and 1eV lower than in $RuCl_3$. The XPS atomic concentrations are given in **Table 5.** For all the samples, chlorine disappears after the reaction and has been replaced by another ligand in the Ru coordination.

Table 3. XPS BE in the fresh catalysts.

Sample	Component	Peak Position (eV)	Component	Peak Position (eV)	Component	Peak Position (eV)
Ru10% COF Tp Pa-1	Ru 3d 5/2	281.9	Ru 3p 3/2	463.4	Cl 2p 3/2	198.7
	Ru 3d 3/2	286.0			Cl 2p 1/2	200.3
Ru10% COF Tp o-Tol	Ru 3d 5/2	281.7	Ru 3p 3/2	462.8	Cl 2p 3/2	198.8
	Ru 3d 3/2	285.8			Cl 2p 1/2	200.4
Ru10% COF TFB Hz	Ru 3d 5/2	281.5	Ru 3p 3/2	462.8	Cl 2p 3/2	198.3
	Ru 3d 3/2	285.7			Cl 2p 1/2	199.9
Ru10% COF TFB o -Tol	Ru 3d 5/2	281.3	Ru 3p 3/2	462.9	Cl 2p 3/2	197.9
	Ru 3d 3/2	285.5			Cl 2p 1/2	199.5
Ru10% COF TFB TAB	Ru 3d 5/2	281.5	Ru 3p 3/2	462.7	Cl 2p 3/2	198.3
	Ru 3d 3/2	285.7			Cl 2p 1/2	199.9

Table 4. XPS BE in the spent catalysts.

Sample	Component	Peak position (eV)	Component	Peak position (eV)
Ru10% COF Tp Pa-1 used	Ru 3d 5/2	281.9	Ru 3p 3/2	463.4
	Ru 3d 3/2	286.0		
Ru10% COF Tp o-Tol used	Ru 3d 5/2	281.8	Ru 3p 3/2	463.2
	Ru 3d 3/2	286.0		
Ru10% COF TFB Hz used	Ru 3d 5/2	281.7	Ru 3p 3/2	463.0
	Ru 3d 3/2	285.9		
Ru10% COF TFB o-Tol used	Ru 3d 5/2	281.5	Ru 3p 3/2	462.8
	Ru 3d 3/2	285.7		
Ru10% COF TFB TAB used	Ru 3d 5/2	281.6	Ru 3p 3/2	462.9
	Ru 3d 3/2	285.8		

Table 5. Atomic concentrations measured by XPS in fresh and spent Ru/COF catalysts.

Sample Identifier	Name	%At. Conc.	At. ratio	Sample Identifier	Name	%At. Conc	At. Ratio
Ru 10% COF Tp Pa-1	O 1s	12.5	Ru/O: 0.19	Ru10% COF Tp Pa-1	O 1s	18.4	Ru/O: 0.09
	C1s	71.3	Ru/C: 0.03		C1s	73.8	Ru/C: 0.02
	N 1s	7.4	Ru/N:0.32		N 1s	6.3	Ru/N: 0.27
	Cl 2p	6.3	Ru/Cl:0.38		Cl 2p	-	Ru/Cl^-
	Ru 3d	2.4			Ru 3d	1.7	
Ru 10% COF Tp o-Tol	O 1s	11.6	Ru/O:0.11	Ru 10% COF Tp o-Tol spent	O 1s	14.4	Ru/O:0.10
	C1s	80.0	Ru/C:0.02		C1s	79.7	Ru/C:0.02
	N 1s	3.6	Ru/N:0.36		N 1s	4.7	Ru/N:0.32
	Cl 2p	3.5	Ru/Cl:0.37		Cl 2p	-	Ru/ Cl^-
	Ru 3d	1.3			Ru 3d	1.5	
Ru 10% COF TFB Hz	O 1s	7.6	Ru/O:0.22	Ru 10% COF TFB Hz spent	O 1s	16.2	Ru/O:0.14
	C1s	73.1	Ru/C: 0.02		C1s	72.1	Ru/C:0.03
	N 1s	13.0	Ru/N:0.13		N 1s	9.7	Ru/N:0.23
	Cl 2p	4.6	Ru/Cl:0.37		Cl 2p	-	Ru/ Cl^-
	Ru 3d	1.7			Ru 3d	2.2	
Ru 10% COF TFB o-Tol	O 1s	8.8	Ru/O:0.11	Ru 10% COF TFB o-Tol spent	O 1s	14.2	Ru/O:0.15
	C1s	82.6	Ru/C:0.01		C1s	78.5	Ru/C:0.03
	N 1s	4.5	Ru/N: 0.22		N 1s	5.2	Ru/N:0.4
	Cl 2p	3.2	Ru/Cl:0.31		Cl 2p	-	Ru/ Cl^-
	Ru 3d	1.0			Ru 3d	2.1	
Ru 10% COF TFB TAB	O 1s	9.2	Ru/O:0.17	Ru 10% COF TFB TAB spent	O 1s	14.1	Ru/O:0.07
	C1s	80.4	Ru/C:0.02		C1s	82.2	Ru/C:0.01
	N 1s	3.9	Ru/N:0.41		N 1s	2.7	Ru/N:0.37
	Cl 2p	4.9	Ru/Cl:0.33		Cl 2p	-	Ru/ Cl^-
	Ru 3d	1.6			Ru 3d	1.0	

Catalytic performance in CO2 hydrogenation to formic acid

The CO_2 hydrogenation tests were conducted in aqueous phase in the autoclave at the total pressure of 40 bar at 90 and 120°C with H_2/CO_2 ratios of 1 and 3. In all the experiments, the same amount of Ru was loaded in the reactor. 1.3 M triethylamine (TEA) was added to increase the equilibrium conversion. Low CO_2 conversions were observed with $RuCl_3$ and $Ru(OH)_3$ as catalysts, while the Ru/COF catalysts exhibited higher activity (**Table 6**), in terms of formic acid rate ($mg_{HCOOH}\ g_{catalyst}^{-1}\ h^{-1}$), Ru/COFs catalysts exhibited great values in comparison with literature (**Table 7**).

Table 6. Catalytic results for the CO_2 hydrogenation to formic acid (The values of formic acid in mg was obtain using ^{1}H NMR liquid state; relevant calculations are available in SI).

Sample	Reactions conditions	mg	μmol ml^{-1}	TON	TOF h^{-1}	$mg_{HCOOH}\ g_{catalyst}^{-1}\ h^{-1}$
Ru 10% COF Tp Pa-1		35	104	80	5.3	5.0
Ru 10% COF Tp o -Tol	90°C/15h	56	168	147	9.8	8.1
Ru 10% COF TFB Hz	20 bar H_2	112	336	508	34	16.2
Ru 10% COF TFB o-Tol	20 bar CO_2	42	126	202	13	6.1
Ru 10% COF TFB TAB		111	334	731	49	16.1
Ru 10% COF Tp Pa-1		33	104	76	76	71.4
Ru 10% COF Tp o -Tol	120°C/1h	37	118	98	98	80.9
Ru 10% COF TFB Hz	30 bar H_2	53	169	243	243	116
Ru 10% COF TFB o -Tol	10 bar CO_2	29	92	140	140	63.2
Ru 10% COF TFB TAB		34	108	222	222	73.6

Only formic acid was detected as a product; no CO, methane, or methanol were observed by GC or ^{1}H NMR. Since the catalysts contain mostly single atom Ru sites, the activity was evaluated as TOF, which corresponds to the amount of CO_2 converted to formic acid per mole of ruthenium per h. The highest activity at both 90 and 120°C was observed over Ru10% COF TFB Hz Ru10% COF TFB TAB, while Ru10% COF Tp Pa-1 and Ru10% COF Tp θ -Tol exhibited the lowest activity.

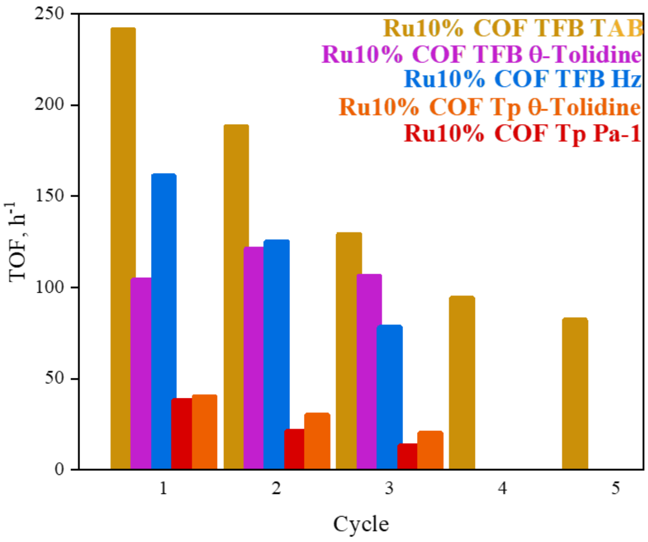

Figure 10. Variation of TOF for the CO_2 hydrogenation over the Ru/COF catalysts in consecutive reactions cycles.

Remarkably, no discernible relation exists between the intrinsic activity of Ru catalysts and their overall surface area (**Table 2**). The surface area of COF is composed of 2D layers. Variations in the arrangement of these layers, leading to distinct surface areas, can be modified through pre-treatment and reaction conditions. **Figure 10** presents the activity of Ru/COF after conducting several reaction cycles. Important, Ru10% COF TFB o-Tol shows unchangeable activity after several cycles.

Table 7. Comparison of catalytic results for the CO_2 hydrogenation to formic acid.

Catalyst	P, bar	T, °C	$t_{reaction}$, h	TON	$mol_{HCOOH}\ g_{catalyst}^{-1}\ h^{-1}$	Reference
Ir/COF	40	80	2	150	1.4	(Gunniya Hariyanandam et al., 2016)
	0	120	2	530	5.1	
Pd/NPMO	0	80	20	1420	1.6	(Betsy et al., 2020)
	0	150	20	1660	1.9	
Au/Al_2O_3	0	70	20	2400	0.26	(Filonenko et al., 2014)
Au/SiO_2	10	90	12	17328	6.1	(Q. Liu et al., 2017)
PdNi/CNTs	0	40	15	5.4	0.004	(Nguyen et al., 2015)
PdAg/NMHCS	0	100	24	169	0.55	(G. Yang et al., 2021b)
	0	100	24	640	4.34	
$Pd/g\text{-}C_3N_4$	0	40	16	72	0.014	(H. Park et al., 2016)
PdCu/MHCS	0	100	24	1432	0.13	(G. Yang et al., 2021a)
Ru/LDH	0	100	24	461	0.007	(Mori et al., 2017)
Pd/C_3N_4	0	80	12	866	0.68	(Shao et al., 2016)
Ru/CTF	0	90	2	720	13.7	(Gunasekar et al., 2018)
	0	120	2	5050	95.7	
Ir/CTF	0	90	2	358	0.45	(Bavykina et al., 2016)
Ir/CTF	0	120	15	24300	5.73	(Gunasekar et al., 2017)
Ir/COF	0	120	2	6402	1.57	(K. Park et al., 2015)
Ru/MCM41	40	90	15	1582	1.76	(Qiyan Wang et al., 2021b)
Ru/COF	40	90	15	731	16.1	This work
	40	120	1	243	116	

Ex-situ and In-situ XAS investigation ofruthenium catalysts

Figures 11a and **12a** display the Ru K-edge *ex-situ* XANES spectra of reference compounds and fresh Ru/COF catalysts, respectively. The XANES spectra of fresh Ru/COF catalysts are rather similar and strongly reassemble those of $RuCl_3$ and $RuCl_3(NH_3)_6$. This observation is consistent with a large amount of chlorine detected in the catalysts by XRF. The results of linear combination fitting of XANES spectra using Ru hydroxide, Ru chloride, Ru chloride (ammonium), Ru oxide and metallic ruthenium for the fresh and spent catalysts are displayed in **Table 8**. The fits are shown in **Figure 13**. All the fresh catalysts present the majority of Ru species as $RuCl_3$ and/or Ru-N complexes, here represented by reference $RuCl_3(NH_3)_6$. The Ru10% COF TFB Hz and Ru10% COF TFB TAB fresh catalysts have the lower amount of metallic Ru, ~11% and ~16%, respectively. Metallic Ru in the fresh catalysts can be possibly produced by reduction of ruthenium species by the COF matrix during the catalyst drying. Notably, these are the most active catalysts, with TOFs higher than 200 h^{-1} (see **Table 6**). The XANES spectra of Ru/COF change after the catalytic reaction (**Figure 12a**). For the most stable catalyst, Ru10% COF TFB o-Tol, the majority of Ru species in the spent catalyst correspond to Ru hydroxide type species. Also, the fraction of metallic Ru does not change in comparison with the fresh counterpart and remains around 25%. This behavior was not observed for the other catalysts. No contribution of Ru chloride to XANES was detected, consistent with chlorine removal from the catalyst during the reaction.

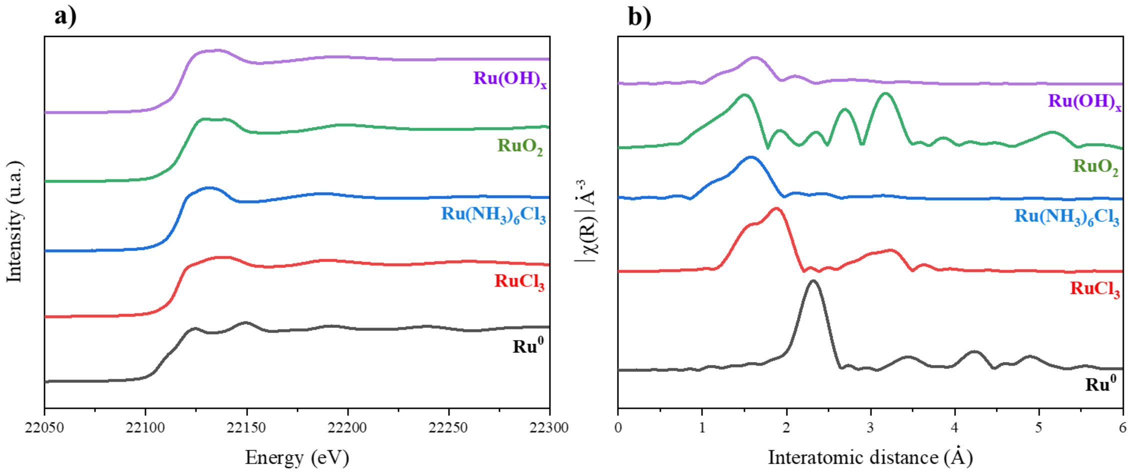

Figure 11. Ru K-edge XANES spectra and EXAFS Fourier transform moduli of reference compounds.

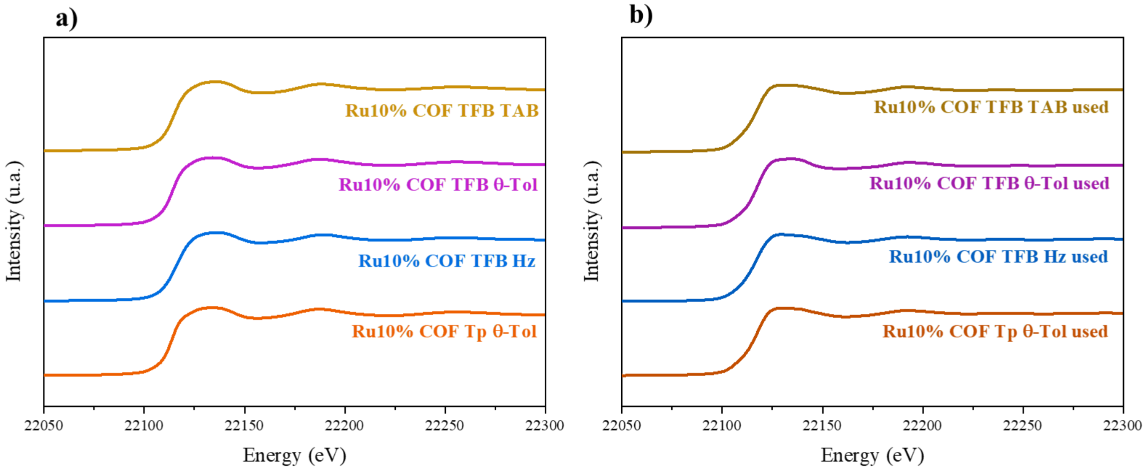

Figure 12. Ru K-edge ex-situ absorption spectra of fresh (a) and spent (b) Ru/COF catalysts.

Table 8. Linear combination fitting results of XANES spectra of fresh and spent Ru/COF catalysts using $RuCl_3(NH_3)_6$, $RuCl_3$, Ru metallic, Ru oxide and Ru hydroxide (relative error of 20%).

Sample	r factor	chi	$RuCl_3(NH_3)_6$	$RuCl_3$	Ru^0	RuO_2	$Ru(OH)_x$
Ru 10% COF Tp Pa-1	0.0035	0.0006	0.4307	0.3245	0.2541		
Ru 10% COF Tp θ-Tol	0.0063	0.0011	0.4900	0.2683	0.2611		
Ru 10% COF Tp θ-Tol spent	0.0002	0.0000 3	0.2993		0.3654	0.34412	
Ru 10% COF TFB Hz	0.0010	0.0002		0.5698	0.1139	0.3115	
Ru 10% COF TFB Hz spent	0.0005	0.0000 7	0.2640		0.3977	0.3442	
Ru 10% COF TFB θ-Tol	0.0052	0.0008	0.4582	0.2909	0.2587		
Ru 10% COF TFB θ-Tol spent	0.0006	0.00009	0.1473		0.2319		0.6199
Ru 10% COF TFB TAB	0.0030	0.0005	0.3447	0.5059	0.1620		
Ru 10% COF TFB TAB spent	0.0002	0.0000 2	0.2478		0.3954	0.3652	

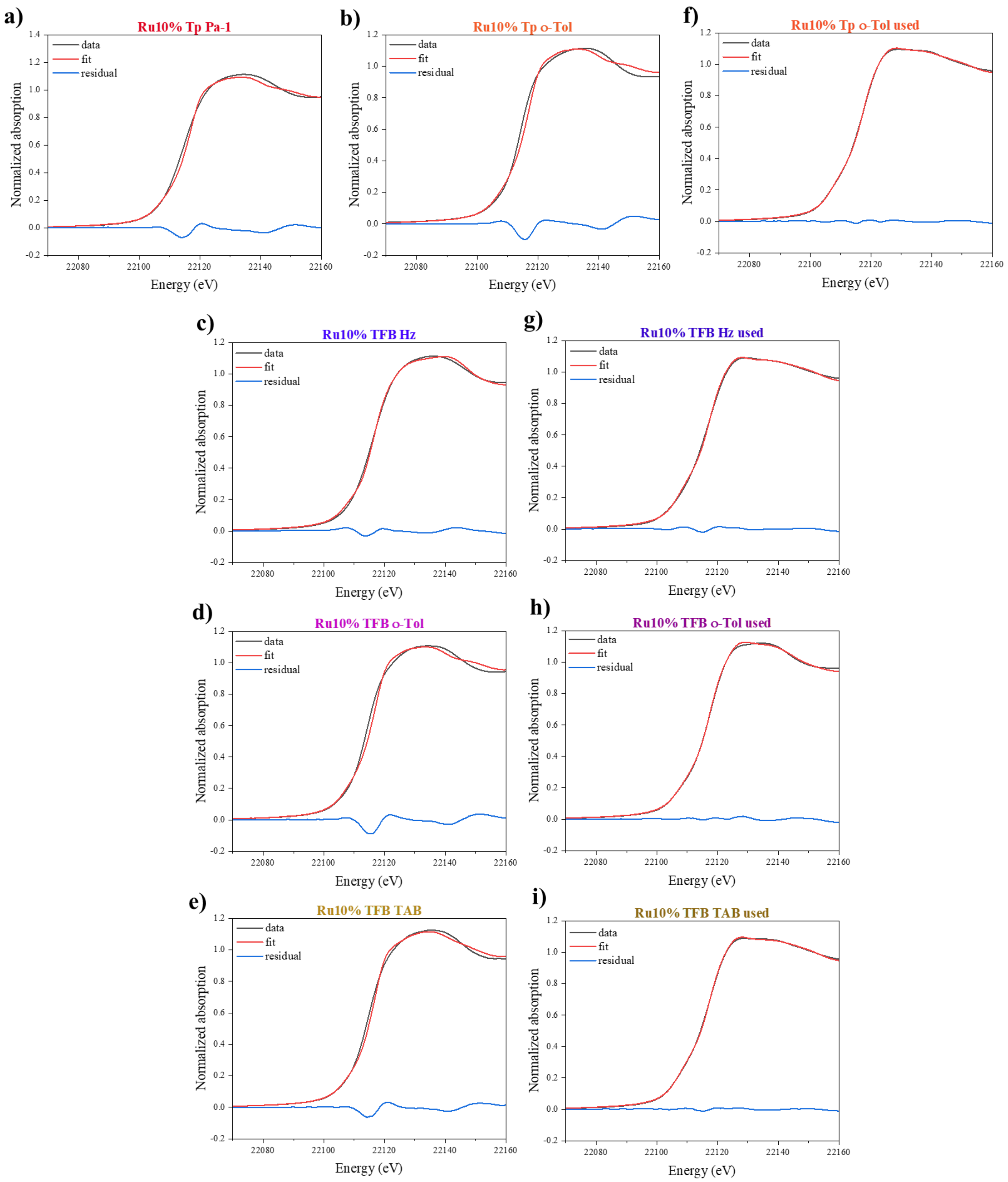

Figure 13. Linear combination XANES fit plots for each sample.

Figure 14 shows the Fourier transform (FT) EXAFS moduli of the fresh catalysts (without phase shift). The fresh Ru/COF catalysts exhibit a broad intense peak at 1.8-1.9 Å. A similar peak was also observed in the FT EXAFS of $RuCl_3$. This suggests that this peak may be related to Ru-

Cl coordination in the first Ru coordination shell. Interestingly, the FT moduli of EXAFS in the Ru/COF catalysts do not show the second peak at 3.35 Å, which was observed for $RuCl_3$.

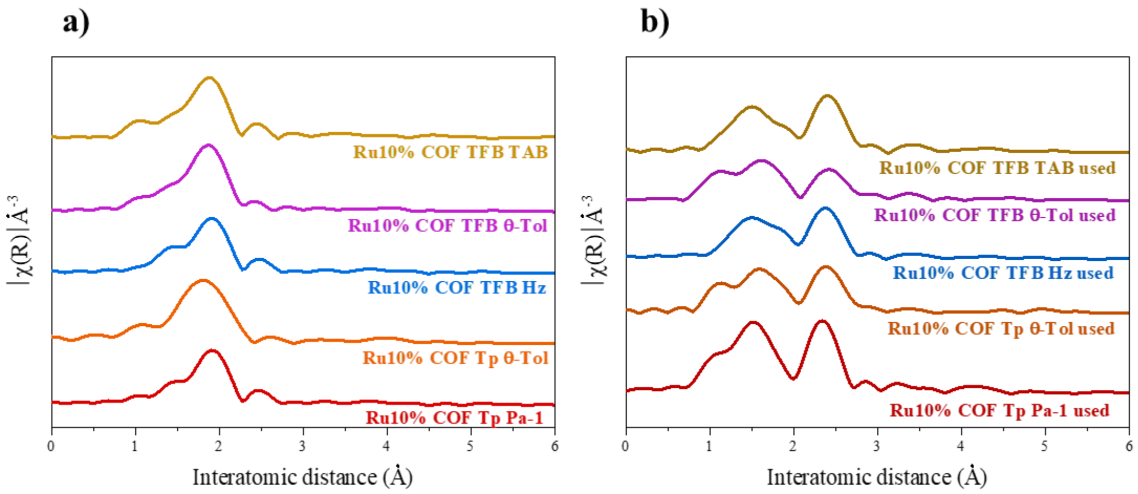

Figure 14. Ru K-edge ex-situ Fourier trabnsform EXAFS of fresh (a) and spent (b) Ru/COF catalysts.

The absence of distinct second coordination shell of $RuCl_3$ in the fresh Ru/COF samples suggests low crystallinity of Ru chloride and possible formation of isolated Ru species. Note that some fraction of Ru metallic phases was detected in the samples from the results of XANES linear combination fitting.

In the spent catalysts (**Figure 14b**), the FT EXAFS moduli show an intense broad peak at 1.6-1.7 Å. The position of this peak is similar to that of the Ru-O coordination in Ru hydroxide, Ru oxide and Ru-N complexes species, and is shifted from the position of Ru-Cl peak in $RuCl_3$. In addition, a new intense peak at 2.3 Å appears in the FT EXAFS. This peak seems to be related to the Ru-Ru coordination in metallic Ru and is indicative of the partial sintering of Ru single atoms into metallic nanoparticles. Interestingly, among the spent Ru/COF catalysts, the Ru-Ru coordination number is smaller in the Ru10% COF TFP o-Tol, which could correspond to a smaller number of metallic Ru atoms in the coordination shell of Ru and a lower extent of Ru reduction in this sample. This is consistent with the assumption that single atom metal species have higher contribution to the CO_2 hydrogenation to formic acid than ruthenium metal nanoparticles.

In order to provide further insights into the evolution of catalyst structure during the reaction, we performed *operando* XAS measurements of Ru10% TFB o-Tol and Ru10% COF TFB TAB at Ru K-absorption edge under the flow of H_2 and CO_2 (H_2/CO=1) at 100°C (**Figure 15**). The evolution of XANES during the reaction was different for the two samples. The XANES spectra of Ru10% TFB o-Tol (**Figure 16a**) show evolution of the Ru K-absorption edge from Ru chloride to that which is more characteristic of Ru hydroxide and Ru-N complexes.

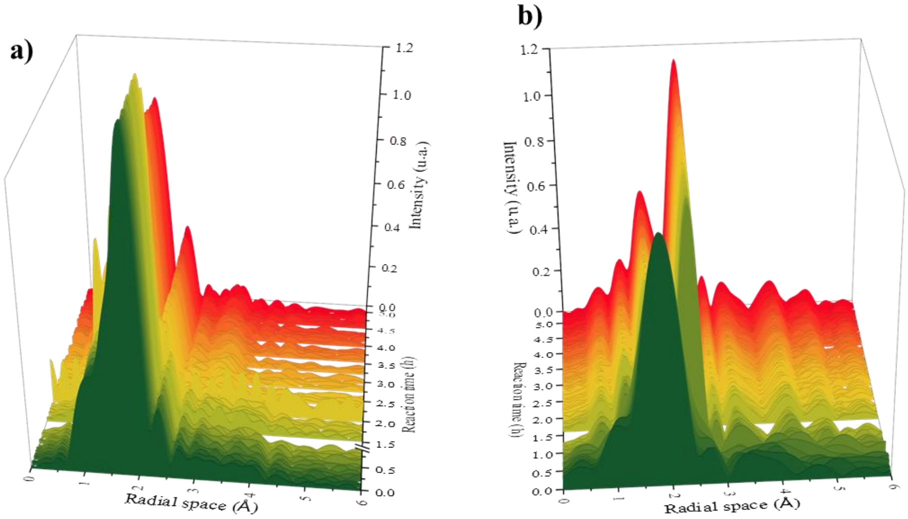

Figure 15. Evolution of *in-situ* XAS spectra of Ru10% COF TFB o-Tol (a) and Ru10% COF TFB TAB (b) during the CO_2 hydrogenation.

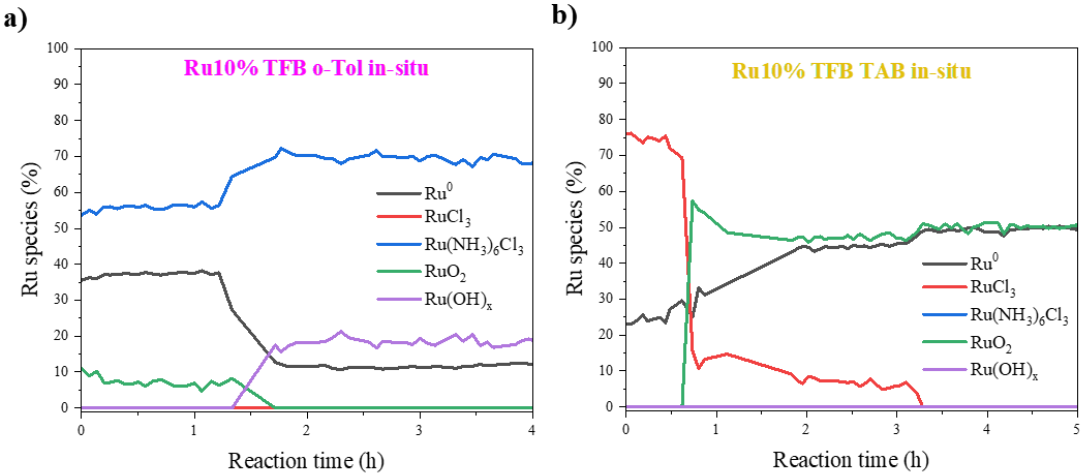

Figure 16. Evolution of phase composition of Ru10% COF TFB o-Tol (a) and Ru10% COF TFB TAB during the CO_2 hydrogenation calculated from LC XAS.

At the same time, the XANES spectra of Ru10% COF TFB TAB (**Figure 16b**) show a steady decrease in the intensity of white line, which corresponds to the increase in the fraction of metallic phase and correspondingly ruthenium reduction. Note that Ru10% COF TFB o-Tol showed stable performance in the CO_2 hydrogenation to formic acid for several cycles, while Ru10% COF TFB-TAB exhibited a major deactivation (**Figure 10**).

The phase composition of Ru catalysts during the reaction was calculated from fitting the *operando* XANES spectra of Ru10% COF TFB o-Tol and Ru10% COF TFB TAB using the spectra of reference compounds (**Figure 16 a** and **b)**. In Ru10% COF TFB o-Tol, the amounts of RuN complexes and Ru hydroxide species increase under the reaction conditions, while the concentration of metallic Ru phases decreases. This observation suggests the redispersion of Ru species and increased interaction of Ru complexes with N species in the COF during the reaction. In contrast, the reaction results in progressive increase in the amount of metallic ruthenium in Ru10% COF TFB-TAB (**Figure 16b**).

The liquid samples collected during *operando* XAS experiments were analyzed by ^1H NMR. The amount of produced formic acid was 0.062 mmol for Ru10% TFB-TAB and 0.022 mmol for Ru10% TFB o-Tol. This corresponds respectively to TON of 24.6 and 3.2 for Ru10% TPB TAB and Ru10% TPB o-Tol. Note that, similar to the batch reaction tests, Ru10% TFB TAB exhibited higher activity than Ru10% TFB o-Tol. Some difference in absolute TON values may be due to different operating conditions in *operando* XAS experiments conducted in flow reactors and in conventional batch catalytic tests.

Structure-performance and stability of ruthenium catalysts supported by COF

A wide range of characterization techniques employed in this work suggests the presence of isolated single-atom ruthenium species in COF catalysts, making COFs a suitable matrix for achieving highly dispersed ruthenium species.

First, let's discuss how the COF structure influences the catalytic performance of ruthenium catalysts in the hydrogenation of CO_2 to formic acid. Our experimental data suggest that at the same Ru content, the COF chemical composition determines to a larger extent the fraction of isolated single-atom ruthenium species. Palkovits(Broicher et al., 2017) et al. recently reported a lower CO_2 hydrogenation rate using iridium single-site catalysts, which was linked to a decrease in the dispersion of iridium. There might be multiple factors influencing the intrinsic activity of a catalyst, such as interactions between the support and metal, and mass transfer of reactants/products. Single ruthenium atoms in the COF materials can be coordinated either by the nitrogen-containing functional groups or possibly by the C=O species. Since the highest activity was observed on the samples without carbonyl groups, we assume that the contribution of the Ru species coordinated by C=O and C-OH groups to the reaction is not very significant. Our results clearly show that the intrinsic catalytic activity is strongly affected by the amount of nitrogen in the catalysts (**Figure 17**). Moreover, the intrinsic catalytic activity of Ru catalysts is almost proportional to the N/Ru ratio in the catalysts. In agreement with the characterization results, this observation underscores the crucial role of nitrogen-containing groups in contributing to ruthenium redispersion. It is also crucial to emphasize that the total amount of N species in the support plays a significant role in the creation of isolated metal atoms. Significant impacts of nitrogen species on anchoring single metal atoms have been previously reported (Dong et al., 2023; Fiorio et al., 2023; Ma et al., 2022) for carbon materials (carbon nanotubes, fibers).

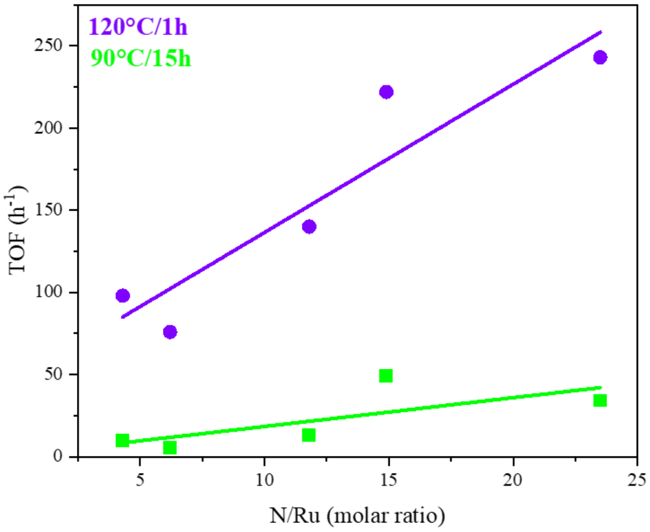

Figure 17. TOF measured on the Ru/COF catalysts at 90 and 120°C as functions of N/Ru experimental molar ratio in the catalysts (from **Table 6**).

In the present work, the highest activity has been achieved in COF, which has the highest capacity for redispersion of ruthenium during the catalyst synthesis, due to a higher fraction of nitrogen in the framework. Besides anchoring Ru single metal atoms, nitrogen functional groups in COF may also play a role in CO_2 hydrogenation, for example, potentially facilitating CO_2 adsorption.

Stability of the single metal ruthenium species during the reaction is another issue which can determine the long-term catalyst productivity. The most active Ru10% COF TFB TAB and TFB Hz loses their activity in the second and third reaction cycles (**Figure 10**), while Ru10% COF TFB o-Tol maintains its catalytic activity. The characterization of the spent catalysts showed partial reduction of Ru oxidized species to metal state in most of catalysts, which results in the appearance of a peak of Ru-Ru coordination in FT EXAFS modulus at 2.3 Å (**Figure 14b**). Higher intensity of the peak of Ru-Ru coordination shell and higher extent of Ru reduction was observed in less stable Ru10% COF TFB TAB and Ru10% COF TFB Hz catalysts. The reduction of ruthenium resulted in a decrease in the concentration of Ru single atom sites. This reduction was less significant for the Ru10% COF TFB o-Tol catalyst. Ruthenium metallic nanoparticles have therefore a much lower efficiency in CO_2 hydrogenation to formic acid compared to ruthenium single-atom species.

Operando XAS experiments have given crucial information about the evolution of Ru phases in the COF-supported Ru10% COF TFB TAB and Ru10% COF TFB o-Tol catalysts during the reaction. Ru species in Ru10% COF TFB TAB underwent gradual reduction to metallic phase during first 2-3 h of reaction in a flow reactor, while redispersion and even possible re-oxidation of ruthenium species were detected in the Ru10% COF TFB o-Tol catalyst (**Figure 16a**). These experiments further confirm importance of Ru dispersion and stability of single atom ruthenium species for obtaining highly active and productive catalysts for CO_2 hydrogenation to formic acid.

Conclusion

Deposition of ruthenium via impregnation over the COF materials results in a large fraction of ruthenium single atom species. In the fresh catalysts, Ru is coordinated by chlorine and located in a close interaction with nitrogen containing groups of COFs. The chlorine atoms are removed from the catalysts during the CO_2 hydrogenation.

The catalytic performance of ruthenium catalysts supported over COF materials is strongly affected by the COF structure. While various catalyst parameters can influence catalytic performance, it was observed that the rate of CO_2 hydrogenation exhibited a nearly proportional relationship with the density of nitrogen species in the COF framework. The effect was attributed to the strong effect of N- species on ruthenium dispersion and anchoring single Ru atoms. A higher fraction of nitrogen in COF leads to a higher fraction of single-atom ruthenium sites. The stability of catalysts was related to the hindered reducibility of ruthenium single atoms during the reaction. The proposed strategy can be extended for the design of numerous SAC metal catalysts supported by COF for different reactions.

References

Al-Salem, S. M., Lettieri, P., & Baeyens, J. (2009). Recycling and recovery routes of plastic solid waste (PSW): A review. *Waste Management*, *29*(10), 2625–2643. https://doi.org/10.1016/j.wasman.2009.06.004

Bavykina, A. V., Rozhko, E., Goesten, M. G., Wezendonk, T., Seoane, B., Kapteijn, F., Makkee, M., & Gascon, J. (2016). Shaping Covalent Triazine Frameworks for the Hydrogenation of Carbon Dioxide to Formic Acid. *ChemCatChem*, *8*(13), 2217–2221. https://doi.org/10.1002/cctc.201600419

Betsy, K. J., Lazar, A., Pavithran, A., & Vinod, C. P. (2020). CO2 Hydrogenation to Formate by Palladium Nanoparticles Supported on N-Incorporated Periodic Mesoporous Organosilica. *ACS Sustainable Chemistry and Engineering*, *8*, 14765–14774. https://doi.org/10.1021/acssuschemeng.0c03860

Broicher, C., Foit, S. R., Rose, M., Hausoul, P. J. C., & Palkovits, R. (2017). A Bipyridine-Based Conjugated Microporous Polymer for the Ir-Catalyzed Dehydrogenation of Formic Acid. *ACS Catalysis*, *7*(12), 8413–8419. https://doi.org/10.1021/acscatal.7b02425

Centi, G., & Perathoner, S. (2004). Heterogeneous catalytic reactions with CO2: Status and perspectives. *Studies in Surface Science and Catalysis*, *153*, 1–8. https://doi.org/10.1016/s0167-2991(04)80212-x

Chernyak, S. A., Corda, M., Dath, J. P., Ordomsky, V. V., & Khodakov, A. Y. (2022). Light olefin synthesis from a diversity of renewable and fossil feedstocks: state-of the-art and outlook. *Chemical Society Reviews*, *51*(18), 7994–8044. https://doi.org/10.1039/d1cs01036k

Côté, A. P., Benin, A. I., Ockwig, N. W., O'Keeffe, M., Matzger, A. J., & Yaghi, O. M. (2005). Porous, Crystalline, Covalent Organic Frameworks. *Science*, *310*(5751), 1166–1170. https://doi.org/10.1126/science.1120411

Dong, X., Jia, Y., Zhang, M., Ji, S., Leng, L., Hugh Horton, J., Xu, C., He, C., Tan, Q., Zhang, J., & Li, Z. (2023). Molten salt-induction of geometrically deformed ruthenium single atom catalysts with high performance for aerobic oxidation of alcohols. *Chemical Engineering Journal*, *451*, 138660. https://doi.org/10.1016/j.cej.2022.138660

Fang, Q., Gu, S., Zheng, J., Zhuang, Z., Qiu, S., & Yan, Y. (2014). 3D microporous base-functionalized covalent organic frameworks for size-selective catalysis. *Angewandte Chemie - International Edition*, *53*(11), 2878–2882. https://doi.org/10.1002/anie.201310500

Filonenko, G. A., Van Putten, R., Schulpen, E. N., Hensen, E. J. M., & Pidko, E. A. (2014). Highly efficient reversible hydrogenation of carbon dioxide to formates using a ruthenium PNP-pincer catalyst. *ChemCatChem*, *6*(6), 1526–1530. https://doi.org/10.1002/cctc.201402119

Fiorio, J. L., Garcia, M. A. S., Gothe, M. L., Galvan, D., Troise, P. C., Conte-Junior, C. A., Vidinha, P., Camargo, P. H. C., & Rossi, L. M. (2023). Recent advances in the use of nitrogen-doped carbon materials for the design of noble metal catalysts. *Coordination Chemistry Reviews*, *481*, 215053. https://doi.org/10.1016/j.ccr.2023.215053

Geng, K., He, T., Liu, R., Dalapati, S., Tan, K. T., Li, Z., Tao, S., Gong, Y., Jiang, Q., & Jiang, D. (2020). Covalent Organic Frameworks: Design, Synthesis, and Functions. *Chemical Reviews*, *120*(16), 8814–8933. https://doi.org/10.1021/acs.chemrev.9b00550

Gunasekar, G. H., Jung, K.-D., & Yoon, S. (2019). Hydrogenation of CO2 to Formate using a Simple, Recyclable, and Efficient Heterogeneous Catalyst. *Inorganic Chemistry, 58*, 3717–3723. https://doi.org/10.1021/acs.inorgchem.8b03336

Gunasekar, G. H., Park, K., Ganesan, V., Lee, K., Kim, N.-K., Jung, K.-D., & Yoon, S. (2017). A Covalent Triazine Framework, Functionalized with Ir/N- Heterocyclic Carbene Sites, for the Efficient Hydrogenation of CO2 to Formate. *Chemistry of Materials, 29*, 6740–6748. https://doi.org/10.1021/acs.chemmater.7b01539

Gunasekar, G. H., Shin, J., Jung, K.-D., Park, K., & Yoon, S. (2018). Design Strategy toward Recyclable and Highly Efficient Heterogeneous Catalysts for the Hydrogenation of CO2 to Formate. *ACS Catalysis, 8*, 4346–4353. https://doi.org/10.1021/acscatal.8b00392

Gunniya Hariyanandam, G., Hyun, D., Natarajan, P., Jung, K. D., & Yoon, S. (2016). An effective heterogeneous Ir(III) catalyst, immobilized on a heptazine-based organic framework, for the hydrogenation of CO2 to formate. *Catalysis Today, 265*, 52–55. https://doi.org/10.1016/j.cattod.2015.10.037

Liu, Q., Yang, X., Li, L., Miao, S., Li, Y., Li, Y., Wang, X., Huang, Y., & Zhang, T. (2017). Direct catalytic hydrogenation of CO2 to formate over a Schiff-base-mediated gold nanocatalyst. *Nature Communications, 8*(1), 1407. https://doi.org/10.1038/s41467-017-01673-3

Lu, Q., & Jiao, F. (2016). Electrochemical CO2 reduction: Electrocatalyst, reaction mechanism, and process engineering. *Nano Energy*, *29*, 439–456. https://doi.org/10.1016/j.nanoen.2016.04.009

Ma, M., Cheng, X., Shi, Z., Zhang, C., Li, Y., Yang, Y., Gong, C., Zhang, Z., Fei, H., Zhu, C., He, Y., & Xie, E. (2022). Role of N in Transition-Metal-Nitrides for Anchoring Platinum-Group Metal Atoms toward Single-Atom Catalysis. *Small Methods*, *6*(7), 2200295. https://doi.org/10.1002/smtd.202200295

Matsubu, J. C., Yang, V. N., & Christopher, P. (2015). Isolated metal active site concentration and stability control catalytic CO2 reduction selectivity. *Journal of the American Chemical Society*, *137*(8), 3076–3084. https://doi.org/10.1021/ja5128133

Mori, K., Taga, T., & Yamashita, H. (2017). Isolated Single-Atomic Ru Catalyst Bound on a Layered Double Hydroxide for Hydrogenation of CO2 to Formic Acid. *ACS Catalysis*, *7*, 3147−3151. https://doi.org/10.1021/acscatal.7b00312

Navarro-Jaén, S., Virginie, M., Bonin, J., Robert, M., Wojcieszak, R., & Khodakov, A. Y. (2021). Highlights and challenges in the selective reduction of carbon dioxide to methanol. *Nature Reviews Chemistry*, *5*(8), 564–579. https://doi.org/10.1038/s41570-021-00289-y

Nguyen, L. T. M., Park, H., Banu, M., Kim, J. Y., Youn, D. H., Magesh, G., Kim, W. Y., & Lee, J. S. (2015). Catalytic CO2 hydrogenation to formic acid over carbon nanotube-graphene supported PdNi alloy catalysts. *RSC Advances*, *5*(128), 105560–105566. https://doi.org/10.1039/c5ra21017h

Ou, M., Tu, W., Yin, S., Xing, W., Wu, S., Wang, H., Wan, S., Zhong, Q., & Xu, R. (2018). Amino-Assisted Anchoring of CsPbBr 3 Perovskite Quantum Dots on Porous g-C 3 N 4 for Enhanced Photocatalytic CO 2 Reduction . *Angewandte Chemie*, *130*(41), 13758–13762. https://doi.org/10.1002/ange.201808930

Park, H., Lee, J. H., Kim, E. H., Kim, K. Y., Choi, Y. H., Youn, D. H., & Lee, J. S. (2016). A highly active and stable palladium catalyst on a g-C3N4 support for direct formic acid synthesis under neutral conditions. *Chemical Communications*, *52*(99), 14302–14305. https://doi.org/10.1039/c6cc07401d

Park, K., Gunasekar, G. H., Prakash, N., Jung, K. D., & Yoon, S. (2015). A Highly Efficient Heterogenized Iridium Complex for the Catalytic Hydrogenation of Carbon Dioxide to Formate. *ChemSusChem*, *8*(20), 3410–3413. https://doi.org/10.1002/cssc.201500436

Richard, A. R., & Fan, M. (2017). Low-Pressure Hydrogenation of CO2 to CH3OH Using Ni-In-Al/SiO2 Catalyst Synthesized via a Phyllosilicate Precursor. *ACS Catalysis*, *7*(9), 5679–5692. https://doi.org/10.1021/acscatal.7b00848

Shao, X., Xu, J., Huang, Y., Su, X., Duan, H., Wang, X., & Zhang, T. (2016). Pd@C3N4 Nanocatalyst for Highly Efficient Hydrogen Storage System Based on Potassium Bicarbonate/Formate. *AIChE Journal, 62*(7), 2410–2418. https://doi.org/10.1002/aic.15218

Singh, V., Jang, S., Vishwakarma, N. K., & Kim, D. P. (2018). Intensified synthesis and post-synthetic modification of covalent organic frameworks using a continuous flow of microdroplets technique. *NPG Asia Materials, 10*(1). https://doi.org/10.1038/am.2017.209

Wang, Q., Santos, S., Urbina-Blanco, C. A., Hernández, W. Y., Impéror-Clerc, M., Vovk, E. I., Marinova, M., Ersen, O., Baaziz, W., Safonova, O. V., Khodakov, A. Y., Saeys, M., & Ordomsky, V. V. (2021). Solid micellar Ru single-atom catalysts for the water-free hydrogenation of CO2 to formic acid. *Applied Catalysis B: Environmental*, *290*(November 2020), 1–9. https://doi.org/10.1016/j.apcatb.2021.120036

Wang, S., Hou, S., Wu, C., Zhao, Y., & Ma, X. (2019). RuCl3 anchored onto post-synthetic modification MIL-101(Cr)-NH2 as heterogeneous catalyst for hydrogenation of CO2 to formic acid. *Chinese Chemical Letters*, *30*(2), 398–402. https://doi.org/10.1016/j.cclet.2018.06.021

Yang, G., Kuwahara, Y., Mori, K., Louis, C., & Yamashita, H. (2021a). Pd–Cu Alloy Nanoparticles Confined within Mesoporous Hollow Carbon Spheres for the Hydrogenation of CO 2 to Formate. *The Journal of Physical Chemistry C*, *125*, 3961−3971. https://doi.org/10.1021/acs.jpcc.0c10962

Yang, G., Kuwahara, Y., Mori, K., Louis, C., & Yamashita, H. (2021b). PdAg alloy nanoparticles encapsulated in N-doped microporous hollow carbon spheres for hydrogenation of CO2 to formate. *Applied Catalysis B: Environmental*, *283*(June 2020), 119628. https://doi.org/10.1016/j.apcatb.2020.119628

Yang, Z. Z., Zhang, H., Yu, B., Zhao, Y., Ji, G., & Liu, Z. (2015). A Tröger’s base-derived microporous organic polymer: Design and applications in CO2/H2 capture and hydrogenation of CO2 to formic acid. *Chemical Communications*, *51*(7), 1271–1274. https://doi.org/10.1039/c4cc08295h

Zhang, W., Yang, Y., Li, Y., Li, F., & Luo, M. (2023). Recent progress on integrated CO2 capture and electrochemical upgrading. *Materials Today Catalysis*, *2*, 100006. https://doi.org/10.1016/j.mtcata.2023.100006

Zhou, Y., Sadia Traore, A., Peron, D. V., Barrios, A. J., Chernyak, S. A., Corda, M., Safonova, O. V., Iulian Dugulan, A., Ersen, O., Virginie, M., Ordomsky, V. V., & Khodakov, A. Y. (2023). Promotion effects of alkali metals on iron molybdate catalysts for CO2 catalytic hydrogenation. *Journal of Energy Chemistry*, *85*, 291–300. https://doi.org/10.1016/j.jechem.2023.06.019

General Conclusions and Perspectives

Energy and environmental impacts are currently crucial issues driving industrial processes (Santos & Alencar, 2019). To tackle the challenges imposed by global warming, an urgent action in terms of decreasing, and eventually stopping, CO_2 emissions is required (Modak et al., 2021). Over the past decades, this necessity drove to an intense research not only into the development of more efficient CO_2 capture technologies but also into methods for the valorization of this carbon containing feedstock.

The use of biomass as raw material for the green syngas production is pointed as a great sustainable route (Santos & Alencar, 2019). The transformation of CO and CO_2, gases directed related to the greenhouse effect, into valuable chemicals products and platform molecules is indeed a good and promising alternative(Q. Cheng et al., 2018).

The search for processes that are able to improve the utilization of renewable carbon resources that lean towards to replace non-renewable fuels in a wide range of applications is a continuous and increasing concern. Technologies of biomass and waste gasification coupled to Fischer-Tropsch synthesis constitute an integrated chemical process to obtain chemical intermediates and fuels from biomass (Santos & Alencar, 2019).

Scientific research on catalysts for CO and CO_2 hydrogenation, is required to enable the development of the field and the large-scale production according to the technical and environmental regulations. Nowadays, Fischer-Tropsch (FT) synthesis is considered a mature technology (Santos & Alencar, 2019), however, even after more than 80 years of research, the unraveling and deeply understanding of the chemistry fundamentals continues to be a challenge for scientists (E. De Smit & Weckhuysen, 2008).

The current outlook of FT process needs improvements to ensure a competitive position in the energy market (Santos & Alencar, 2019). To reach a sustainable FT process performance, it is required efficient catalysts with extended lifetime and selectivity and a detailed description of reaction kinetics to maximize the commercial-scale reactor design.

Exploration of the potential of different support materials for mediation of metal active species in CO and CO_2 hydrogenation reactions, combined with the evaluation of synergic effects between the support materials and the metal species along with their catalytic performance, is the main goals of this thesis. It is an efficient and robust research strategy to contribute to the advancement of industrial and environmental sustainability.

General conclusion

The most important stages in the design of FT catalysts are the synthesis, the characterization and the evaluation of catalytic performance. The different routes of catalysts synthesis, pretreatments and activation may provide efficient tools in order to control the structure and the chemical, physical and mechanical properties of the catalysts. The catalyst should exhibit high stability during FT synthesis and its cost should be moderate to allow possible industrial utilization.

The goal of FT catalyst preparation is to generate a significant concentration of stable metal surface sites. The size of supported metallic or carbide nanoparticles could be also important. The equilibrium between dispersion and reducibility of metal species can be obtained using different supports, pretreatments and methods of deposition.

In this work, we were able to synthetize iron and copper mono- and bimetallic catalysts, supported in multi-walled highly nanotubes, which were submitted to two different pretreatment procedures. The confinement of these metal species is important, since it may enhance reaction rates and selectivity, stabilize reactive and/or unstable molecules and even change its physical properties.

The FT synthesis was performed using the Fe and Cu-based catalysts in order to investigate the nanoconfinement effects and the intrinsic activity of these metals. The complexity of the iron chemical structure and its dynamic nature under FT conditions complicate any straightforward interpretation of structure-catalytic performance relationships (E. De Smit & Weckhuysen, 2008). Moreover, many significant modifications of catalyst structure could occur during the FT reactor start up and on-stream during FT synthesis, which could be related to different phenomena.

Interestingly, the approach using bimetallic iron-copper catalysts resulted in a high CO hydrogenation rate. A remarkable mobility of both metal species during activation and reaction conditions, that may occur due to the CNTs defects provoked in the pretreatment and impregnation procedures, resulted in the enhancement of iron-copper interaction. The understanding of the catalyst modifications under the influence of the FT reaction medium represents a significant challenge in the design of FT catalysts. The most relevant information about the active phases could be extracted from in-situ and operando measurements because the catalyst structure and catalytic performance can evolve during different pretreatments and FT reaction.

We performed near ambient pressure X-Ray photoelectron spectroscopy (NAP-XPS) to observe and evaluate the modifications of the studied catalysts during the catalyst activiation and reaction. The observed transformation and migration of iron and copper species affected the localization of these metal species and the interaction between them.

Interetsingly, the number of the iron active sites interacting with copper is not much affected by the initial localization of these two species deposited over CNT during the impregnation but by the migration of iron and copper during the catalyst activation and catalytic reaction. Moreover, the nanoconfinement contributed to the relative stability of iron nanoparticles inside CNTs. However, for monometallic catalysts, the catalytic performance is principally a function of iron dispersion, while the intrinsic activity of iron sites (TOF) is not much influenced by the nanoconfinement inside CNTs.

Regarding the hydrogenation of CO_2 to formates, although several catalytic systems have been proven to work and to produce formates at decent reaction rates, to the best of our knowledge, the economic feasibility of this technology has not been demonstrated. Formic acid is seen as a potencial way of chemically storing hydrogen, due to its advantages to storage, easy handling, refueling, and transportation (Bulushev & Ross, 2018). The catalyst is the key component of different CO_2 hydrogenation processes (Sun et al., 2021). A suitable catalyst reduces the energy consumption and facilitate the elementary steps. Generation of a specific product with high selectivity will greatly reduce the cost of separation and purification.

The catalytic reduction of CO_2 with H_2 is complicated, due to the requirementes for the simultaneous activation of both gases. Covalent organic frameworks (COFs), new and promising materials, have been found to show applications in many fields, suggesting their versatile application as porous materials. Besides, COFs have some advantages over conventional porous materials, such as the crystalline nature of their frameworks that allows the dispersion of catalytically active sites in large-range ordered structures and the possibility to introduce compatible multi-active sites, tuning these materials towards a plenty of different applications.

Currently, COF-based catalytic systems active in CO_2 hydrogenation under mild conditions are still limited. In general, the COFs design allows its pores to be decorated with various catalytic active sites, becoming a supported catalyst with tunable properties. The well dispersed isolated single atom sites and confinement effects can lead to superior performance in comparison with homogeneous catalysts. Particularly, covalent triazine framework (CTF) supported Ir complex catalysts could promote the synthesis of formic acid with high efficiency. The imine-linked COFs have been widely exploited in gas separation, sensing, photon conduction, drug delivery, chiral chemistry and optoelectronics fields.

We have synthetised enamine, azine and imine-linked COFs and impregnate them with ruthenium chloride. In the fresh catalysts, Ru is coordinated by chlorine and located in a close interaction with nitrogen containing groups of COFs and the chlorine atoms are removed from the catalysts during the reaction. The COFs used allowed the high dispersion of ruthenium which resulted in a large fraction of ruthenium single atom species.

The application of Tp and TFB-COFs for CO_2 hydrogenation to formic acid revealed the strong effect of the COFs structure on the catalytic performance of the Ru catalysts. While various catalyst parameters can influence catalytic performance, it was observed that the intinsic reaction rate of CO_2 hydrogenation (TOF) exhibited a nearly proportional relationship with the density of nitrogen species in the COF framework. The N-content of COFs also affected the ruthenium dispersion and anchored, higher the N-fraction, higher the fraction of single-atom Ru sites. The total weight-normalized activity of Ru catalysts was proportional to the total number of Ru single sites and their intrinsic catalytic activity. The stability of the catalyst is attributed to its capability of prevent the reduction of Ru into metallic phase during reaction. We investigated these Ru/COFs catalysts using *in-situ* X-Ray absorption spectroscopy (XAS) which allowed to obtain an evolution of the ruthenium phases during reaction, along with an approximated composition profile of the catalysts before and after reaction.

The approach based on the use of Tp and TFB-COFs as supports for Ru catalysts for CO_2 hydrogenation to formic acid improves Ru dispersion, even at higher amounts, prevents the sintering of the catalyst, and enables reaching the highest overall reaction rates. The proposed strategy can further be extended for the design of others single atoms catalysts supported by COF for different reactions.

Perspectives

The design of catalysts for FT synthesis that present a better balance between activity, selectivity and stability is still a fundamental necessity. Along with the activity-selectivity balance, the cost of catalysts production and its recyclability are two important factors that can not be dismissed. To elevate the scale and TRL level from laboratory to industrial one, the challenge is even bigger. However, the fundamental understanding of the catalytic process, at a nanoscale or atomic level, is also necessary for the elucidation of the parameters affecting the reaction, to enable the achievement of the final goal: the ideal FT catalyst.

To study the mechanisms of CO and CO_2 conversions, efficient tools should be used, both experimental and computational. The catalyst characterization techniques are always in development and older techniques have been constantly improved. Along with the many available techniques, the most important and promising developments in catalyst characterization are increasing applications of the in-situ techniques. This approach enables the study of catalysts during the different stages of pretreatments and reactions, even at conditions near to the actual one, thus gaining important insights into the structure-performance of the catalyst.

Another important field that requires selectivity’s improvement is the low temperature process. The homogeneous catalysts are the predominant option for industrial process, which explains why the design of effective and stable heterogeneous catalysts is extremely demanding. Exploring new and existing materials for the preparation of heterogeneous catalysts, evaluation of reaction conditions, solvents and promoters, together with the investigation of the mechanisms involved and the main parameters affecting activity and stability, are the keys for satisfying this demand (Bulushev & Ross, 2018).

Without doubt, we can afirm that COFs have enormous potential as smart materials making possible to achieve great advancements within the field of heterogeneous catalysis. Although the number of reports on COFs applied to CO and CO_2 hydrogenation reactions is still limited, this area will expand rapidly (Abednatanzi et al., 2022). The particular advantage of COF materials is the opportunity to achieve a higher density of single-atom sites, resulting in higher reported weight-based catalytic performance.

Despite much progress being made over the last 5 years, the structure-performance relationships of COFs remains uncertain and the elaboration of functional COFs with desired characteristics remains a challenging work (Bagheri et al., 2021).

The COF-based systems for CO_2 conversion must evolve to a possible large-scale use in industry, where the preparation of the catalyst needs to be economic. But so far, the cost of COFs-based materials is relatively high and needs to be lowered for large-scale production.

The process optmization requires mild conditions to decrease the cost of energy and higher life span of the catalyst. The reactor design could also evolve, which means modification of the shape of catalysts from powders (the actual form and not so industrially favorable) to porous granules or coated membranes. These improvements may lead to better catalytic performance and selectivity (Garba et al., 2021).

The interest in using confinement to accelerate reactions and enhance selectivity is still a hot topic, however there is not much literature describing the ways in which confined spaces stabilize reactive species, and even less reports describing the ways in which confined spaces modulate the physical properties of molecules (Grommet et al., 2020).

Future advancements should achieve a greater understanding of the synergy between nanoconfinement and reactive species and molecules (Grommet et al., 2020).

References

Abednatanzi, S., Najafi, M., Gohari Derakhshandeh, P., & Van Der Voort, P. (2022). Metal- and covalent organic frameworks as catalyst for organic transformation: Comparative overview and future perspectives. *Coordination Chemistry Reviews*, *451*, 214259. https://doi.org/10.1016/j.ccr.2021.214259

Bagheri, A. R., Aramesh, N., Sher, F., & Bilal, M. (2021). Covalent organic frameworks as robust materials for mitigation of environmental pollutants. *Chemosphere*, *270*, 129523. https://doi.org/10.1016/j.chemosphere.2020.129523

Bulushev, D. A., & Ross, J. R. H. (2018). Heterogeneous catalysts for hydrogenation of CO 2 and bicarbonates to formic acid and formates. *Catalysis Reviews*, *60*(4), 566–593. https://doi.org/10.1080/01614940.2018.1476806

Cheng, Q., Tian, Y., Lyu, S., Zhao, N., Ma, K., Ding, T., Jiang, Z., Wang, L., Zhang, J., Zheng, L., Gao, F., Dong, L., Tsubaki, N., & Li, X. (2018). Confined small-sized cobalt catalysts stimulate carbon-chain growth reversely by modifying ASF law of Fischer–Tropsch synthesis. *Nature Communications*, *9*(1), 3250. https://doi.org/10.1038/s41467-018-05755-8

De Smit, E., & Weckhuysen, B. M. (2008). The renaissance of iron-based Fischer-Tropsch synthesis: On the multifaceted catalyst deactivation behaviour. *Chemical Society Reviews*, *37*(12), 2758–2781. https://doi.org/10.1039/b805427d

Garba, M. D., Usman, M., Khan, S., Shehzad, F., Galadima, A., Ehsan, M. F., Ghanem, A. S., & Humayun, M. (2021). CO2towards fuels: A review of catalytic conversion of carbon dioxide to hydrocarbons. *Journal of Environmental Chemical Engineering*, *9*(2), 104756. https://doi.org/10.1016/j.jece.2020.104756

Grommet, A. B., Feller, M., & Klajn, R. (2020). Chemical reactivity under nanoconfinement. *Nature Nanotechnology*, *15*(4), 256–271. https://doi.org/10.1038/s41565-020-0652-2

Modak, A., Ghosh, A., Bhaumik, A., & Chowdhury, B. (2021). CO2 hydrogenation over functional nanoporous polymers and metal-organic frameworks. *Advances in Colloid and Interface Science*, *290*, 102349. https://doi.org/10.1016/j.cis.2020.102349

Santos, R. G. dos, & Alencar, A. C. (2019). Biomass-derived syngas production via gasification process and its catalytic conversion into fuels by Fischer Tropsch synthesis: A review. *International Journal of Hydrogen Energy*, *xxxx*. https://doi.org/10.1016/j.ijhydene.2019.07.133

Sun, R., Liao, Y., Bai, S. T., Zheng, M., Zhou, C., Zhang, T., & Sels, B. F. (2021). Heterogeneous catalysts for CO2hydrogenation to formic acid/formate: From nanoscale to single atom. *Energy and Environmental Science*, *14*(3), 1247–1285. https://doi.org/10.1039/d0ee03575k

Scientific communication

Published paper: **Fellenberg Ana K.**, Ahmed Addad, Jingping Hong, Pardis Simon, Yuliia Kosto, Břetislav Šmíd, Gang Ji, Andrei Y. Khodakov. *Iron and copper nanoparticles inside and outside carbon nanotubes: Nanoconfinement, migration, interaction and catalytic performance in Fischer-Tropsch synthesis*. Journal of Catalysis, 404, 2021, 306-323.

Accepted paper: **Fellenberg Ana K.**, Ahmed Addad, Sergei A. Chernyak, Yong Zhou, Massimo Corda, Danilo O. de Souza, Olga V. Safonova, Vlad Martin-Diaconescu, Vitaly V. Ordomsky, Gang Ji, Andrei Y. Khodakov. *Covalent Organic Frameworks for Design of Ruthenium Catalysts with High Single-Atom Site Density for* CO_2 *Hydrogenation into Formic Acid*. Cell Reports Physical Science, 2024.

Conference: **Ana K. Fellenberg**, Ahmed Addad, Jingping Hong, Pardis Simon, Yuliia Kosto, Břetislav Šmíd, Gang Ji and Andrei Y. Khodakov. The role of nanoconfinement of iron and copper nanoparticles in carbon nanotubes applied in Fischer-Tropsch synthesis. European Congress and Exhibition on Advanced Materials and Process, 2021, oral presentation.

Acknowledgements

First of all, I would like to thank my supervisors Dr. Andrei Khodakov and Dr. Gang Ji for all their support and guidance during my thesis. The opportunity you gave me is for sure the most important step for my professional career. Thank you very much to accepted me and trusted me to develop this project. Above all, thank you very for your understanding in all the difficult moments. Without doubt you were fundamental to the development of this work.

I wish to express my gratitude to all the members of UMET and to the entire UCCs team for their warm reception. I would like to extend my gratitude to all people who collaborated, somehow, to this work, hopping not forget to mention anyone. Thank you very much to Ahmed Addad for his dedication and commitment. I thank Pardis Simon for her assistance and excellence in work. Thanks to Danilo de Souza for the fruitfull discussions and imparted knowledge. I also would like to thanks Jingping Hong, Yuliia Kosto, Břetislav Šmíd, Sergei Chernyak, Yong Zhou, Massimo Corda, Olga Safonova, Vlad Martin-Diaconescu, Vitaly Ordomsky, Olivier Gardoll, Joëlle Thuriot-Roukos, Jean-Charles Morin, Martine Trentesaux, Marc Bria, Bertrand Revel, Laurence Burylo, Florent Blanchard, Melanie Dubois and Stephane Chambrey.

I want to thank to the friendship builded during these years, specially to Paola Arango for her unbelievable patience and for the love and care she always dedicated to me (Paoliiita: gracias por compartir la vida conmigo, por la terapia gratis, gracias por corregir mi español tan corroncho y por la comida); and Jiyng, my best photographer and tent partner, long-distance friend and retired office colleague (looking forward to your vacations in France); I am sure this journey was challenging for us, but we supported each other and we made it. Thank to Alan Barrios, for his priceless partnership (which included move equipments and gas bottles even when is raining), thanks for always listening me, for all the moments you helped me, gracias por los chismes y chistes. Amaury, thanks for your amazing friendship, listening and for your patient (merci pour les classes de français). I had the pleasure of meeting many special and dear people who were also part of my journey: Josué, Yamid, Maria, Ines and Ruth (Alvaro, Sara and soon Emma). I was really lucky to meet such good people.

Finally, I thank my family, my mom Dalia and my father Ernesto, *in memorian*, for raising me the best you could, thanks for the principles and lessons I have learned with you. Thank to my

sister Soila, my best example of woman, you showed me what means to be resilient. Thank to my husband Tiago for loving and believing me, even when I no longer did (te amo marido). I also thanks for the emotional support of Banguela, Dakota, Camila, Coline and the substantial help of lamotrigine, lorazépam, amitriptyline, mirtrazapine and sertraline.